Structural behaviour of contemporary vaulted spaces with complex ashlars: the Abeille’s sail vault

Politecnico di Bari

Maria Francesca Sabbà

Structural behaviour of contemporary vaulted spaces with complex ashlars: the Abeille's sail vault

Philosophiae Doctor Thesis
DESIGN FOR HERITAGE: KNOWLEDGE AND INNOVATION
SSD: ICAR/09 – STRUCTURAL ENGINEERING

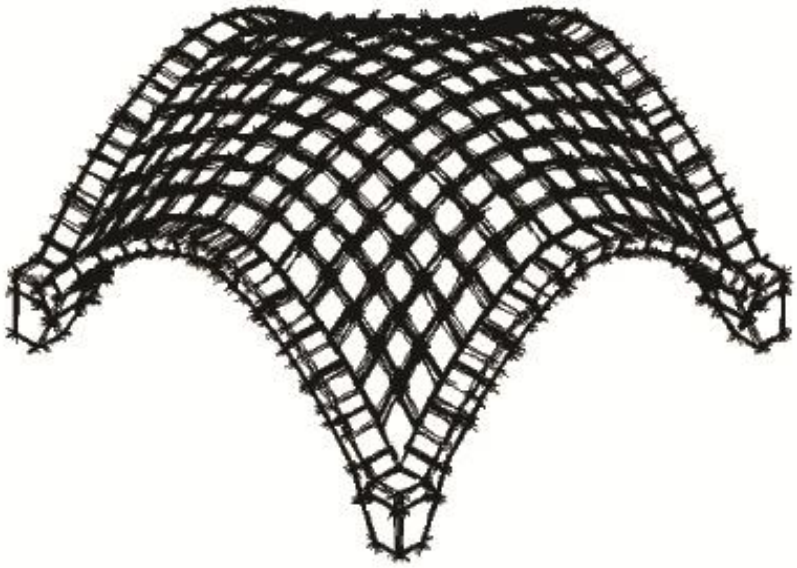

Supervisor: Prof. Dora Foti
Co-Supervisor: Prof. Giuseppe Fallacara
Coordinator of Ph.D. Program: Prof. Carlo Moccia

ArCoD Politecnico di Bari
DIPARTIMENTO DI ARCHITETTURA, COSTRUZIONE E DESIGN

2023 – XXXV Cycle

*"Un concio alla **VOLTA**..."*

*Cit. **A. M.***

INDEX

ABSTRACT

The aim of the research is to investigate the static and dynamic behaviour of contemporary vaulted spaces, generated by the *Flat Vault of Abeille* patented in 1699. In fact, its reinterpretation and its use in architecture can both enhance the existing architectural heritage and characterize the new construction of building through the use of traditional construction materials and techniques. It follows that the identification of this "new type" of vault is essential to design it correctly and to optimize the geometry for structural purposes.

The *Abeille-Type* ashlar is a polyhedron that has two axial sections, in the shape of an isosceles trapezoid, oriented in opposite directions. The arrangement of the ashlar takes place in the two orthogonal directions creating a bidirectional flat plate, with a single type of optimized ashlar, whose geometry guarantees the mutual support of the individual blocks of the vaulted system, once assembly is complete. Starting from this ashlar and applying its deformation on curved surfaces, it is therefore possible to design "contemporary" types of vaults, characterized by complex ashlars in order to optimized both an aesthetic-formal and a structural function.

The research proposes to apply already consolidated structural analysis methodologies – on traditional vaults – on this structure and describes the results of an experimental with quasi-static tests on a 1:8 small-scale vault model made of 3D printed blocks assembled with dry joints. In particular, shear in-plane and tilting tests were carried out by means of manual actuators and controlled with incremental displacements. Different configurations are investigated both for the shear failure (simple or pure shear) and the tilting collapse (different in-plane angle). The results experimentally obtained were analysed in terms of damage/collapse mechanisms, strengths capacity and ultimate displacements.

The Distinct Element Method (DEM) will be used for the numerical analyzes, being until now the most accurate and realistic for masonry structures, since it can take into consideration their discontinuous nature and the interlocking/toothing of the individual elements. In fact, it allows to investigate the vault ashlars as rigid and separate entities, witch interact with each other through the block planar interfaces; so the stability and the deformation of the whole vault is managed by the join contacts.

Both experimental and numerical results furnish important data to formulate the behaviour of this vault. After the validation the results are extended to a full-scale vault by means of the similarity criteria, whose efficacy in the generalization of the results from the model to the prototype is demonstrated. In this way, the model can be finally adopted to simulate the behaviour of a contemporary vault with the *Abeille-Type* ashlars.

Keywords: Abeille's vault, dry-joint arch, masonry vault, tilting test, in-plane shear mechanism, out-of-plane, Distinct Element Method (DEM).

1. INTRODUCTION AND STATE OF ART

1.1. General context and purpose

In recent years, in the field of construction techniques, an important and increasingly investigated topic is the analysis of the structural behaviour of masonry vaults, since they represent one of the most recurrent types of horizontal structural elements in traditional architecture and historic buildings, widespread on a large scale in all European countries. However, this structural typology is among the most vulnerable supporting elements to dynamic actions, as is also demonstrated by the numerous post-earthquake inspection campaigns – systematically carried out on churches, monumental and ordinary buildings in historic centers – in Italy (Amatrice 2016, Emilia 2012, L'Aquila 2009) and in other European country (Lorca 2011, Mamurras 2019), all areas characterized by a high level of seismicity. Therefore, the evaluation of their structural safety and the determination of their mechanical behaviour were of primary importance for engineering and architectural research to preserve the historical heritage and for the economic and social implications resulting from their damage or collapse. Of particular importance were the studies and experiments conducted by Van Mele and Mc Inerney (McInerney & Dejong, 2015; van Mele et al., 2012), for the quasi-static tests, and by DeJong, De Lorenzis and Ochsendorf (de Lorenzis et al., 2007; DeJong & Ochsendorf, 2006) for the dynamic ones.

Several studies have been devoted to the structural behaviour of masonry vaults. The use of limit analysis, introduced by Heyman (Heyman, 1978, 1995), provides fundamental information regarding static behaviour and stability. Many experimental studies analyzed the structural behaviour of arches and vaults under horizontal actions, focusing particularly on their dynamic response (Bianchini et al., 2019, 2022; de Lorenzis et al., 2007; Gaetani et al., 2016; Shapiro, 2012; Silvestri et al., 2021; Williams et al., 2012). Other researches were focused on displacement-controlled tests by applying widening and closing displacements at the springings, but mainly at static conditions (Carfagnini et al., 2018; G. Milani et al., 2016; Theodossopoulos et al., 2016) or quasi-static (Gaetani et al., 2016; G. Milani et al., 2016). All these works have used computational methods to investigate the strength of these forms, including Finite Element Method (FEM) and/or Distinct Element Method (DEM) approaches.

Starting from this topic, it was decided to expand the investigations not only on the known types of vaulted spaces but also on new ones. There are two reasons, to revive traditional construction techniques – such as stone masonry – for new constructions, experimenting with new forms and the possibility of a more considered and suitable for damaged buildings, generally belonging to the historical heritage or, thus following *Valadier*'s acclaimed theories of restoration for which the distinguishability of the integrative intervention with respect to the pre-existing part is preferable, integrating the gaps in a recognizable way through the distinction of the material or the shapes. In this perspective or in the perspective of expan-

sions/integrations on existing historical structures, the idea of reinterpreting the *Flat Vault of Abeille*, patented in 1699, is based. The aim of the research is to investigate the structural behaviour of contemporary vaulted spaces, generated by complex ashlars. In fact, its reinterpretation and its use in architecture can both enhance the existing architectural heritage and characterize the new construction of building through the use of traditional construction materials and techniques. The DEM will be used for the analyses, being until now among the most accurate and realistic for masonry structures, since it considers their nature and the toothing of the individual elements. In fact, it allows to investigate the vault ashlars as separate and interacting entities/blocks, which through planar interfaces interact with each other, deforming, thus being able to manage contact and stability.
So, the aim of this research is the study of the mechanical behaviour of contemporary vault spaces (*cross*, *sail*, etc.) on curved spatial geometries starting from the *Abeille-Type* ashlar.
The methodology will include:

- Optimization of the vault model with structural purposes for the various types, choosing one case study;
- Identification of the structural behaviour (shear and horizontal loads) of *Abeille's* vault chosen, with quasi-static experimental tests through a small-scale model made with 3D-Printing;
- Realization of numerical DEM model, to investigate the interfaces of the individual monolithic blocks and the overall behaviour of the structure;
- Comparison and validation of the investigated contemporary vaulted spaces with *Abeille-Type* ashlar.

1.2. Research goals

The proposed project focuses on the seismic behaviour of contemporary and complex vaults, based on stereotomic geometry, to understand the structural behaviour and the vulnerability of this vaulted elements. Within the global context examined, this research work proposes an approach for the validation of small-scale models of masonry structures using distinct element analysis. This allows to reproduce the specific conditions that characterize the mechanical behaviour of real masonry structures. So, by exploiting the possibilities offered by 3D printing technologies and the consequent creation of models – that are only apparently different from masonry structures in real scale, as they are capable of consistently simulating the interfacial conditions between the ashlar s– it is possible to analyse and define the real structural behaviour of the vaults in question. Finally, the expected outcome will be the understanding of the modes of failure (cracking patterns and collapse mechanisms) of complex vaults under quasi-static dynamic excitations to correctly design these "new" vaults. In fact, the structural behaviour of a complex spatial vaults (sail/domed vault) with the Abeille-Type ashlar has never been directly studied before.

1.3. Outline of the thesis

The thesis is divided into six chapters. In the first chapter the context and the general goals are explained, in addition to the state of art, viz. the overview of the theories and experiments present in the scientific literature on the behaviour of masonry structures subjected to static and dynamic actions.
The second chapter summarizes the problems concerning the structural behaviour of masonry vaults and the related theories of mechanics; furthermore, the approaches to modeling at global and local scales for a material that follows Heyman's Theory –"Non-Resistant to Tensile" (Heyman, 1995)– are explored.
The third chapter explains the theory at the basis of the Distinct Element Method (DEM) and, in particular, the laws at the basis of the contacts between the rigid element interfaces, specifying the theory on which the software used for the numerical analyses of the research is based.
In the fourth chapter, the theory of the design of the scale tests is reported through the similarity criteria and the 3D-printed model produced with the mechanical characterization of the material are described in detail. The set-up and the results of all the experimental tests performed and analyzed in the laboratory are also presented.
The fifth chapter is dedicated to the description and validation of the numerical simulation of the tests carried out experimentally, therefore the set-ups and the results are reported. A full-scale simulation is also shown.
The last chapter is dedicated to a reflection on the results obtained from the experimental and numerical tests performed on the model and on the critical issues encountered, as well as possible future applications.

1.4. State of arts on the vaults

1.4.1. Generalities and shape evolution

In the context of architectural and static solutions, the vaults are presented as elements with distinct structural configurations. They can be visually differentiated by their geometric shapes and classified into two main groups: translation vaults and rotation vaults. Translation vaults are formed by the movement of a straight line along a curve, while rotation vaults arise from the rotation of a curve around an axis. The *barrel vault* belongs to the first group and it is the simplest shape being composed of arches arranged side by side on two parallel walls. This type of vault is commonly utilized in elongated rooms due to its flexibility. The *cross vault* (or *groin vault*) and *pavilion or cloister vault* are formed by the intersection of two orthogonal barrel vaults, either by simple union or intersection of volumes. These vaults are characterized by four webs and four edges or ribs (Figure 1-1).

a. b. c.

Figure 1-1. Geometric configurations of vaults: a. barrel vault; b. cross vault; c. pavilion vault.

The barrel vaults, cross vaults and pavilion vaults belong to the most common typologies in historic buildings. On the other hand, the second group includes *domes* in their diverse shapes, *sail vaults*, and other derivatives that provide valuable aesthetic and formal solutions (Figure 1-2). Consequently, these forms are mainly employed in prestigious constructions of historical and cultural heritage.

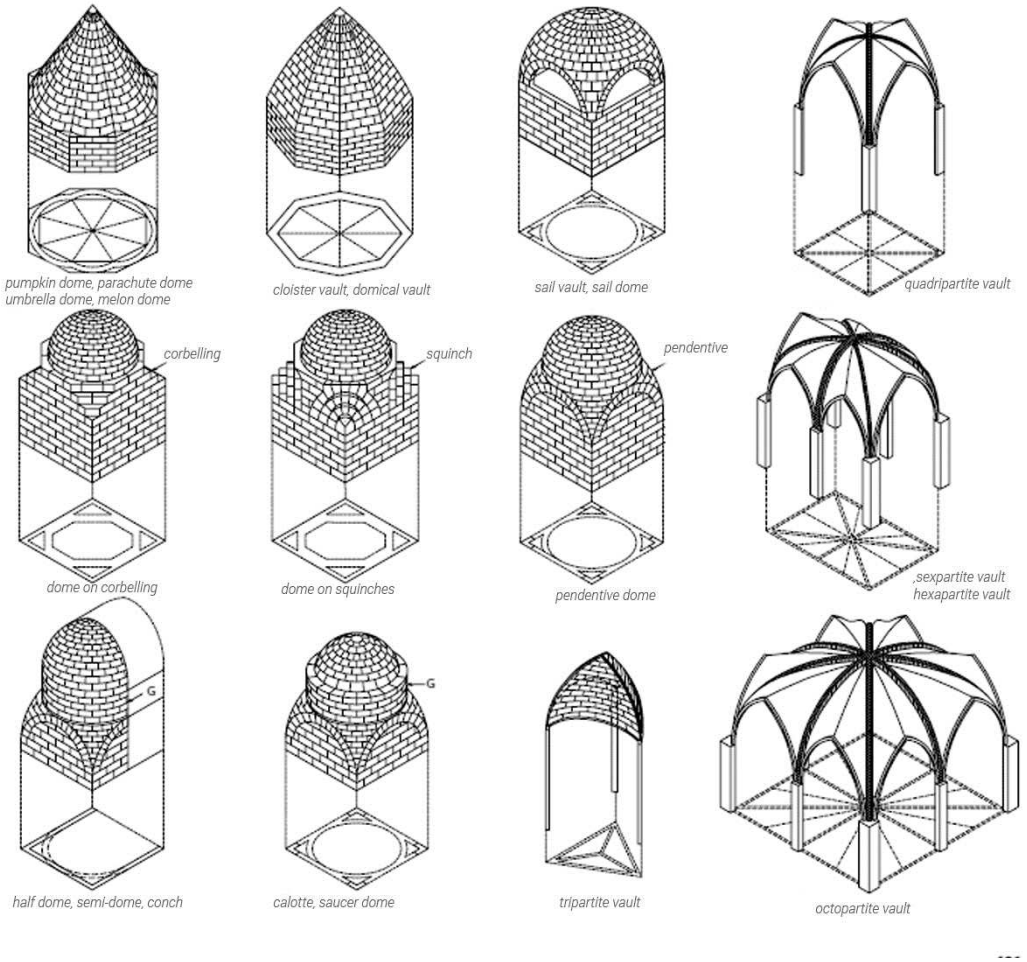

Figure 1-2. Domes, sail vaults and their derivates vaults (Davies & Jokiniemi, 2008)

Given the abundance of feasible geometric configurations, one may question the factors underlying the preference for specific typologies. Economic considerations, executive complexi-

ties, knowledge of techniques, availability, and properties of materials that best suit certain types are all likely to play a role. Static requirements, such as the distribution of weights and thrusts on the impost walls, as well as the need to create openings in the perimeter walls, and other constraints linked to the layout of the environment and intended use, offer a comprehensive perspective of the factors guiding the selection process. Notably, the self-weight of the vault significantly affects the static behaviour and is directly related to the geometric configuration of the structure. Specifically, for the same covered area, pavilion vaults exhibit considerably greater weight compared to barrel vaults due to the greater structural volume, whereas cross vaults are the lightest.

Additionally, the composition of the internal structure can vary widely, ranging from concretion of aggregates with different densities to brick, or even concretion with internal brick ribs, and so on.

The type of masonry pattern employed represents a significant feature of the building and plays a crucial role within a structural system that depends on the transfer of actions between the blocks composing the vault itself. For example, Figure 1-3 shows the case of cross vaults, by varying the masonry patterns –parallel and orthogonal– the behaviour changes. It can be assimilated as a three-dimensional shell in the parallel model and a set of adjacent arcs in the orthogonal model one.

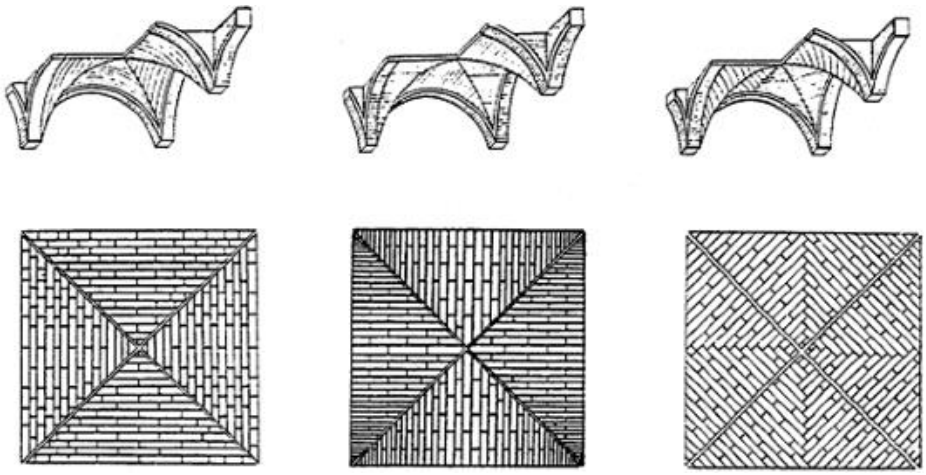

a. b. c.

Figure 1-3. Masonry schemes of a cross vault: a. parallel pattern; b. orthogonal pattern; c. herringbone pattern (Cattari et al., 2008).

To obtain a comprehensive understanding of the mechanical behaviour of vaults, it is important to investigate the similarities among these structural elements, which possess a natural ability to resist the stresses induced from static and dynamic loads. Given the diversification in shapes and conformation of vaulted ceiling systems, the task of analyzing the statics, the evolution of cracking states and dynamic behaviour in the event of collapse is inherently complex.

In light of the numerous possible geometric configurations, some factors favored certain vault types over others in different social and historical contexts. Therefore, the following para-

graphs provide a brief historical overview of the formal and technical advancements in masonry vaulted roofs throughout history.

1.4.2. Static of the vaults

In the field of architecture, vaults have been a recurring architectural and static solution, particularly in past architectural styles. The study of such artifacts requires historical knowledge of the design and sizing techniques employed in the past. This knowledge is also helpful in understanding the behaviour of an "*ashlar*" arch, which can be deduced from the initial arch based on an appropriate subdivision, particularly in its more recent evolutions. It is thus possible to manually analyze the behaviour of such arches from a static point of view.

During the early Roman imperial period, *Plinio the Elder* may have had direct testimony of the construction technique used for vaults, which involved the use of pozzolanic mortars with great binding capacity and light materials like tuff and pumice. This mixture, which was practically fluid during construction, was used to fill the empty spaces resulting from the lattices of brick arches that served as the ribs of the vault. The resulting mass was a single block that was highly rigid and capable of resisting the laws of statics and dynamics during an earthquake. *Plinio* himself considered corners walls, doorways, and vaults as the safest parts of a building during an earthquake, as he stated in his work "*tutissimi sunt aedificiorum fornices*" (Plinio the Elder, 78 C.E.).

While corner walls and doorways remain effective even with modern construction techniques and technologies, the effectiveness of vaults and domes has been questioned since the Lisbon disaster of 1755. Their use was eventually banned in construction techniques, which were sanctioned by specific regulations issued after the Calabrian-Sicilian earthquake of 1909.

In the construction of vaults, the horizontal forces resulting from ground movements can lead to disconnection and collapse of the structure. Contrary to what the Romans had done using pozzolanic mortars and lightweight masonry, in later periods, the vaults were built using stone that was shaped and placed in contact without the use of mortars, or with the interposition of thick layers of mortar that relied on the precision of the machined pieces or available materials on the construction site. These later constructions are highly sensitive to support movements and are susceptible to changes in shape without collapsing, except under extreme conditions such as earthquakes.

It should be noted that changes in shape under normal operating conditions generally occur in the mortar joints, which break and open, causing the faces of the masonry blocks to rotate with respect to each other or causing one block to slide relative to the other. The ability of thin masonry vaults to accommodate support movements with variations in shape is a characteristic that is absent in Roman vaults and in later constructions built using the same technique, which are much thicker than the maximum length of the covered compartment. To better understand this difference, it is advisable to begin by examining the simplest problem, that of the arch, before delving into the topic of vaults.

1.4.3. The origin of the masonry arch (Greek, Roman and Gothic architecture)

John Ruskin (1853) uses a few elementary symbols which allow him to establish the differences between Greek, Romanesque and Gothic architecture.

There are three fundamental symbols: a rectilinear segment (*flat lintel or arch* in Figure 1-4.a), an arched curvilinear segment (*round arch* in Figure 1-4.b), a segmental element with downward concavity (*triangular or pointed arch* in Figure 1-4.c). So combining these symbols it is possible to obtain abstract schemes, symbolic forms capable of recalling significant elements of the entire history of the built environment.

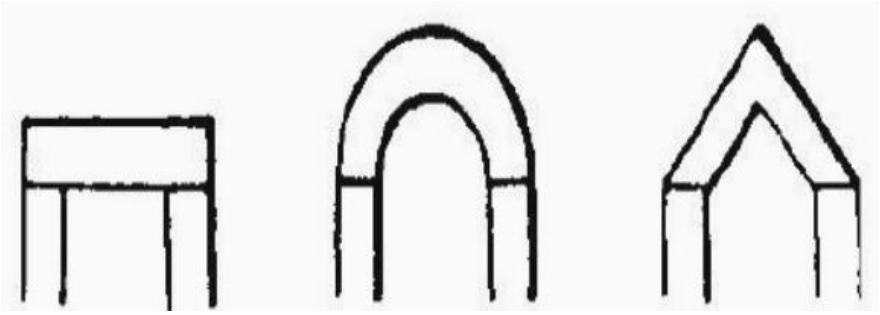

a. b. c.

Figure 1-4. Abstract symbol of arches:a. lintel arch for Greek architecture; b. round arch for Norman or Romanesque architecture; c. pointed arch for Gothic architecture (John Ruskin, 1853).

The arch is a structural element that can effectively absorb and distribute gravitational loads by utilizing its curved design. This results in predominantly compressive forces that act upon the ashlars comprising the arch. The vertical elements, known as piers, support the arch at its two ends, creating a mutual contrast. Rather than serving as a decorative element, the arch represents a static principle that embodies the isostatic compression of the structure. The *natural arch* concept emerged through observation of a wall with an opening. Above the inflected architrave, a breaking mechanism generates a crack between the stationary and moving masonry, which could potentially cause a portion of the wall to collapse while leaving the statics of the rest of the wall almost unaffected. This fissure, also known as a detachment line, forms an arc shape. (See Figure 1-5)

a. b.

Figure 1-5. Examples of natural crack with an arc path above an opening in the wall structure.

The initial attempts to apply the principle of the natural arch resulted in the assembling of masonry ashlars arranged with horizontal joints, each progressively projecting further, thus leading to the creation of pseudo-arches as *flat arch*. These rely on the cantilever balance, primarily governed by the equivalence of the external moment with that of the internal rotation of the constraint. As a result, there is a need for smaller protrusions and, consequently, pointed profiles closer to the ideal line. Occasionally, the inclined shape can acquire formal significance, making the structure lighter and achieving a continuous profile through the triangular conformation of the ashlars. Notably, the Lion Gate (Figure 1-6.a) and the entrance to the Treasury of Atreus (Figure 1-6.b), both in Mycenae (14^{th}-12^{th} century BC), exemplify this type of pseudo-arch. The first structural example shows the big squared stones utilized to construct the walls, where the doors consist of two jambs and an imposing lintel in a trilithic structure.

a. b.

Figure 1-6. Mycenae, Greece (14^{th}-12^{th} century BC): a. Lion Gate (https://i.pinimg.com/originals/ae/3a/75/ae3a7536ee8dd70e4d9ccdceb04ce4b2.jpg); b. Entrance to Treasury of Atreus (https://mydbook.giuntitvp.it/app/statics/contents/books/GIAC45_65685Q/html/60/assets/images/060_a.jpg).

Other examples in Italian peninsula are the tombs of Populonia. In particular, Figure 1-7 shows a tomb as aedicula of 6^{th}-5^{th} century BC, consisting of a rectangular chamber delimited by rows of local stone, covered by a watershed roof made of stone slabs perfectly moulded, with straight intrados and extrados.

Figure 1-7. Etruscan tomb, Populonia – Italy (https://blogcamminarenellastoria.files.wordpress.com/2021/07/8-la-tomba-del-bronzetto-di-offerente.jpg).

In this example the distance between the supporting walls, resembling columns, significantly

surpasses the limit stipulated by *Vitruvius* to avoid the breakage of a single block used as a lintel between two supporting walls. The arch is the simplest pushing structure that can be achieved with the minimum number of distinct and unconnected elements, facilitating an examination of its behaviour to highlight the fundamental aspects of arched constructions (Di Pasquale, 1996). For simplicity, Di Pasquale assumes that the supporting walls are composed of a single block and considers the generic vertical section of the building as shown in Figure 1-8.

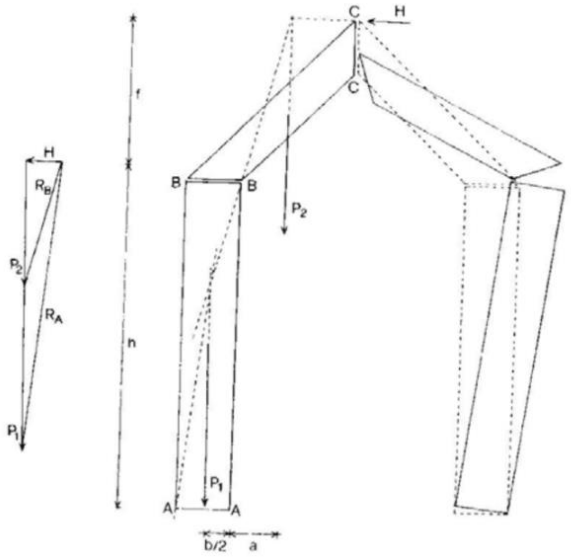

Figure 1-8. Failure mechanism: rotation around points A, B, C (Di Pasquale, 1996).

With reference to *Newton*'s third principle, it is established that the internal loads are, point by point, equal and opposite; each of them acts on an infinitesimal surface element so that the resultant must coincide with the resultant that is transmitted through the joint.

The normal pressures σ_n which are transmitted in a generic section through the joints must be of compression if there is no element between the blocks, such as mortar, capable of performing a binding action, but in any case, it is assumed that the ashlars are simply contact (Di Pasquale, 1996). The resultant of these elementary pressures will then be applied in a point of the section; analogous observations on the tangential components whose resultant must lie on the section itself; therefore, it follows that the overall resultant must have the same point of application as the resultant σ_n. Therefore, if it were external to the section of the joint, the equilibrium would be impossible because tensile stresses would be necessary, which is excluded.

The limiting case occurs when the point of application of the resultant of the internal actions (the center of pressure) is on the edge of the joint.

In its elementary state, the *arch*, as it is presently known, is attributed to the Romans, who, through the assimilation of Greek and Etruscan methodologies that pervaded the Italian peninsula, perfected and developed them to attain an incomparable grade of proficiency in both the materials employed and the construction techniques employed. The genesis of this form is conceivably rooted in structural exigencies; utilizing predominantly brick, the utilization of

arches proved to be more economical than the trilithic scheme, as the latter necessitates a substantial monolithic lintel. During the classical era, it was deemed aesthetically improper for an *arch* to "rest" on a column, as it would diminish the column's architectural significance by interrupting its connection to the *trabeation*. However, in the Paleo-Christian period, arches began to directly rest on the columns' capitals. This was due to the partly decline of the geometric sensibility for the *classic style* after the downfall Roman Empire, which caused a change in architectural norms.

Initially, Roman architecture extensively utilized arches constructed from large stone ashlars or bricks arranged radially, with smaller elements and mortar inserted between them on the extrados. However, the advent of improved construction techniques, particularly the use of pozzolanic mortars mixed with aggregates of varying sizes, facilitated the widespread adoption of the technique of vaults in *opus caementicium*.

Within one of his definitions, Viollet-le-Duc (1863) establishes that a block of masonry constructed in the Roman method is a singular and rigid block, while a squared, compact, and void-free section of masonry, consisting of variously sized parts, constitutes a collection of rigid blocks. The cohesive strength that exists in the former is distributed in all directions, whereas in the latter, it is exclusively entrusted to gravity, which only acts in the vertical direction to hold the parts together. The behaviour of cases that lie between these two extremes is contingent on factors such as mortar resistance and friction between the parts. Ideally, *opus caementicium* vaults should have functioned like a single block of stone or a monolith, without exerting any horizontal thrusts on the retaining walls. However, due to limited tensile strength, they cracked and acted on the walls as if they were composed of distinct ashlars. This was likely the rationale for the Roman practice of constructing *opus caementicium* vaults with meridian rows of bricks, connected by bipedal bricks arranged at regular intervals and hydraulic-setting cement added to an aggregate (Figure 1-9).

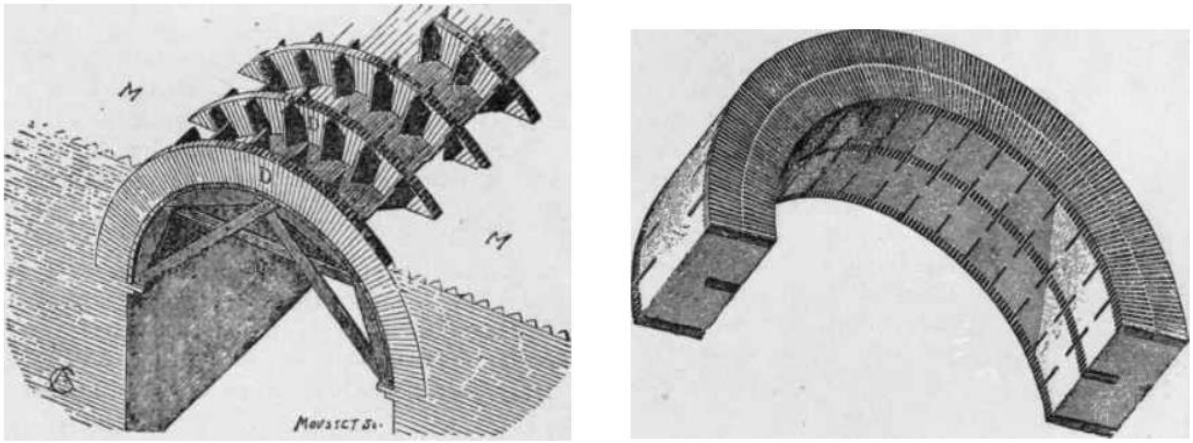

a. b.

Figure 1-9. Barrel vaults in *opus caementicium* (The Colliery Engineer Co., 1899): a. axonometric view only with bricks; b. axonometric view filled with hydraulic-setting cement added to an aggregate.

The use of “ribbed” vaults was a significant advancement as it allowed for the distribution of the mass of mortar in the voids between the brick rows, while also accommodating for natural

cracking within the structure. The arch was a prominent feature of Romanesque architecture, primarily used for aesthetic purposes in areas with a high presence of unqualified manpower. However, some exceptions displayed sophisticated technical devices, aesthetics, and construction intentions due to the presence of stable and specialized workers. The structures were entirely constructed with masonry, ensuring greater lightness and elasticity. This development was a novelty and marked the transition from the Romanesque to the Gothic period. As a result, increasingly enterprising vaulted structures were applied compared to the previous period.

In the context of medieval architecture, the builders did not have the technical instruments to perfectly execute the Roman forms found in their catalogs and abacus. Consequently, their constructions were not structurally efficient, as the stone facings and mediocre mortar used in their pillars and walls often led to uneven settlements and subsequent cracking. However, by the 11th century, vaults were being constructed using small stone ashlars or brick, creating a more flexible system that could accommodate any movements in the perimeter walls. This initial modification alone, however, was insufficient to prevent structural collapses. To mitigate this, transversal arches composed of squared stones were inserted at regular intervals, beginning at the most resistant support points and arched under the intrados of the vaults.

Viollet-le-Duc (1863) misleadingly referred to as "elasticity," the adaptability of thin vaults, analyzing the materials and medieval construction techniques, providing interesting static interpretations on the behaviour of the structures. These transversal arches functioned as elastic perimeter scaffolding, accommodating the movements of the pillars and lending support to the masonry built above them (Figure 1-10).

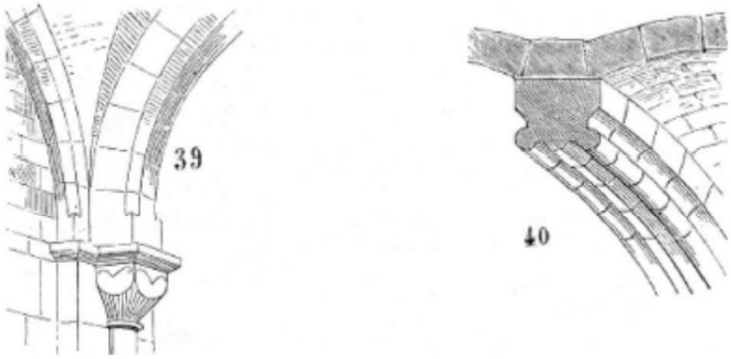

Figure 1-10. The *Arcs Doubleaux* (double arch) of a 12th century cathedral (Viollet-le-Duc, 1863)

Numerous studies have revealed significant challenges associated with evaluating the efficacy of the structural components comprising medieval vaults, which vary based on the historical period, materials used, and construction techniques employed. A noteworthy innovation of Gothic architecture is the absence of the thick masonry masses characteristic of Romanesque architecture. Instead of relying on walls to bear the weight of the structure, Gothic architecture distributes the load solely on pillars located inside and surrounding the perimeter, supported by secondary structures such as *flying buttresses* (or *rampant arch*) and *buttresses*. The external walls provide only an infill function (see Figure 1-11).

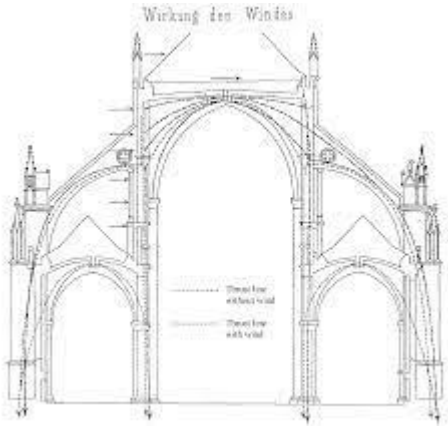

Figure 1-11. Mechanic equilibrium of gothic flying buttress (Fuentes, 2018)

In the construction of Gothic cathedrals, the master builders endeavored to counteract the lateral thrusts generated by the vaulted ceilings by employing counterthrusts, such as flying buttresses, or by vertically transmitting the thrust using vertical weights, namely *pinnacles*, thereby creating a dynamic system. The static system adopted by medieval architects relied on delegating the load-bearing structure of the lateral naves with the responsibility of ensuring the stability of the central nave. This structural arrangement gave rise to several distinctive features of Gothic cathedrals, such as *ribbed cross vaults* with *pointed arches*, the reduction of wall mass, and the slenderization of structures to the point of rendering them skeletal. The elimination of the load-bearing function of the wall permitted the creation of walls of light, adorned with splendid *lancet* or *rose windows*, which corresponded to a complex network of external load-bearing elements.

The objective of achieving bright and spacious interiors in sacred buildings was accomplished through the increasingly refined and innovative use of the construction principles of the cross vault and the pointed arch. The *pointed arch*, which first emerged in the *Ile de France* region around 1120-1130 A.D. as transverse and longitudinal arches, not only conferred static benefits but also afforded formal advantages by allowing for the positioning of the vault's and arches' keystones at the desired heights. As a result, the plan was no longer constrained by the square shape that had prevailed in the Romanesque era but could also include rectangular shapes.

Gothic aesthetics will be intricately linked to structural theory, which will appeal to engineers of iron and novel materials of the 19th century. In contemporary times, the issue of masonry constructions and their interpretation should be approached differently, without the use of present-day tools, concepts, and theories. The theoretical knowledge of a mechanical phenomenon refers to the capacity to demonstrate in abstract terms what must occur. The manner in which the large masonry frameworks of Romanesque and Gothic cathedrals were created through a clever arrangement of stones and bricks is currently perceived in terms of tensions, deformations, and pressure curves. However, it is preposterous to suggest that the builders of that era had access to concepts and theories that were only discovered and advanced towards the end of the 17th century.

Critics of the history of scientific thought have clarified the terms of the issue also at the base of the constructive technique:
"*… our conception of technology is both inert and limited. Education in schools only skims the surface of its first secrets. The technique cannot be summarized in textbooks and manuals. It is a perpetual discovery [...] since the technique, considered in this way, i.e. as the instrument and even the true substance of the experiment, becomes a process of fundamental knowledge that repeats a creative process*." (Hilberry et al., 1964)

1.4.4. Elements of the arch and vault mechanic theory from the Renaissance to 19th century

The evolution and knowledge over time underlying the mechanical functioning of the arch and vaults was based on that of the masonry arch. Its static functioning was ignored for a long time, discovered in fact only in the 19th century, when the science of constructions reached its maturity. All the treatise writers speak of the arch and the dimensions to be assigned to avoid its collapse, from *Vitruvius* to the Renaissance.
The Italian Renaissance revitalized the aesthetic value of the round arch by incorporating it with the rules of the Greek trilithic system. This renewal of the architectural role of the arch was further developed by *Leon Battista Alberti*, who did not make a distinction between beams and arches. In facts, he regarded an arch as a curved beam, and a beam as a column positioned transversely on supports, both consisting of a single block of stone. *Alberti* identified three types of arches: a *rounded arch* (so a perfect semicircle); *segmental arch* and *pointed arch* acute. The most stable are the *rounded arch*, which could support itself without a chain, as noted by Alberti (1452).
In accordance with the principles of architectural mechanics, an arch composed of several ashlars intrinsically possesses lesser structural integrity in comparison to an arch constructed from a single monolithic block, which embodies highest solidity. Alberti's assertion regarding the impossibility of determining the magnitude of thrust from an arch fashioned purely from form, without considering the resistance of the material as rigid, is valid. This is because the value of thrust is a direct result of the deformability of the material. If the material is non-deformable, the system remains in equilibrium, even when the thrust is considered to be zero. However, when the arch consist of several ashlars, a distinct mechanism capable of activating under load is presented. The number of mechanisms activated increases with the number of ashlars employed. Alberti's statement regarding the functionality of the *round arch* is veritable and stands as the first articulation of its kind in architectural treatises (Alberti, 1452):

- *"...you don't see how it (the arch) can disconnect on its own; unless one ashlar pushes the other out;"*
- *"even if they were willing to try to undermine each other, the very presence of the weights ... is enough to prevent it;"*
- *"the keystone ... it is hard to see how it can find the strength to push out the adjacent ash-*

lars;"

- *"…those that follow them, occupying the sides of the arch, will be held easily… by the balancing of the weights;"*
- *"finally, the ashlars placed at the two lower ends, it is not understood how they can move once the others, placed above them, remain still in their place;"*

"Therefore, whole arches do not need a chian since they are able to maintain themselves." (Alberti, 1452)

Through the examination of the semicircle shape, from which the arch with ashlars begins, Alberti discerned a similarity to the wedge – one of *Archimedes' five simple machines* that was later investigated by *Heron*. This observation constituted Alberti's initial attempt to provide an explanation, as shown in Figure 1-12.

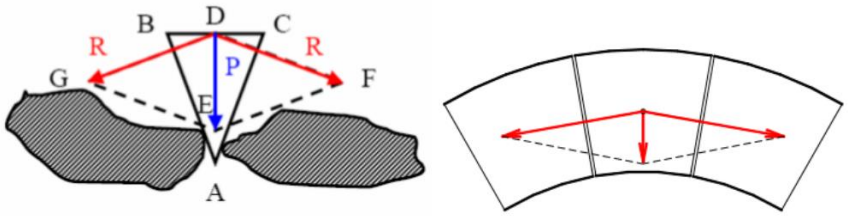

Figure 1-12. The separation of parts demonstrates the force exerted by each ashlar (wedge) on its adjacent ones.

According to *Alberti*, the terminal wedges of the round arch, which he referred to as ashlars, are immovable and exert a downward force that is counteracted by the supports. Thus, the *round arch*, unlike the segmental arch, does not require a chain as it does not exert any thrust. The wedge analogy was further developed in the late 17th century with a more suitable language for the description of mechanical behaviour, and it was translated into mathematical terms based on *Galileo*'s contribution to the resistance of solids.

However, the first systematic study on the *round arch* is due to *Leonardo da Vinci*. In the *Madrid Codes,* he determines the weight of each ashlar on the inclined plane that supports it and studies the fractures that are generated and the collapse mechanism of the arches (Figure 1-13).

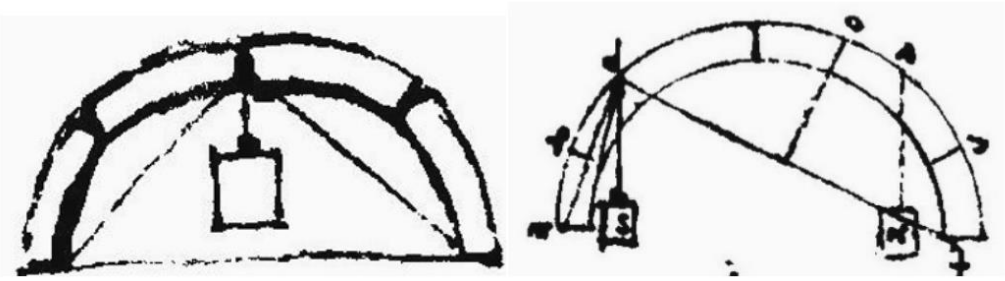

Figure 1-13. The *Madrid Codes* of *Leonardo*: arc failure patterns due to concentrated loads.

It will then be *De la Hire* in 1684 (de La Hire, 1730) who will succeed in formulating the first theory for the calculation of arches –and their line of thrust– which however neglects the friction between the ashlars. The turning point will be precisely the discovery of friction, thanks

to *C. Coulomb* who, in his *"Essai sur une application des règles de maxi-mis & minimis à quelques problèmes de statique, relatifs à l'architecture*", exhibited his studies on the barrel vault and elaborated a theory relating both to frictionless vaults and to those in which it is present.

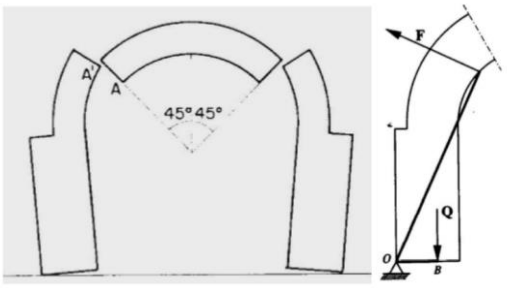

Figure 1-14. Arc collapse mechanism according to *de la Hire* (de La Hire, 1730).

Coulomb's discussion on the vaults with friction and cohesion constitutes the general solution for the collapse analysis of the masonry arch. He introduces a method for determining four thrust values as the angular position of the joint varies, which allows the selection of the maximum thrust values (when the balance of the ashlar refers to inward falling movements) and those of minimum (when the balance is it refers to the displacements due to outward lifting). However, this method was not correct, and *Columb's theory* will be perfected by *Persy* in 1825, *Navier* in 1826 and *Michon* in 1857 with the exhaustive treatment of the eight collapse modes for a symmetrical arch. The theoretical contribution of the three authors can be summed up with the introduction of a new parameter, namely that of the thrust position.

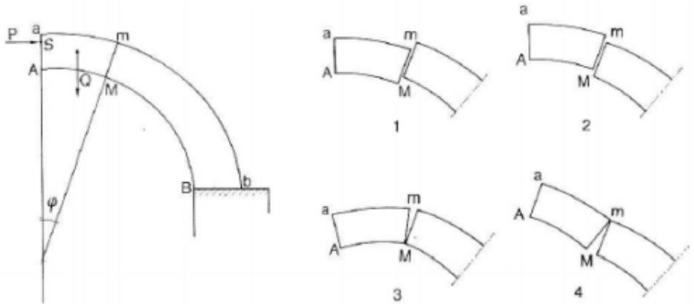

Figure 1-15. *Coulomb*'s study schemes of the broken vault.

In the 19th century the debate became increasingly rich in interventions, with the introduction of new materials and new concepts. The method of calculating masonry arches that is still used today, i.e. the *Méry* method, to which we owe the introduction of the "pressure curve", dates back to 1840. The search for him was based on *Navier*'s interpretation of stability (Navier, 1827). Méry (1840) defined that the pressure curve should remain contained within the middle third of the arch in each of its sections and should pass in particular from its upper extreme in key and from the lower one in the "breaking joints", configuring itself with the limit curve for the occurrence of tensile stresses in the joints.

The arch is a structural element capable of recovering, with its curvilinear trajectory, the stresses deriving from gravitational loads, transforming them into prevailing compressive

forces which act on the ashlars forming part of the arch, which are supported by mutual contrast, since they are supported at the two ends by vertical elements, defined piers. In conclusion, it is not a decorative element, it is a static principle, a predominantly compressed structure which represents the embodiment of the isostatic compression of the structure.

REFERENCES

Abbas, N., Calderini, C., Cattari, S., Lagomarsino, S., Rossi, M., Corradini, R. G., Marghella, G., & Piovanello, V. (2010). DELIVERABLE D4 Classification of the cultural heritage assets , description of the target performances and identification of damage measures. In PERPETUATE PERformance-based aPproach to Earthquake proTection of cUlturAl heriTage in European and mediterranean countries.

Abeille Joseph. (1699). Flat Vault of Abeille .

Abruzzese, D., Como, M., & Lanni, G. (1995). Some results on the strength evaluation of vaulted masonry structures. Structural Studies of Historical Buildings IV-Vol. 1: Architectural Studies, Materials and Analysis, 431–440.

Admane, H. A., & Murnal, P. B. (2017). Analysis of Masonry Structures : a Review. International Journal for Research Trends and Innovation, 2(5).

Aita, D., Barsotti, R., & Bennati, S. (2020). Equilibrium analysis of a sail vault in livorno's fortezza vecchia through a modern re-edition of the stability area method. Lecture Notes in Mechanical Engineering. https://doi.org/10.1007/978-3-030-41057-5_81

Akleman, E., Krishnamurthy, V. R., Fu, C. A., Subramanian, S. G., Ebert, M., Eng, M., Starrett, C., & Panchal, H. (2020). Generalized abeille tiles: Topologically interlocked space-filling shapes generated based on fabric symmetries. Computers and Graphics (Pergamon), 89. https://doi.org/10.1016/j.cag.2020.05.016

Alberti, L. B. (1452). De re ædificatoria (Nicolò di Lorenzo).

Alforno, M., Monaco, A., Venuti, F., & Calderini, C. (2021). Validation of Simplified Micro-models for the Static Analysis of Masonry Arches and Vaults. International Journal of Architectural Heritage, 15(8). https://doi.org/10.1080/15583058.2020.1808911

Alforno, M., Venuti, F., Monaco, A., & Calderini, C. (2022). Seismic behaviour of cross vaults with different brick pattern. Bulletin of Earthquake Engineering, 20(8). https://doi.org/10.1007/s10518-022-01347-6

Andreev, K., Sinnema, S., Rekik, A., Allaoui, S., Blond, E., & Gasser, A. (2012). Compressive behaviour of dry joints in refractory ceramic masonry. Construction and Building Materials, 34. https://doi.org/10.1016/j.conbuildmat.2012.02.024

Andreu, A., Gil, L., & Roca, P. (2007). Computational Analysis of Masonry Structures with a Funicular Model. Journal of Engineering Mechanics, 133(4). https://doi.org/10.1061/(asce)0733-9399(2007)133:4(473)

Andrusko, P. A. (2014). Stereotomy: Stone Architecture and New Research by Giuseppe Fallacara. Nexus Network Journal, 16(2). https://doi.org/10.1007/s00004-014-0197-5

Angelillo, M., Babilio, E., & Fortunato, A. (2013). Singular stress fields for masonry-like vaults. Continuum Mechanics and Thermodynamics, 25(2–4). https://doi.org/10.1007/s00161-012-0270-9

Avelino, R., Iannuzzo, A., van Mele, T., & Block, P. (2021). New Strategies to Assess the Safety of Unreinforced Masonry Structures Using Thrust Network Analysis. https://doi.org/10.23967/sahc.2021.162

Bacigalupo, A., Brencich, A., & Gambarotta, L. (2013). A simplified assessment of the dome and drum of the Basilica of S. Maria Assunta in Carignano in Genoa. Engineering Structures, 56. https://doi.org/10.1016/j.engstruct.2013.05.006

Bacigalupo, A., Brencich, A., & Gambarotta, L. (2015). On the Statics of the Dome of the Basilica of S. Maria Assunta in Carignano, Genoa. In Masonry Structures: Between Mechanics and Architecture. https://doi.org/10.1007/978-3-319-13003-3_6

Baraccani, S., Zauli, L., Theodossopoulos, D., & Silvestri, S. (2020). Experimental test on a fibre-reinforced scaled cross vault subjected to in-plane shear displacements at the springings. Construction and Building Materials, 265. https://doi.org/10.1016/j.conbuildmat.2020.120305

Barberio, M., Colella, M., & Fallacara, G. (2016). Stereotomy, Sustainable Construction and Didactics. Case study: a new Museum for Matera, European Capital of Culture 2019. 3 Rd International Balkans Conference on Challenges of Civil Engineering, May 2016.

Bianchini, N., Mendes, N., Calderini, C., Candeias, P. X., Rossi, M., & Lourenço, P. B. (2022). Seismic response of a small-scale masonry groin vault: experimental investigation by performing quasi-static and shake table tests. Bulletin of Earthquake Engineering, 20(3). https://doi.org/10.1007/s10518-021-01280-0

Bianchini, N., Mendes, N., Lourenço, P. B., Calderini, C., & Rossi, M. (2019). Seismic assessment of masonry cross vaults through numerical nonlinear static and dynamic analysis. COMPDYN Proceedings, 1. https://doi.org/10.7712/120119.6942.18709

Binda, L., & Saisi, A. (2005). Research on historic structures in seismic areas in Italy. In Progress in Structural Engineering and Materials (Vol. 7, Issue 2). https://doi.org/10.1002/pse.194

Block, P. (2009). Thrust Network Analysis: Exploring Three-dimensional Equilibrium. In PhD thesis.

Block, P., Ciblac, T., & Ochsendorf, J. (2006). Real-time limit analysis of vaulted masonry buildings. Computers and Structures, 84(29–30). https://doi.org/10.1016/j.compstruc.2006.08.002

Block, P., & Lachauer, L. (2014). Three-dimensional (3D) equilibrium analysis of gothic masonry vaults. International Journal of Architectural Heritage, 8(3). https://doi.org/10.1080/15583058.2013.826301

Block, P., Lachauer, L., & Rippmann, M. (2014). Thrust network analysis: Design of a cut–stone masonry vault. In Shell Structures for Architecture: Form Finding and Optimization (Vol. 9781315849270). https://doi.org/10.4324/9781315849270

Block, P., & Ochsendorf, J. (2007). Thrust network analysis: A new methodology for three-dimensional equilibrium. Journal of the International Association for Shell and Spatial Structures, 48(155).

Brencich, A., Gambarotta, L., & Ghia, A. (2014). History-based assessment of the dome of the Basilica of S. Maria of carignano in Genoa. International Journal of Architectural Heritage, 8(5). https://doi.org/10.1080/15583058.2012.727063

Briccolati Bati, S., Feletti, I., Ranocchiai, G., Rovero, L., & Rapallini, M. (2002). Costruzioni voltate in muratura: indagine teorico sperimentale su prototipi di volte a crociera da impiegare nella ricostruzione dei centri antichi vulnerati dai recenti sismi (Libreria Alfani, Ed.; pp. 41–108). Libreria Alfani.

Brocato, M., & Mondardini, L. (2012). A new type of stone dome based on Abeille's bond. International Journal of Solids

and Structures, 49(13), 1786–1801. https://doi.org/10.1016/j.ijsolstr.2012.03.036
Brocato, M., & Mondardini, L. (2013). The proposal of an ancient technique for modern construction: A stone reciprocal structure. Structures and Architecture: Concepts, Applications and Challenges - Proceedings of the 2nd International Conference on Structures and Architecture, ICSA 2013, 472–479.
Buckingham, E. (1914). On physically similar systems; Illustrations of the use of dimensional equations. Physical Review, 4(4). https://doi.org/10.1103/PhysRev.4.345
Bui, T. T., & Limam, A. (2012). Masonry walls under membrane or bending loading cases: Experiments and discrete element analysis. Civil-Comp Proceedings, 99. https://doi.org/10.4203/ccp.99.119
Bui, T. T., Limam, A., Sarhosis, V., & Hjiaj, M. (2017). Discrete element modelling of the in-plane and out-of-plane behaviour of dry-joint masonry wall constructions. Engineering Structures, 136. https://doi.org/10.1016/j.engstruct.2017.01.020
Calderini, C. (2004). The effect of the masonry pattern on the global behaviour of vaults. Proceedings of the 4th International Conference on Structural Analysis of Historic Construction.
Calderini, C., & Lagomarsino, S. (2006). A micromechanical inelastic model for historical masonry. Journal of Earthquake Engineering, 10(4). https://doi.org/10.1080/13632460609350605
Calderini, C., & Lagomarsino, S. (2015). Seismic Response of Masonry Arches Reinforced by Tie-Rods: Static Tests on a Scale Model. Journal of Structural Engineering, 141(5). https://doi.org/10.1061/(asce)st.1943-541x.0001079
Calderini, C., Rossi, M., Lagomarsino, S., Cascini, L., & Portioli, F. (2017). Experimental and numerical analysis of seismic response of unreinforced masonry cross vaults. International Conference on Advances in Experimental Structural Engineering, 2017-September. https://doi.org/10.7414/7aese.T5.136
Caliò, I., Cannizzaro, F., & Pantò, B. (2012). A macro-element approach for modeling the nonlinear behaviour of monumental buildings under static and seismic loadings. World Conference in Earthquake Engineering.
Caliò, I., Marletta, M., & Pantò, B. (2012). A new discrete element model for the evaluation of the seismic behaviour of unreinforced masonry buildings. Engineering Structures, 40. https://doi.org/10.1016/j.engstruct.2012.02.039
Camata, G., Marano, C., Sepe, V., Spacone, E., Siano, R., Petracca, M., Roca, P., & Pelà, L. (2022). Validation of non-linear equivalent-frame models for irregular masonry walls. Engineering Structures, 253. https://doi.org/10.1016/j.engstruct.2021.113755
Cancino, C., Farneth, S., Garnier, P., Neumann, J. V., & Webster, F. (2014). Estudio de daños a edificaciones históricas de tierra después del terremoto del 15 de agosto del 2014 en Pisco, Perú. . Getty Conservation Institute.
Cangi, G. (2005). Manuale del recupero strutturale ed antisismico. (In Italian). DEI.
Carfagnini, C., Baraccani, S., Silvestri, S., & Theodossopoulos, D. (2017). Pseudo-static response of masonry cross vaults to imposed shear displacements at the springings. Key Engineering Materials, 747 KEM. https://doi.org/10.4028/www.scientific.net/KEM.747.456
Carfagnini, C., Baraccani, S., Silvestri, S., & Theodossopoulos, D. (2018). The effects of in-plane shear displacements at the springings of Gothic cross vaults. Construction and Building Materials, 186. https://doi.org/10.1016/j.conbuildmat.2018.07.055
Cattari, S., Resemini, S., & Lagomarsino, S. (2008). Modelling of vaults as equivalent diaphragms in 3D seismic analysis of masonry buildings. Structural Analysis of Historic Construction: Preserving Safety and Significance - Proceedings of the 6th International Conference on Structural Analysis of Historic Construction, SAHC08, 1. https://doi.org/10.1201/9781439828229.pt5
Ceradini, V. (1996). Modelli sperimentali di volte in tufo e mattoni. La Meccanica Delle Murature Tra Teoria e Progetto .
Chácara E., C. J. (2018). Macro-Element Nonlinear Dynamic Analysis for the Assessment of the Seismic Vulnerability of Masonry Structures. (PhD thesis). PhD Thesis, February.
Clemente, P. (1998). Introduction to dynamics of stone arches. Earthquake Engineering and Structural Dynamics, 27(5). https://doi.org/10.1002/(SICI)1096-9845(199805)27:5<513::AID-EQE740>3.0.CO;2-O
Colombo, C., Fernandes, L., Savalle, N., & Lourenço, P. B. (2021, June 4). TILTING TESTS FOR MASONRY STRUCTURES: DESIGN AND PRELIMINARY NUMERICAL MODELING. 14th Canadian Masonry Symposium.
Colombo, C., Savalle, N., Mehrotra, A., Funari, M. F., & Lourenço, P. B. (2022). Experimental, numerical and analytical investigations of masonry corners: Influence of the horizontal pseudo-static load orientation. Construction and Building Materials, 344, 127969. https://doi.org/https://doi.org/10.1016/j.conbuildmat.2022.127969
Creazza, G., Matteazzi, R., Saetta, A., & Vitaliani, R. (2002). Analyses of Masonry Vaults: A Macro Approach based on Three-Dimensional Damage Model. Journal of Structural Engineering, 128(5). https://doi.org/10.1061/(asce)0733-9445(2002)128:5(646)
Croci, G. (1998). The collapses occurred in the Basilica of St Francis of Assisi and in the Cathedral of Noto. In P. Roca, J. L. González, E. Oñate, & P. B. Lourenço (Eds.), Structural analysis of historical constructions II. Possibilities of numerical and experimental techniques (pp. 297–317). International Center for Numerical Methods in Engineering.
Cundall, P. A., & Hart, R. D. (1992). Numerical modelling of discontinua. In Engineering Computations (Vol. 9, Issue 2). https://doi.org/10.1108/eb023851
Cundall, P. A., & Strack, O. D. L. (1979). A discrete numerical model for granular assemblies. Geotechnique, 29(1). https://doi.org/10.1680/geot.1979.29.1.47
D'Altri, A. M., Sarhosis, V., Milani, G., Rots, J., Cattari, S., Lagomarsino, S., Sacco, E., Tralli, A., Castellazzi, G., & de Miranda, S. (2020). Modeling Strategies for the Computational Analysis of Unreinforced Masonry Structures: Review and Classification. Archives of Computational Methods in Engineering, 27(4). https://doi.org/10.1007/s11831-019-09351-x
Dantec Dynamics. (n.d.). Istra 4D.
Davies, N., & Jokiniemi, E. (2008). Dictionary of Architecture and Building Construction. In Dictionary of Architecture and Building Construction. https://doi.org/10.4324/9780080878744
D'Ayala, D. F., & Tomasoni, E. (2011). Three-dimensional analysis of masonry vaults using limit state analysis with finite friction. In International Journal of Architectural Heritage (Vol. 5, Issue 2). https://doi.org/10.1080/15583050903367595

de Canio, G., Clemente, P., Mongelli, M., Rinaldis, D., Roselli, I., Calderini, C., & Rossi, M. (2012). Results of experimental test on damage measures and reference values to be considered. PERPETUATE (EU-FP7 Research Project), Deliverable D12.

de La Hire, P. (1730). Traitéde Méchanique. Parigi : Mémoires de l'Académie Royale des Sciences.

de Lorenzis, L., DeJong, M., & Ochsendorf, J. (2007). Failure of masonry arches under impulse base motion. Earthquake Engineering and Structural Dynamics, 36(14). https://doi.org/10.1002/eqe.719

de Luca, A., Giordano, A., & Mele, E. (2004). A simplified procedure for assessing the seismic capacity of masonry arches. Engineering Structures, 26(13). https://doi.org/10.1016/j.engstruct.2004.07.003

de Matteis, G., & Mazzolani, F. M. (2010). The Fossanova church: Seismic vulnerability assessment by numeric and physical testing. In International Journal of Architectural Heritage (Vol. 4, Issue 3). https://doi.org/10.1080/15583050903078903

DeJong, M. J., de Lorenzis, L., Adams, S., & Ochsendorf, J. A. (2008). Rocking stability of masonry arches in seismic regions. Earthquake Spectra, 24(4). https://doi.org/10.1193/1.2985763

DeJong, M. J., & Ochsendorf, J. (2006). Analysis of vaulted masonry structures subjected to horizontal ground motion.

Di Pasquale, S. (1996). L'arte del costruire: tra conoscenza e scienza (Marsilio).

Dimitrakopoulos, E. G., & DeJong, M. J. (2012). Revisiting the rocking block: Closed-form solutions and similarity laws. Proceedings of the Royal Society A: Mathematical, Physical and Engineering Sciences, 468(2144). https://doi.org/10.1098/rspa.2012.0026

Fagone, M., Rotunno, T., & Bati, S. B. (2016). The Groin Vaults of St. John Hospital in Jerusalem: An Experimental Analysis on a Scale Model. International Journal of Architectural Heritage, 10(7). https://doi.org/10.1080/15583058.2016.1158331

Fallacara, G. (2006). Digital Stereotomy and Topological Transformations. . Proceedings of the Second International Congress on Construction History , 1075-1092.

Fallacara, G., & Barberio, M. (2018). Stereotomy 2.0: Informing the future of Digital Stereotomy. In: Nexus Network Journal (peer-reviewed journal) (G. Fallacara & M. Barberio, Eds.). Birkhäuser/Springer-Basel.

Fallacara, G., Barberio, M., & Colella, M. (2019). Topological interlocking blocks for architecture: From flat to curved morphologies. In Springer Series in Materials Science (Vol. 282). https://doi.org/10.1007/978-3-030-11942-3_14

Fallacara, G., Ferrero, M., & Minenna, V. (2015). Nuovi Sistemi Voltati Stereotomici: Progetto, Calcolo e Costruzione.

Fallacara, G., Scaltrito, G., & Vacca, V. (2019). Hypar dome: Stereotomy 2.0's experiments on 3D-printed stereotomic domes. Proceedings of the International Fib Symposium on Conceptual Design of Structures, 427–434.

Fantetti, A., Tamatam, L. R., Volvert, M., Lawal, I., Liu, L., Salles, L., Brake, M. R. W., Schwingshackl, C. W., & Nowell, D. (2019). The impact of fretting wear on structural dynamics: Experiment and Simulation. Tribology International, 138. https://doi.org/10.1016/j.triboint.2019.05.023

Ferrario, L., Marini, A., Andreis, V., Zanotti, S., Riva, P., & Giuriani, E. P. (2012). Behaviour and retrofitting of single-leaf vaults under distributed horizontal forces. . In Jerzy Jasieńko (Ed.), Structural Analysis of Historical Constructions, (pp. 1503–1511).

Foti, D., Vacca, V., & Facchini, I. (2018). DEM modeling and experimental analysis of the static behavior of a dry-joints masonry cross vaults. Construction and Building Materials, 170. https://doi.org/10.1016/j.conbuildmat.2018.02.202

Foti, P., Fraddosio, A., Lepore, N., & Piccioni, M. (2016). Three-dimensional lower-bound analysis of masonry structures. Structures and Architecture - Proceedings of the 3rd International Conference on Structures and Architecture, ICSA 2016. https://doi.org/10.1201/b20891-77

Fraternali, F. (2010). A thrust network approach to the equilibrium problem of unreinforced masonry vaults via polyhedral stress functions. Mechanics Research Communications, 37(2). https://doi.org/10.1016/j.mechrescom.2009.12.010

Freitas, F., Barros, J., & Fonseca, P. (1998). Manual book of the structures testing system - SENTUR. (in Portuguese). University of Minho.

Frézier, A. F. (1739). Traité de Stéréotomie .

Fuentes, P. (2018). Mechanics of flying buttresses: The case of the cathedral of Mallorca. Journal of Mechanics of Materials and Structures, 13(5). https://doi.org/10.2140/JOMMS.2018.13.617

Gaetani, A. (2020). Seismic Performance of Masonry Cross Vaults : Learning from Historical 4 Developments and Experimental Testing. Sapienza University of Rome.

Gaetani, A., Bianchini, N., & Lourenço, P. B. (2021). Simplified micro-modelling of masonry cross vaults: Stereotomy and interface issues. International Journal of Masonry Research and Innovation, 6(1). https://doi.org/10.1504/IJMRI.2021.112076

Gaetani, A., Lourenço, P. B., Monti, G., & Moroni, M. (2017). Shaking table tests and numerical analyses on a scaled dry-joint arch undergoing windowed sine pulses. Bulletin of Earthquake Engineering, 15(11). https://doi.org/10.1007/s10518-017-0156-0

Gaetani, A., Monti, G., Paolone, A., Lourenço, P. B., & Milani, G. (2016). Seismic capacity of masonry groin vaults through upper bound limit analysis. Structural Analysis of Historical Constructions: Anamnesis, Diagnosis, Therapy, Controls - Proceedings of the 10th International Conference on Structural Analysis of Historical Constructions, SAHC 2016. https://doi.org/10.1201/9781315616995-204

Gesualdo, A., Brandonisio, G., De-Luca, A., Iannuzzo, A., Montanino, A., & Olivieri, C. (2019). Limit analysis of cloister vaults: The case study of Palazzo Caracciolo di Avellino. Journal of Mechanics of Materials and Structures, 14(5), 739–750. https://doi.org/10.2140/jomms.2019.14.739

Giresini, L., Butenweg, C., Andreini, M., de Falco, A., & Sassu, M. (2014). Numerical Calibration Of A Macro-Element For Vaulted Systems In Historic Churches.

Giuffrè, A. (1994). Seismic safety and strengthening of historical buildings and urban fabrics. Earthquake Engineering, 10th World Conference.

Heyman, J. (1978). Equilibrium of Shell Structures. The Antiquaries Journal, 58(2). https://doi.org/10.1017/s0003581500056237

Heyman, J. (1995). The stone skeleton: structural engineering of masonry architecture. The Stone Skeleton: Structural Engi-

neering of Masonry Architecture. https://doi.org/10.1115/1.2787238
Heyman, J. (1998). Structural Analysis. In Choice Reviews Online (Issue 03). Cambridge University Press. https://doi.org/10.1017/CBO9780511529580
Hilberry, H. H., Focillon, H., Bony, J., & King, D. (1964). The Art of the West in the Middle Ages. Art Journal, 24(1). https://doi.org/10.2307/774767
Huntley, H. E. (1967). Dimensional analysis. Dover Publications.
Itasca Consulting Group Inc. (n.d.). 3DEC – Three-Dimensional Distinct Element Code.
Jasiński, R., & Grzyb, K. (2020). Proposal of empirical homogenization of masonry wall made of AAC masonry units. IOP Conference Series: Materials Science and Engineering, 960(2). https://doi.org/10.1088/1757-899X/960/2/022084
John Ruskin. (1853). The Stones of Venice.
Joshi, R. (2022). Calibration of FEM Models of Historic Masonry Structures and its Application on a Local Historic Structure.
Kartal, M. E., Mulvihill, D. M., Nowell, D., & Hills, D. A. (2011). Determination of the Frictional Properties of Titanium and Nickel Alloys Using the Digital Image Correlation Method. Experimental Mechanics, 51(3). https://doi.org/10.1007/s11340-010-9366-y
Kollerathu, J. A., Krishnachandran, S., & Menon, A. (2016). Modelling and seismic analysis of existing masonry structures. Structural Analysis of Historical Constructions: Anamnesis, Diagnosis, Therapy, Controls - Proceedings of the 10th International Conference on Structural Analysis of Historical Constructions, SAHC 2016. https://doi.org/10.1201/9781315616995-33
Kulatilake, P. H. S. W., Shreedharan, S., Sherizadeh, T., Shu, B., Xing, Y., & He, P. (2016). Laboratory Estimation of Rock Joint Stiffness and Frictional Parameters. Geotechnical and Geological Engineering, 34(6). https://doi.org/10.1007/s10706-016-9984-y
Lagomarsino, S. (2015). Seismic assessment of rocking masonry structures. Bulletin of Earthquake Engineering, 13(1). https://doi.org/10.1007/s10518-014-9609-x
Lagomarsino, S., Penna, A., Galasco, A., & Cattari, S. (2013). TREMURI program: An equivalent frame model for the nonlinear seismic analysis of masonry buildings. Engineering Structures, 56. https://doi.org/10.1016/j.engstruct.2013.08.002
Large elastic deformations of isotropic materials. I. Fundamental concepts. (1948). Philosophical Transactions of the Royal Society of London. Series A, Mathematical and Physical Sciences, 240(822). https://doi.org/10.1098/rsta.1948.0002
Lemos, J. v. (2007). Discrete element modeling of masonry structures. International Journal of Architectural Heritage, 1(2). https://doi.org/10.1080/15583050601176868
Lemos, J. v. (2008). Modeling of Historical Masonry with Discrete Elements. In III European Conference on Computational Mechanics. https://doi.org/10.1007/1-4020-5370-3_23
Lemos, J. v. (2019). Discrete element modeling of the seismic behavior of masonry construction. Buildings, 9(2). https://doi.org/10.3390/buildings9020043
Livesley, R. K. (1992). A computational model for the limit analysis of three-dimensional masonry structures. Meccanica, 27(3). https://doi.org/10.1007/BF00430042
Lourenço, P. B., Bianchini, N., & Gaetani, A. (2020). Simplified micro-modelling of masonry cross vaults: stereotomy and interface issues. International Journal of Masonry Research and Innovation, 1(1). https://doi.org/10.1504/ijmri.2020.10032218
Lourenço, P. B., Oliveira, D. v., Roca, P., & Orduña, A. (2005). Dry Joint Stone Masonry Walls Subjected to In-Plane Combined Loading. Journal of Structural Engineering, 131(11). https://doi.org/10.1061/(asce)0733-9445(2005)131:11(1665)
Lourenço, P. B., Rots, J. G., & Blaauwendraad, J. (1998). Continuum Model for Masonry: Parameter Estimation and Validation. Journal of Structural Engineering, 124(6). https://doi.org/10.1061/(asce)0733-9445(1998)124:6(642)
Maia Avelino, R., Iannuzzo, A., van Mele, T., & Block, P. (2021). Assessing the safety of vaulted masonry structures using thrust network analysis. Computers and Structures, 257. https://doi.org/10.1016/j.compstruc.2021.106647
Marini, A., Giardina, G., Riva, P., & Giuriani, E. (2008). Seismic behaviour of barrel vault systems. Structural Analysis of Historic Construction: Preserving Safety and Significance - Proceedings of the 6th International Conference on Structural Analysis of Historic Construction, SAHC08, 1. https://doi.org/10.1201/9781439828229.ch46
Mark, R., Abel, J. F., & O'Neill, K. (1973). Photoelastic and finite-element analysis of a quadripartite vault. Experimental Mechanics, 13(8). https://doi.org/10.1007/bf02322391
Marmo, F., Masi, D., Mase, D., & Rosati, L. (2019). Thrust network analysis of masonry vaults. International Journal of Masonry Research and Innovation, 4(1–2). https://doi.org/10.1504/IJMRI.2019.096828
Marseglia, P. S., Micelli, F., Leone, M., & Aiello, M. A. (2014). Modeling of masonry vaults as equivalent diaphragms. Key Engineering Materials, 628. https://doi.org/10.4028/www.scientific.net/KEM.628.185
McInerney, J., & Dejong, M. J. (2015). Discrete Element Modeling of Groin Vault Displacement Capacity. International Journal of Architectural Heritage, 9(8). https://doi.org/10.1080/15583058.2014.923953
Méry, E. (1840). Sur l'équilibre des voutes en berceau. In Annales des Ponts et des Chaussées.
Milani, E., Milani, G., & Tralli, A. (2008). Limit analysis of masonry vaults by means of curved shell finite elements and homogenization. International Journal of Solids and Structures, 45(20). https://doi.org/10.1016/j.ijsolstr.2008.05.019
Milani, G., & Lourenço, P. B. (2012). 3D non-linear behavior of masonry arch bridges. Computers and Structures, 110–111. https://doi.org/10.1016/j.compstruc.2012.07.008
Milani, G., Rossi, M., Calderini, C., & Lagomarsino, S. (2016). Tilting plane tests on a small-scale masonry cross vault: Experimental results and numerical simulations through a heterogeneous approach. Engineering Structures, 123. https://doi.org/10.1016/j.engstruct.2016.05.017
Mirabella Roberti, G., & Calvetti, F. (2020). Distinct element analysis of stone arches. In Arch Bridges. https://doi.org/10.1201/9781003078494-27
Mohebkhah, A., Tasnimi, A. A., & Moghadam, H. A. (2008). Nonlinear analysis of masonry-infilled steel frames with openings using discrete element method. Journal of Constructional Steel Research, 64(12).

https://doi.org/10.1016/j.jcsr.2008.01.016
Mouzakis, C., Adami, C. E., Karapitta, L., & Vintzilou, E. (2012). Seismic behaviour of a rehabilitated cross vault. . In Jerzy Jasieńko (Ed.), Structural Analysis of Historical Constructions (pp. 1665–1673).
Munjiza, A. (2004). Front Matter. In The Combined Finite-Discrete Element Method. https://doi.org/10.1002/0470020180.fmatter
Naik, P. M., Bhowmik, T., & Menon, A. (2021). Estimating joint stiffness and friction parameters for dry stone masonry constructions. International Journal of Masonry Research and Innovation, 6(2). https://doi.org/10.1504/ijmri.2021.113934
Navier, C. (1827). Mémoire sur le lois del'équilibreet du mouvement des solides élastiques. .
Nodargi, N., & Bisegna, P. (2022). Generalized thrust network analysis for the safety assessment of vaulted masonry structures. Engineering Structures, 270, 114878. https://doi.org/10.1016/j.engstruct.2022.114878
NTC 2018 – Nuove norme sismiche per il calcolo strutturale (D.M. 17/01/2018) - In Italian, 2018.
Numerical Modelling of Discrete Materials in Geotechnical Engineering, Civil Engineering and Earth Sciences. (2004). In Numerical Modelling of Discrete Materials in Geotechnical Engineering, Civil Engineering and Earth Sciences. https://doi.org/10.1201/9780203023983
Ochsendorf, J. (2002). Collapse of masonry structures. University of Cambridge.
O'Dwyer, D. (1999). Funicular analysis of masonry vaults. Computers and Structures, 73(1–5). https://doi.org/10.1016/S0045-7949(98)00279-X
Oliveira, R. L. G., Rodrigues, J. P. C., Pereira, J. M., Lourenço, P. B., & Ulrich Marschall, H. (2021). Normal and tangential behaviour of dry joints in refractory masonry. Engineering Structures, 243. https://doi.org/10.1016/j.engstruct.2021.112600
Olmati, P., Gkoumas, K., & Bontempi, F. (2019). Simplified FEM modelling for the collapse assessment of a masonry vault. Frattura Ed Integrita Strutturale, 13(47). https://doi.org/10.3221/IGF-ESIS.47.11
Oppenheim, I. J. (1992). The masonry arch as a four-link mechanism under base motion. Earthquake Engineering & Structural Dynamics, 21(11). https://doi.org/10.1002/eqe.4290211105
Oppenheim, I. J., Gunaratnam, D. J., & Allen, R. H. (1989). Limit State Analysis of Masonry Domes. Journal of Structural Engineering, 115(4). https://doi.org/10.1061/(asce)0733-9445(1989)115:4(868)
Otter, J. R. H., Poppard, A. J. S., Lane, R. G. T., Welch, A. K., King, I. P., Wood, W. L., Cubitt, N. J., Hayes, R. J., Hobbs, R. E., Zienkiewicz, O. C., Bickley, W. G., Majid, K. I., Snell, C., Walker, B. A., Postlethwaite, R. W., & Cassell, A. C. (1967). DISCUSSION. DYNAMIC RELAXATION. Proceedings of the Institution of Civil Engineers, 37(4). https://doi.org/10.1680/iicep.1967.8278
Papantonopoulos, C., Psycharis, I. N., Papastamatiou, D. Y., Lemos, J. v., & Mouzakis, H. P. (2002). Numerical prediction of the earthquake response of classical columns using the distinct element method. Earthquake Engineering and Structural Dynamics, 31(9). https://doi.org/10.1002/eqe.185
Payne, A., & Issa, R. (2009). The Grasshopper Primer, Second Edition for version 0.6.0007.
Pelà, L., Aprile, A., & Benedetti, A. (2009). Seismic assessment of masonry arch bridges. Engineering Structures, 31(8). https://doi.org/10.1016/j.engstruct.2009.02.012
Penna, A., Bracchi, S., Salvatori, C., Morandini, C., & Rota, M. (2022). Extending Analysis Capabilities of Equivalent Frame Models for Masonry Structures (pp. 473–485). https://doi.org/10.1007/978-3-031-15104-0_29
Piccioni, M. D., Olivieri, C., Fraddosio, A., Castellano, A., & Elia, I. (2021). A new experimental approach for small-scale dynamic tests on masonry arches aimed at seismic assessment. International Journal of Masonry Research and Innovation, 6(4). https://doi.org/10.1504/ijmri.2021.10039003
Piermarini, E. E. Antonio. (2013). The dynamic behavior of the Basilica of San Francesco of Assisi [PhD Thesis]. Massachusetts Institute of Technology.
Plinio the Elder. (78 C.E.). Naturalis Historia: Vol. II.
Podestà, S. (2012). Verifica sismica di edifici in muratura. Aggiornamento a NTC e Linee guida per la valutazione e riduzione della vulnerabilità sismica. (in Italian)]. Dario Flaccovio.
Pope, L., & Ward, C. (2008). Manual on Test Sieving Methods. In Manual on Test Sieving Methods, 4th Edition, Prepared by ASTM Committee E29 as Guidelines for Establishing Sieve Analysis Procedures. https://doi.org/10.1520/mnl10684m
Psycharis, I. N., Lemos, J. v., Papastamatiou, D. Y., Zambas, C., & Papantonopoulos, C. (2003). Numerical study of the seismic behaviour of a part of the Parthenon Pronaos. Earthquake Engineering and Structural Dynamics, 32(13). https://doi.org/10.1002/eqe.315
Pulatsu, B., Gonen, S., Lourenço, P. B., Lemos, J. v, & Hazzard, J. (2022). Computational investigations on the combined shear–torsion–bending behavior of dry-joint masonry using DEM. Computational Particle Mechanics. https://doi.org/10.1007/s40571-022-00493-7
Python Software Foundation ("PSF"). (n.d.). The Python Language Reference — Python 3.9.5 documentation.
Quinonez, A., Zessin, J., Nutzel, A., & Ochsendorf, J. (2010). Small-Scale Models for Testing Masonry Structures. Structural Analysis of Historic Constructions, 133, 497–502. https://doi.org/10.4028/www.scientific.net/AMR.133-134.497
Rafiee, A., Vinches, M., & Bohatier, C. (2008). Application of the NSCD method to analyse the dynamic behaviour of stone arched structures. International Journal of Solids and Structures, 45(25–26). https://doi.org/10.1016/j.ijsolstr.2008.07.034
Restrepo Vélez, L. F., Magenes, G., & Griffith, M. C. (2014). Dry stone masonry walls in bending-Part I: Static tests. International Journal of Architectural Heritage, 8(1). https://doi.org/10.1080/15583058.2012.663059
Robert McNeel & Associates. Copyright © 1993-2022. All rights reserved. (n.d.). Rhinoceros.
Roca, P., Pellegrini, L., Oñate, E., & Hanganu, A. (1998). Analysis of the structure of Gothic cathedrals: application to Barcelona cathedral. In P. Roca, J. L. Gonúlez, E. Oñate, & P. B. Lourenço (Eds.), STRUCTURAL ANALYSIS OF HISTORICAL CONSTRUCTIONS II (pp. 231–258). CIMNE.
Romano, A., & Grande E. (2008). Masonry barrel vaults: influence of the pattern. The 14 Th World Conference on Earthquake Engineering.
Rossi, M. (2015). Evaluation of the Seismic Response of Masonry Cross Vaults [Ph.D.]. UNIVERSITÀ DEGLI STUDI DI

GENOVA - SCUOLA POLITECNICA.
Rossi, M., Barentin, C. C., van Mele, T., & Block, P. (2017). Collapse analysis of unreinforced masonry vaults using 3D-printed scale-model testing. International Conference on Advances in Experimental Structural Engineering, 2017-September. https://doi.org/10.7414/7aese.T2.130
Rossi, M., Calderini, C., & Lagomarsino, S. (2016). Experimental testing of the seismic in-plane displacement capacity of masonry cross vaults through a scale model. Bulletin of Earthquake Engineering, 14(1). https://doi.org/10.1007/s10518-015-9815-1
Rossi, M., Calderini, C., Lagomarsino, S., & Milani, G. (2014). Seismic response of masonry vaulted structures: experimen tal and numerical modelling. Proceedings of the 9th International Masonry Conference.
Rossi, M., Calderini, C., Milani, G., & Lagomarsino, S. (2015). Numerical and experimental analysis of an in-scale masonry cross-vault prototype up to failure. AIP Conference Proceedings, 1702. https://doi.org/10.1063/1.4938934
Rossi, M., Calderini, C., Roselli, I., Mongelli, M., Canio, G. de, & Lagomarsino, S. (2020). Seismic analysis of a masonry cross vault through shaking table tests: The case study of the Dey Mosque in Algiers. Earthquake and Structures, 18(1). https://doi.org/10.12989/eas.2020.18.1.057
Rossi, M., Calvo Barentin, C., van Mele, T., & Block, P. (2017). Experimental study on the behaviour of masonry pavilion vaults on spreading supports. Structures, 11. https://doi.org/10.1016/j.istruc.2017.04.008
Sánchez Peña, M. (2020). Estudio y análisis de la bóveda plana de Joseph Abeille. Escuela Técnica Superior de Arquitectura de Madrid UPM.
Sarhosis, V., Asteris, P., Wang, T., Hu, W., & Han, Y. (2016). On the stability of colonnade structural systems under static and dynamic loading conditions. Bulletin of Earthquake Engineering, 14(4). https://doi.org/10.1007/s10518-016-9881-z
Sarhosis, V., Garrity, S. W., & Sheng, Y. (2015). Influence of brick-mortar interface on the mechanical behaviour of low bond strength masonry brickwork lintels. Engineering Structures, 88. https://doi.org/10.1016/j.engstruct.2014.12.014
Sarhosis, V., Oliveira, D. v., Lemos, J. v., & Lourenco, P. B. (2014). The effect of skew angle on the mechanical behaviour of masonry arches. Mechanics Research Communications, 61. https://doi.org/10.1016/j.mechrescom.2014.07.008
Sarhosis, V., & Sheng, Y. (2014). Identification of material parameters for low bond strength masonry. Engineering Structures, 60. https://doi.org/10.1016/j.engstruct.2013.12.013
Sarhosis, V., Tsavdaridis, K. D., & Giannopoulos, I. (2014). Discrete Element Modelling of Masonry Infilled Steel Frames with Multiple Window Openings Subjected to Lateral Load Variations. The Open Construction and Building Technology Journal, 8(1). https://doi.org/10.2174/1874836801408010093
Shapiro, E. E. (2012). Collapse mechanisms of small-scale unreinforced masonry vaults [Ph.D. Thesis]. Massachusetts Institute of Technology.
Silvestri, S., Baraccani, S., Foti, D., Ivorra, S., Theodossopoulos, D., Vacca, V., Roman, J. O., Cavallini, L., Mokhtari, E., White, R., Dietz, M., & Mylonakis, G. (2021). Shaking table testing of groin vaults made by 3D printers. Soil Dynamics and Earthquake Engineering, 150. https://doi.org/10.1016/j.soildyn.2021.106880
STAND4Heritage funded by EU Project. (2020). STAND4Heritage.
Szołomicki, J. P. (2009, July). STRUCTURAL BEHAVIOUR OF MASONRY VAULTS. 18th International Conference on the Application of Computer Science and Mathematics in Architecture and Civil Engineering.
Thanoon, W. A. M., Alwathaf, A. H., Noorzaei, J., Jaafar, M. S., & Abdulkadir, M. R. (2008). Finite element analysis of interlocking mortarless hollow block masonry prism. Computers and Structures, 86(6). https://doi.org/10.1016/j.compstruc.2007.05.022
The Colliery Engineer Co. (1899). A Treatise On Architecture And Building Construction. Vol II: Masonry. Carpentry. Joinery.
Theodossopoulos, D., Makoond, N., & AKL, L. (2016). The Effect of Boundary Conditions on the Behaviour of Pointed Masonry Barrel Vaults: Late Gothic Cases in Scotland. The Open Construction and Building Technology Journal, 10(1). https://doi.org/10.2174/1874836801610010274
Theodossopoulos, D., Sinha, B. P., & Usmani, A. S. (2003). Case Study of the Failure of a Cross Vault: Church of Holyrood Abbey. Journal of Architectural Engineering, 9(3). https://doi.org/10.1061/(asce)1076-0431(2003)9:3(109)
Tralli, A., Alessandri, C., & Milani, G. (2014). Computational Methods for Masonry Vaults: A Review of Recent Results. The Open Civil Engineering Journal, 8(1). https://doi.org/10.2174/1874149501408010272
van Mele, T., McInerney, J., DeJong, M. J., & Block, P. (2012). Physical and Computational Discrete Modelling of Masonry Vault Collapse. Structural Analysis of Historical Constructions, Vols 1-3.
Vella, I. M., & Kotnik, T. (2016). Geometric Versatility of Abeille Vault. Proceedings of the 34th International Conference on Education and Research in Computer Aided Architectural Design in Europe, 2(Figure 1).
Viollet-le-Duc, E. (1863). Dictionnaire raisonné de l'architecture française du XIe au XVIe siècle (BANCE — MOREL).
Walker, P., McCombie, P., & Claxton, M. (2007). Plane strain numerical model for drystone retaining walls. Proceedings of the Institution of Civil Engineers: Geotechnical Engineering, 160(2). https://doi.org/10.1680/geng.2007.160.2.97
Williams, M. S., Albuerne, A., Lawson, V., & Yip, F. (2012). Model scale shaking table tests on masonry barrel and cross vaults. 15th World Conference in Earthquake Engineering.
Wolfe, W. S. (1921). Graphical Analysis. . McGraw-Hill .
Wykeham Farrance - Controls group. (n.d.). SHEARMATIC EmS.
Zheng, H., Zheng, S., Niu, L., & Zhu, L. (2019). Seismic simulation and verification of masonry structure based on equivalent frame model. *World Earthquake Engineering*, 35(1).
Zucchini, A., & Lourenço, P. B. (2002). A micro-mechanical model for the homogenisation of masonry. *International Journal of Solids and Structures*, *39*(12). https://doi.org/10.1016/S0020-7683(02)00230-5

2. THE STRUCTURAL BEHAVIOUR OF MASONRY VAULTS

2.1. Main issues

Vaulted structures are a commonly used horizontal architectural feature in both monumental and ordinary buildings within historical centers. When conducting seismic vulnerability assessments for historical masonry buildings, comprehending the seismic behaviour of vaults is crucial, as it can have a significant impact on the response of the entire building in which they are integrated.

When analyzing the seismic response of masonry buildings, it is typical to consider two modes of response. The first mode assumes a global response of the entire building, which is justified by strong connections between the vertical (such as walls and pillars) and horizontal (such as floor slabs, roof, and ceiling) structural elements. These connections ensure a shared collaboration and "box-behaviour". The second mode assumes a lack of coupling between structural elements and focuses on analyzing the response of individual portions of the building that show independent behaviour (Carfagnini et al., 2017, 2018; Chácara E., 2018; Lagomarsino, 2015; Podestà, 2012). This research specifically focuses on the first mode of collapse, which necessitates three-dimensional modeling of buildings.

Evaluating the behaviour of horizontal structural elements, particularly vaulted structures, two perspectives can be considered: the "local" and "global". Damage to vaults can have significant consequences on the seismic vulnerability assessment of historical buildings. On one hand, local failure can result in the loss of cultural heritage assets. On the other hand, the response of vaults can impact the overall behaviour of the building they belong to.

Typically, the study of vault behaviour at the local scale involves evaluating their seismic capacity and predominant modes of damage. Vaults are primarily subject to forces proportional to their mass, and their response is dependent on factors such as geometry, materials, and construction details. Single-leaf vaults are particularly vulnerable even to earthquakes of low intensity (Ferrario et al., 2012). The main scientific works addressing this scale of analysis employ established modeling tools commonly used for bidimensional analysis of curved structures (e.g., Equilibrium Limit Analysis approach, Finite Element methods, Distinct Element methods) adapted accordingly to describe three-dimensional behaviour.

To analyze the global response, it is necessary to investigate how vaults interact with the vertical structures they are situated on and other structural elements such as tie-rods. When considering such interactions, it is important to take into account not only the unique characteristics of the vaults themselves (e.g. geometry, materials, construction details), but also the relative stiffness of the masonry structures and the boundary conditions, see Figure 2-1. Although some studies have been conducted in this area, it continues to be a relevant and ongoing topic.

Figure 2-1. Church of San Giuliano di Puglia in Campobasso (Italy). Seismic damage (2002 Earthquake) at global scale of masonry cross vaults.

Most of the studies in the literature are focused on the two-dimensional analysis of vaults under static and/or dynamic actions, modeling them as a sequence of arches and thus extending the classical theory of limit analysis of arches to spatial structures. For example, the "Equivalent Frame Models" is frequently adopted (Camata et al., 2022; Lagomarsino et al., 2013; Penna et al., 2022; Zheng et al., 2019), requiring a lower and more reasonable computational effort and involve a limited number of mechanical parameters that consent an use more suitable for practical engineering aims, encouraged also by the Italian Building Code (NTC 2018). However, this hypothesis can be reliable for the analysis of barrel vaults, but it is not always the most appropriate solution for studying complex vault systems, which have a non-negligible three-dimensional behaviour. The works that consider a three-dimensional response, on the other hand, for the most part deal with the analysis of the static behaviour of the vaults, adopting Thrust Network Analysis (Avelino et al., 2021; Block, 2009; Block et al., 2014; Block & Ochsendorf, 2007; Maia Avelino et al., 2021; Marmo et al., 2019; Nodargi & Bisegna, 2022) or a non-linear continuum or distinct models developed within the Finite Element Method. The latter is probably the most adopted modelling approach for the analysis (Alforno et al., 2022; Jasiński & Grzyb, 2020; Joshi, 2022; Olmati et al., 2019; Thanoon et al., 2008), being generally accurate with detailed and commercial tools. In addition, the Distinct Element Method (DEM) is increasingly used in civil engineering, especially for the study of masonry structure (Bui et al., 2017; Colombo et al., 2022; D. Foti et al., 2018; Pulatsu et al., 2022). The DEM falls within the simplified micro-modelling approach and involves modelling the materials as an assemblage of distinct blocks or particles interacting along their boundaries. In this way, the heterogeneous nature of masonry joints is explicitly described (Gaetani, 2020).

In the present research, the interest is focused on the DEM approach, that is able to consider the complexity required in analysing the three-dimensional behaviour of vaulted structures

characterized by spatial shapes.

Experimental investigations are a useful tool for examining these issues. They serve two purposes: firstly, to identify the primary 3D damage mechanisms affecting vaults, which can be compared to damage detected in post-earthquake surveys; and secondly, to establish experimental reference data that can support in estimating mechanical parameters, for exemple elastic stiffness, maximum strength, and ultimate displacement capacity (Rossi, 2015).

The subsequent sections aim to demonstrate the current state-of-the-art in analyzing the seismic behaviour of vaults. This will include a description of the modeling methods used for seismic analysis at both local (§ 2.1.1) and global (§ 2.1.2) scales, as well as a discussion of the primary literature on experimental analyses carried out on either full-scale or reduced-scale models (§ 2.2).

2.1. Modelling approaches (20th and 21st century)

2.1.1. Local scale modeling

Three main approaches are used in the development of tools for simulating the 3D response of vaults, including the use of Limit Analysis as graphical/analytical methods or the Macro-Block Model, the Continuum Constitutive Laws Model, and the Distinct Model. Several in-depth reviews have been conducted on these methods, including works by Abbas et al., 2010, Admane & Murnal, 2017, D'Altri et al., 2020, Kollerathu et al., 2016, Tralli et al., 2014 which discuss the advantages and disadvantages of each approach for analyzing masonry vaulted structures.

Many studies in the literature have attempted to model vaults using Limit Analysis tools, which are well-established. However, these methods are only suitable for simple vaulted structures with a single curvature (such as barrel vaults and domes), and are not applicable to more complex three-dimensional structures. In this approach, vaults are analyzed as "slices" or a series of independent adjacent arches without transverse connection. Both static and dynamic actions can be considered when studying the response of vaults subjected to their own inertial forces.

The common response to dealing with static actions involves using either the static or kinematic Limit Analysis approaches, as noted by various authors (Block et al., 2006; Heyman, 1995, 1998; Livesley, 1992; Oppenheim et al., 1989). The Static (or Lower Bound) Theorem assumes that a purely compressive structure, when subjected to its own weight, is in equilibrium with any external loads if it contains at least one line of thrust that lies entirely within the section (Heyman, 1995). The applied load is considered a lower-bound of the actual ultimate load that could lead to failure. On the other hand, the Kinematic (or Upper Bound) Theorem aims to find the collapse mechanism that corresponds to the minimum load multiplier associated with positive work of the loads. The Uniqueness Theorem also applies, meaning that a limit condition is reached when a collapsing mechanism that is both statically and kinematically admissible can be found. When a thrust line becomes tangent to the boundaries, it causes

hinges, and if this occurs, the load becomes the true ultimate load, the mechanism is the true ultimate mechanism, and the thrust line is the only possible one (Andreu et al., 2007). The collapse multiplier, represented as λ, is proportional to the weight of the structure and represents the multiplier coefficient of the ultimate load.

Oppenheim et al., (1989) used the thrust line construction (Lower-Bound approach) to study the equilibrium of a dome under static loads and determined the minimum thickness required. They analyzed the dome by assuming that cracks develop along the meridians that subdivide the structure, treating each portion as an arch and resolving the forces in its curvature plane.

Bacigalupo et al. (2013, 2015) and Brencich et al. (2014) discussed the safety assessment of the dome of *S. Maria in Carignano* in Genoa. They used a simplified procedure based on static and kinematic Limit Analysis theorems to understand the behaviour of the structure. The researchers first examined kinematically admissible mechanisms and then equilibrated the stress fields (as shown in Figure 2-2). They found that identifying collapse mechanisms was challenging due to the dome's complex three-dimensional response. Their interesting contribution was to consider additional collapse mechanisms involving the tambour. They compared their analysis results with those obtained using FEM.

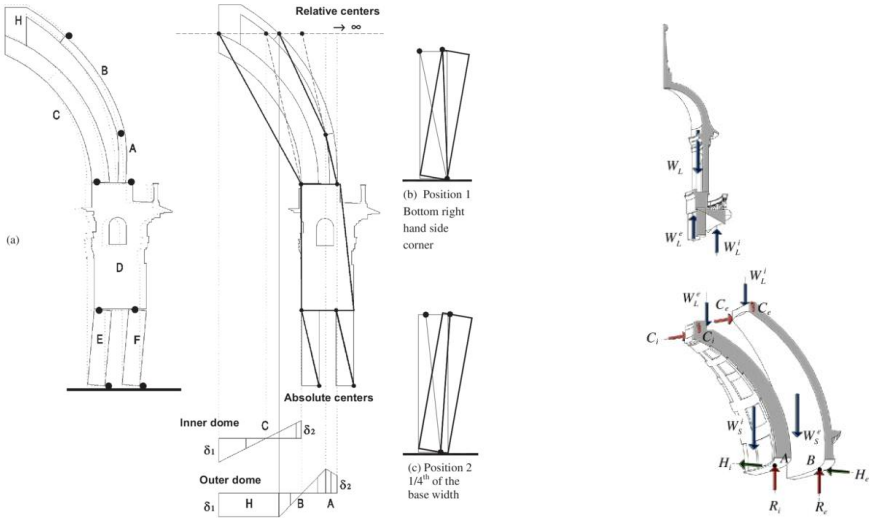

Figure 2-2. Basilica of *S. Maria of Carignano* Genoa (Italy): a. Global kinematic mechanism of dome-tambour system; b. Thrust line/surfaces in the latern and two ogival shells of the dome (Brencich et al., 2014).

Although the bi-dimensional modeling approaches mentioned above can be used to analyze masonry barrel vaults, they are not suitable for vaults with a double-curved shape, such as pavilion vaults, cloister vaults, or cross vaults, due to their significant three-dimensional behaviour. An early example of a pseudo-3D equilibrium analysis is shown in Figure 2-3, which depicts an pointed cross vault from a graphic statics textbook published in the 20th century (Wolfe, 1921). This method involves slicing the web vault into a set of arches and verifying the statics by combining their thrust lines on the diagonal arch. However, this traditional manual thrust line analysis method can be complex and difficult.

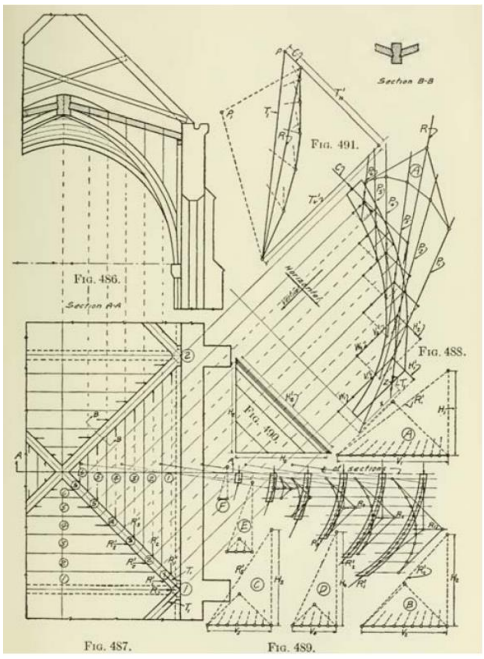

Figure 2-3. Wolfe's graphical analysis of a square-bayed rib vault (Wolfe, 1921).

In recent times, a considering number of studies have proposed analytical tools that utilize Limit Analysis and thrust of lines. These tools are fast and can be applied in real-time. In O'Dwyer (1999) the concept of 3D funicular networks –also known as Thrust Networks Approach (TNA)– was introduced. The TNA discretizes the principal stress path of masonry vaults into a 3D forces network that flows towards the vault's support structure. O'Dwyer used optimization methods to identify possible compression-only networks that were contained within the structure's thickness. Other researchers such as (Andreu et al., 2007; Angelillo et al., 2013; Avelino et al., 2021; Block, 2009; Block et al., 2014; Block & Lachauer, 2014; P. Foti et al., 2016; Fraternali, 2010; Gesualdo et al., 2019; Maia Avelino et al., 2021) have expanded on O'Dwyer's work on the TNA method. They have explored various force paths that are influenced by different variables such as boundary conditions, the role and effect of cross-ribs, the presence of cracks and other pathologies, and the impact of fill above the haunches (see Figure 2-4).

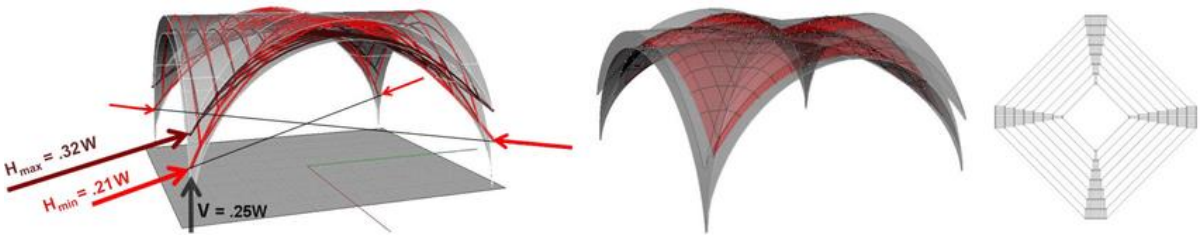

a. b c.

Figure 2-4. Groin vault (Block, 2009): a. Possible thrust values for this groin vault range from 21% to32% of its total weight; b. 3-D web and rib action with the forces mainly spanning between the ribs; c. representation in the dual grid.

In 2011, D'Ayala and Tomasoni developed an analytical method utilizing Static Limit Analysis with finite friction to investigate the behaviour of pavilion vaults. Their findings indicated

that vaults cannot be simplified as a series of adjacent arches without transversal connection, and thus their three-dimensional effects must be taken into account. Other researchers (Abruzzese et al., 1995; Clemente, 1998; de Lorenzis et al., 2007; de Luca et al., 2004; DeJong et al., 2008; DeJong & Ochsendorf, 2006; Oppenheim, 1992) have used kinematic Limit Analysis tools to study the response of arches under dynamic actions. While this approach can be extended to describe the behaviour of barrel vaults, it is not suitable for more complex vaults due to the lack of information regarding their main mechanisms of damage.

The Continuous Model and the Discontinuous Model are two other approaches to 3D modeling that offer a higher level of detail. The Continuous Model, also known as Macro-Modelling Finite Element Models, treats masonry as a homogeneous continuum material and uses constitutive laws based on experimental tests or homogenization procedures (Alforno et al., 2022; Calderini & Lagomarsino, 2006; Joshi, 2022; Olmati et al., 2019; Pelà et al., 2009; Roca et al., 1998; Zucchini & Lourenço, 2002). These laws are defined using two approaches: the phenomenological approach, which uses experimental tests to determine stress-strain relationships and limit domains, and the micromechanical approach, which uses homogenization procedures to determine the constitutive laws of an equivalent material; i.e. a Representative Volume Element (REV). While less detailed, these models can be used for complex geometries and are suitable for larger structural portions.

In contrast, the Discontinuous Model, also known as Micro-Modelling or Discrete Element Method Models, treats masonry as a discontinuous material made up of different blocks and, if there was the mortar joints, that interact through contact laws. So, blocks are modelled by using continuum elements that are assembled by joints modelled as linear or non-linear interface or contact elements (Lourenço et al., 1998). These models can capture complex behaviour such as cracking and fragmenting processes and are suitable for analyzing localized phenomena. However, they involve computationally effort due to the need to analyze each individual block or joints, which limits their application to large-scale structures. Nonetheless, advances in parallel computing techniques and high-performance computing resources have made them more feasible for increasingly complex simulations. Generally, two types of models adopt this approach: the micro-modelling Finite Element Models and the Distinct Element Models.

Certain application of continuous models to analyze vaults are portrayed. In literature there are not specific example about the Abeille’s vault.

Continuous models have been utilized for analyzing vaults in various applications, but there are no explicit cases of the Abeille's vault in literature. As depicted in their research, Alforno et al., (2022) and Calderini (2004) examined the response of a cloister vault to an asymmetrical load to assess the impact of block assembly on vault behaviour (shown in Figure 2-5). They conducted incremental static analyses to evaluate the vault, which was modeled using finite homogenized shell elements.

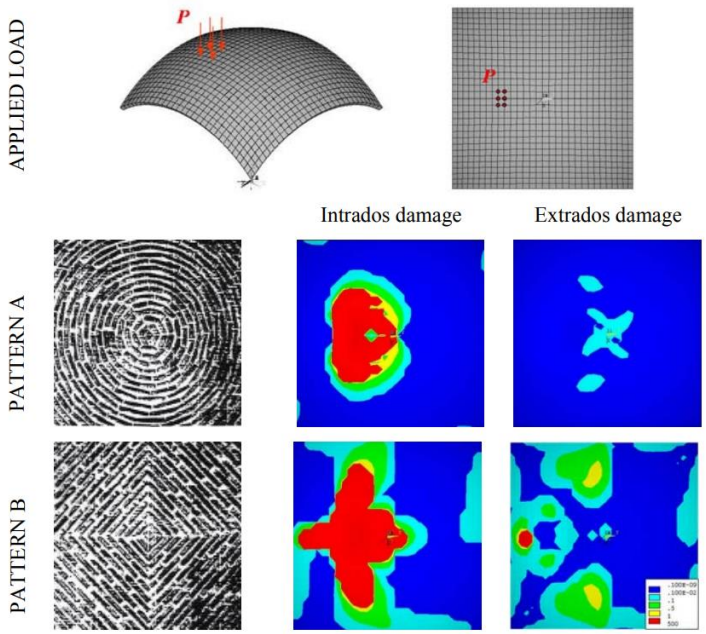

Figure 2-5. Analysis of cloister vault. On the right, the masonry patterns considered. On the left, damage to the mortar bed joints (Calderini, 2004).

In 2009, Szołomicki analyzed the response of both barrel and cross vaults modeled with shell elements using homogenized limit analysis. He varied geometrical proportions and constraints to obtain results. Creazza et al., (2002) compared the results of experimental tests on a barrel and cross-ribbed vault with numerical analysis results using quadratic brick elements and a homogenization procedure developed for concrete.

Various authors have compared the results of analysis performed by Continuous and Discontinuous Models, specifically the macro-modeling Finite Element Models. Romano & Grande E (2008) analyzed the behaviour of a barrel vault using eight-nodes brick elements and compared linear and non-linear analysis results using both continuum and distinct models. E. Milani et al. (2008) proposed a new six-node triangular curved element for kinematic limit analysis of masonry shells and compared results with those obtained by a proposed macro-modelling approach.

In Tralli et al. (2014) and G. Milani & Lourenço (2012) Limit Analyses and static non-linear analyses were performed on different typologies of vault. They were modeled as an assemblage of 3D rigid infinitely resistant six-node and eight-node elements, respectively, interacting on non-linear interfaces (Figure 2-6).

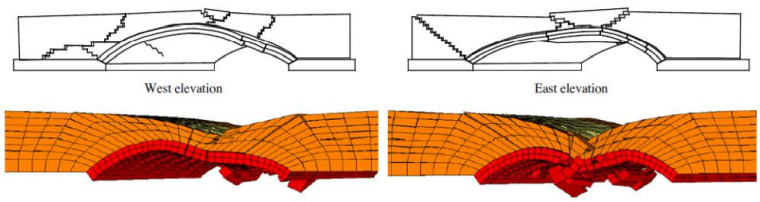

Figure 2-6. Bridge's model: comparison between experimental and numerical results, by using a simplified micro-modeling approach (G. Milani & Lourenço, 2012).

A different type of modeling method known as the Distinct Element Models, was coined by Cundall & Strack (1979) and utilizes a discontinuous approach. These models differ from macro-modeling methods in that they may have certain limitations such as the breakdown of their logic when numerous intersecting interfaces are utilized, lack of an automatic recognition system for new contacts, and being limited to small displacements and rotations, which is often due to adaptation from existing continuum programs.

Masonry is represented as a material composed of individual blocks or block assemblies that can be either rigid or deformable and are connected by contact interfaces to prevent interpenetration between adjacent elements. Distinct Element Models based software automatically identifies new contacts between blocks resulting from block motion and applies the standard equations of rigid body dynamics to their constitutive laws. In Sarhosis & Sheng (2014) study, a Distinct Element code (3DEC - Itasca Consulting Group Inc., n.d.) was used to examine the impact of skew angle on the load-carrying capacity of a barrel vault. Another type of Discontinuous Model, known as NSCD (Non-Smooth Contact Dynamics), was utilized by Rafiee et al. (2008) to evaluate the seismic response of the Arles aqueduct, as shown in Figure 2-7, which is subjected to displacement.

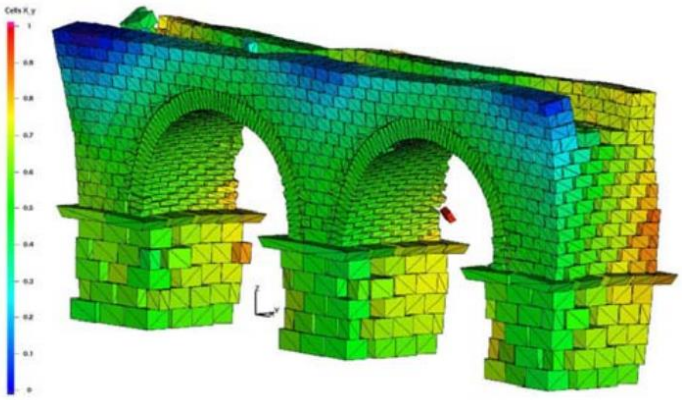

Figure 2-7. Distinct Element model of an arched bridge subjected to a seismic excitation. Lateral perspective view of the deformed shape (Rafiee et al., 2008).

Caliò et al. (2012) has proposed a three-dimensional Discontinuous Model that can predict the non-linear behaviour of masonry shell elements. The model is an extension of a three-dimensional rectangular macro-element that was initially proposed for simulating the seismic response of masonry buildings (Caliò, Marletta, et al., 2012), and it can be applied to curved structures as well. The model comprises a quadrilateral element with rigid edges and hinged vertices, which are connected by diagonal springs to simulate the in-plane shear deformability. Adjacent quadrilateral elements interact with each other along the *rigid layer edge* through a distribution of non-linear springs that have limited tension strength. Additionally, the interfaces have springs orthogonal to the rigid layer that control the in-plane and out-of-plane sliding and torsional behaviour. Figure 2-8 shows a diagrammatic representation of the model, and an example of its application to a masonry dome is illustrated in Figure 2-9.

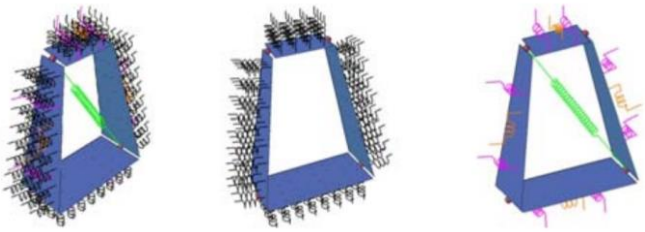

Figure 2-8. Quadrilateral Distinct Element Model and distribution of non-linear spring describing its behaviour (Caliò, Marletta, et al., 2012).

a. b. c. d.

Figure 2-9. Masonry Dome: a. Design, b. Application of the discontinuous approach with discretization of the structure; c. deformed configuration at collapse by considering a non-linear response, d. elastic response (Caliò, Cannizzaro, et al., 2012).

It is crucial to note that the methods described above, while sometimes only applied to static analyses, are generally readily applicable to seismic forces and can serve as a reliable reference.

2.1.2. Global scale modeling

As mentioned in Section § 2.1, there has been limited research on the global-scale modeling of vaults. In the field of Equivalent Frame Models, two options for modeling floor slabs – rigid or infinitely deformable– have consequences for vaults and timber floor slabs, as already explained. Cattari et al. (2008) proposed the definition of a macro-element for vaults (implemented in 3Muri software) and used FEM approach to establish a functional relationship between the elastic stiffness properties of the vault and those of an equivalent plane shell element. This element may have an isotropic or orthotropic membrane response, as shown by Figure 2-10. The researchers conducted parametric analyses on various vault types, including barrel vault, cross vault, and cloister vault, by varying proportions such as thickness-to-span ratios and rise-to-span ratios, constraint conditions, and masonry texture patterns (parallel, orthogonal, and oblique). The results, as shown in Figure 2-11.a, indicate that as the rise-to-span ratio increases, the stiffness of barrel vaults orthogonal to their directrix becomes negligible. The stiffness value of cross vaults provides the highest contribution, but it is not affected by increasing their thickness. On the other hand, the response of cloister vaults, which are less stiff, is significantly influenced by variations in thickness. Figure 2-11.b illustrates the results of tangential stiffness.

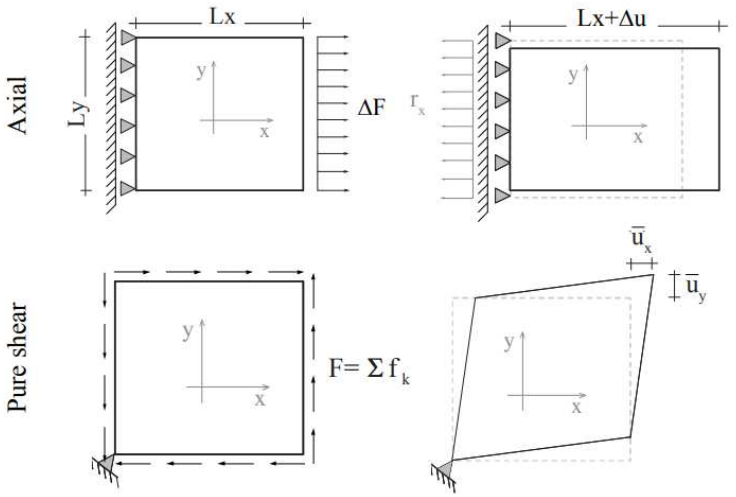

Figure 2-10. Configuration of the considered boundary conditions to evaluate in-plane axial and pure shear distortion mechanisms (Cattari et al., 2008).

The cross vaults show lower stiffness and greater sensitivity to variations in thickness-to-span ratio, whereas cloister and barrel vaults remain unaffected by such variations. Apart from these findings, nonlinear simulations were conducted to investigate two aspects: first, the decay of stiffness in the early nonlinear response, and second, the failure mechanism under varying loads and changes in masonry patterns.

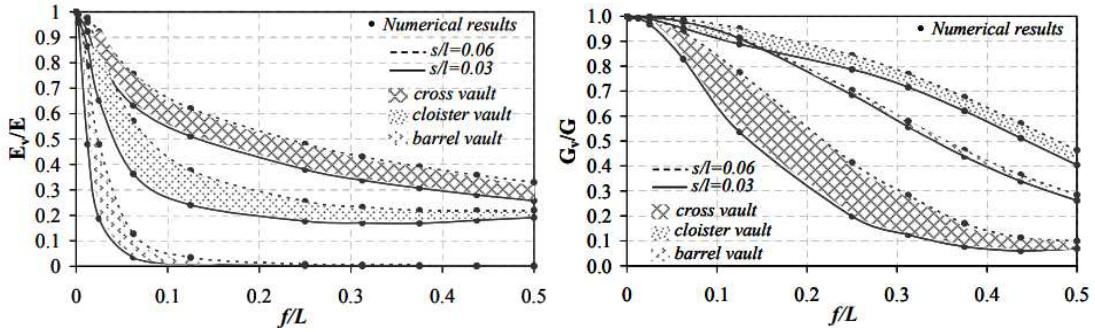

a. b.

Figure 2-11. Stiffness variation with respect to rise-to-span and thickness-to-span values: a. Normal stiffness; b. Tangential stiffness. (Cattari et al., 2008).

Marseglia et al. (2014) employed the modelling approach presented in Cattari et al. (2008) to analyze the *Salento* or *Leccesi vaults*, which are distinctive vaults discovered in the Apulia region of Italy. The study, which included both barrel and cross vaults, showcased the unique masonry patterns of these vaults, as depicted in Figure 2-12. The research findings revealed that the edge vault behaves similarly to the cross vault, while the square vault is more rigid. Additionally, the study considered imposing restrictions at various elevations (on the abutments and kidneys).

On the other hand, Giresini et al. (2014) proposed a simplified model that replicates several types of vaulted systems by estimating the stiffness of an equivalent structure made up of three pairs of links (as illustrated in Figure 2-13). The longitudinal and transverse behaviours are represented by two pairs, and the diagonal pair is responsible for the shear response. To

calculate the equivalent stiffness of each link, a small displacement is applied, and the sum of reaction forces returned by the system is computed. Then, the equivalent stiffness of each link is translated into steel links with a cross-section. The efficacy of the simplified model is validated by comparing the results of linear and nonlinear static and dynamic analyses through a Finite Element Model.

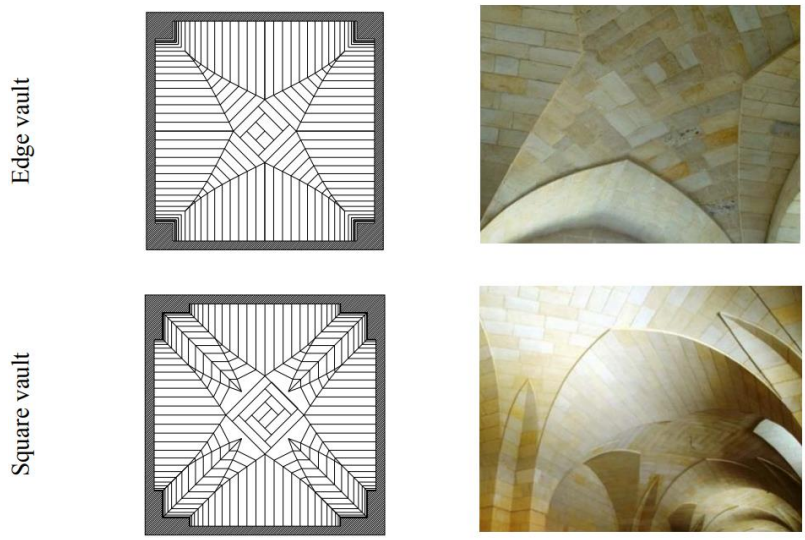

Figure 2-12. Common masonry patterns of *Leccesi* vaults (Marseglia et al., 2014).

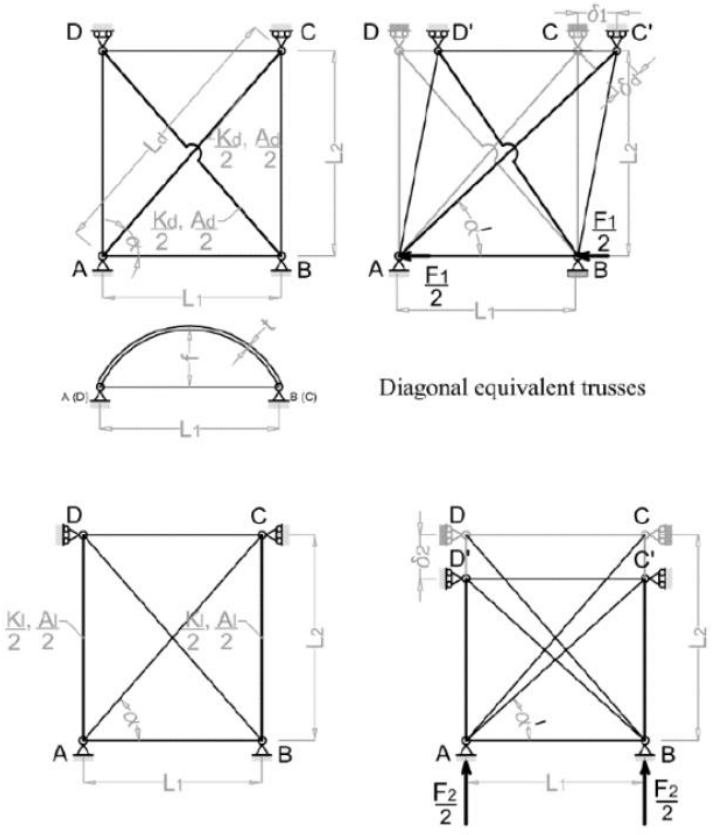

Figure 2-13. Simplified macro-element model for vaults simulating their response in term of equivalent stiffness of a truss system (Giresini et al., 2014).

2.2. Experimental investigations

In recent experimental studies, bidimensional curved structures have been analyzed for their seismic response under both static and dynamic loads. In this work, only those relating vaults (e.g. barrel, pavilion and cross vaults) are presented; even if in literature there are more cases for the arches (Calderini & Lagomarsino, 2015; DeJong et al., 2008; Ferrario et al., 2012; Gaetani et al., 2017; Piccioni et al., 2021).

The first example of an experimental test on a vault small-scale model compared to a numerical one is that of Mark et al. (1973). In particular, the 1:50 model represented two bays of the choir vaulting of Cologne Cathedral and was constructed by cast epoxy. The test simulated the static dead load. A finite-element analysis, based on the photo-elastic-model geometry, was performed. Stress resultants and reactions predicted by the two approaches was comparable.

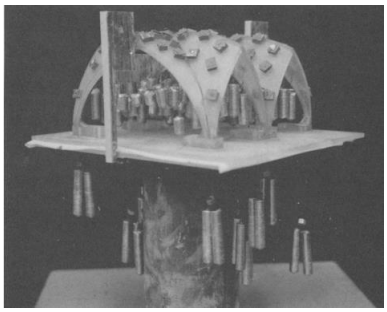

Figure 2-14. Photoelastic- model laoding (Mark et al., 1973).

Ferrario et al. (2012) conducted an experimental investigation on a full-scale model of a single-leaf barrel vault (shown in Figure 2-17c) to assess its response to horizontal loads. To achieve this, a specialized testing apparatus (shown in Figure 2-17a) capable of tilting both clockwise and counter-clockwise was devised (as shown in Figure 2-17b). Tilting the specimen gradually applies the horizontal components of its gravity loads. The study's experimental findings revealed that the development of each new plastic hinge resulted in an abrupt and significant reduction in stiffness. To address this issue, the researchers suggested a strengthening intervention using lightweight ribs.

a. b.

Figure 2-15. Test of the full-scale model of the single-leaf barrel vault: a. General view, b. Special testing bench (Ferrario et al., 2012).

In Marini et al. (2008), the response of a full-scale model of a barrel vault on buttresses with

tie-rods was investigated by applying cyclic horizontal loads using an external pulley system. The study's outcomes, presented in force/displacement curves, indicated a moderately ductile response with minimal energy dissipation capacity. Furthermore, the tension in the tie-rod increased with the four-hinge mechanism, which is likely due to the increase in arch span during the rocking of buttresses.

Several studies have examined the three-dimensional behaviour of vaulted structures, with some investigating their seismic response through the application of static/dynamic forces or through displacement-controlled tests. For example, in Ceradini (1996), full-scale brick cross and tuff cloister vaults were tested by allowing for the spread of two adjacent abutments while anchoring the others. The abutments were then moved using a hydraulic jack under controlled force, resulting in a displacement equal to 2.45% of the total span and the development of the typical three-hinge mechanism. Following this, the vaults were retrofitted and tested again up to 3.5% of their span after bringing the abutments back to their initial positions.

In Briccolati Bati et al. (2002) a complete study in which different load conditions was carried out with symmetric and asymmetric boundary conditions, on a model of 2.3x2.3 m^2, where strengthening techniques (mainly ties and Glass Fibre Reinforced Polymer externally bonded reinforcement) were evaluated.

Theodossopoulos et al. (2003) conducted a comparable test to investigate the response of a cross vault, using a 1:4 scale model made of wood. In this study, the abutments were progressively allowed to move in a displacement-controlled manner until the vault collapsed at 3.1% of the span. Information was provided on the order of vertical deflection.

Williams et al. (2012) tested both 1:25 scale models of barrel and cross vaults on a shaking table. The models were subjected to a series of mono-directional pulses of increasing amplitude and a given frequency. The researchers recorded different hinge locations by varying the shaking amplitudes required to cause failure.

Mouzakis et al. (2012) tested a cloister vault supported by walls on a shaking table in both its un-strengthened and strengthened conditions. During the most severe impulse motion (which corresponded to 150% of the Irpinia earthquake signal), the specimen suffered multiple damages due to the out-of-plane mechanism of a wall, which caused cracks to develop between the vaults and the walls. However, the chosen intervention techniques were successful in significantly increasing the maximum base acceleration.

In the large European FP6 project PROHITECH, De Matteis & Mazzolani, (2010) focused on the seismic behaviour of the church of the Fossanova Abbey (Priverno, Italy). Aiming at investigating the seismic vulnerability of such a structural typology, experimental and numeric analyses have been carried out. On the 1:5.5 reduced scale model ambient vibration tests were carried out and numeric modal identification analyses by FEM were applied, after the first tests it was refined to reproducing the dynamic complex behaviour of the structure. Finally, a shaking-table test on a has been carried out checking the dynamic response as well as the constancy of the previous numeric study.

Figure 2-16. The 1:5.5 scale model and positioning on the shaking table(de Matteis & Mazzolani, 2010).

A shaking table test was conducted on a 1:5 scale model of a generic Algerian Mosque cross vault with asymmetric boundary conditions in de Canio et al. (2012) and Rossi et al. (2020) (Figure 2-17). The model included wooden elements at the base of the ogival arch and was tested with and without two steel bars connecting opposite sides of the vault. The test involved applying a mono-directional input and progressively scaling the Peak Ground Acceleration (PGA) to perform an Incremental Dynamic Analysis. The vault experienced an out-of-plane mechanism resulting in the development of a typical four-hinge mechanism and ultimately collapsed at 0.4 g.

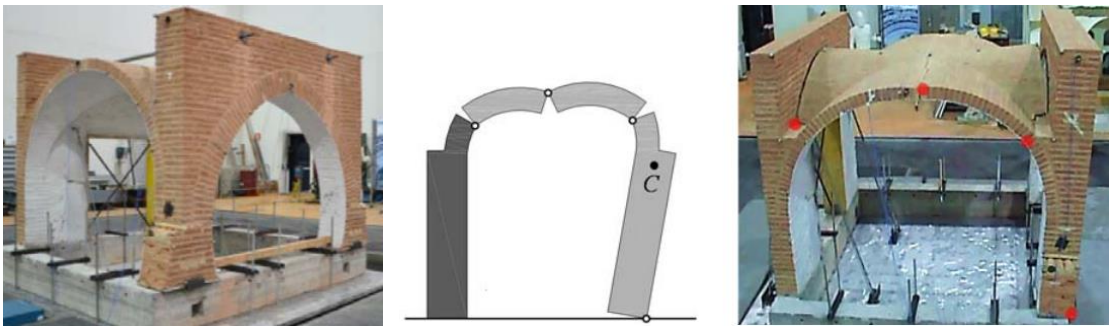

a. b. c.

Figure 2-17. The 1:5 scale model of the cross vault: a. general view; b. Scheme of collapse mechanism; c. Vault damaged (De Canio et al., 2012)

Shapiro (2012) conducted a extensive campaign on seismic response of barrel and groin vaults using 3D-printed scale models. Both displacement control and static force were used to evaluate collapse multipliers of gravity loads. The collapse mechanisms of groin and barrel vaults due to spreading supports can be seen in Figure 2-18.a and Figure 2-19.a, respectively. Average values of maximum support displacements achieved from barrel and groin vaults are presented in

Table 2-1, where two different angles of emplacement equal to 110° and 130° were considered. Multiple action directions were taken into account during the tests on a tilting plane to explore the behaviour under various accelerations that might occur during an actual seismic event (Figure 2-18.b., Figure 2-18.c., Figure 2-19.b. and Figure 2-19.c). The average values of the collapse angle and the equivalent accelerations are shown in

Table 2-2.

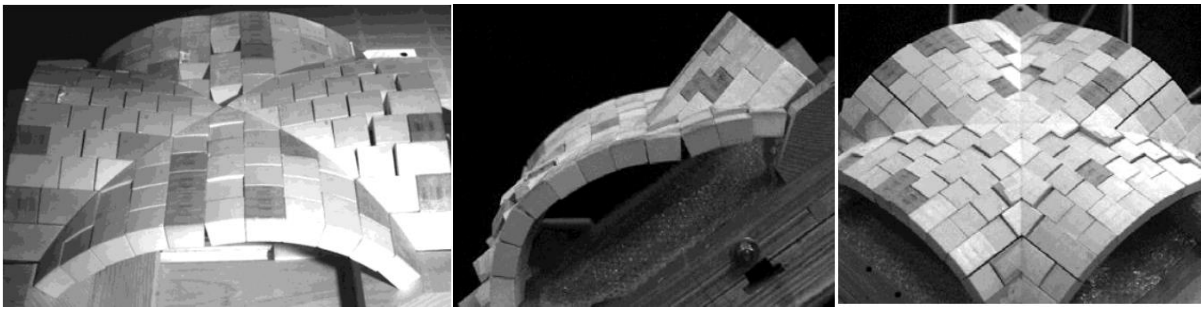

a. b. c.

Figure 2-18. Cross vault collapse mechanism: a. longitudinal openings of two adjacent abutments (hinge on the crown); b. tilting in-plane angle = 0°; c. tilting in-plane angle = 45° (Shapiro, 2012).

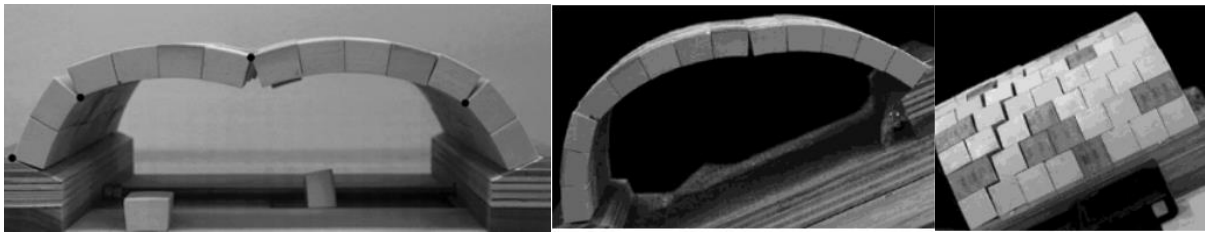

a. b. c.

Figure 2-19. Barrel vault collapse mechanism: a. longitudinal openings of two adjacent abutments (hinge on the crown); b. tilting in-plane angle = 0°; c. tilting in-plane angle = 45° (Shapiro, 2012).

Table 2-1. Average results of span increase at collapse (Shapiro, 2012).

Vault type	Initial span [mm]	Distance spread [mm]	Percent increasemeter
Barrel (130°)	308	23	7.5%
Barrel (130°)	278	26	9.4%
Groin (110°)	278	27	9.7%

Table 2-2. Average results of span increase at collapse (Shapiro, 2012).

Vault type	Orientation	Collapse angle	Horizontal acceleration
Barrel (130°)	Parallel	24.2°	0.45 g
	Perpendicular	27.6°	0.52 g
	45°	30.5°	0.59 g
Groin (110°)	Parallel	33.7°	0.67 g
	Perpendicular	38.6°	0.80 g

Seismic actions were simulated in various tests by implementing diverse displacement configurations to the abutments. Quinonez et al. (2010) conducted experiments on two 3D-printed small-scale models of a dome, subjected to uniform radial displacements (as shown in Figure 2-20). The findings indicated that a symmetrical six-hinge mechanism occurred, with one extrados hinge around the crown, an intrados above the second course of blocks, and the third hinge at the base of blocks leading to collapse.

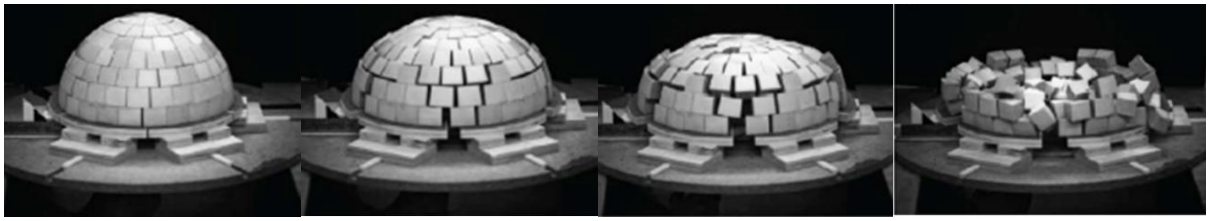

a. b. c. d.

Figure 2-20. 7 Small scale domes made of 3D printed blocks tested to collapse due to outward support displacements (Quinonez et al. 2010).

Van Mele et al. (2012) conducted an experiment on a 1:10 small-scale cross vault constructed using 3D printed blocks. The experiment involved moving one of the abutments in three different directions –diagonal, transverse, and vertical– as shown in Figure 2-21. The researchers analyzed the 3D collapse mechanisms and maximum displacements of the vault and compared the experimental results with those obtained from numerical incremental analyses using a Distinct Element Model (3DEC software -Itasca Consulting Group Inc., n.d.). The authors observed that diagonal displacements caused the vault to spread out similar to an arch supported on spreading supports, whereas transverse and vertical displacements resulted in shear and twist mechanisms.

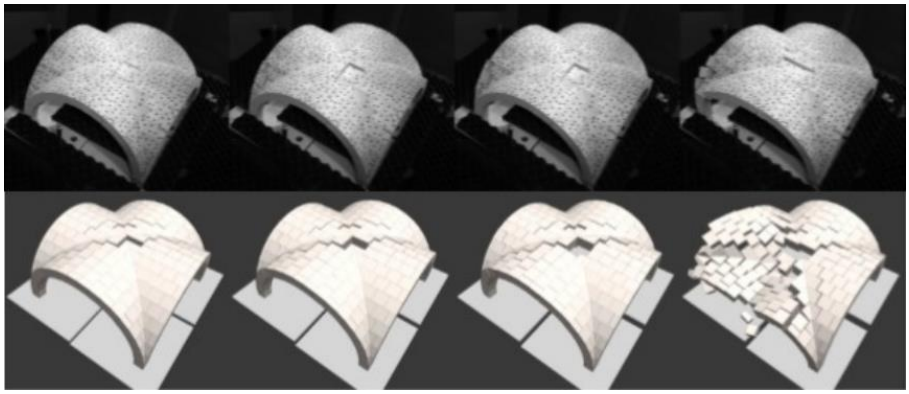

Figure 2-21. Vertical displacement: physical model (above), computational model (bottom)(van Mele et al., 2012).

Among the few experimental work that has described and simulated the in-plane shear behaviour on small-scaled vaults there is that of Rossi (2015); in particular this1:5 scale sample of a cross vault, built with the 3D printing ashlars (filled with metal sheets) and dry joints, was investigated by in numerous researches (Bianchini et al., 2019, 2022; Gaetani, 2020; G. Milani et al., 2016; Rossi, 2015; Rossi et al., 2014, 2015, 2016). In particular, it was test for in-plane shear distortion (simple and pure), longitudinal opening and closing mechanism, tilting and shaking test. In general, for each test the values obtained from numerical tests has higher than the experimentation ones. From the shear results a pronounced ductile response has been highlighted. For the dynamic tests, horizontal displacements were imprinted on the support surface, simulating the distorting action of an earthquake, and observing the typical “four hinges” damage mechanism and a breaking mechanism along the diagonal of the vault (Figure 2-22). The experimental results were then compared with the results of non-linear FEM nu-

merical analyses, in which the vault was discretized through 8-node brick elements and “dry joint” interface sections. By comparing the two models, a good correspondence of the results was obtained. Subsequently a numerical analysis of the same model has been performed using a discrete methodology, with infinitely rigid block elements connected by interfaces with elastic-plastic behaviour, planar elements with four nodes, and the "dry joints" are simulated giving a low value of cohesion and friction. The numerical results compare well with the experimental ones, outlining also in this case the typical three-dimensional collapse behaviour.

a. b. c.

Figure 2-22. Rossi (2015) vault: a. set-up quasi-static test; b. Damage cracks; c. Four- hinge mechanism.

Later, Gaetani (2020) performed new numerical analyzes on the same experimental campaign. The FEM analyses were aimed at understanding the influence of the interface stiffness in two different experimental configurations: in-plane shear distortion and tilting test. The model was implemented adopting a moderately different block pattern and dimensions of the blocks used in the experimental tests. The motivations of this choice were the sensible reduction of DOFs and of the amount of interface elements (the only source of physical nonlinearities), as well as the overall simplicity of the pattern adopted. In terms of catching the failure mechanism, no significant differences were notable between the experimental and numerical results, with an overall good matching of the crack pattern. The study on this vault concerning a physical and several computational model, has significant information on the three-dimensional collapse behaviour and on the final displacement capacity of the structure were provided.

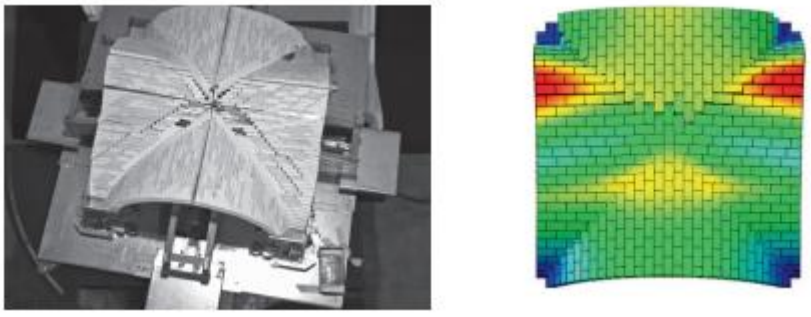

Figure 2-23. Comparison between the experimental and numerical failure mechanism according to different seismic directions (9°) with Kn = Kt = 1 MPa/mm (azimuth view) (Gaetani, 2020).

Fagone et al. (2016) has analyzed the groin vault of St. John Hospital in order to verify the effectiveness of continuous carbon fiber reinforced polymer sheets reinforcement, bonded at the extrados of vaults them-self. Laboratory tests were carried out on a 1:5 scale model, built with materials and construction techniques like those of the real building, and were performed on

the un-strengthened and strengthened vault. The experimental results shown that the strengthening system is able to increase the collapse load of the vault, without substantial variation of the initial stiffness.

In Rossi, Calvo Barentin, et al. (2017) the investigation of the structural behaviour of a pavilion vault was carried out considering spreading supports by means of experimental tests on a 3D–printed scale model made of distinct blocks. Both the collapse mechanisms and the ultimate displacement capacity was analyzed and the experimental data was compared with the results obtained by thrust line analysis. This type of analysis demonstrated a good prediction also for 3D collapse by making specific assumptions that take into account some three-dimensional effects.

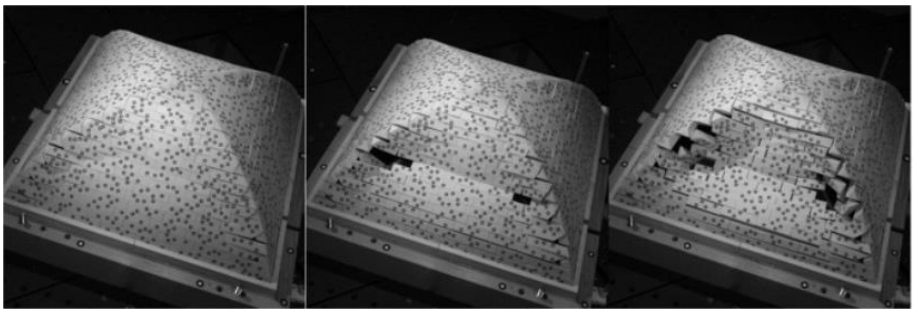

Figure 2-24. Exemple of collapse mechanism of the vault's model (Test T6) (Rossi, Calvo Barentin, et al., 2017).

In this work Foti et al. (2018) study the dynamic and static three-dimensional behaviour of a dry-assembled masonry cross vault, through the comparison of Distinct Element Modeling results and laboratory tests' results on a physical model obtained by mean of 3D printing. The work consists of the first phase where different masonry patterns (parallel, orthogonal) were numerically compares and a second one where a comparison between the static behaviour of the computational and the real scaled models (1 m × 1 m) are compered. The results obtained from the numerical and the experimental tests are in agreement and the pattern certainly influenced the overall behaviour of the vault.

Figure 2-25. Progression of diagonal displacement test: collapse mechanism (D. Foti et al., 2018).

Baraccani et al. (2020) investigates and compare in this work the behaviour of unreinforced and reinforced cross vaults subjected to static shear deformation at the springings through an experimental campaign made on 1:4 scaled model Figure 2-23. The tests are performed in pseudo-static case, applying shear displacements to two abutments until failure. The two models have shown a similar collapse displacement, roughly around 5.5% of the nave arch

span, but a completely different structural response. In fact, for the unreinforced model, the collapse is gradual assisted by partial collapses (blocks falling from webs) observed starting from 3% spread of the longitudinal span, while the reinforced model presents a sudden collapse and no damage is observed in the reinforced portion until total collapse.

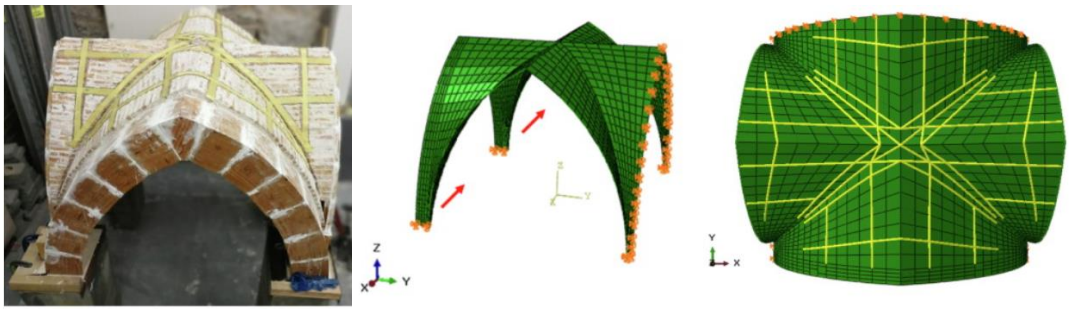

a. b. : c.

Figure 2-26.The reinforced vault: a. the small-scale experimental model; b. 3D view of numerical model; c. FRP reinforced numerical model (Baraccani et al., 2020).

Alforno et al. (2021) has conducted test on scaled cross vaults assembling blocks made with the 3D technique with dry joints. Tests performed the longitudinal opening with the movement of two of the four supports, simple shear test and tilting test. Observing the data obtained from the tilting test and comparing them with the numerical analyzes in Figure 2-27, it can be seen that the numerical results overestimate the effective collapse capacity of the structure.

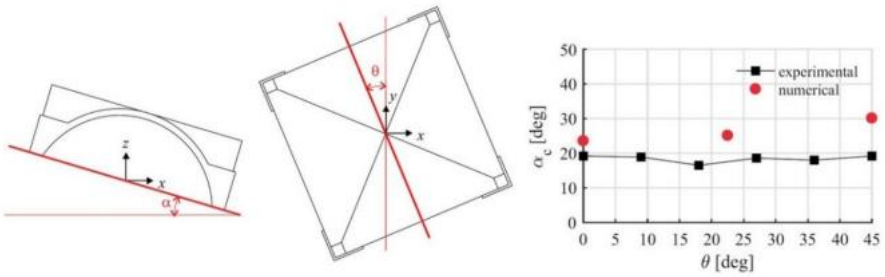

Figure 2-27. Comparison between numerical and experimental results conducted through tilting tests (Alforno et al., 2021)

Silvestri et al. (2021) carried out an experimental study of the dynamic and seismic response of a 2×2 m^2 in plan groin vault model, through the use of a shaking table. The blocks are formed by a 3D-printed plastic skin filled with mortar to provide stiffness and mass. Dry joints are guaranteed and support boundary conditions involving four lateral confinement modes, leading to various vault configurations. White-noise, sinusoidal and earthquake motions were imposed in one horizontal direction, with progressively increasing amplitude and different frequencies, up to collapse. The model exhibited a strong non-linear behaviour, characterized by decreasing fundamental frequency and increasing damping with increasing table acceleration. Failure mechanisms and collapse accelerations were found to mainly depend on base restraint conditions.

Figure 2-28. The vault set-up with four 2 cm-thick Plexiglas panels (Silvestri et al., 2021).

2.3. Reinterpretation of the Vault in Architecture: "The Flat Vault of Abeille"

2.3.1. Historical development

The license of the "flat vault" designed by the French engineer Joseph Abeille (1669–1752) was dated 1699 and published in Machines et inventions approuvées par l'Académie Royale des Sciences (Abeille Joseph, 1699).

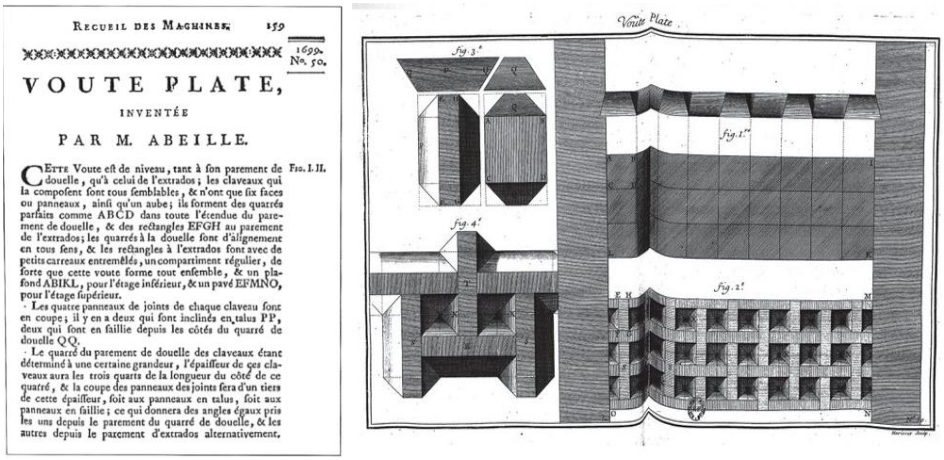

RECUEIL DES MACHINES. 159

1699. No. 50.

VOUTE PLATE,

INVENTÉE

PAR M. ABEILLE.

CETTE Voute eſt de niveau, tant à ſon parement de douelle, qu'à celui de l'extrados; les claveaux qui la compoſent ſont tous ſemblables, & n'ont que ſix faces ou panneaux, ainſi qu'un aube; ils forment des quarrés parfaits comme ABCD dans toute l'écendue du parement de douelle, & des rectangles EFGH au parement de l'extrados; les quarrés à la douelle ſont d'alignement en tous ſens, & les rectangles à l'extrados ſont avec de petits carreaux entremêlés, un compartiment régulier, de ſorte que cette voute forme tout enſemble, & un plafond ABIKL, pour l'étage inférieur, & un pavé EFMNO, pour l'étage ſupérieur. FIG. I. II.

Les quatre panneaux de joints de chaque claveau ſont en coupe; il y en a deux qui ſont inclinés en talus PP, deux qui ſont en ſaillie depuis les côtés du quarré de douelle QQ.

Le quarré du parement de douelle des claveaux étant déterminé à une certaine grandeur, l'épaiſſeur de ces claveaux aura les trois quarts de la longueur du côté de ce quarré, & la coupe des panneaux des joints ſera d'un tiers de cette épaiſſeur, ſoit aux panneaux en talus, ſoit aux panneaux en ſaillie; ce qui donnera des angles égaux pris les uns depuis le parement du quarré de douelle, & les autres depuis le parement d'extrados alternativement.

Figure 2-29. *Flat Vault of Abeille* patented in 1699, in *Machines et inventions approuvées par l'Académie Royale des Sciences* (Abeille Joseph, 1699; Fallacara et al., 2015).

This flat vault is realized by the repetition, in a rectangular matrix, of *Abeille-Type* standard ashlar. The latter is a polyhedron that has two axial sections, in the shape of an isosceles trapezoid, oriented in opposite directions. The pattern of the ashlar takes place in the two orthogonal directions creating a bidirectional flat plate, with a single type of optimized ashlar, whose geometry guarantees the mutual support of the individual blocks of the vaulted system, once assembly is complete. So, the static behaviour of such solution is the same as that of a bidirectional plane that works identically in both directions.

Geometrically, the vault can also be divided into surfaces and is made up of an extrados (which will be the floor of the upper floor) and an intrados (which will be the ceiling of the

lower floor). The upper surface corresponds to a series of rectangles and the lower surface forms a grid of squares. By joining the two faces only with inclined planes, the geometry of the piece is formed. Arranging the pieces in alternate directions, each piece is supported by the two adjacent pieces, as already explained, leaving a square grid on the intrados and a series of pyramidal holes on the extrados.

In 1704 the Carmelite Jean Truchet, also known as Father Sebastien (1657–1729) in "Mémoire concernant les voutes plates" published in Recueil de l'Académie Royale des Sciences described a patent to solve the problem of the pyramidal holes present in the solution of Abeille (Figure 2-30). Truchet's ashlar possesses a squared lower base and an upper one resulting in a mixed line (composed by four identical circular arcs, arranged in pairs on parallel sides of the square to form concave and convex curves and jointed by means of ruled surfaces).

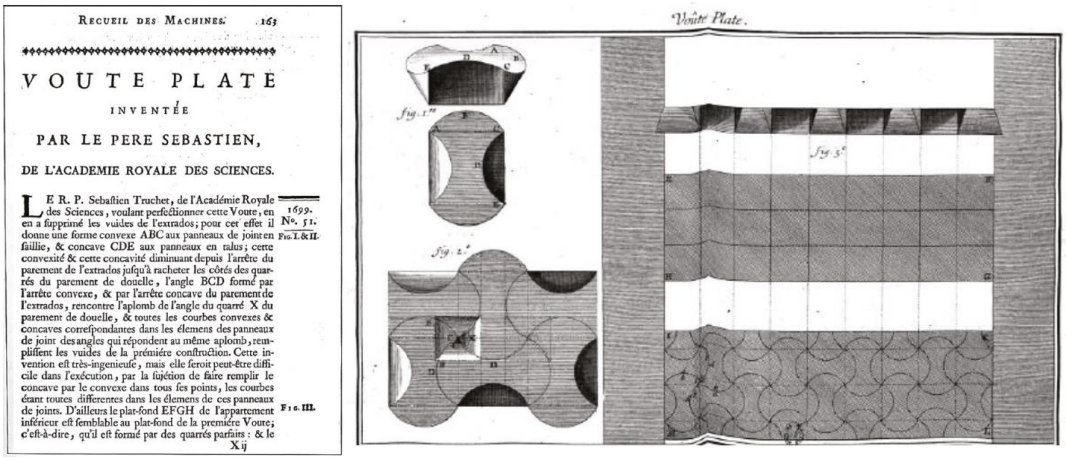

RECUEIL DES MACHINES. 163

VOUTE PLATE
INVENTÉE
PAR LE PERE SEBASTIEN,
DE L'ACADEMIE ROYALE DES SCIENCES.

LE R. P. Sebastien Truchet, de l'Académie Royale des Sciences, voulant perfectionner cette Voute, en a supprimé les vuides de l'extrados; pour cet effet il donne une forme convexe ABC aux panneaux de joint en faillie, & concave CDE aux panneaux en talus; cette convexité & cette concavité diminuant depuis l'arrête du parement de l'extrados jusqu'à racheter les côtés des quarrés du parement de douelle, l'angle BCD formé par l'arrête convexe, & par l'arrête concave du parement de l'extrados, rencontre l'aplomb de l'angle du quarré X du parement de douelle, & toutes les courbes convexes & concaves correspondantes dans les élemens des panneaux de joint des angles qui répondent au même aplomb, remplissent les vuides de la prémiére construction. Cette invention est très-ingenieuse, mais elle seroit peut-être difficile dans l'exécution, par la sujétion de faire remplir le concave par le convexe dans tous ses points, les courbes étant toutes differentes dans les élemens de ces panneaux de joints. D'ailleurs le plat-fond EFGH de l'appartement inférieur est semblable au plat-fond de la premiére Voute; c'est-à-dire, qu'il est formé par des quarrés parfaits: & le

1699. N°. 51. PLS. I. & II. FIG. III.

Xij

Voute Plate.

Figure 2-30. *Flat Vault of Truchet* patented in 1704, in *Machines et inventions approuvées par l'Académie Royale des Science* (Fallacara et al., 2015) *s.*

Amédée François Frézier, in his book (Frézier, 1739), continued with the pattern designs proposed by Truchet, devising different ashlar-types as Figure 2-31 shown, as variations of the Abeille's ones, with which to make this type of vault. The proposed vaults differ from those of Abeille in the shape of the pieces, some even being a composition of two different pieces.

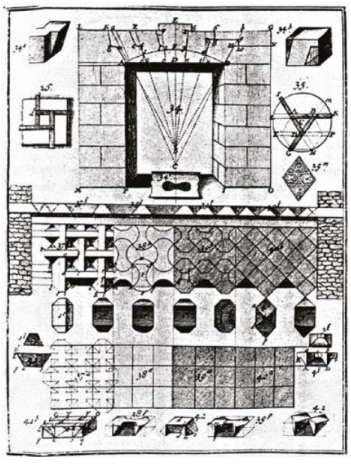

Figure 2-31. Scheme of flat vault ashlar-types developed by *Flat Vault of Frézier* (Fallacara et al., 2015).

In recent years the shape and technology used in the Abeille vault has been studied and adapted for many sterometric studies (Akleman et al., 2020; Andrusko, 2014; Barberio et al., 2016; Brocato & Mondardini, 2012, 2013; Fallacara et al., 2015; Vella & Kotnik, 2016). In fact, its geometry lends well to being deformed and adapted on curvilinear spatial surfaces. So, starting from this ashlar and applying its deformation on curved surfaces, it is therefore possible to design new types of vaults, characterized by ashlars that, through their mutual toothing, improve the joints and the friction between the blocks, as well as create ribs which have both an aesthetic-formal and a structural function.
This type of vault can be optimized in order to have the possibility to ceiling spaces with complex structure. For this reason, this vault was chosen for the design of numerous vaulted spaces of the new generation and to produce expositive prototypes presented during cultural events since 2005 (Figure 2-32).

Figure 2-32 C. D'Amato and G. Fallacara, *Abeille Gate*, Biennale di Venezia, 2006 (Fallacara, Barberio, et al., 2019).

2.3.2. Theoretical concepts for the stereometric deformation of a flat to curvilinear surface

A vaulted space can be defined as a portion of space delimited by flat surfaces of tread and perimetration, and by curved covering surfaces, which constitute the true region for the characterization of the perceived area. The curved line, with any mathematical complexity, can be designed and built in two basic ways: with a tool that can draw the curved (i.e.: compass, algorithm, etc.), or by bending a straight line (Fallacara, Barberio, et al., 2019). The latter mode is totally attuned to the topological view. The method is starting from a very simple consideration, viz. the observation that most of the vaulted systems can be imagined as a discontinuous structure or masonry wall that has been folded and/or deformed to obtain its final geometrical conformation, with due simplifications and specifications (Fallacara, Barberio, et al., 2019). This method uses the technique of bending, thanks to software providing three-dimensional (3D) modelling and the parametric-variational one, thus being based on the topological geometry and its functions of deformation. By using some tools (§ 4.3.1) for spatial transformation and volumetric deformation of a shape, a correspondence between a flat surface and a spatial one is realized. The modelling process is thus considered as a flexible sculp-

ture of the three-dimensional digital data. Every simple starting shape can be modified by means of parametric topological deformations to achieve the desired final object. In so doing, the final object is achieved in an indirect way, and not directly through the canonical modelling that, in the case of complex objects, would involve major difficulties for the 3D modelling. Such deformations are made possible thanks to the subdivision of the surface by tessellation, according to a predetermined polygonal pattern: each intersection between the vertices is behaving like an articulated joint (Fallacara, Barberio, et al., 2019). This process only produces a transformation of the geometry, which becomes the object of future evaluation. Considering the deformation processes that have led to the final configuration of a stereotomic system, the simple and appropriate solid modelling start from the possibility of altering or deforming it in various ways, also by assigning more modifiers to the same object (§ 4.3.1).
In this research, the objects of the topological manipulation have been referring to the ashlar-type of "Abeille's flat vault".

REFERENCES

Abbas, N., Calderini, C., Cattari, S., Lagomarsino, S., Rossi, M., Corradini, R. G., Marghella, G., & Piovanello, V. (2010). DELIVERABLE D4 Classification of the cultural heritage assets, description of the target performances and identification of damage measures. In PERPETUATE PERformance-based aPproach to Earthquake proTection of cUlturAl heriTage in European and mediterranean countries.

Abeille Joseph. (1699). Flat Vault of Abeille.

Abruzzese, D., Como, M., & Lanni, G. (1995). Some results on the strength evaluation of vaulted masonry structures. Structural Studies of Historical Buildings IV-Vol. 1: Architectural Studies, Materials and Analysis, 431–440.

Admane, H. A., & Murnal, P. B. (2017). Analysis of Masonry Structures : a Review. International Journal for Research Trends and Innovation, 2(5).

Akleman, E., Krishnamurthy, V. R., Fu, C. A., Subramanian, S. G., Ebert, M., Eng, M., Starrett, C., & Panchal, H. (2020). Generalized abeille tiles: Topologically interlocked space-filling shapes generated based on fabric symmetries. Computers and Graphics (Pergamon), 89. https://doi.org/10.1016/j.cag.2020.05.016

Alforno, M., Monaco, A., Venuti, F., & Calderini, C. (2021). Validation of Simplified Micro-models for the Static Analysis of Masonry Arches and Vaults. International Journal of Architectural Heritage, 15(8). https://doi.org/10.1080/15583058.2020.1808911

Alforno, M., Venuti, F., Monaco, A., & Calderini, C. (2022). Seismic behaviour of cross vaults with different brick pattern. Bulletin of Earthquake Engineering, 20(8). https://doi.org/10.1007/s10518-022-01347-6

Andreu, A., Gil, L., & Roca, P. (2007). Computational Analysis of Masonry Structures with a Funicular Model. Journal of Engineering Mechanics, 133(4). https://doi.org/10.1061/(asce)0733-9399(2007)133:4(473)

Andrusko, P. A. (2014). Stereotomy: Stone Architecture and New Research by Giuseppe Fallacara. Nexus Network Journal, 16(2). https://doi.org/10.1007/s00004-014-0197-5

Angelillo, M., Babilio, E., & Fortunato, A. (2013). Singular stress fields for masonry-like vaults. Continuum Mechanics and Thermodynamics, 25(2–4). https://doi.org/10.1007/s00161-012-0270-9

Avelino, R., Iannuzzo, A., van Mele, T., & Block, P. (2021). New Strategies to Assess the Safety of Unreinforced Masonry Structures Using Thrust Network Analysis. https://doi.org/10.23967/sahc.2021.162

Bacigalupo, A., Brencich, A., & Gambarotta, L. (2013). A simplified assessment of the dome and drum of the Basilica of S. Maria Assunta in Carignano in Genoa. Engineering Structures, 56. https://doi.org/10.1016/j.engstruct.2013.05.006

Bacigalupo, A., Brencich, A., & Gambarotta, L. (2015). On the Statics of the Dome of the Basilica of S. Maria Assunta in Carignano, Genoa. In Masonry Structures: Between Mechanics and Architecture. https://doi.org/10.1007/978-3-319-13003-3_6

Baraccani, S., Zauli, L., Theodossopoulos, D., & Silvestri, S. (2020). Experimental test on a fibre-reinforced scaled cross vault subjected to in-plane shear displacements at the springings. Construction and Building Materials, 265. https://doi.org/10.1016/j.conbuildmat.2020.120305

Barberio, M., Colella, M., & Fallacara, G. (2016). Stereotomy, Sustainable Construction and Didactics. Case study: a new Museum for Matera, European Capital of Culture 2019. 3 Rd International Balkans Conference on Challenges of Civil Engineering, May 2016.

Bianchini, N., Mendes, N., Calderini, C., Candeias, P. X., Rossi, M., & Lourenço, P. B. (2022). Seismic response of a small-scale masonry groin vault: experimental investigation by performing quasi-static and shake table tests. Bulletin of Earthquake Engineering, 20(3). https://doi.org/10.1007/s10518-021-01280-0

Bianchini, N., Mendes, N., Lourenço, P. B., Calderini, C., & Rossi, M. (2019). Seismic assessment of masonry cross vaults through numerical nonlinear static and dynamic analysis. COMPDYN Proceedings, 1. https://doi.org/10.7712/120119.6942.18709

Binda, L., & Saisi, A. (2005). Research on historic structures in seismic areas in Italy. In Progress in Structural Engineering and Materials (Vol. 7, Issue 2). https://doi.org/10.1002/pse.194

Block, P. (2009). Thrust Network Analysis: Exploring Three-dimensional Equilibrium. In PhD thesis.

Block, P., Ciblac, T., & Ochsendorf, J. (2006). Real-time limit analysis of vaulted masonry buildings. Computers and Structures, 84(29–30). https://doi.org/10.1016/j.compstruc.2006.08.002

Block, P., & Lachauer, L. (2014). Three-dimensional (3D) equilibrium analysis of gothic masonry vaults. International Journal of Architectural Heritage, 8(3). https://doi.org/10.1080/15583058.2013.826301

Block, P., Lachauer, L., & Rippmann, M. (2014). Thrust network analysis: Design of a cut–stone masonry vault. In Shell Structures for Architecture: Form Finding and Optimization (Vol. 9781315849270). https://doi.org/10.4324/9781315849270

Block, P., & Ochsendorf, J. (2007). Thrust network analysis: A new methodology for three-dimensional equilibrium. Journal of the International Association for Shell and Spatial Structures, 48(155).

Brencich, A., Gambarotta, L., & Ghia, A. (2014). History-based assessment of the dome of the Basilica of S. Maria of carignano in Genoa. International Journal of Architectural Heritage, 8(5). https://doi.org/10.1080/15583058.2012.727063

Briccolati Bati, S., Feletti, I., Ranocchiai, G., Rovero, L., & Rapallini, M. (2002). Costruzioni voltate in muratura: indagine teorico sperimentale su prototipi di volte a crociera da impiegare nella ricostruzione dei centri antichi vulnerati dai recenti sismi (Libreria Alfani, Ed.; pp. 41–108). Libreria Alfani.

Brocato, M., & Mondardini, L. (2012). A new type of stone dome based on Abeille's bond. *International Journal of Solids* and Structures, 49(13), 1786–1801. https://doi.org/10.1016/j.ijsolstr.2012.03.036.

Brocato, M., & Mondardini, L. (2013). The proposal of an ancient technique for modern construction: A stone reciprocal structure. In Structures and Architecture: Concepts, Applications and Challenges - Proceedings of the 2nd International Conference on Structures

and Architecture, ICSA 2013 (pp. 472–479).

Bui, T. T., & Limam, A. (2012). Masonry walls under membrane or bending loading cases: Experiments and discrete element analysis. Civil-Comp Proceedings, 99. https://doi.org/10.4203/ccp.99.119

Bui, T. T., Limam, A., Sarhosis, V., & Hjiaj, M. (2017). Discrete element modelling of the in-plane and out-of-plane behaviour of dry-joint masonry wall constructions. Engineering Structures, 136. https://doi.org/10.1016/j.engstruct.2017.01.020

Calderini, C. (2004). The effect of the masonry pattern on the global behaviour of vaults. Proceedings of the 4th International Conference on Structural Analysis of Historic Construction.

Calderini, C., & Lagomarsino, S. (2006). A micromechanical inelastic model for historical masonry. Journal of Earthquake Engineering, 10(4). https://doi.org/10.1080/13632460609350605

Calderini, C., & Lagomarsino, S. (2015). Seismic Response of Masonry Arches Reinforced by Tie-Rods: Static Tests on a Scale Model. Journal of Structural Engineering, 141(5). https://doi.org/10.1061/(asce)st.1943-541x.0001079

Caliò, I., Cannizzaro, F., & Pantò, B. (2012). A macro-element approach for modeling the nonlinear behaviour of monumental buildings under static and seismic loadings. World Conference in Earthquake Engineering.

Caliò, I., Marletta, M., & Pantò, B. (2012). A new discrete element model for the evaluation of the seismic behaviour of unreinforced masonry buildings. Engineering Structures, 40. https://doi.org/10.1016/j.engstruct.2012.02.039

Camata, G., Marano, C., Sepe, V., Spacone, E., Siano, R., Petracca, M., Roca, P., & Pelà, L. (2022). Validation of non-linear equivalent-frame models for irregular masonry walls. Engineering Structures, 253. https://doi.org/10.1016/j.engstruct.2021.113755

Carfagnini, C., Baraccani, S., Silvestri, S., & Theodossopoulos, D. (2017). Pseudo-static response of masonry cross vaults to imposed shear displacements at the springings. Key Engineering Materials, 747 KEM. https://doi.org/10.4028/www.scientific.net/KEM.747.456

Carfagnini, C., Baraccani, S., Silvestri, S., & Theodossopoulos, D. (2018). The effects of in-plane shear displacements at the springings of Gothic cross vaults. Construction and Building Materials, 186. https://doi.org/10.1016/j.conbuildmat.2018.07.055

Cattari, S., Resemini, S., & Lagomarsino, S. (2008). Modelling of vaults as equivalent diaphragms in 3D seismic analysis of masonry buildings. Structural Analysis of Historic Construction: Preserving Safety and Significance - Proceedings of the 6th International Conference on Structural Analysis of Historic Construction, SAHC08, 1. https://doi.org/10.1201/9781439828229.pt5

Ceradini, V. (1996). Modelli sperimentali di volte in tufo e mattoni. La Meccanica Delle Murature Tra Teoria e Progetto .

Chácara E., C. J. (2018). Macro-Element Nonlinear Dynamic Analysis for the Assessment of the Seismic Vulnerability of Masonry Structures. (PhD thesis). PhD Thesis, February.

Clemente, P. (1998). Introduction to dynamics of stone arches. Earthquake Engineering and Structural Dynamics, 27(5). https://doi.org/10.1002/(SICI)1096-9845(199805)27:5<513::AID-EQE740>3.0.CO;2-O

Colombo, C., Savalle, N., Mehrotra, A., Funari, M. F., & Lourenço, P. B. (2022). Experimental, numerical and analytical investigations of masonry corners: Influence of the horizontal pseudo-static load orientation. Construction and Building Materials, 344, 127969. https://doi.org/https://doi.org/10.1016/j.conbuildmat.2022.127969

Como, M. (2013) Statics of Historic Masonry Constructions. Berlin, Heidelberg: Springer (Springer Series in Solid and Structural Mechanics). doi: 10.1007/978-3-642-30132-2.

Creazza, G., Matteazzi, R., Saetta, A., & Vitaliani, R. (2002). Analyses of Masonry Vaults: A Macro Approach based on Three-Dimensional Damage Model. Journal of Structural Engineering, 128(5). https://doi.org/10.1061/(asce)0733-9445(2002)128:5(646)

Cundall, P. A., & Hart, R. D. (1992). Numerical modelling of discontinua. In Engineering Computations (Vol. 9, Issue 2). https://doi.org/10.1108/eb023851

Cundall, P. A., & Strack, O. D. L. (1979). A discrete numerical model for granular assemblies. Geotechnique, 29(1). https://doi.org/10.1680/geot.1979.29.1.47

D'Altri, A. M., Sarhosis, V., Milani, G., Rots, J., Cattari, S., Lagomarsino, S., Sacco, E., Tralli, A., Castellazzi, G., & de Miranda, S. (2020). Modeling Strategies for the Computational Analysis of Unreinforced Masonry Structures: Review and Classification. Archives of Computational Methods in Engineering, 27(4). https://doi.org/10.1007/s11831-019-09351-x

De Canio, G., Clemente, P., Mongelli, M., Rinaldis, D., Roselli, I., Calderini, C., & Rossi, M. (2012). Results of experimental test on damage measures and reference values to be considered. PERPETUATE (EU-FP7 Research Project), Deliverable D12.

De Lorenzis, L., DeJong, M., & Ochsendorf, J. (2007). Failure of masonry arches under impulse base motion. Earthquake Engineering and Structural Dynamics, 36(14). https://doi.org/10.1002/eqe.719

De Luca, A., Giordano, A., & Mele, E. (2004). A simplified procedure for assessing the seismic capacity of masonry arches. Engineering Structures, 26(13). https://doi.org/10.1016/j.engstruct.2004.07.003

De Matteis, G., & Mazzolani, F. M. (2010). The Fossanova church: Seismic vulnerability assessment by numeric and physical testing. In International Journal of Architectural Heritage (Vol. 4, Issue 3). https://doi.org/10.1080/15583050903078903

DeJong, M. J., de Lorenzis, L., Adams, S., & Ochsendorf, J. A. (2008). Rocking stability of masonry arches in seismic regions. Earthquake Spectra, 24(4). https://doi.org/10.1193/1.2985763

DeJong, M. J., & Ochsendorf, J. (2006). Analysis of vaulted masonry structures subjected to horizontal ground motion.

Fagone, M., Rotunno, T., & Bati, S. B. (2016). The Groin Vaults of St. John Hospital in Jerusalem: An Experimental Analysis on a Scale Model. International Journal of Architectural Heritage, 10(7). https://doi.org/10.1080/15583058.2016.1158331

Fallacara, G., Barberio, M., & Colella, M. (2019). Topological interlocking blocks for architecture: From flat to curved morphologies. In Springer Series in Materials Science (Vol. 282). https://doi.org/10.1007/978-3-030-11942-3_14

Fallacara, G., Ferrero, M., & Minenna, V. (2015). Nuovi Sistemi Voltati Stereotomici: Progetto, Calcolo e Costruzione.

Ferrario, L., Marini, A., Andreis, V., Zanotti, S., Riva, P., & Giuriani, E. P. (2012). Behaviour and retrofitting of single-leaf vaults under dis-

tributed horizontal forces. . In Jerzy Jasieńko (Ed.), Structural Analysis of Historical Constructions, (pp. 1503–1511).

Foti, D., Vacca, V., & Facchini, I. (2018). DEM modeling and experimental analysis of the static behavior of a dry-joints masonry cross vaults. Construction and Building Materials, 170. https://doi.org/10.1016/j.conbuildmat.2018.02.202

Foti, P., Fraddosio, A., Lepore, N., & Piccioni, M. (2016). Three-dimensional lower-bound analysis of masonry structures. Structures and Architecture - Proceedings of the 3rd International Conference on Structures and Architecture, ICSA 2016. https://doi.org/10.1201/b20891-77

Fraternali, F. (2010). A thrust network approach to the equilibrium problem of unreinforced masonry vaults via polyhedral stress functions. Mechanics Research Communications, 37(2). https://doi.org/10.1016/j.mechrescom.2009.12.010

Frézier, A. F. (1739). Traité de Stéréotomie .

Gaetani, A. (2020). Seismic Performance of Masonry Cross Vaults : Learning from Historical 4 Developments and Experimental Testing. Sapienza University of Rome.

Gaetani, A., Lourenço, P. B., Monti, G., & Moroni, M. (2017). Shaking table tests and numerical analyses on a scaled dry-joint arch undergoing windowed sine pulses. Bulletin of Earthquake Engineering, 15(11). https://doi.org/10.1007/s10518-017-0156-0

Gesualdo, A., Brandonisio, G., De-Luca, A., Iannuzzo, A., Montanino, A., & Olivieri, C. (2019). Limit analysis of cloister vaults: The case study of Palazzo Caracciolo di Avellino. Journal of Mechanics of Materials and Structures, 14(5), 739–750. https://doi.org/10.2140/jomms.2019.14.739

Giresini, L., Butenweg, C., Andreini, M., de Falco, A., & Sassu, M. (2014). Numerical Calibration Of A Macro-Element For Vaulted Systems In Historic Churches.

Giuffrè, A. (1994). Seismic safety and strengthening of historical buildings and urban fabrics. Earthquake Engineering, 10th World Conference.

Heyman, J. (1995). The stone skeleton: structural engineering of masonry architecture. The Stone Skeleton: Structural Engineering of Masonry Architecture. https://doi.org/10.1115/1.2787238

Heyman, J. (1998). Structural Analysis. In Choice Reviews Online (Issue 03). Cambridge University Press. https://doi.org/10.1017/CBO9780511529580

Itasca Consulting Group Inc. (n.d.). 3DEC – Three-Dimensional Distinct Element Code.

Jasiński, R., & Grzyb, K. (2020). Proposal of empirical homogenization of masonry wall made of AAC masonry units. IOP Conference Series: Materials Science and Engineering, 960(2). https://doi.org/10.1088/1757-899X/960/2/022084

Joshi, R. (2022). Calibration of FEM Models of Historic Masonry Structures and its Application on a Local Historic Structure.

Kollerathu, J. A., Krishnachandran, S., & Menon, A. (2016). Modelling and seismic analysis of existing masonry structures. Structural Analysis of Historical Constructions: Anamnesis, Diagnosis, Therapy, Controls - Proceedings of the 10th International Conference on Structural Analysis of Historical Constructions, SAHC 2016. https://doi.org/10.1201/9781315616995-33

Lagomarsino, S. (2015). Seismic assessment of rocking masonry structures. Bulletin of Earthquake Engineering, 13(1). https://doi.org/10.1007/s10518-014-9609-x

Lagomarsino, S., Penna, A., Galasco, A., & Cattari, S. (2013). TREMURI program: An equivalent frame model for the nonlinear seismic analysis of masonry buildings. Engineering Structures, 56. https://doi.org/10.1016/j.engstruct.2013.08.002

Lemos, J. v. (2007). Discrete element modeling of masonry structures. International Journal of Architectural Heritage, 1(2). https://doi.org/10.1080/15583050601176868

Livesley, R. K. (1992). A computational model for the limit analysis of three-dimensional masonry structures. Meccanica, 27(3). https://doi.org/10.1007/BF00430042

Lourenço, P. B., Rots, J. G., & Blaauwendraad, J. (1998). Continuum Model for Masonry: Parameter Estimation and Validation. Journal of Structural Engineering, 124(6). https://doi.org/10.1061/(asce)0733-9445(1998)124:6(642)

Maia Avelino, R., Iannuzzo, A., van Mele, T., & Block, P. (2021). Assessing the safety of vaulted masonry structures using thrust network analysis. Computers and Structures, 257. https://doi.org/10.1016/j.compstruc.2021.106647

Marini, A., Giardina, G., Riva, P., & Giuriani, E. (2008). Seismic behaviour of barrel vault systems. Structural Analysis of Historic Construction: Preserving Safety and Significance - Proceedings of the 6th International Conference on Structural Analysis of Historic Construction, SAHC08, 1. https://doi.org/10.1201/9781439828229.ch46

Mark, R., Abel, J. F., & O'Neill, K. (1973). Photoelastic and finite-element analysis of a quadripartite vault. Experimental Mechanics, 13(8). https://doi.org/10.1007/bf02322391

Marmo, F., Masi, D., Mase, D., & Rosati, L. (2019). Thrust network analysis of masonry vaults. International Journal of Masonry Research and Innovation, 4(1–2). https://doi.org/10.1504/IJMRI.2019.096828

Marseglia, P. S., Micelli, F., Leone, M., & Aiello, M. A. (2014). Modeling of masonry vaults as equivalent diaphragms. Key Engineering Materials, 628. https://doi.org/10.4028/www.scientific.net/KEM.628.185

Milani, E., Milani, G., & Tralli, A. (2008). Limit analysis of masonry vaults by means of curved shell finite elements and homogenization. International Journal of Solids and Structures, 45(20). https://doi.org/10.1016/j.ijsolstr.2008.05.019

Milani, G., & Lourenço, P. B. (2012). 3D non-linear behavior of masonry arch bridges. Computers and Structures, 110–111. https://doi.org/10.1016/j.compstruc.2012.07.008

Milani, G., Rossi, M., Calderini, C., & Lagomarsino, S. (2016). Tilting plane tests on a small-scale masonry cross vault: Experimental results and numerical simulations through a heterogeneous approach. Engineering Structures, 123. https://doi.org/10.1016/j.engstruct.2016.05.017

Mirabella Roberti, G., & Calvetti, F. (2020). Distinct element analysis of stone arches. In Arch Bridges. https://doi.org/10.1201/9781003078494-27

Mohebkhah, A., Tasnimi, A. A., & Moghadam, H. A. (2008). Nonlinear analysis of masonry-infilled steel frames with openings using discrete element method. Journal of Constructional Steel Research, 64(12). https://doi.org/10.1016/j.jcsr.2008.01.016

Mouzakis, C., Adami, C. E., Karapitta, L., & Vintzilou, E. (2012). Seismic behaviour of a rehabilitated cross vault. . In Jerzy Jasieńko (Ed.), Structural Analysis of Historical Constructions (pp. 1665–1673).

Nodargi, N., & Bisegna, P. (2022). Generalized thrust network analysis for the safety assessment of vaulted masonry structures. Engineering Structures, 270, 114878. https://doi.org/10.1016/j.engstruct.2022.114878

NTC 2018 – Nuove norme sismiche per il calcolo strutturale (D.M. 17/01/2018) - In Italian, 2018.

Numerical Modelling of Discrete Materials in Geotechnical Engineering, Civil Engineering and Earth Sciences. (2004). In Numerical Modelling of Discrete Materials in Geotechnical Engineering, Civil Engineering and Earth Sciences. https://doi.org/10.1201/9780203023983

O'Dwyer, D. (1999). Funicular analysis of masonry vaults. Computers and Structures, 73(1–5). https://doi.org/10.1016/S0045-7949(98)00279-X

Olmati, P., Gkoumas, K., & Bontempi, F. (2019). Simplified FEM modelling for the collapse assessment of a masonry vault. Frattura Ed Integrita Strutturale, 13(47). https://doi.org/10.3221/IGF-ESIS.47.11

Oppenheim, I. J. (1992). The masonry arch as a four-link mechanism under base motion. Earthquake Engineering & Structural Dynamics, 21(11). https://doi.org/10.1002/eqe.4290211105

Oppenheim, I. J., Gunaratnam, D. J., & Allen, R. H. (1989). Limit State Analysis of Masonry Domes. Journal of Structural Engineering, 115(4). https://doi.org/10.1061/(asce)0733-9445(1989)115:4(868)

Otter, J. R. H., Poppard, A. J. S., Lane, R. G. T., Welch, A. K., King, I. P., Wood, W. L., Cubitt, N. J., Hayes, R. J., Hobbs, R. E., Zienkiewicz, O. C., Bickley, W. G., Majid, K. I., Snell, C., Walker, B. A., Postlethwaite, R. W., & Cassell, A. C. (1967). DISCUSSION. DYNAMIC RELAXATION. Proceedings of the Institution of Civil Engineers, 37(4). https://doi.org/10.1680/iicep.1967.8278

Papantonopoulos, C., Psycharis, I. N., Papastamatiou, D. Y., Lemos, J. v., & Mouzakis, H. P. (2002). Numerical prediction of the earthquake response of classical columns using the distinct element method. Earthquake Engineering and Structural Dynamics, 31(9). https://doi.org/10.1002/eqe.185

Pelà, L., Aprile, A., & Benedetti, A. (2009). Seismic assessment of masonry arch bridges. Engineering Structures, 31(8). https://doi.org/10.1016/j.engstruct.2009.02.012

Penna, A., Bracchi, S., Salvatori, C., Morandini, C., & Rota, M. (2022). Extending Analysis Capabilities of Equivalent Frame Models for Masonry Structures (pp. 473–485). https://doi.org/10.1007/978-3-031-15104-0_29

Piccioni, M. D., Olivieri, C., Fraddosio, A., Castellano, A., & Elia, I. (2021). A new experimental approach for small-scale dynamic tests on masonry arches aimed at seismic assessment. International Journal of Masonry Research and Innovation, 6(4). https://doi.org/10.1504/ijmri.2021.10039003

Podestà, S. (2012). Verifica sismica di edifici in muratura. Aggiornamento a NTC e Linee guida per la valutazione e riduzione della vulnerabilità sismica. (in Italian)]. Dario Flaccovio.

Psycharis, I. N., Lemos, J. v., Papastamatiou, D. Y., Zambas, C., & Papantonopoulos, C. (2003). Numerical study of the seismic behaviour of a part of the Parthenon Pronaos. Earthquake Engineering and Structural Dynamics, 32(13). https://doi.org/10.1002/eqe.315

Pulatsu, B., Gonen, S., Lourenço, P. B., Lemos, J. v, & Hazzard, J. (2022). Computational investigations on the combined shear–torsion–bending behavior of dry-joint masonry using DEM. Computational Particle Mechanics. https://doi.org/10.1007/s40571-022-00493-7

Quinonez, A., Zessin, J., Nutzel, A., & Ochsendorf, J. (2010). Small-Scale Models for Testing Masonry Structures. Structural Analysis of Historic Constructions, 133, 497–502. https://doi.org/10.4028/www.scientific.net/AMR.133-134.497

Rafiee, A., Vinches, M., & Bohatier, C. (2008). Application of the NSCD method to analyse the dynamic behaviour of stone arched structures. International Journal of Solids and Structures, 45(25–26). https://doi.org/10.1016/j.ijsolstr.2008.07.034

Roca, P., Pellegrini, L., Oñate, E., & Hanganu, A. (1998). Analysis of the structure of Gothic cathedrals: application to Barcelona cathedral. In P. Roca, J. L. Gonúlez, E. Oñate, & P. B. Lourenço (Eds.), STRUCTURAL ANALYSIS OF HISTORICAL CONSTRUCTIONS II (pp. 231–258). CIMNE.

Romano, A., & Grande E. (2008). Masonry barrel vaults: influence of the pattern. The 14 Th World Conference on Earthquake Engineering.

Rossi, M. (2015). Evaluation of the Seismic Response of Masonry Cross Vaults [Ph.D.]. UNIVERSITÀ DEGLI STUDI DI GENOVA - SCUOLA POLITECNICA.

Rossi, M., Calderini, C., & Lagomarsino, S. (2016). Experimental testing of the seismic in-plane displacement capacity of masonry cross vaults through a scale model. Bulletin of Earthquake Engineering, 14(1). https://doi.org/10.1007/s10518-015-9815-1

Rossi, M., Calderini, C., Lagomarsino, S., & Milani, G. (2014). Seismic response of masonry vaulted structures: experimen tal and numerical modelling. Proceedings of the 9th International Masonry Conference.

Rossi, M., Calderini, C., Milani, G., & Lagomarsino, S. (2015). Numerical and experimental analysis of an in-scale masonry cross-vault prototype up to failure. AIP Conference Proceedings, 1702. https://doi.org/10.1063/1.4938934

Rossi, M., Calderini, C., Roselli, I., Mongelli, M., Canio, G. de, & Lagomarsino, S. (2020). Seismic analysis of a masonry cross vault through shaking table tests: The case study of the Dey Mosque in Algiers. Earthquake and Structures, 18(1). https://doi.org/10.12989/eas.2020.18.1.057

Rossi, M., Calvo Barentin, C., van Mele, T., & Block, P. (2017). Experimental study on the behaviour of masonry pavilion vaults on spreading supports. Structures, 11. https://doi.org/10.1016/j.istruc.2017.04.008

Sarhosis, V., Asteris, P., Wang, T., Hu, W., & Han, Y. (2016). On the stability of colonnade structural systems under static and dynamic loading conditions. Bulletin of Earthquake Engineering, 14(4). https://doi.org/10.1007/s10518-016-9881-z

Sarhosis, V., Garrity, S. W., & Sheng, Y. (2015). Influence of brick-mortar interface on the mechanical behaviour of low bond strength ma-

sonry brickwork lintels. Engineering Structures, 88. https://doi.org/10.1016/j.engstruct.2014.12.014

Sarhosis, V., Oliveira, D. v., Lemos, J. v., & Lourenco, P. B. (2014). The effect of skew angle on the mechanical behaviour of masonry arches. Mechanics Research Communications, 61. https://doi.org/10.1016/j.mechrescom.2014.07.008

Sarhosis, V., & Sheng, Y. (2014). Identification of material parameters for low bond strength masonry. Engineering Structures, 60. https://doi.org/10.1016/j.engstruct.2013.12.013

Sarhosis, V., Tsavdaridis, K. D., & Giannopoulos, I. (2014). Discrete Element Modelling of Masonry Infilled Steel Frames with Multiple Window Openings Subjected to Lateral Load Variations. The Open Construction and Building Technology Journal, 8(1). https://doi.org/10.2174/1874836801408010093

Shapiro, E. E. (2012). Collapse mechanisms of small-scale unreinforced masonry vaults [Ph.D. Thesis]. Massachusetts Institute of Technology.

Silvestri, S., Baraccani, S., Foti, D., Ivorra, S., Theodossopoulos, D., Vacca, V., Roman, J. O., Cavallini, L., Mokhtari, E., White, R., Dietz, M., & Mylonakis, G. (2021). Shaking table testing of groin vaults made by 3D printers. Soil Dynamics and Earthquake Engineering, 150. https://doi.org/10.1016/j.soildyn.2021.106880

Szołomicki, J. P. (2009, July). STRUCTURAL BEHAVIOUR OF MASONRY VAULTS. 18th International Conference on the Application of Computer Science and Mathematics in Architecture and Civil Engineering.

Thanoon, W. A. M., Alwathaf, A. H., Noorzaei, J., Jaafar, M. S., & Abdulkadir, M. R. (2008). Finite element analysis of interlocking mortarless hollow block masonry prism. Computers and Structures, 86(6). https://doi.org/10.1016/j.compstruc.2007.05.022

Theodossopoulos, D., Sinha, B. P., & Usmani, A. S. (2003). Case Study of the Failure of a Cross Vault: Church of Holyrood Abbey. Journal of Architectural Engineering, 9(3). https://doi.org/10.1061/(asce)1076-0431(2003)9:3(109)

Tralli, A., Alessandri, C., & Milani, G. (2014). Computational Methods for Masonry Vaults: A Review of Recent Results. The Open Civil Engineering Journal, 8(1). https://doi.org/10.2174/1874149501408010272

van Mele, T., McInerney, J., DeJong, M. J., & Block, P. (2012). Physical and Computational Discrete Modelling of Masonry Vault Collapse. Structural Analysis of Historical Constructions, Vols 1-3.

Vella, I. M., & Kotnik, T. (2016). Geometric Versatility of Abeille Vault. Proceedings of the 34th International Conference on Education and Research in Computer Aided Architectural Design in Europe, 2(Figure 1).

Walker, P., McCombie, P., & Claxton, M. (2007). Plane strain numerical model for drystone retaining walls. Proceedings of the Institution of Civil Engineers: Geotechnical Engineering, 160(2). https://doi.org/10.1680/geng.2007.160.2.97

Williams, M. S., Albuerne, A., Lawson, V., & Yip, F. (2012). Model scale shaking table tests on masonry barrel and cross vaults. 15th World Conference in Earthquake Engineering.

Wolfe, W. S. (1921). Graphical Analysis. . McGraw-Hill .

Zheng, H., Zheng, S., Niu, L., & Zhu, L. (2019). Seismic simulation and verification of masonry structure based on equivalent frame model. World Earthquake Engineering, 35(1).

Zucchini, A., & Lourenço, P. B. (2002). A micro-mechanical model for the homogenisation of masonry. International Journal of Solids and Structures, 39(12). https://doi.org/10.1016/S0020-7683(02)00230-5

3. NUMERCAL MODELING OF THE DISTINCT ELEMENT

3.1. Introduction to Distinct Elements Method (DEM)

This chapter offers a general description of the numerical models adopted in the analyses presented in the next chapters. The main characteristics of the Distinct Elements Method (DEM) are described in order to justify the use of this tool for the study of the multi-body structures object of the present work.

Modeling using discontinuous elements can be carry out using Finite Element Methods (FEM) adopting fitting interface elements, thus modelling the masonry as a continuous element with a dense mesh as joints. Distinct Element (DE) modeling, on the other hand, considers the structure as an assembly of distinct bodies interacting with each other through their perimeter surface. The difference between the methodologies it gradually becomes more and more evident.

The Distinct Element Method (DEM) falls within the general classification of discontinuous analysis techniques. It is a numerical method that can be used for simulating the mechanical behaviour of systems composed of disjointed bodies with geometric boundaries able to define the distinction from contiguous unities. It allows to represent the mechanical behaviour and the interaction of blocks, assuming the joints as contact surfaces. The use of this approach is intended to describe directly the evident non-linear character of masonry structures, including joint sliding phenomena or their disjunction, which could cause large relative displacements between blocks, changing the structural geometry. The preferred field of application is the analysis of structural collapses, modeled through pseudo-static or dynamic processes, in the context of safety assessment of existing studies.

The first development of distinct element models was motivated by the sliding analysis of earth and rock masses. The conceptual model of a rock mass seen as a set of rigid blocks was already common in the 1960s in the field of rock mechanics, but the analytical methods using only allowed to deal with simpler problems.

The DEM was developed by Cundall (Cundall & Hart, 1992; Cundall & Strack, 1979) as a numerical approach to the resolution of mechanical problems concerning rocks with the presence of discontinuities.

The procedure to arrive at the solution involved the integration of the equations of motion of the blocks, which it allowed the possibility of considering large displacements, to be able to update the positions in sequence of the blocks. Static solutions were obtained by using an artificial viscous damping, as in the approximate dynamic methods. Therefore, from the very beginning, this numerical technique could simulate the static and dynamic behaviour of sets of discrete bodies interacting with each other, subjected to arbitrary movements. These key concepts also find application in many types of masonry structures, in which deformation and collapse are governed by discontinuities, as in the mater work of Heyman (Heyman, 1995). Also the analyses of simple buildings –one or two levels– are also sometimes based on a macro-block representation (Binda

& Saisi, 2005; Giuffrè, 1994). DEM can be considered as an extension of these analytical techniques to more complex systems, both in terms of geometry, and of assumptions adopted for the behaviour of the materials of which they are made, i.e. the contact laws.

The fundamental characteristic of DE models consists in representing the examined object as a set of interacting mechanical blocks. The joints are seen as surfaces where contact between blocks takes place, governed by appropriate constitutive laws. Therefore, the starting point of a DE model consists of a discontinuous system, in contrast to the FE method, which starts from the representation of a continuous body. There are some characteristics that make DEM distinguishable from FEM:

- DE models have rigid blocks, and the deformability of the system is concentrated between the joints, even if today, many DE models include formulations with deformable blocks, in fact nowadays DEM is very often combined with FEM for modelling the deformation of the bodies (Munjiza, 2004);
- In the majority of DE models, the interaction between blocks is represented by sets of contact points or groups of edge-to-edge contacts, without the possibility of obtaining a distribution uniformity of stresses on the entire contact surface. In general, a deformable block can be independently discretized from neighboring ones;
- DE models are designed to allow complete separation between the blocks, and most of them allow the analysis to continue in the regime of the displacements;
- DE models tend to employ "time-stepping" algorithms to solve quasi-static problems.

Today, this numerical approach is presented in the commercial codes UDEC (Universal Distinct Element Code) and 3DEC® software for two and three dimensional simulations, respectively (Itasca Consulting Group Inc., n.d.). In the last decades, the software has been used for a range of applications, including masonry wall panels (Bui et al., 2017; Bui & Limam, 2012; Sarhosis et al., 2015; Sarhosis & Sheng, 2014), retaining walls (Walker et al., 2007), masonry-infilled steel frames with openings (Mohebkhah et al., 2008; Sarhosis, Oliveira, et al., 2014; Sarhosis, Tsavdaridis, et al., 2014) stone masonry arches, vaults and aqueducts (D. Foti et al., 2018; Mirabella Roberti & Calvetti, 2020; "Numerical Modelling of Discrete Materials in Geotechnical Engineering, Civil Engineering and Earth Sciences," 2004; Sarhosis, Oliveira, et al., 2014; Silvestri et al., 2021) and column-architrave structures under seismic action (Papantonopoulos et al., 2002; Psycharis et al., 2003; Sarhosis et al., 2016).

3.2. Principles of mechanical modeling

The representation of the contact in many DE models is based on assumptions about the points where it occurs: the interaction between the blocks is represented by a series of contact points and each force of contact is a function of the relative displacement of the block at that point.

These point contacts are assigned an area so that stresses can be calculated using the normal constitutive bonds of the joints, typically formulated in terms of stresses and relative displacements.

The main advantage of this approach lies in its generality and simplicity, being able to handle the various types of geometric interaction and allowing large displacements of the blocks.
In particular, this approach allows a transition between the case of contact between faces and the case of actual point contact, such as the interaction between a vertex and a surface. Obviously, the accuracy of the stress distribution obtained on the contact surfaces is greater with elements of junction, and therefore DE codes require more contact points if accurate contact stress values are researched (Lemos, 2007).
In 3D analyses, there are many possible interaction combinations between faces, edges, and vertices which increase the complexity of the problem and its numerical implementation. The 3DEC® Software (Cundall & Hart, 1992; Itasca Consulting Group Inc., n.d.) adopts a punctual representation of contact based on two types of interaction: vertex-face contact and edge-edge (Figure 3-1). With these two types of punctual contacts, it is possible to address the various types of interaction between polyhedral blocks.

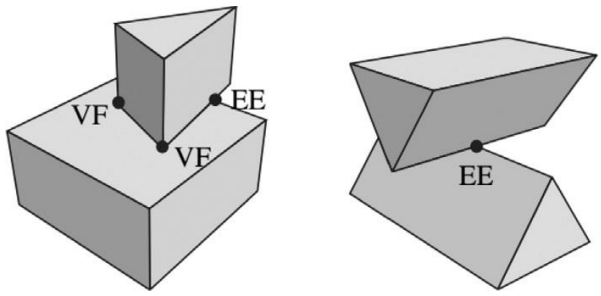

Figure 3-1. Representation of the interaction between blocks via Vertex-Face (VF) and Edge-Edge (EE) contact points in 3DEC® (Cundall & Hart, 1992): a. Face-Face case; b. Edge-Edge case. (Itasca Consulting Group Inc., n.d.).

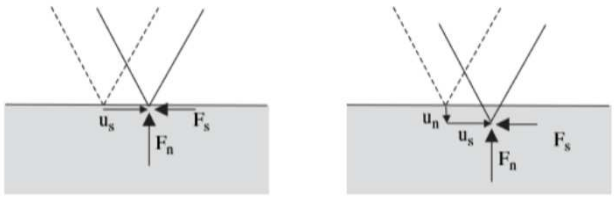

Figure 3-2. Contact typology: a. Rigid contact; b. Deformable contact. (Itasca Consulting Group Inc., n.d.)

Cundall & Hart (1992) have classified the representation of the mechanical behaviour of contacts in models with distinct elements in two general classes (Figure 3-2):

- Model with rigid contact, in which the non-overlapping condition between the blocks is enforced;
- Model with deformable contact, in which the stiffness of the contact is defined along the direction normal and tangential and correlates the contact stresses with the relative displacements of the blocks. For this reason, there are small overlap when the contact is in compression.

3.2.1. Representation of the contact

The rigid contact assumption is typically adopted in rigid block analyses using solutions linear in which the non-overlapping conditions can be assimilated to constraints. The contact approach deformable is preferred in many formulations to distinct elements.

It is possible to consider both the contact stiffness in the normal direction and in the tangential direction, such as penalty coefficients that allow the user to define an amount of overlap which can be tolerated. However, in the modeling of masonry structures, the normal stiffness assumes not only the meaning of a simple numerical entity but has a precise physical meaning: in the case of joints with mortar, it can be related to the thickness and mechanical properties of the mortar. In the case of dry joints, the irregular contact produces tensions and therefore localized deformations on the surface of the block. So, the interface's constitutive relations can be defined in terms of the stresses and relative displacements across the joint and these are assumed to be linear in both directions:

$$\sigma_N = k_N \cdot u_N \qquad (3.\ 1)$$

where σ_N is the normal stress, u_N the relative normal displacement between adjacent blocks and k_N the constant of stiffness in that direction (Figure 3-3).

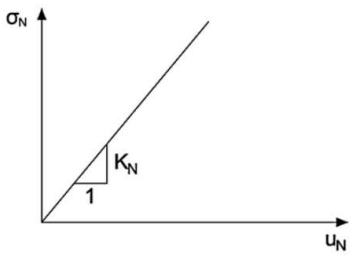

Figure 3-3. Linear elastic constitutive relation.

In the tangential direction the Coulomb friction model is the most used for joints in the masonry. Some formulations involving rigid contact effort in implementing this criterion, while in the deformable contact models a elastic behaviour - perfectly plastic in shear. In the elastic phase the behaviour is described from the linear law:

$$\tau_S = k_S \cdot u_S \qquad (3.\ 2)$$

where τ_S is the tangential stress, us the relative tangential displacement between adjacent blocks and k is the stiffness constant in that direction (Figure 3-4).

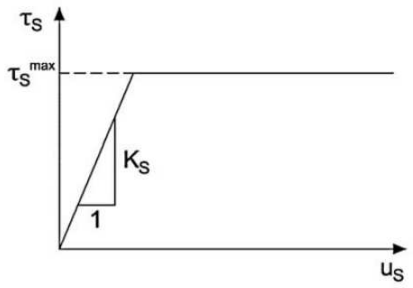

Figure 3-4. Elastic-perfectly plastic constitutive relation.

The maximum value of the tangential stress beyond which the behaviour becomes perfectly plastic is given by Coulomb's law of friction:

$$\tau_S^{max} = c + \sigma_N^{max} \cdot tan\,\varphi \qquad (3.\ 3)$$

where c is the cohesion and φ the angle of internal friction of the material of which the joint is composed.

3.2.2. Contact forces

One of the peculiarities of the DEM lies in the ability to recognize contacts, impacts and disconnections of bodies automatically. Contact forces are applied only when the contact between two bodies is detected: these interactions can be due to identified contacts, existing contacts, or relative displacements or rotations between bodies in contact. Although contact between colliding bodies requires the analysis of complex phenomena such as the dissipation of energy in the system and the local deformation of bodies, it is possible to account for these effects by modeling the contact using springs and dampers, while the bodies simulated are usually assumed to be infinitely stiff. The final deformation of a system so defined – infinitely rigid and with distinct bodies – is considered to be due to displacements and relative movements, assuming that the deformation pertaining to the single bodies is negligible.

The normal and tangential directions are defined with respect to the contact surface between the bodies, determined for each step of the analysis. The Coulomb's friction law is considered in tangential directions to simulate potential sliding between individual units. This keeps the bodies in direct contact to slide one with respect to the other along these surfaces, when in a defined direction, the reached value of the tangential force is higher than the maximum tension established by Coulomb's friction law.

At each step of the analysis, the mutual contact forces – acting between each element of simulated structural system – is defined through an algorithm capable of carrying out this recognition.

Contact is established for each interval of the simulation and are automatically adjusted accord-

ingly generate equivalent springs and dampers, applied to the interface of the bodies in the normal and tangential direction (Figure 3-5).

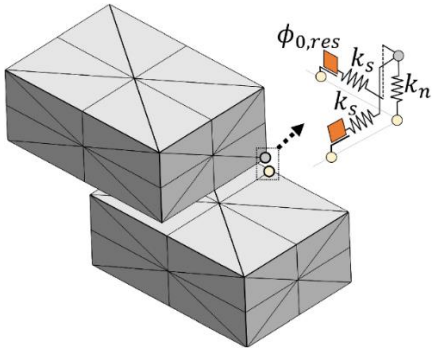

Figure 3-5. Representation of the springs and dampers in a contact point (Pulatsu et al., 2022).

Based on the area of the region of overlap and the relative velocity between contiguous bodies, they have been calculated the elastic ($F^{elastic}$) and damping (F^{damp}) contact forces in the normal and tangential directions, applying the following equations:

$$F_N(t+\Delta t) = F_N^{elastic}(t+\Delta t) + F_N^{damp}(t+\Delta t) = A_c(t)k_N + V_N^{rel}C_N \quad (3.\ 4)$$

$$F_S(t+\Delta t) = F_S^{elastic}(t+\Delta t) + F_S^{damp}(t+\Delta t) = V_S^{rel}\cdot\Delta t\cdot k_S + V_N^{rel}C_S \quad (3.\ 5)$$

In Eq.s (3.4) and (3.5), the subscripts *N* and *S* indicate the normal direction and respectively tangential. Consequently, k_N and k_S are the stiffnesses, V_N^{rel} and V_S^{rel} the velocities, C_N and C_S the damping coefficients in the relative directions and A_C the area of the contact region. Being the damping proportional to the velocity, the magnitude of the damping force is a function of the relative velocity of the rigid blocks in contact. To limit the force in the tangential direction, the frictional force is considered below a certain threshold value provided by Coulomb's friction law expressed as follows:

$$|F_S(t+\Delta t)| \le |\mu\cdot F_N(t+\Delta t)| \quad (3.\ 6)$$

where μ represents the coefficient of friction.

3.2.3. Equations of motion

Generally, DEM is based on an explicit time integration method that solves the equations of block system motion by an explicit finite difference method. During the motion the forces –as evaluated by the Eq.s (3. 4) and (3. 5)– are applied at the points of contact of the simulated bodies, while the weight forces are applied in the centers of mass of the same. The equations of the motion are formulated and solved taking into account all the forces and moments applied to each

body, and providing its displacements (or velocities), which define the position up-dated at each step of the simulation. The equations thus obtained are then integrated in explicit form for each discrete body, using the method of centered finite differences, to calculate successively the displacements and rotations of each body at time t+Δt. In particular, these entities are determined starting from the dynamic equilibriums at the instant *t*, and are characterized by the following Eq.s (3. 7):

$$U_x(t+\Delta t) = \frac{\Delta t^2}{m}\left\{F_x^{contact} - \frac{m}{\Delta t^2}U_x(t-\Delta t) + \frac{2m}{\Delta t^2}U_x(t)\right\}$$
$$U_y(t+\Delta t) = \frac{\Delta t^2}{m}\left\{F_y^{contact} + mg - \frac{m}{\Delta t^2}U_y(t-\Delta t) + \frac{2m}{\Delta t^2}U_y(t)\right\} \quad (3.\ 7)$$
$$\vartheta_z(t+\Delta t) = \frac{\Delta t^2}{l_0}\left\{M_x^{contact} - \frac{l_0}{\Delta t^2}\vartheta_z(t-\Delta t) + \frac{2l_0}{\Delta t^2}\vartheta_z(t)\right\}$$

where U_x and U_y are the displacements in the x and y directions while θ_z is the rotation around the z axis. At the same manner F_x and F_y are the contact forces in the x and y direction respectively and M_z is the moment of the axis z. Finally, m and l_0 are the mass and rotational inertia of the body. This process is repeated iteratively through new cycles that improve the determination and resolution of the contact, and the numerical solution of the motion equations until the simulation ends.

The numerical analysis assumes that speeds and accelerations are constant during each time step. The DEM methodology is based on the concept that such a time interval is small enough, so that no variation can propagate between the discrete elements for the entire duration of the calculation step. To this end, a suitably small timestep –which is automatically calculated by the program and is directly proportional to the smallest nodal mass and inversely proportional to the maximum contact stiffness of the system intervals are– used in order of 10^{-6} s, to be able to satisfactorily capture the impact and contacts between the bodies of the simulated system.

3.3. 3DEC® (DEM Software)

The software used for the modeling in this research is 3DEC®, developed by (Itasca Consulting Group Inc., n.d.). 3DEC® is a three-dimensional numerical program based on the element method distinct for discontinuous modeling. The basis of this program is numerical formulation extensively tested and used in the two-dimensional version, UDEC(Itasca Consulting Group Inc., n.d.).

3DEC® is based on a Lagrangian computational scheme which is particularly appropriate for modeling large displacements and deformations of a multi-body system. The characteristics of 3DEC® can be summarized in the following:

- the object can be modeled as a 3D assembly of rigid or deformable blocks;
- the discontinuities are assimilated through interactions along the contour of the distinct

blocks;

- the continuous or discontinuous behaviour of the joints is generated on a statistical basis;
- 3DEC® employs a time-explicit solution algorithm (Lemos, 2007) that estimates both large displacements and rotations, and allows calculations in the time domain;
- 3DEC® can be programmed using the FISH language (abbreviation of FLACish, FISH has been originally developed for the two-dimensional continuous finite difference program, FLAC® by (Itasca Consulting Group Inc., n.d.)). FISH is an open programming language, so is possible writing new functions to expand the possibilities provided to the user for specific needs.

The model definition in 3DEC® corresponds to the domain discretization by a series of blocks. Blocks can take any arbitrary geometry and may be different from each other in size and shape. Individual blocks can be rigid or deformable. Rigid blocks are used when the behaviour of the system is dominated by the joints. Alternatively, the blocks are modelled as deformable and the complexity of the deformation of the blocks depends on the number of zone elements into which they are divided. Zones follow the constitutive model assigned to them; in this way, the strain is estimated for each separate block (Bui et al., 2017). The interfaces between blocks are simulated by the Mohr-Coulomb interface model with a tension cut-off, which considers both shear and tensile failure.

In 3DEC®, the material parameters for the linear, isotropic, elastic model are the Poisson ratio (υ), the density (γ) normal and tangential interface stiffnesses –jk_n and jk_s respectively– that depends from elastic modulus (E) and shear modulus (G).

Another parameter is the mechanical damping, that is used in the distinct element method to solve two general classes of problems: static (non-inertial) solutions and dynamic solutions. For static analysis, the approach is conceptually like dynamic relaxation, proposed by (Otter et al., 1967). Two alternative forms of velocity-proportional damping are available in 3DEC®: adaptive global damping and local damping (Bui et al., 2017). Into the latter category, 3DEC® provides a particular form of damping, in which the damping force on a node is proportional to the magnitude of the unbalanced force (Bui et al., 2017). For this scheme, the direction of the damping force is such that energy is always dissipated. From (Itasca Consulting Group Inc., n.d.), it is recommended to use local damping for static analyses with the default damping value of 0.8. This is generally appropriate to minimize oscillations that may arise when abrupt failure occurs in the model.

REFERENCES

Binda, L., & Saisi, A. (2005). Research on historic structures in seismic areas in Italy. In Progress in Structural Engineering and Materials (Vol. 7, Issue 2). https://doi.org/10.1002/pse.194

Bui, T. T., & Limam, A. (2012). Masonry walls under membrane or bending loading cases: Experiments and discrete element analysis. Civil-Comp Proceedings, 99. https://doi.org/10.4203/ccp.99.119

Bui, T. T., Limam, A., Sarhosis, V., & Hjiaj, M. (2017). Discrete element modelling of the in-plane and out-of-plane behaviour of dry-joint masonry wall constructions. Engineering Structures, 136. https://doi.org/10.1016/j.engstruct.2017.01.020

Cundall, P. A., & Hart, R. D. (1992). Numerical modelling of discontinua. In Engineering Computations (Vol. 9, Issue 2). https://doi.org/10.1108/eb023851

Cundall, P. A., & Strack, O. D. L. (1979). A discrete numerical model for granular assemblies. Geotechnique, 29(1). https://doi.org/10.1680/geot.1979.29.1.47

Foti, D., Vacca, V., & Facchini, I. (2018). DEM modeling and experimental analysis of the static behavior of a dry-joints masonry cross vaults. Construction and Building Materials, 170. https://doi.org/10.1016/j.conbuildmat.2018.02.202

Giuffrè, A. (1994). Seismic safety and strengthening of historical buildings and urban fabrics. Earthquake Engineering, 10th World Conference.

Heyman, J. (1995). The stone skeleton: structural engineering of masonry architecture. The Stone Skeleton: Structural Engineering of Masonry Architecture. https://doi.org/10.1115/1.2787238

Itasca Consulting Group Inc. (n.d.). 3DEC – Three-Dimensional Distinct Element Code.

Lemos, J. v. (2007). Discrete element modeling of masonry structures. International Journal of Architectural Heritage, 1(2). https://doi.org/10.1080/15583050601176868

Mirabella Roberti, G., & Calvetti, F. (2020). Distinct element analysis of stone arches. In Arch Bridges. https://doi.org/10.1201/9781003078494-27

Mohebkhah, A., Tasnimi, A. A., & Moghadam, H. A. (2008). Nonlinear analysis of masonry-infilled steel frames with openings using discrete element method. Journal of Constructional Steel Research, 64(12). https://doi.org/10.1016/j.jcsr.2008.01.016

Numerical Modelling of Discrete Materials in Geotechnical Engineering, Civil Engineering and Earth Sciences. (2004). In Numerical Modelling of Discrete Materials in Geotechnical Engineering, Civil Engineering and Earth Sciences. https://doi.org/10.1201/9780203023983

Otter, J. R. H., Poppard, A. J. S., Lane, R. G. T., Welch, A. K., King, I. P., Wood, W. L., Cubitt, N. J., Hayes, R. J., Hobbs, R. E., Zienkiewicz, O. C., Bickley, W. G., Majid, K. I., Snell, C., Walker, B. A., Postlethwaite, R. W., & Cassell, A. C. (1967). DISCUSSION. DYNAMIC RELAXATION. Proceedings of the Institution of Civil Engineers, 37(4). https://doi.org/10.1680/iicep.1967.8278

Papantonopoulos, C., Psycharis, I. N., Papastamatiou, D. Y., Lemos, J. v., & Mouzakis, H. P. (2002). Numerical prediction of the earthquake response of classical columns using the distinct element method. Earthquake Engineering and Structural Dynamics, 31(9). https://doi.org/10.1002/eqe.185

Psycharis, I. N., Lemos, J. v., Papastamatiou, D. Y., Zambas, C., & Papantonopoulos, C. (2003). Numerical study of the seismic behaviour of a part of the Parthenon Pronaos. Earthquake Engineering and Structural Dynamics, 32(13). https://doi.org/10.1002/eqe.315

Pulatsu, B., Gonen, S., Lourenço, P. B., Lemos, J. v, & Hazzard, J. (2022). Computational investigations on the combined shear–torsion–bending behavior of dry-joint masonry using DEM. Computational Par-

ticle Mechanics. https://doi.org/10.1007/s40571-022-00493-7

Sarhosis, V., Asteris, P., Wang, T., Hu, W., & Han, Y. (2016). On the stability of colonnade structural systems under static and dynamic loading conditions. Bulletin of Earthquake Engineering, 14(4). https://doi.org/10.1007/s10518-016-9881-z

Sarhosis, V., Garrity, S. W., & Sheng, Y. (2015). Influence of brick-mortar interface on the mechanical behaviour of low bond strength masonry brickwork lintels. Engineering Structures, 88. https://doi.org/10.1016/j.engstruct.2014.12.014

Sarhosis, V., Oliveira, D. v., Lemos, J. v., & Lourenco, P. B. (2014). The effect of skew angle on the mechanical behaviour of masonry arches. Mechanics Research Communications, 61. https://doi.org/10.1016/j.mechrescom.2014.07.008

Sarhosis, V., & Sheng, Y. (2014). Identification of material parameters for low bond strength masonry. Engineering Structures, 60. https://doi.org/10.1016/j.engstruct.2013.12.013

Sarhosis, V., Tsavdaridis, K. D., & Giannopoulos, I. (2014). Discrete Element Modelling of Masonry Infilled Steel Frames with Multiple Window Openings Subjected to Lateral Load Variations. The Open Construction and Building Technology Journal, 8(1). https://doi.org/10.2174/1874836801408010093

Silvestri, S., Baraccani, S., Foti, D., Ivorra, S., Theodossopoulos, D., Vacca, V., Roman, J. O., Cavallini, L., Mokhtari, E., White, R., Dietz, M., & Mylonakis, G. (2021). Shaking table testing of groin vaults made by 3D printers. Soil Dynamics and Earthquake Engineering, 150. https://doi.org/10.1016/j.soildyn.2021.106880

Walker, P., McCombie, P., & Claxton, M. (2007). Plane strain numerical model for drystone retaining walls. Proceedings of the Institution of Civil Engineers: Geotechnical Engineering, 160(2). https://doi.org/10.1680/geng.2007.160.2.97

4. EXPERIMENTAL CAMPAIGN ON A CONTEMPORARY VAULT MODEL

4.1. Objectives and layout of the experimental campaign

Experimental campaigns have always been adopted to investigate the static and dynamic behaviour of structures and the influence of one on the other, as it is not always easy to understand it only through the state of damage or the use of numerical models alone. In fact, the experimentation used in addition to numerical models allows to obtain actual information on structural response, constituting a more coherent methodology for investigating the structural phenomena where there are a high number of variables, and in some cases the model test may be the only solution to the problem.

In literature several significant experimental tests specifically investigating the seismic response of masonry vaults are available closely related to the global structure response but none about the Abeille vault's behaviour. Despite everything, the dynamic behaviour of masonry arches and other types of curved masonry structures is, surprisingly, a very little investigated field from an experimental point of view even if, above all in very complex situations such as those in exam, experimentation plays a crucial role in guiding modeling choices especially for very complex problems like the ones in question. This is due to the difficulty of carrying out full-scale experiments on very heavy constructions, which are difficult and expensive to build in laboratory. The same is true for small-scale experimental campaign, capable of representing some characteristics of real dynamic behaviour, but which often present very different interface and/or inertial response conditions compared to a real structure. A selection of the most relevant experimental evidence on vaults has already been described in § 2.2.

As explained in detail in § 2.1, the main aim of this research is to investigate the seismic response of these masonry vaults at both local and global scale. For this reason, two different conditions have been considered:

- Vaults subjected to differential horizontal displacements, where the seismic acceleration excites the supporting structures (the walls, piers, abutments and pillars of the building); so, vault is thus indirectly loaded by the differential displacements/accelerations produced on its supports.
- Vault subjected to horizontal forces proportional to their mass, where the latter is directly excited by seismic acceleration and its abutments are fixed (i.e. fastened securely).

In order to describe both behaviours, two different types of experimental tests have been designed: Indirect Seismic Action tests (ISA) and Direct Seismic Action tests (DSA). The ISA tests evaluate displacement and the strength capacity of vaults under different displacement patterns. Indeed, the aim of DSA testing is the evaluation of the collapse multipliers for different directions of seismic action. In both cases, the 3D damage mechanisms identification of the structure

has been one of the goals.

It is important to point out that although in scale models, quasi-static tests are usually considered more reliable than dynamic ones, since the behaviour due to the latter type of action depends significantly on the dimensions and mass of the model. At the same time, generally the resistance to horizontal actions of "multi-body" structures subject to unilateral constraints is only studied with a quasi-static approach that allows to identify the minimum load value, beyond which the instability of the structure occurs. For these two reasons, in order to understand and investigate the dynamic behaviour of these structures it was decided to use the DSA methodology with tilting tests, as initial dynamic test, compared to shaking table tests.

In this work, the behaviour of actual masonry vaults has been based on the hypotheses stated by Heyman (Heyman, 1995, 1998). These hypotheses assert that the masonry material (stone or brick with either mortar or dry joints) behaves like an assemblage of rigid blocks subjected only to compressive forces, with a tendency to crack as soon as tensile stresses begin to develop. So, the constitutive model of "Non-Resistant to Tensile" is infinite strength to compression, and zero tensile strength, it has no sliding allowed and negligible elastic strains. This model can be used to analyze masonry structure, including vaulted and arched structures, because of the following assumptions:

- The compressive stresses between the blocks does not lead to the crushing strength of the material and this is a realistic assumption;
- Only compressive forces can be transmitted between masonry elements because the joints have a weak behaviour (Heyman, 1998);
- Friction between blocks – in some cases also interlocked – is relatively high to ensure that they not slide with respect to each other. This assumption is reasonable, even if in some masonry structures is possible to find occasional evidence of sliding.

These hypotheses imply that the stability of masonry structures is more important than stress, and that the governing behaviour depends on geometry rather than material properties. As a result, the elastic calculation of stresses is not relevant, and elastic deformations may be omitted. Consequently, to be coherent with these hypotheses, the small-scale specimen has been suitably designed and fabricated in order to:

- Respecting geometric similarity requirements, by using sufficiently rigid material for the applied load (rigidity assumption);
- Creating a sufficiently high angle of friction in order to avoid sliding phenomena;
- Allowing only the transmission of compressive forces at blocks interfaces (i.e. no tension).

In this experimentation, as better illustrated in § 4.3.2, the small-scale specimen of the vault has been built by respecting the geometry at both “macro-scale” referred to its span, rise, thickness, etc., and “micro-scale”, that means the scaling of brick blocks dimensions, the stereometry, the pattern, etc.

The selected material for the specimen should be indifferent, unless it is sufficiently rigid with respect to the applied loads, and its friction coefficient should be comparable with the masonry material. In this case, the small-scale blocks are made of plastic with an infill equal to 70%. The

adoption of 1:8 scale is merely practical as the impossibility to realize a full-scale model in the laboratory and the need to easily manage the overall experimental set-up (instrumentation, control of force/displacement application, etc.).

The adoption of these hypotheses implies that the results of the tests should reproduce the same damage mechanisms of the equivalent full-scale structure, while the results in terms of forces and displacements should be subjected to scaling factors. These latter may be analyzed through proper dimensional and by respecting the similarity requirements.

4.2. Theory of scaled tests design

4.2.1. General aspects

Experimental investigations can be carried out on specimens of different scales, including full-scale and small-scale. Employing small-scale specimens offers advantages such as reduced costs and laboratory space requirements for the construction and load equipment of test structures. However, it is essential to adhere to similitude requirements to ensure that the experimental results are useful and applicable to full-scale prototypes of vaults.

The Dimensional Analysis is a noteworthy technique used in engineering and the physical sciences to simplify physical properties and experimental variables into fundamental dimensions, including *length* (L), *mass* (M), and *time* (t). This technique facilitates the study of interrelationships of systems (or models of systems) and their properties and avoids the nuisance of incompatible units. Dimensional analysis provides a "check" for mathematical models of real situations; in fact, for such a model to be useful, it must be dimensionally faithful to the original.

Π-Theorem (Buckingham, 1914) is one of the principal methods of dimensional analysis: *A physical relationship between some dimensional (generally speaking) quantity and several dimensional governing parameters can be rewritten as a relationship between some dimensionless parameter and several dimensionless products of the governing parameters; the number of dimensionless products is equal to the total number of governing parameters minus the number of governing parameters with independent dimensions*.

Any mathematical governing equation that describes some aspect of nature must be in a dimensionless homogeneous form. The theorem states that if a variable A_1 depends upon the independent variables $A_2, A_3, \ldots, A_n$, then the functional relationship can be set equal to zero in the form $f(A_1, A_2, A_3, \ldots, A_n) = 0$. If these n variables can be described in terms of r dimensional units, then the Π-Theorem states that they can be grouped in $n - r$ dimensionless terms that are called pi (π) terms.

Considering that the pi (π) terms represent dimensionless product of the n physical variables and $m = n\text{-}r$ –where r represents the number of the fundamental measures that are involved in the physical variables– it is possible combining the variables into convenient groupings (π terms) to reduce the total number of variables and respect the similitude requirements in model and prototype forcing the π terms to be equal.

The choice of the basic unit of measure is arbitrary and, according to it, the derived physical variables change. Therefore, an equation is dimensionally homogeneous if its structure does not depend on the adopted measuring system. Once defined the basic unit of measure, those derived are obtained by means of relationships definition. These latter should follow some relevant rules:

- arbitrary coefficients should not be adopted, since the equations must be homogeneous;
- the equations should be monomial since they must respect the principle of homogeneity.

In order to apply the *Buckingham Theorem*, appropriate π terms must be selected while taking into account a group of physical variables known as dimensional independent, and then defining residual variables, known as dimensional dependent, through their representation as a combination of products. In the selection process, all variables must be encompassed, and the terms m must be independent. Furthermore, multiple sets of π terms can be identified for a given problem, and there is no definitive method for grouping the π terms, as it is a matter of personal preference.

When implementing dimensional analysis in structural models, three primary types of models can be distinguished:

- the *true model*, which maintains complete similarity;
- the *adequate model*, which maintains *"first-order"* similarity. It means that, if there is a special insight into a problem, then it may be possible to consider some stipulations, initially defined by proper dimensional analysis, as *"second-order"* importance. Thus, the model must satisfy the first-order stipulations, neglecting certain second-order ones;
- the "*distorted model"*, which fails to satisfy one or more of the "*first-order"* stipulations.

While it is ideal to have complete similarity, economic and technological constraints often prevent achieving it with the related prototype. Therefore, by disregarding certain *second-order effects*, it is possible to accurately forecast the behaviour of a prototype.

4.2.2. Dimensional analysis and similarity criteria

The use of modeling in experimentation helps determine the optimal properties for future operational conditions. It's crucial to understand how to scale up the results of a model experiment to the full-scale object being modeled; otherwise, modeling is pointless. The correct modeling relies on the concept of physically similar phenomena, which is a natural extension of the similarity concept in geometry. Similar physical phenomena only differ in their dimensional governing parameter's numerical values, while their corresponding dimensionless parameters Π_1, …, Π_m remain the same. In accordance with the adopted definition for similar phenomena, the quantities Π_1, …, Π_m are labeled similarity parameters.

Suppose a *prototype* requires modeling with a similarly reproducing model to achieve the desired properties. In that case, the relationship between the parameter a and governing parameters a_1, …, a_k, b_1,…, b_m is:

$$a = f(a_1, \dots, a_k, b_1, \dots, b_k) \qquad (4.\ 1)$$

Since the two phenomena are similar, the function *f* remains the same, even if the governing parameters $a_1, \ldots, a_k, b_1, \ldots, b_m$ and the determined parameters *a* differ in numerical values. As a result, the relationship for both the *prototype P* (4.2) and the *model M* (4.3) can be expressed in the same form:

$$a^{(P)} = f(a_1^{(P)}, \ldots, a_k^{(P)}, b_1^{(P)}, \ldots, b_k^{(P)}) \quad (4.\ 2)$$

$$a^{(M)} = f(a_1^{(M)}, \ldots, a_k^{(M)}, b_1^{(M)}, \ldots, b_k^{(M)}) \quad (4.\ 3)$$

Through Dimensional Analysis and considering the condition for similarity criteria, the dimensionless parameters to be determined for the model and for the prototype are equal to:

$$\Pi^{(P)} = \Pi^{(M)} \quad (4.\ 4)$$

so, returning to dimensional parameters,

$$a^{(P)} = a^{(M)} \left(\frac{a_1^{(P)}}{a_1^{(M)}}\right)^p \ldots \left(\frac{a_k^{(P)}}{a_k^{(M)}}\right)^r \quad (4.\ 5)$$

which is a simple rule for scaling the results of measurements on a similar model up to the prototype.

4.2.3. Use of the similarity criterion on the vault model

In literature there are some examples on the use of the similarity criterion on masonry structure (Dimitrakopoulos & DeJong, 2012), in particular for the vault (Bianchini et al., 2022; Gaetani, 2020; Lourenço et al., 2020; Rossi, 2015; Rossi et al., 2016). The similarity criterion is employed to extrapolate experimental test results from a small-scale model to a real masonry cross-vault. The aim is to identify the parameters that define the simplified response of the vault, enabling the proposal of a macro-element model for implementation in the 3D global model of the masonry building, as as will be done in § 5.3. As the proposed laws describing the macro-element are expressed by piecewise linear force-displacement curves, the values of strength $F^{(M)}$ and displacement $u^{(M)}$ of the model can be scaled to define each point of the prototype curve, characterized by a strength value $F^{(P)}$ and an ultimate displacement $u^{(P)}$. It's also interesting to determine the scaled value of stiffness $k^{(P)}$ from the value of $k^{(M)}$, even though it can be defined by the linear part's strength and displacement points.

The parameters governing the response of the vault to gravity loads and imposed displacements

at the springs include: (i) Geometric parameters such as span l, thickness t, rise of the vault r. (ii) Strength parameters of masonry material like compressive f_m, tensile f_t, cohesion c, friction angle μ. (iii) Elastic moduli, including Young's modulus E and shear modulus G. (iv) Unit weight γ (assuming no point load is applied to the vault). Additionally, it's worth noting that the experimentation maintains the same shape of blocks and masonry pattern in both the model and the prototype.

It is well known (Block et al., 2006; de Lorenzis et al., 2007; Lemos, 2008; Ochsendorf, 2002) that the response of masonry arched and vaulted structures depends more on the geometry and on loads distribution than the material strength and elasticity. According to Heyman's theorem (Heyman, 1995), the collapse mechanism of a structure can be analyzed based on certain assumptions such as rigid blocks, no tensile strength, infinite compressive strength, and absence of sliding. In this context, evaluating the strength parameters is important in small-scale model experiments as demonstrated by Quinonez et al. (2010). The friction angle is a critical parameter among the strength parameters as it is dimensionless and must have the same value in both the model and the prototype to avoid affecting the results. If the friction angle value in the model is higher or lower than in the prototype, it could activate different mechanisms, making it a *first-order* parameter. Instead, *tensile strength* and *cohesion* between blocks in the model are usually ignored in Limit Analysis, as they are usually low in traditional solid bricks masonry with lime mortar joints. Hence, they are of *second-order* importance. Additionally, compressive strength is usually high compared to the compressive stresses induced in vaults by dead loads. In general, vault collapse does not occur due to compressive failure of the elements. Furthermore, laboratory tests performed in this research showed no compressive failure. Therefore, *compressive strength* is also of *second-order* importance.

The stiffness of the vaults is determined by the force-displacement relation, and it is influenced by both the elastic parameters of masonry and the onset and progression of damage such as cracks, which are related to the masonry pattern and geometry. Although the unit weight has a minor impact on stiffness, increasing it can enhance contact in the interfaces and thus increase the overall stiffness. Hence, the stiffness (k) is primarily associated with the elastic moduli (E, G).

Regarding strength, Heyman's theorem of Limit Analysis applied to masonry structures shows that the geometry and distribution of loads primarily determine strength, which, in this case, only depends on the unit weight. However, since the actual vault masonry is not infinitely rigid, the elastic moduli may have a slight impact on strength.

In the end, the ultimate displacement can be considered to primarily depend on the geometric scale. This perspective is adopted by modern seismic codes that implement drift limits for the in-plane response of masonry panels, which disregard stiffness and strength. However, in previous Italian seismic codes, the analysis of masonry buildings was conducted using the ultimate displacement evaluated in terms of ductility, commencing from the yield displacement that is implicitly linked to strength and stiffness. Consequently, strength and stiffness can be considered of *second order* importance, as the ultimate displacement slightly increases with strength and de-

creases slightly with stiffness.

In this phenomenon, two crucial measures must be considered, namely the span (l) and unit weight (γ), or elastic modulus (E). Specifically, the unit weight (γ) is used to assess strength, while the elastic modulus (E) is utilized to evaluate stiffness. These two parameters are considered the most significant input factors for the two response parameters. It is noteworthy that in the case of a "true" model, the outcome is not affected by this selection. Therefore, by neglecting the strength parameters of masonry (excluding friction), the model's three parameters can be expressed in this manner:

$$\begin{aligned} \frac{F}{l^3\gamma} &= f\left(\frac{t}{l}, \frac{r}{l}, \frac{L}{l}, \mu, \frac{E}{\gamma l}\right) \\ \frac{k}{l^2\gamma} &= f\left(\frac{t}{l}, \frac{r}{l}, \frac{L}{l}, \mu, \frac{E}{\gamma l}\right) \\ \frac{u}{l} &= f\left(\frac{t}{l}, \frac{r}{l}, \frac{L}{l}, \mu, \frac{E}{\gamma l}\right) \end{aligned} \qquad (4.\ 6)$$

In order to have a “true” model which respects the similitude requirements, it is necessary to check if the dimensionless parameters that involve the force assume the same value in the model and the prototype, so that:

$$\begin{aligned} \frac{E^{(P)}}{l^{(P)}\gamma^{(P)}} &= \frac{\alpha_E}{\alpha_l \alpha_\gamma} \frac{E^{(M)}}{l^{(M)}\gamma^{(M)}} \\ \frac{\alpha_E}{\alpha_l \alpha_\gamma} &= 1 \end{aligned} \qquad (4.\ 7)$$

where $\alpha_E = E^{(P)}/E^{(M)}$, $\alpha\gamma = \gamma^{(P)}/\gamma^{(M)}$; $\alpha_l = l^{(P)}/l^{(M)}$.

Therefore, the three parameters necessary to define the macro-element model of the vault prototype, can be obtained from the results of small-scale model by the following relations:

$$\begin{aligned} F^{(P)} &= \alpha_l^3\, \alpha_\gamma\, F^{(M)} = \alpha_F\, F^{(M)} \\ k^{(P)} &= \alpha_l \alpha_E\, k^{(M)} = \alpha_k\, k^{(M)} \\ u^{(P)} &= \alpha_l\, u^{(M)} \end{aligned} \qquad (4.\ 8)$$

If alternate values are assigned to the block masonry of the prototype, the dimensionless parameters $E/l\gamma$ may not match those of the model, resulting a *distorted* model as described in § 4.2.1. As a result, values for the macro-element model of the prototype cannot be determined using (4.8), unless the aforementioned dimensionless parameter is considered of *second order* im-

portance. This would make the *adequate model* as described in § 4.2.1.

Figure 4-1 illustrates the impact of a *distorted model*, depicting two scenarios where the behaviour of the prototype and the model differ after adimensionlization. In both cases, the dimensionless coefficient $E/l\gamma^{(P)}$ is greater than that of the model due to higher stiffness ($k^{(P)} > k^{(M)}$). Furthermore, displacement is lower in the prototype in both cases, while the strength behaves oppositely.

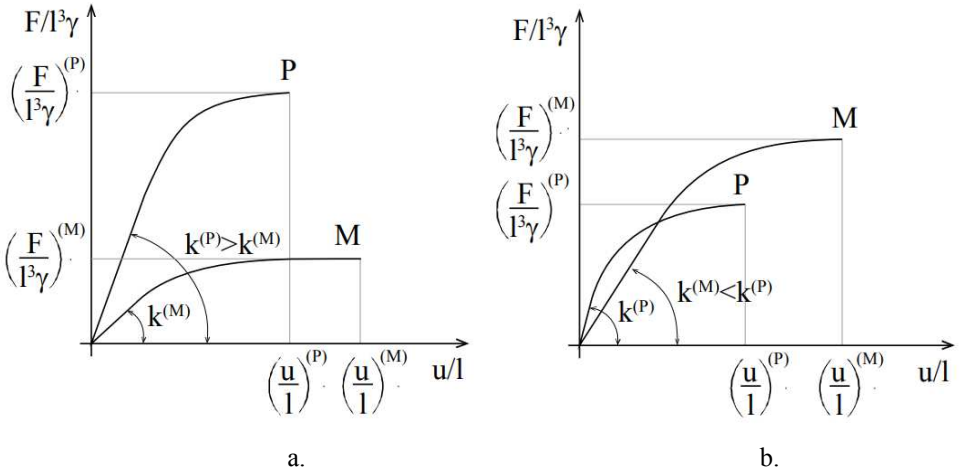

a. b.

Figure 4-1. Example of different behaviour between model (M) and prototype (P) caused by the fail of similarity criterion (*distorted model*). (Rossi, 2015)

When dealing with *distorted models*, it may be necessary to consider more than two parameters as fundamental for adimensionalization. This approach is similar to what was employed by (Huntley, 1967), who utilized multiple lengths (to differentiate geometric scales in different directions) or masses (to distinguish weight from inertial action).

In the case of the analyzed masonry vault, both γ and E can be independently considered. Consequently, equations (4.6) are modified as follows:

$$\frac{F}{l^{3-c_k}\ \gamma^{1-c_k}\ E^{c_k}} = f_F\left(\frac{t}{l}, \frac{r}{l}, \mu\right)$$

$$\frac{k}{l^{1+c_k}\ \gamma^{c_k}\ E^{1-c_k}} = f_k\left(\frac{t}{l}, \frac{r}{l}, \mu\right) \qquad (4.\ 9)$$

$$\frac{u}{l^{1+c_k}\ \gamma^{c_k}\ E^{-c_k}} = f_u\left(\frac{t}{l}, \frac{r}{l}, \mu\right)$$

where coefficients c_F, c_k, c_u are appropriate constants that must assume values between 0 and 0.5 for the specific problem. This is because: (i) the strength F of the vault, when subjected to shear distortion, is primarily influenced by the unit weight rather than the elastic modulus; (ii) the stiffness k is more affected by the elastic modulus rather than the unit weight; and (iii) the ultimate displacement u may slightly increase with the unit weight but decrease with the elastic modulus. Accurately determining these coefficients requires detailed numerical simulations or

experimental tests using a *true* or at least an *adequate* model. However, it is possible to examine the sensitivity of the prototype's estimated values to these coefficients to obtain acceptable estimates.

4.3. Design of the physical model

The aim of this research is the study of the mechanical behaviour of contemporary vault spaces on curved spatial geometries with complex ashlars. The analyzed vault is generated starting from the *Flat Vault of Abeille* (§ 2.3). In particular, for this study a sail/domed vault typology was chosen to spatially reinterpret the vault and its specific type of ashlar.
Below the geometry, its optimization and the realization of the model in 3D-printing are presented.

4.3.1. Parametric and optimized generation of a contemporary vault

The vaulted space has always represented the ideal ambit in which to operate the more sophisticated and complex reflections on the construction of architecture. This is particularly true for the stereotomic architecture. In this case, the curved line that is defining the archivolted systems is the geometrical locus establishing a concavity and a convexity, with any mathematical complexity, can be designed and built in two basic ways: with a tool that can draw the curved (i.e.: compass, algorithm, etc.), or by bending a straight line. The latter mode is totally attuned to the topologic view. The idea of "potential flexibility" and "manipulation" of the vaulted stone space is at the basis of the method that is linking topology and stereotomy, and that will be now described.
The method is starting from a very simple consideration, that is the observation that most of the vaulted systems can be imagined as a discontinuous structure or masonry wall that has been folded and/or deformed to obtain its geometrical final conformation, with the due simplifications and specifications (Fallacara, 2006).
At the basis of the research, there was the Abeille's ashlar-type: its geometric invariant and proportional parameters that configure the base of the ashlar it-self (Sánchez Peña, 2020) and static invariant, that is the capacity of providing static balance of the architectural system of dry-stone joint.
Secondly, it was decided to carry out a unique model both for the 3D printing of the geometry and for the structural numerical analysis in order to have an appropriate validation and to optimize the construction of the vault.
In 3DEC® –the structural software utilized for the numerical model–, masonry units are represented as an assembly of rigid or deformable blocks, and blocks are represented as convex polyhedra in 3D with each face being a planar convex polygon with rectilinear edges (Lemos, 2019). Rigid blocks do not change their geometry under applied loading. Deformable blocks are discretized into triangular zones of uniform stress characteristics (Itasca Consulting Group Inc., n.d.).

For this reason, considering the both the case, the software cannot create or import concave elements but only convex and planar entities. This problem led to split and parcelling out the special complex solids in smaller ones that could be joined at a later step within the tool. In particular, for a structure made up of all convex ashlars as in the case study and designed in Rhinoceros® (Robert McNeel & Associates. Copyright © 1993-2022. All rights reserved, n.d.), this problem was solved by optimizing the shape of the ashlar in Grasshopper® (Payne & Issa, 2009), a plug-in that functions parametrically. The combination of these two tools allows the triangular tessellation of a surface without discretization, preserving the continuity of the intrados and extrados curvature through the facetizing of the original ashlar surfaces (mesh made up of hexagons) after flattening them (Figure 4-2). Finally, each shape is formed by adjacent coplanar triangles that can be assembled into polygonal faces. The complete process performed is explained in detail in (Barberio et al., 2016).
In this way the final vault obtained is a complex curved geometry easily importable in 3DEC®.

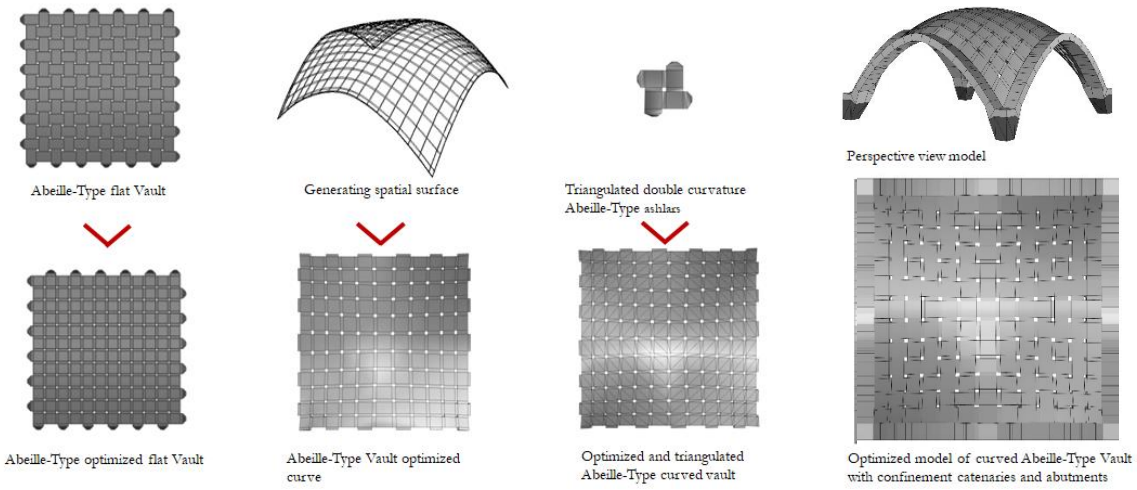

Figure 4-2. Process for the realization of optimized *Abeille-Type Vault.*

4.3.2. Production of the physical model

The physical model is made with 3D-printed distinct plastic blocks with dry joints. All the blocks of the vault, the scaffolding and the specimens for the material characterization were made by a 3D printer at the "CREA 3D S.R.L" (Italy).
A sand-based coating was applied to the vault blocks to make the behaviour of the model as close as possible to the real one of a stone masonry vault and to control the adequate friction between the blocks. In fact, this coating increases the roughness of the plastic material, actually too low and therefore increase the angle of friction between the different blocks. In this way, the joints have a friction angle comparable with the typical ones of solid stone masonry blocks, so these may be considered rigid and infinitely resistant in compression. This methodology has been already used also in other studies such as Gaetani (2020). The fiction angle is a non-dimensional parameter, so the sliding between the blocks provided by the model is representative

of the global behaviour. This type of model was choice for two different reasons:

- As explain by (Heyman, 1995) the structural response of masonry vaults depends on stability rather than on strength;
- The repeatability of tests for several times; it depends by the material of the model, the moderate costs and short setup.

For these reasons this experimental method has been often used for in different scientific works to assess the behaviour and failure modes of masonry structure (Bianchini et al., 2019, 2022; Calderini et al., 2017; Calderini & Lagomarsino, 2015; Quinonez et al., 2010; Rossi, Barentin, et al., 2017; Rossi et al., 2014, 2015, 2020; Shapiro, 2012; van Mele et al., 2012) as shown in §2.2.
The particular shape of this vault was generated starting by the "Abeille Flat Vault" (Akleman et al., 2020; Vella & Kotnik, 2016) and it was made possible by the stereotomy studies of real stone and masonry vaults (Andrusko, 2014; Fallacara, Scaltrito, et al., 2019; Fallacara & Barberio, 2018), as shown in § 2.3.2 and 4.3.1. So, every block was carefully designed in shape and dimensions to play an key role in the stability and static equilibrium of the vault.
The global dimensions of the model vault (Figure 4-3) were decided to fit it on the testing device of the Institute of Science and Innovation for Bio-Sustainability Laboratory (IB-S Lab) at the University of Minho, that has in plan a dimension of 700x700 mm^2. This led to have a physical model occupying 700x700x390 mm^3 approximately. So, the tests were performed on a 1:8 scale at the end, considering that the hypothetical prototype square base vault should have a side equal to 5.60 m and a rise of 3.15 m (Figure 4-4). As literature demonstrates other scaling factor are possible see § 2.2.
The model was truncated at the base to consider the effect of embedment in the perimeter walls and stiff abutment. In fact, as remarked in (Silvestri et al., 2021) several studies of damage of historic buildings in seismic events reveal that failure of vaults did not initiate at their abutments, but at a slightly higher level, being essentially embedded into support elements to counteract the outward thrust (Cancino et al., 2014; Croci, 1998; Piermarini, 2013). For this reason, this approximation is recurrent in the literature to understand and predict the response of masonry vaults to seismic action.

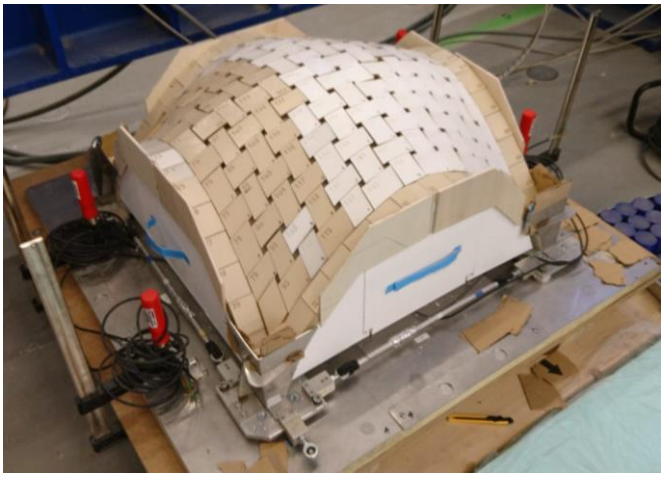

Figure 4-3. Scale 3D Printing model in PLA (Poly-Lactic Acid).

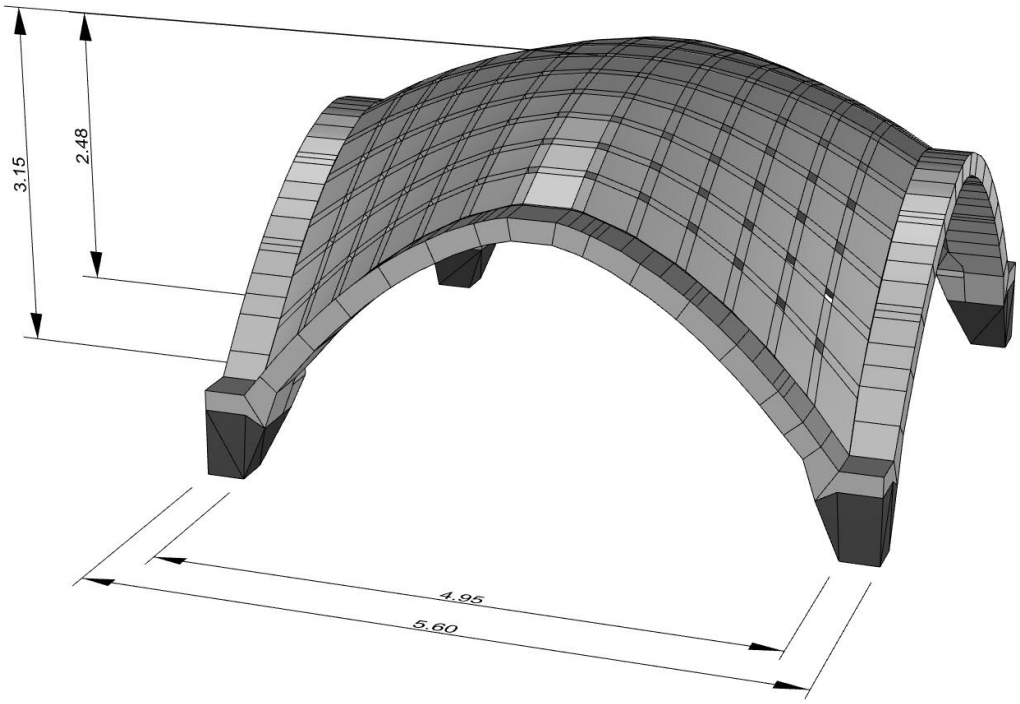

Figure 4-4. Hypothetical real size of vault (Rhinoceros® Model (Robert McNeel & Associates. Copyright © 1993-2022. All rights reserved, n.d.))

The vault consists of 235 blocks, everyone with different size and shape by faithfully and formally reproducing the "real" vault (Figure 4-5). The vault is doubly symmetrical, but the two diagonals have different ashlars, as shown in the diagram in the Figure 4-5. However different, these blocks are similar to trapezoidal prisms that function in contrast due to their stereotomic nature, having started from a deformation in space of the "Abeille vault"; their average dimensions are equal to 30x70x25 mm^3 (Figure 4-6). At the base, there are four equal rigid plastic abutments on which the entire model is set up that are integral part of testing device (red in Figure 4-5 and dark grey in Figure 4-8). The real dimensions of the physical model were in the end equal to 69x69x38 mm^3 (Figure 4-7). Although it has been attempted to pay as much attention as possible during the modeling on Rhinoceros® and 3D printing phase there were small dimensional differences mainly related to the printing process, as will be explained below. The equivalent span (l) of the scale model is equal to 608 mm, while the entire vault rise (r) to 365 mm (Figure 4-5, Figure 4-8).

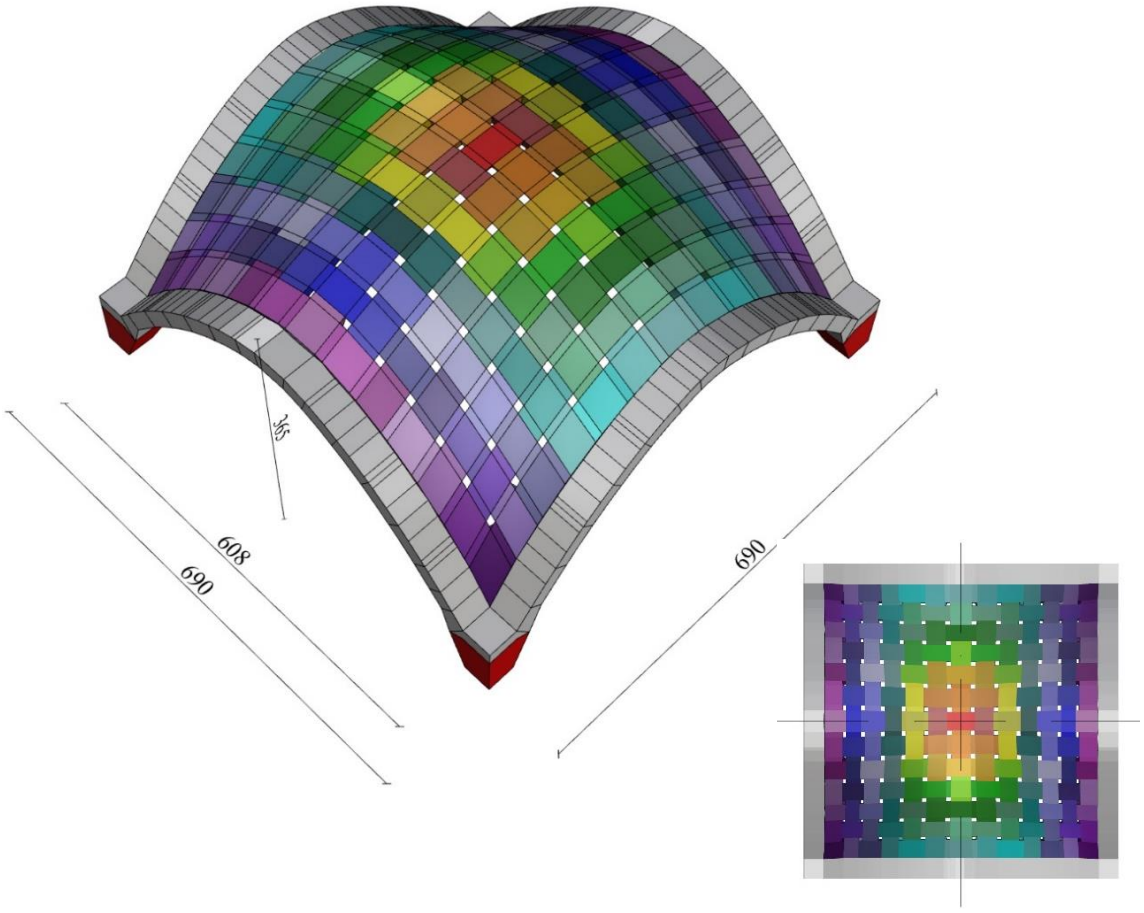

a. b.

Figure 4-5. Vault model geometry and indication of different ashlars: a. Prospective view; b. Scheme (top view).

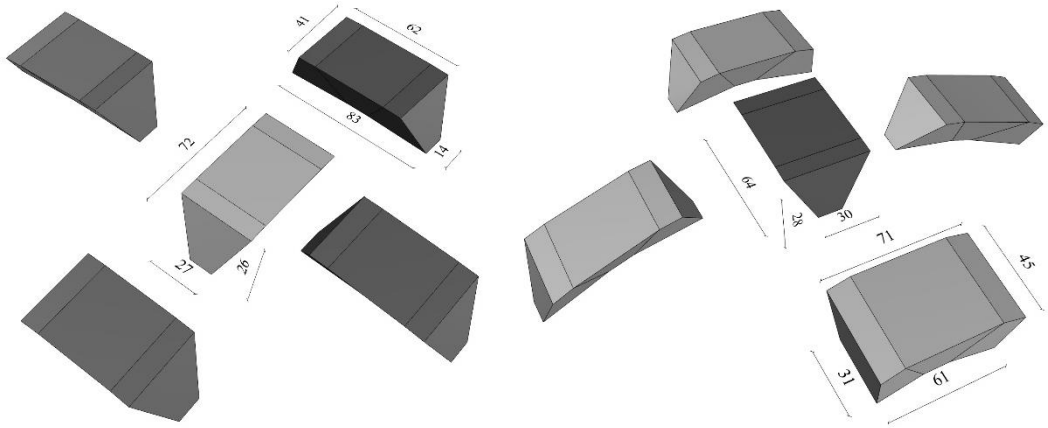

Figure 4-6. Geometry of different example ashlars with various shape e dimension.

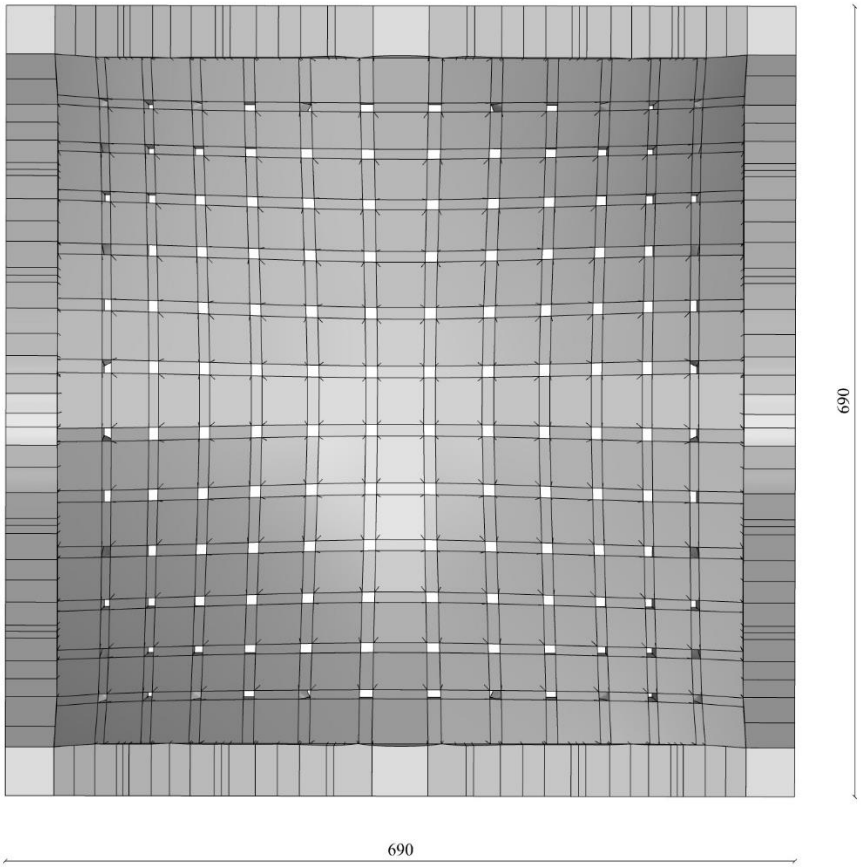

Figure 4-7. Top view of the geometric model recalibrated on the effective final dimensions of the physical model.

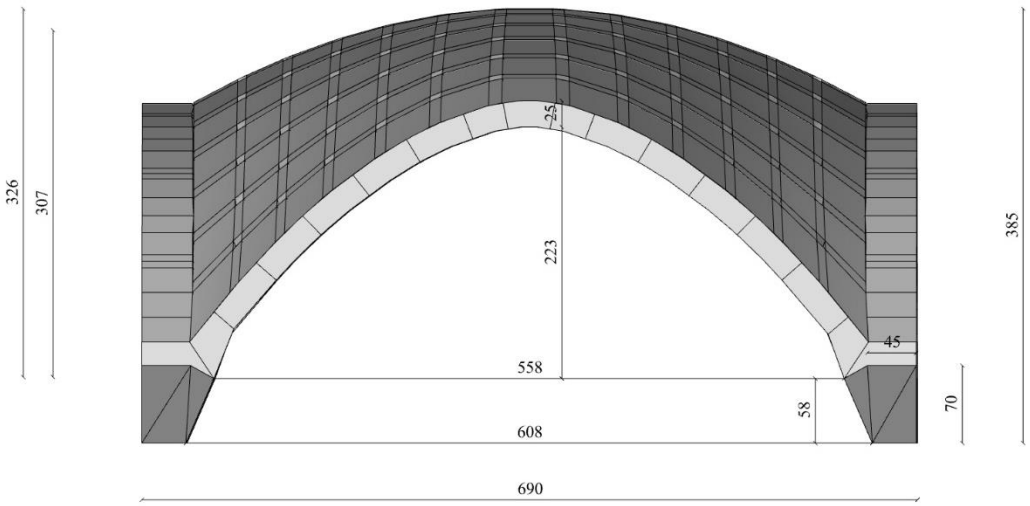

Figure 4-8. Lateral view of the geometric model recalibrated on the effective final dimensions of the physical model.

The 3D printed blocks were made of Polylactic Acid (PLA) which is a completely biodegradable and compostable polymer obtained from the processing of plants rich in dextrose, such as corn. The 3D printer is the *S5* by *Ultimaker*© and the printing resolution used in terms of layer height was 0.05 mm. Table 4-1 shows the properties of the PLA (*fabbrix*©) with a block infill material of 50% and
Table 4-2 shows the filament specifications and print settings.

Table 4-1. Properties of the PLA (fabbrix) with an infill of 50%.

Properties	Value		Standard
Physical			
Density [g/cc]	1.24		ASTM D1505
Mechanical			
	zy direction	xy direction	
Tensile Strength [MPa]	21.8	34.6	ISO 527
Elastic Modulus [MPa]	1639	2001	ISO 527
Elongation at break [%]	2.83	4.72	ISO 527
Energy at break [J]	1.3	5	ISO 527
Thermal			
Melting Point [°C]	145-160		ASTM D3418
Glass Transition Temperature [°C]	60		ASTM D3418

Table 4-2. Filament specifications and print settings.

Characteristics	Value
Diameter [mm]	0.05
Roundness Deviation [%]	max 2%
Print Temperature [°C]	200
Print Speed [mm/s]	50
Bed Temperature [°C]	35
Cooling Fan [%]	100

The vault blocks were designed to have an infill to the 70% (with a specific weight $\gamma = 7.6 \pm 0.2$ kN/m^3) to acquire the minimum necessary weight for tests, in fact the low density of the plastic material could compromise the model stability under accidental actions. The infill value of the scaffolding was in a range of 20-30 %, in this case it is not necessary having an important weight, on the contrary this is damaging in the disassembly phases; the different percentage of filling depends on the realization of edges areas and on the particular geometry of the scaffolding blocks. Finally, the specimens were realized with an infill of 70% as the model blocks, in order to test the material with the same physical and mechanical characteristics.
Before the 3D printing, two actions were performed on each block of the geometric model:

- the extrados face was made flat in order to allow the printing itself, considering that all the

faces of the blocks are curvilinear (see § 4.3.1);

- the extrados is numbered, so that exactly and easily reproduce the model in each test.

It is important to underline regarding the printing phase that the method of 3D Printing used is based on the printing of layers one above the other (along Z axis). This implies that there is an increase in size due to the extrusion dimensions of the material in the XY plane of printing that unfortunately does not occur in the Z direction. In fact, the extruder (nozzle) acts only in the XY plane and not in the XZ and YZ, so the model dimension in the Z direction remains always unchanged from to the initial one. This leads to different dimensional changes in space, considering the planes XY, XZ and YZ. For this reason, various printing tests were made on some blocks taken as samples. At last, the physical model was printed with a size equal to the 98% of the Rhino model (1:8 scaled model), percentage which guaranteed the best compromise to correct the increase in size in the XY plane and the absence of that along the Z axis.

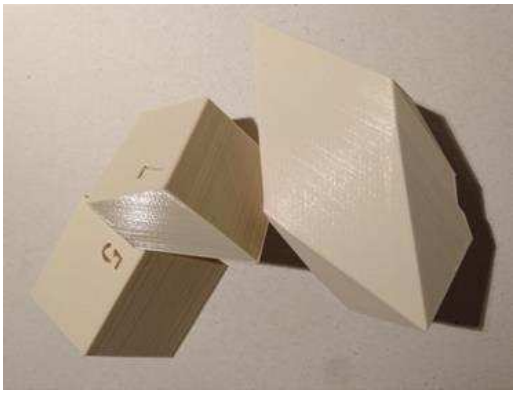

Figure 4-9. The final blocks 3D printed in PLA.

As Figure 4-9 shows, the blocks printed with the characteristics described above were too smooth. So, to increase the frictional and dissipative properties of the interfaces, a sand-based coating –epoxy resin plus sand– was applied to the vault blocks to make the behaviour of the model as close as possible to the real one of a stone masonry vault and to control the adequate friction between the blocks. This treatment did not affect the size of the blocks too much, as the latter were printed with a 98% reduction percentage which after printing was estimated to be a bit excessive. In fact, this coating increases the roughness of the plastic material, actually too low and therefore increase the friction angle between the different blocks. Similar treatment was applied also in other studies (i.e., Gaetani et al., 2017) since the material properties, namely mass density, elasticity, strength, etc., do not affect the problem in similarities laws (de Lorenzis et al., 2007; Dimitrakopoulos & DeJong, 2012; McInerney & Dejong, 2015), moreover, the mixure did not undergo significant deterioration during the test campaign. This coating was made with the use of:

- The epoxy laminating resin “S&P Resin 55 HP” by “*Simpson Strong-Tie*” with a thickness of approximately 0.5 mm (Figure 4-10.a): transparent two-component epoxy resin with a formulated amine hardener;
- The fine sand that according to the American Standard Test Sieve (ASTM) (Pope & Ward,

2008), in particular, the ATSM E 11-70, was sieved with Mesh 80 in order to obtain a maximum grain value of 0.18 mm.

The sand was generously donated by the company "*Nogueira - Materiais de Construção*" (Guimarães, PT). To select the appropriate grain, also with respect to the scale of the model, i.e. the fine grain, the sand was left 24 hours in the drying oven (Figure 4-10.b). Subsequently it was sieved with sieves ATSM E 11-70 Meshes 40, 60 and finally 80 to obtain the desired particle size (Figure 4-11).

a. b.

Figure 4-10. Coating base materials: a. Epoxy resin; b. Dry sand.

a. b.

Figure 4-11**.** ATSM E 11-70 sieves: a. Meshes 40; b. Sand sieved with Sieve Mesh 80.

Before carrying out the coating, the paper tape was applied to all the faces of the blocks (vault and confinement arches) which did not require this finish. Subsequently the epoxy resin was made, and a container was prepared with the sieved sand in order to apply a very thin film of epoxy resin (0.5 mm) with a brush and tapping the affected faces on the sand, in both cases being careful to eliminate the excess material. The blocks were left to rest for 48 hours (Figure 4-12). To make the quantity of sand homogeneous on all the faces and on all the blocks, sandpaper was passed over all the interested faces, finally the paper tape was removed (Figure 4-13).

Figure 4-12. Block Resting.

a. b.

Figure 4-13. Final Coating of Block: a. Before the removal of paper tape; b. Final blocks.

In order to assemble the model, a temporary supporting structure (centering or scaffolding) was realized in PLA. This vault required the design of an ad hoc scaffolding. In fact, the rise of the confinement arches –equal to 281 mm– did not coincide with that of the vault itself –equal to 365 mm– being higher as shown in Figure 4-8. So, the scaffolding was divided into twelve pieces located on two levels (Figure 4-14). These pieces have such a geometry and configuration (handles, teeth and notches) which is why the central pieces of the lower level (light petrol) can slide first and then it is possible remove the pieces of the lower corners (medium petrol) and the four upper ones (dark petrol) by working in quadrants.

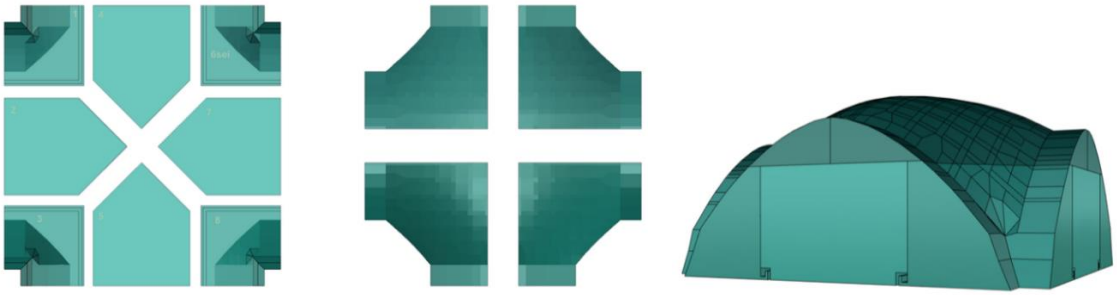

a. b. c.

Figure 4-14. Scaffolding Model: a. Plan lower level (8 pieces); b. Plan upper level (4 pieces); c. Prospective.

Figure 4-15 shows a sequence of images describing the assembling of the vault. It is important to underline that the first blocks to be set are those of the arches, since they require a very careful positioning to guarantee the good confinement and stability of the others blocks. To allow the perfect positioning of the latter, plywood profiles were added at a later stage, cut ad hoc, on the four upper pieces of the scaffolding as showed in Figure 4-16. In a second time the vault was assembled in quadrants, realizing the four “corners” of the geometry of this kind of sail/domed vault. To make this operation easier and faster, all the blocks have a “assembly code” made up of two symbols with different colors: the dot indicates the fourth vault and the dash the row to which they belong. The entirely constructed vault is shown in Figure 4-17 and Figure 4-18.

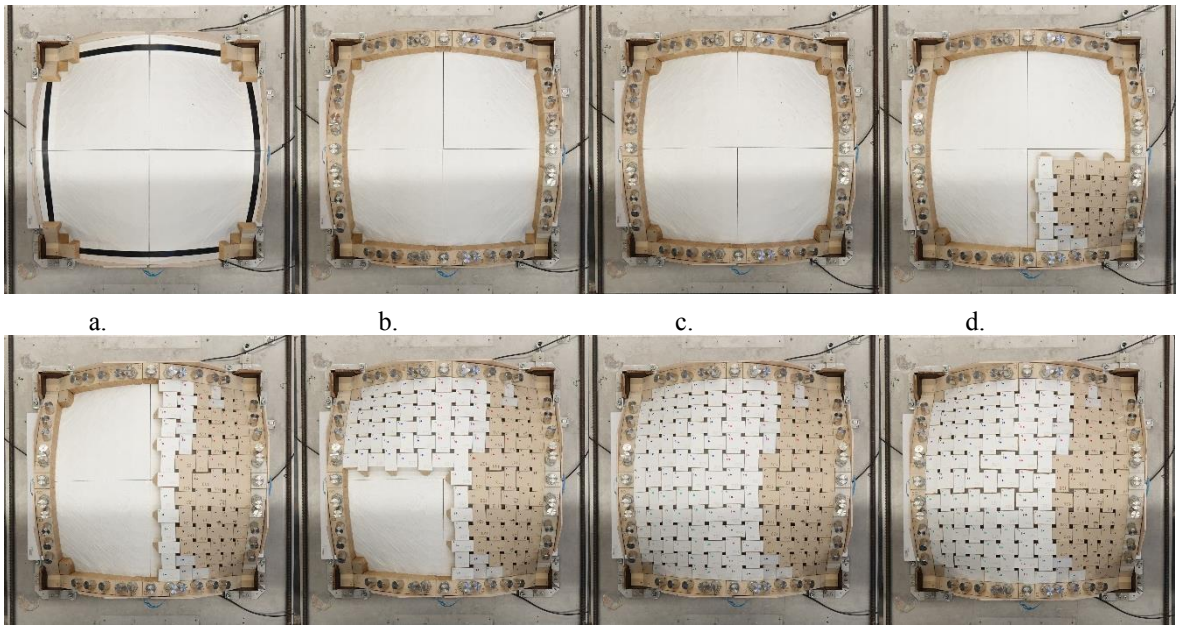

a. b. c. d.

e. f. g. h.

Figure 4-15. Step pf the construction of the vault.

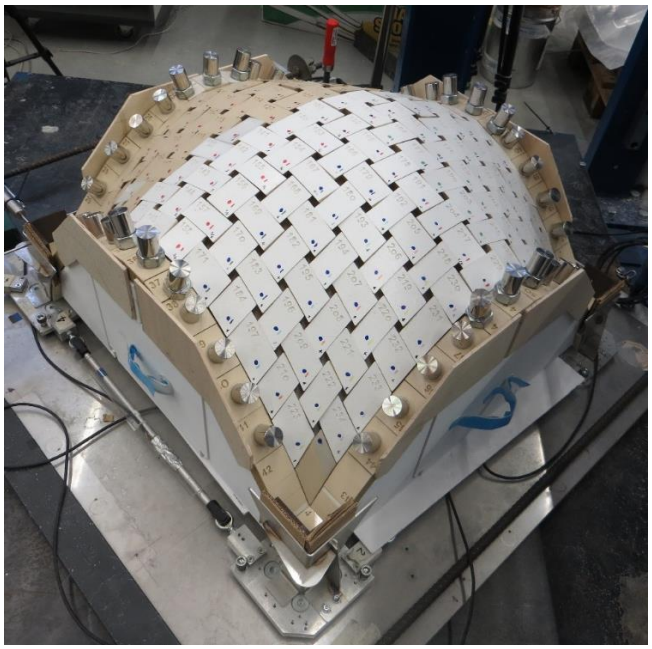

Figure 4-16. View of the vault before the disassembling of the scaffolding.

Figure 4-17. View of the vault after the disassembling of the scaffolding.

a. b. c.

Figure 4-18. Bottom views of the vault.

As already written, the physical model was adapted to a device and set-up already existing at IB-S Lab and was before printed in Italy. Even if the utmost attention is paid, to try to adapt the original vault model to the set-up in the modeling and printing phase – after some assembly tests – some calibrations and adjustments were carried out on the model, as shown below:

- Positioning of bracket in PLA and/or corrugated cardboards at the corners to reduce the size of the set-up, as the estimated 98% reduction was excessive after the assembly (Figure 4-16, Figure 4-17 and Figure 4-19);
- Some blocks in correspondence with the abutments of the original set-up were rigidly fixed together with hot glue (shown in the Figure 4-15.a); in particular for each support: the calibration block between the abutment and the structure (arches and vault) and the first two ashlars of each confinement arch in contact with this last block;
- Positioning of insulating tape on the intrados of the four confinement arches, this adjustment, comparable to placement of FRP, actually did not make a great contribution, as after the scaffolding disassembly this often detached from the blocks and also from what emerged from the test results (Figure 4-15.a);
- Positioning of steel elements on the blocks of the confinement arches in order to increase the weight and simulate the necessary stability –without the positioning of vertical elements (plexiglass/wooden walls) around the four sides of the vault (as shown (Silvestri et al., 2021)– also considering the non-presence of the haunch filling (Figure 4-16 and Figure 4-17); in particular, an attempt was made to simulate the weight of a possible overlying wall, so cylindrical steel elements (with diameter equal to 25 mm and high equal to 30 mm) weighing 115.3 g were positioned on the eleven central arches blocks and for the keystones (composed by the central three blocks of the arches) a steel bolt weighing of 52 g was added to cylindrical elements the for a total weight of 167.3 g;
- The blocks of the confinement arches were rigidly joined two by two with hot glue, except for the keystones which are made up of three initial blocks, to increase the confinement of the system; therefore, at the end from the initial eleven blocks the arches are composed of five macro-blocks;
- Insertion of further elements to obtain the necessary contrast between the various blocks (Figure 4-15.h and Figure 4-18); in particular these elements were made with corrugated cardboard sheets on which the sand-coating was applied with the same methodology used

for the blocks.

a. b. c.

Figure 4-19. Details in correspondence of the abutments: a. Lateral view with PLA bracket; b. Upper view with PLA bracket; c. Lateral view with corrugated cardboards elements.

The final weight of the whole structure is about 15.60 kg.

It is considered necessary to highlight that:

- The scale of the model was not freely chosen, this has been calibrated to fit the existing set-up at the IB-S Lab; in any case, the imposed scale made it possible to comfortably carry out the tests in the laboratory without any difficulty which would not have been possible with a larger and heavier model;
- The color of the blocks does not indicate different physical and mechanical characteristics, simply due to haste in producing the model, the company used the PLA filaments already available in the warehouse. So, the raw material for making the blocks is the same for the whole structure;
- The applied sand coating allowed to get an angle of friction between the blocks sufficiently high so to avoid sliding –equivalent to stone material– as shown by Figure 4-20;
- The equivalent Young's Modulus (E) of the PLA blocks –infill of 70%– must be enough high on respect to the external loads as to consider it as a rigid material, in accordance with Heyman hypothesis.

Figure 4-20. Interlocking between the blocks and contribution of the friction angle due to the sand coating.

4.3.3. Mechanic characterization of the arch and vault block material

To assess the mechanical properties material of these blocks a testing campaign was performed to know four fundamental characteristics:

- The Young's Modulus (E);
- The Interface Normal Stiffness or Axial Joint Stiffness (jk_n);
- The Interface Tangential Stiffness or Shear Joint Stiffness (jk_s);
- The Friction angle (μ).

For each characteristic different test was performed:

- Compressive test for E with cylindric specimens: 50x125 mm (dxh);
- Compressive test for jk_n with two cylindric specimens: 50x62.5 mm (dxh);
- Shear-box test for jk_s and μ with a square base parallelepiped specimen: 59x59x30 mm (lxwxh).

As shown in Figure 4-21, the samples for identifying the values of jk_n, jk_s and μ –the properties necessary to describe the contact and the interaction of the blocks– were superficially treated with the same block sand-coating on the concerned sides. Furthermore, it is highlighted that the pair of cylindrical specimens –necessary to carry out the test for the definition of jk_n– if overlapping have the same dimensions as the specimen necessary for the identification of E, being subjected to the same test.

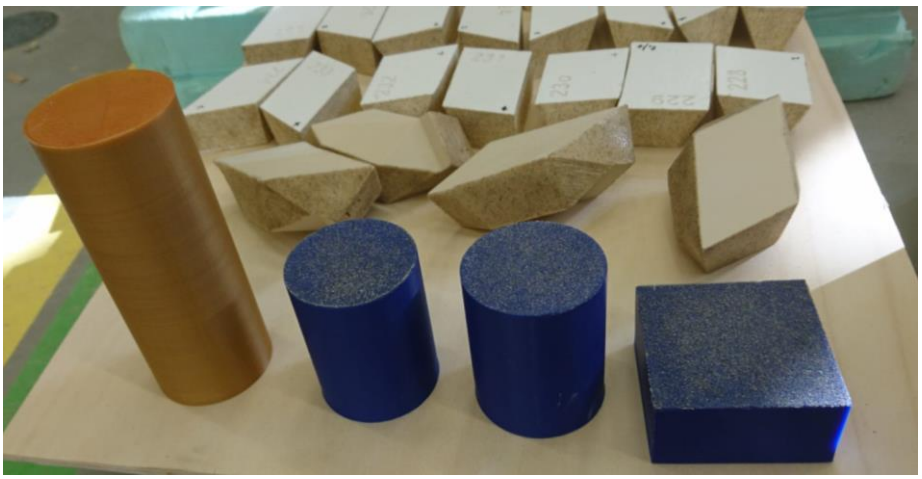

Figure 4-21. Specimens for material characterization tests; from left to right: a cylindrical specimen for the determination of E, pair of cylindrical specimens for the determination of jk_n and a parallelepiped specimen for the determination of jk_s and μ.

The compressive tests were carried out using a closed loop equipment of the University of Minho "*Testing system - SENTUR*" (Freitas et al., 1998) to which is placed "*Forç_523_300kN*", the actuator used to measure/impose the force. The software used to program and record the tests are *Dyna Tester V3*. All the Linear Displacement Variable Transducers (LVDTs) used in the characterization tests are designed and manufactured by *RDP group*; in particular, LTDV *156763* was used to have the external control and have ± 12.5 mm of linear measuring length and 0.09% of accuracy, the LVDTs (*164441, 125468* and *152390*) placed inside the two aluminum rings –

especially used in cylindrical compression tests to measure the local deformations on the samples– have 0.05% of accuracy and the first two have ± 2.5 mm of linear measuring length while the third ± 5.0 mm (Figure 4-22).

A first controlled displacement test was carried out to measure and evaluate the maximum compressive force value as reference for subsequent tests (E and jk_n) and to understand the compressive behaviour of the material; the settings were: amplitude (equal to the maximum displacement) of 50 mm, load speed of 0.015 mm/s and acquisition frequency equal to 2 Hz. The test was manually stopped when the displacement reached the value of 22 mm, due to an excessive plastic deformation. The displacement values were measured by the internal actuator and verified for possible extraneous displacements by a LVDT, as showed in Figure 4-23.a. The reference value obtained is equal to 83.63 kN.

In a second time, after having carried out the tests necessary to identify module E, all the remaining n. 6 specimens were brought to failure by compression stress test by setting an amplitude of 40 mm, a rate of 0.015 mm/s and an acquisition frequency equal to 8 Hz. Also, this second set of tests was manually stopped; in particular, the test on specimens 4 and 5 was stopped at smaller displacement values due to an excessive plastic deformation. Three LVDTs have been added to the previous set-up, applying two rings and blocked at a height of 1/3 and 1/3 directly on the specimen, as visible in Figure 4-22 (b., c. and d.), Figure 4-23.b and Figure 4-24. Table 4-3 shows the compressive force and strength values of the total seven specimens tested in compression until the failure, the average values obtained and the standard deviations. The force-displacement graphs obtained for the n. 7 tests are also shown from Figure 4-25 to Figure 4-31, only with the data of the internal actuator (blue line) and the external control LVDT *156763* (red line).

In the end the determined average values for the maximum compressive force and the compressive strength are respectively equal to 89.30 kN and 11.37 N/mm^2.

a. b. c. d.

Figure 4-22. Linear Transductor Equipment: a. LTDV *156763*; b. LVDT *164441*; c. LVDT *125468*; d. LVDT *152390*.

a. b.

Figure 4-23. Set-up for the individuation of the compressive force value of PLA (70% infill): a. Set-up of the first test; b. Set-up of the other tests.

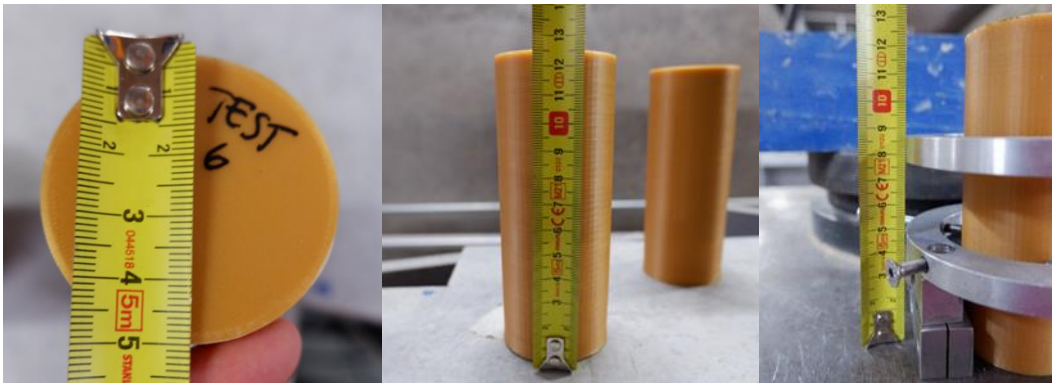

a. b. c.

Figure 4-24. Dimensions of PLA specimens (70% infill) and set-up aluminum rings: a. Diameter; b. High; c. Position of aluminum rings.

Table 4-3. Maximum values of Force and Compressive Strength obtained by Tests.

Test 1	Test 2	Test 3	Test 4	Test 5	Test 6	Test 7	**Average**
Maxium Load [kN]							
83.63	91.19	92.44	87.87	90.00	90.06	89.93	**89.30**
Standard Deviation							
2.86							
Coefficient of Variation							
0.03 = 3%							
Compressive Strength [N/mm^2]							
10.65	11.61	11.77	11.19	11.46	11.47	11.45	**11.37**
Standard Deviation							
0.36							
Coefficient of Variation							
0.03 = 3%							

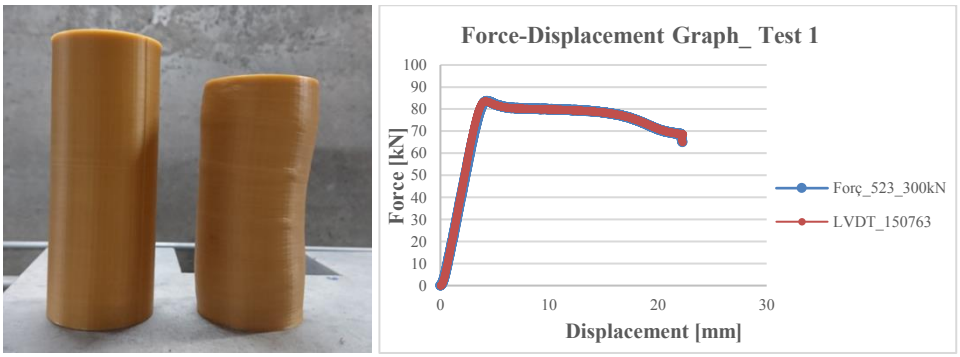

a. b.

Figure 4-25. Test 1: a. Lateral view deformed specimen; b. Force-Displacement Graphs.

a. b. c.

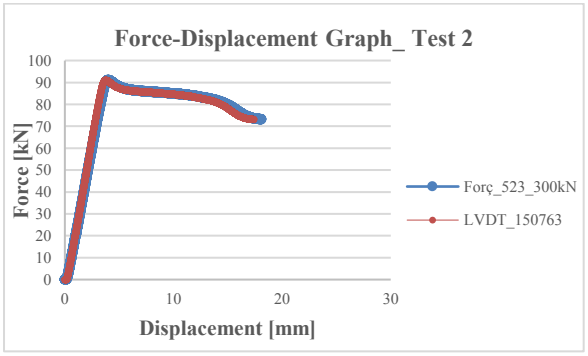

d.

Figure 4-26. Test 2: a. Top view comparison specimens before and after test; b. Later view 1 deformed specimen; c. Lateral view 2 deformed specimen; d. Force-Displacement Graphs.

a. b. c.

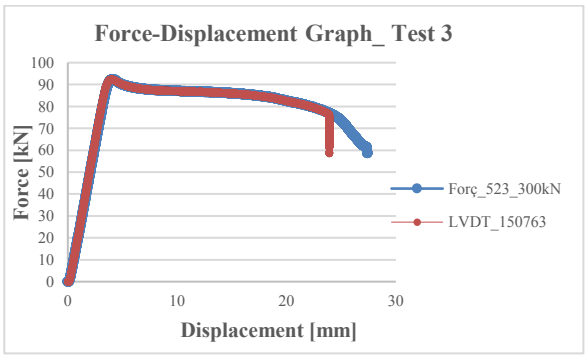

d.

Figure 4-27. Test 3: a. Top view deformed specimen; b. Later view 1 deformed specimen; c. Lateral view 2 deformed specimen; d. Force-Displacement Graphs.

a. b. c.

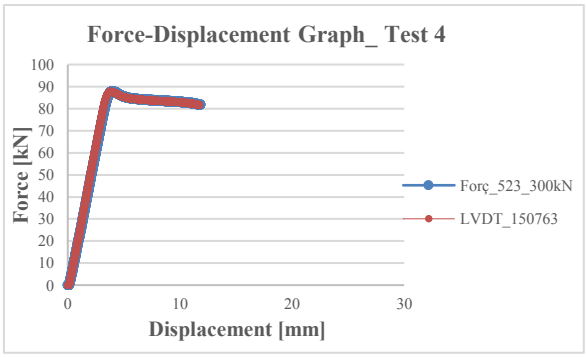

d.

Figure 4-28. Test 4: a. Top view deformed specimen before and after test; b. Later view 1 deformed specimen; c. Lateral view 2 deformed specimen; d. Force-Displacement Graphs.

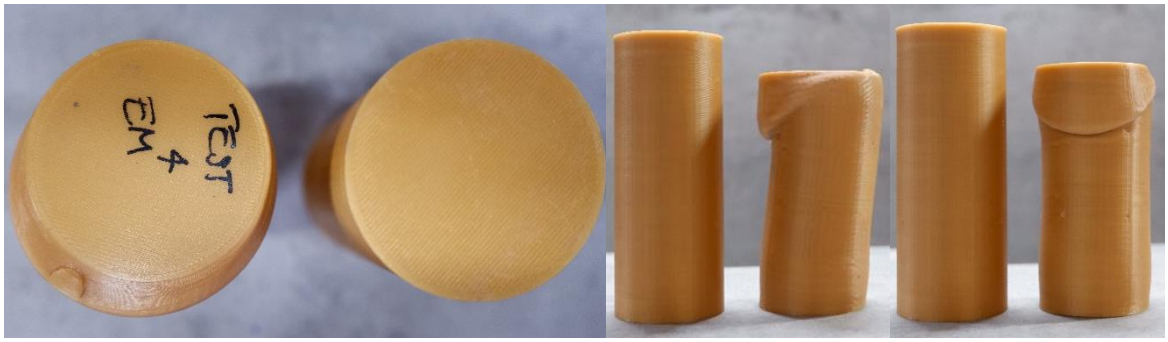

a. b. c.

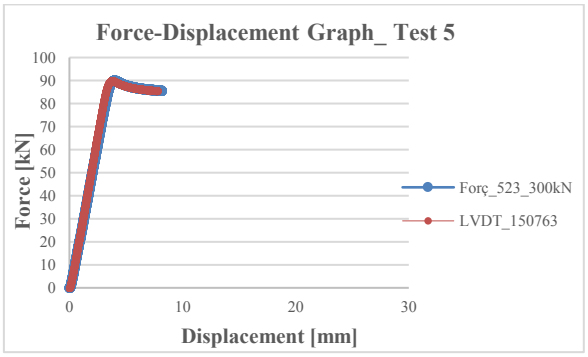

d.

Figure 4-29. Test 5: a. Top view deformed specimen before and after test; b. Later view 1 deformed specimen; c. Lateral view 2 deformed specimen; d. Force-Displacement Graphs.

a. b. c.

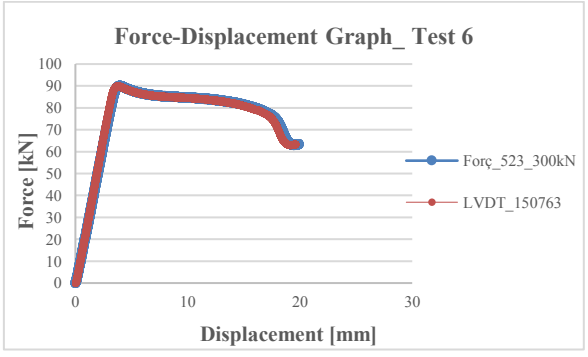

d.

Figure 4-30. Test 6: a. Top view deformed specimen before and after test; b. Later view 1 deformed specimen; c. Lateral view 2 deformed specimen; d. Force-Displacement Graphs.

a. b. c.

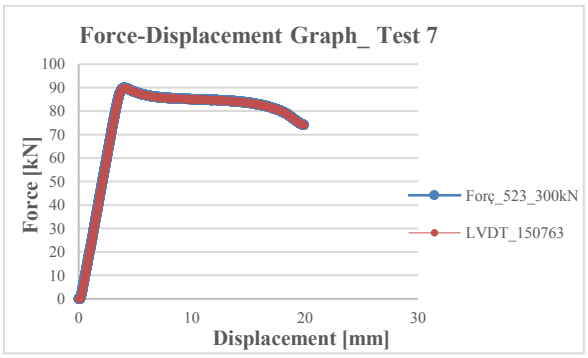

d.

Figure 4-31. Test 7: a. Top view deformed specimen; b. Later view 1 deformed specimen; c. Lateral view 2 deformed specimen; d. Force-Displacement Graphs.

The value of the Young's Modulus *E* is equal to the slope of the elastic segment of the stress-deformation curve ("Large Elastic Deformations of Isotropic Materials. I. Fundamental Concepts," 1948). To identify it, No. 6 specimens were tested without reaching the break with controlled force compression tests. The No. 6 tests were performed with the same equipment described above. The test consisted of a settling pre-load equal to 2 kN, which became a new reference load, before No. 4 consecutive cycles of loading and de-loading. The maximum force applied was equal to 22 kN (~ 25% of the maximum estimated load in elastic phase) with a rate of 0.3 kN/s; each loading and de-loading phases are always spaced out by 30 s of settling. To analyze the data, the first load cycle has been eliminated, in order to reduce material and equipment settling errors, as visible in the Figure 4-32.

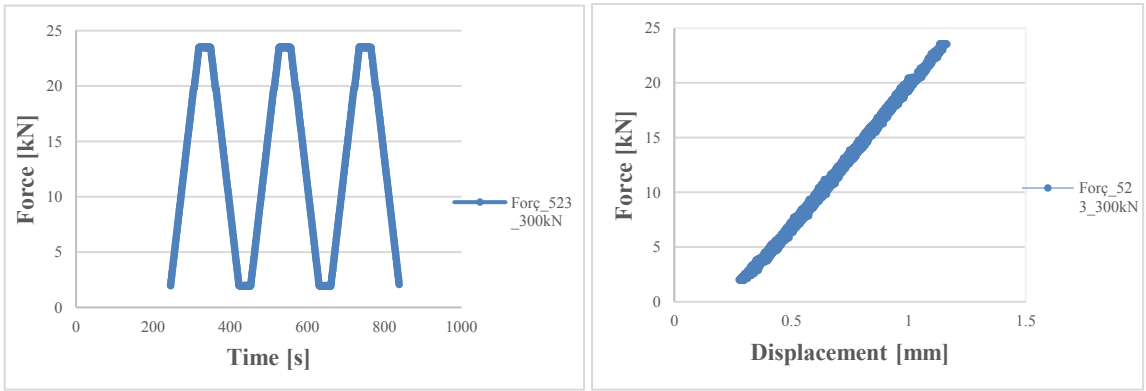

Figure 4-32. Time History of applied force to analyze the data (3 cyc) and Force-Displacement Graph (Test 1).

The displacement and the consequent deformation were obtained in a precise way, using LVDTs (*164441*, *125468* and *152390*) positioned directly on the specimen in order to be able to measure specific and localized displacements of the deformation. This occurred using a aluminum ring in which there are three screws which allow direct hooking to the specimen; this was positioned at a height of h/3 from the top of the specimen (where h represents the total height of the specimen). In this ring there are also three holes in which the LVDTs have been passed so that they are directly positioned on the specimen and not on the test actuator. Another aluminum ring equal to the first but without holes was positioned at a height of h/3 from the base of the specimen. The use of this last ring is necessary to be able to lay the LVDT tips in order to obtain the necessary measurement. The weight of the upper set-up part – the additional press element (equal to 1.23 kg) – was also considered to precisely define the total stress (see Figure 4-33). From Figure 4-22 to Figure 4-33 this equipment and this test set-up were shown.

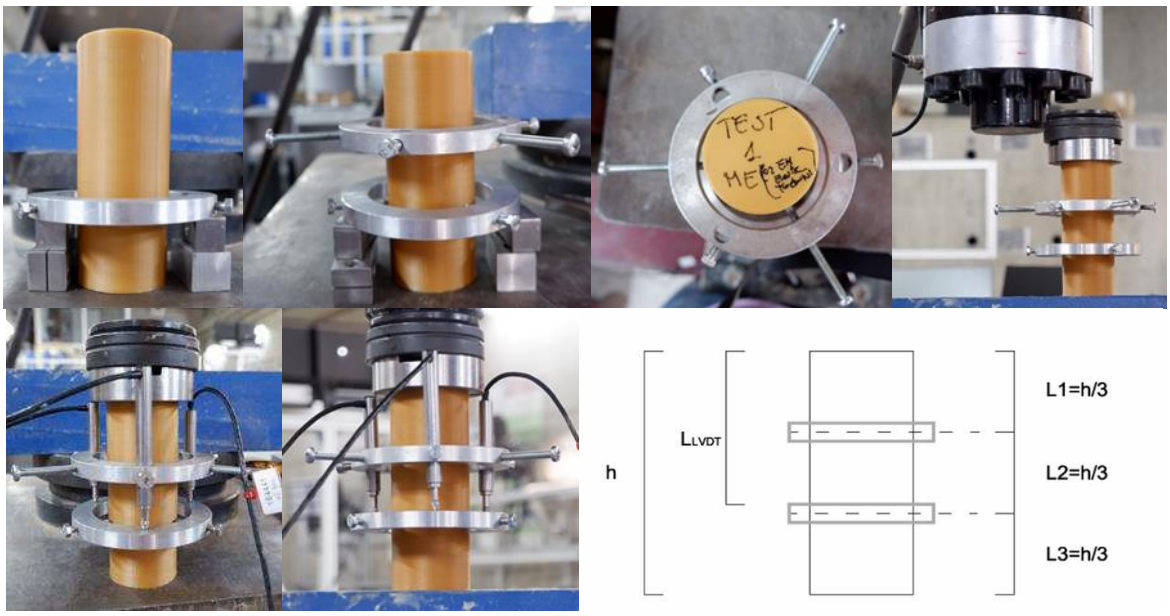

Figure 4-33. Phases of assembly of the rings and LVDTs and graphic drawing of their positioning.

For each test, the displacement data of the n. 3 LVDTs were measured, so three stress-strain curves can be obtained from the processing of these data. A single curve was achieved from the mean curve of the latter. The slope of this indicates the average value of the elastic module E about the specimen.

The data of the three individual curves only for the first test is shown below, for all the other tests the average curve and the relative slope values are directly shown, as can be seen from Figure 4-34 to Figure 4-39. The

Table 4-4 shows the values of each test, the final mean value, the standard deviation and the coefficient of variation. In the end the estimated average values for the Young's Modulus is equal to 1656.5 N/mm^2.

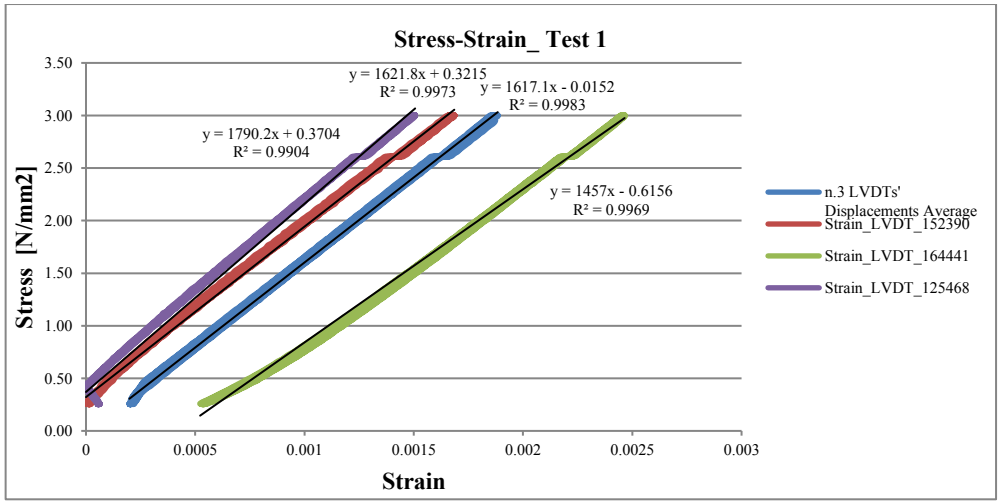

Figure 4-34. Stress-Strain graph of Test 1 for all LVDTs and the average value; indication of the linear regression and the R-squared value.

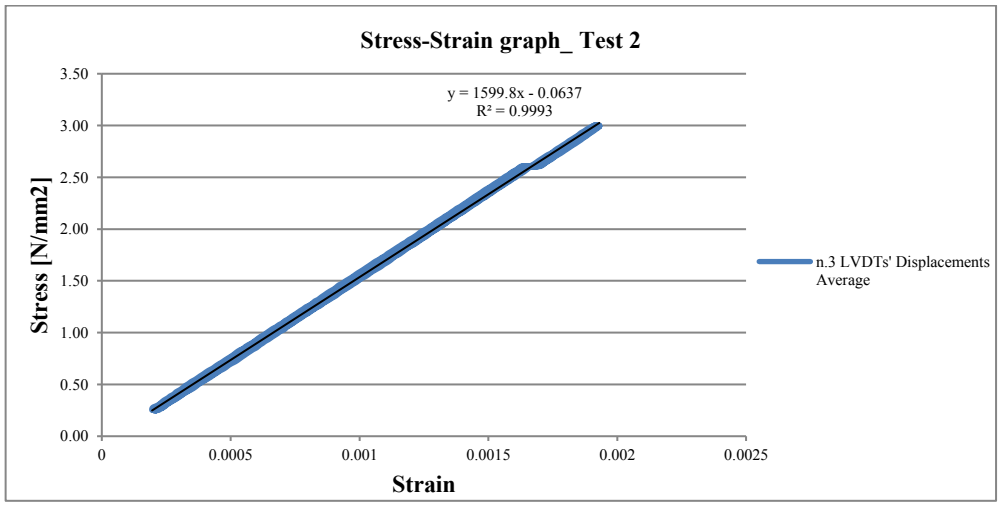

Figure 4-35. Stress-Strain graph of Test 2 for the average value with the indication of the linear regression and the R-squared value.

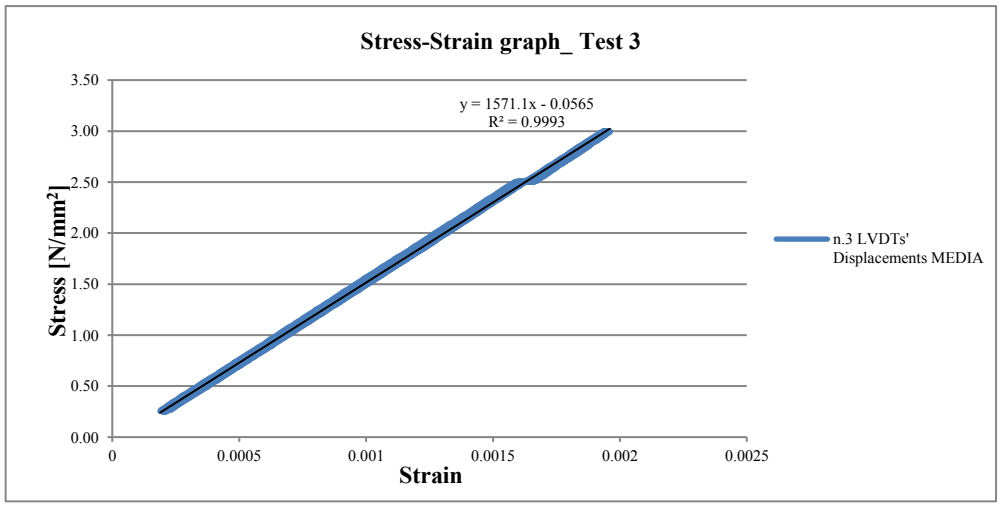

Figure 4-36. Stress-Strain graph of Test 3 for the average value with the indication of the linear regression and the R-squared value.

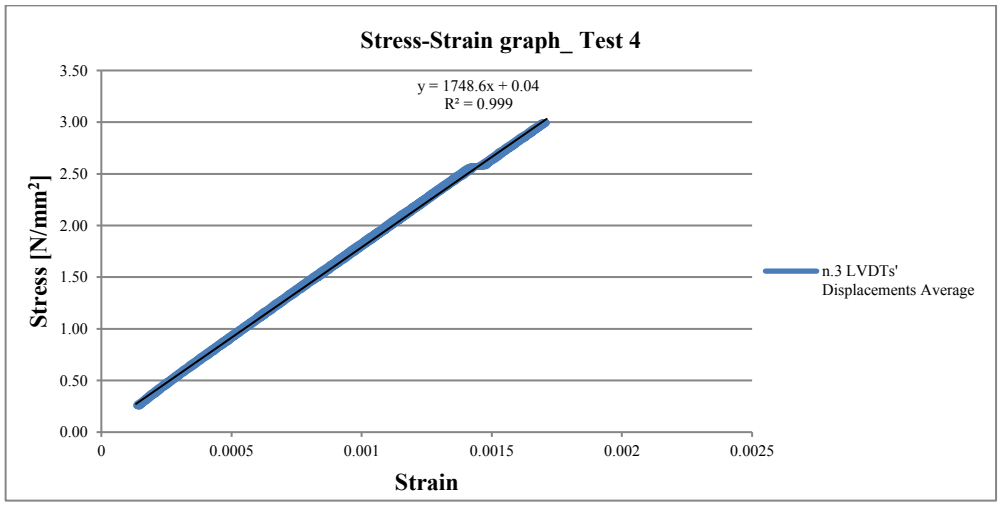

Figure 4-37. Stress-Strain graph of Test 4 for the average value with the indication of the linear regression and the R-squared value.

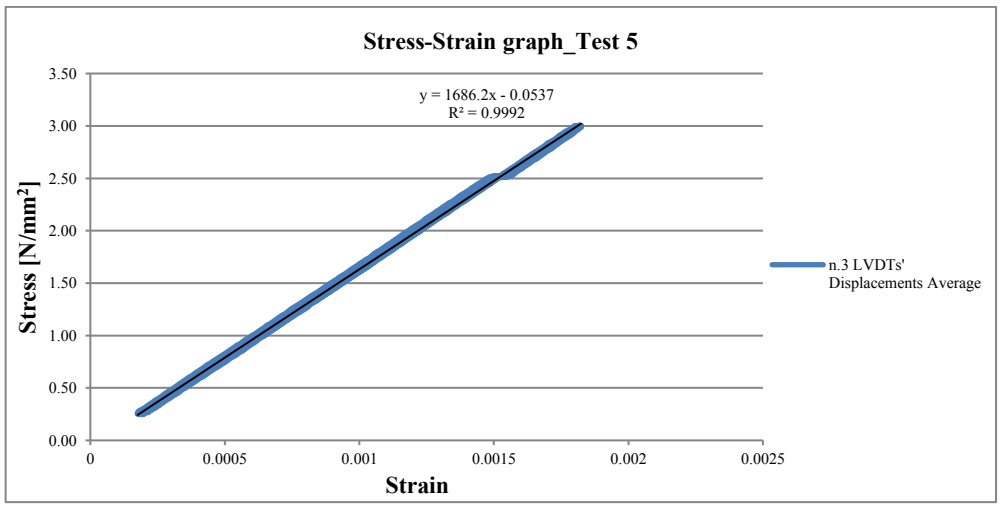

Figure 4-38. Stress-Strain graph of Test 5 for the average value with the indication of the linear regression and the R-squared value.

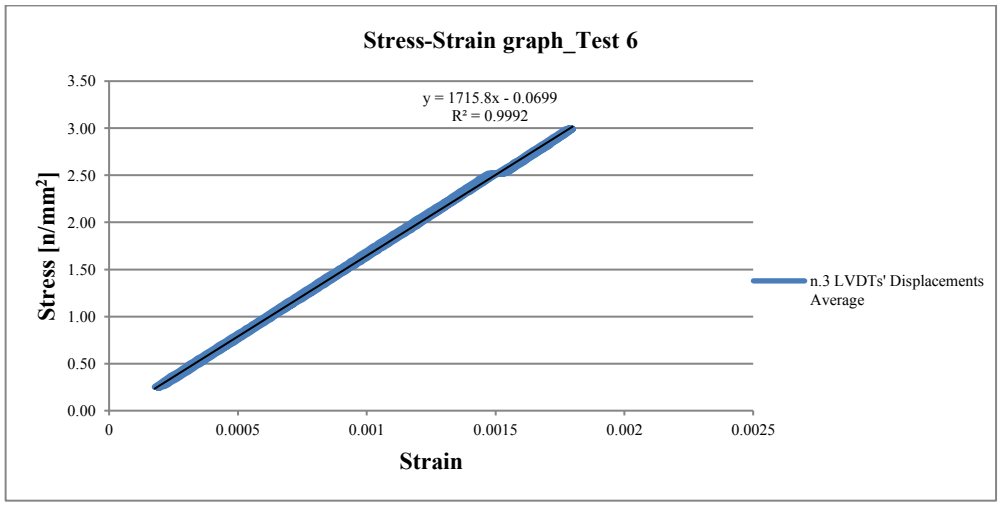

Figure 4-39**.** Stress-Strain graph of Test 6 for the average value with the indication of the linear regression and the R-squared value.

Table 4-4**.** Average values of Young's Modulus (E) obtained by Tests.

Av. Test 1	Av. Test 2	Av. Test 3	Av. Test 4	Av. Test 5	Av. Test 6	**Average**
			N/mm^2			
1617.6	1599.8	1571.1	1748.6	1686.2	1715.8	**1656.52**
Standard Deviation						
70.57						
Coefficient of Variation						
0.04 = 4%						

After identifying the elastic modulus of the material, the tests to define the normal and the tangential joint stiffness were performed. They constitute critical numerical parameters in distinc element modelling approaches, though no clear guidelines already exist to support their identification. This study followed the experimental methodology for rock blocks being developed at the University of Minho and already used in (Colombo et al., 2022).

Before to identify the jk_n, the first specimen divided in two blocks was tested with a uniaxial compression test with controlled displacement like the first test performed on the specimen for the elastic modulus. This test is similar both for equipment and for imposed parameters. In fact, only an external control LVDT (*156763*) was used, and the parameters set were: amplitude equal to the 50 mm, load speed of 0.015 mm/s and acquisition frequency equal to 8. The test was manually stopped when the displacement reached the value of 21 mm, due to an excessive plastic deformation. The displacement values were measured by the internal actuator and verified for possible extraneous displacements by a LVDT, as showed in Figure 4-23.a. The reference value obtained is equal to 86.41 kN, consistent with the previous average value.

This test was performed to understand if a different behaviour of the material occurred, considering that the specimen has the same dimensions as the previous one but is divided in two blocks and the interface between these two is constituted by the sand coating; so, to understand the behaviour of the interface. As can be seen from the Force-Displacement graph in the Figure 4-40.f., effectively in the first compression phase (0÷3 kN), during the settling time, the interface and the sand placed on the two adjacent faces react causing a characteristic micro-displacements due to the grains (clearly visible from the red line), moreover these grains lead to have a non-rectilinear line in the graph which is actually a broken line (zigzagged), for this reason graphically even if the red line is thin it appears thick. Figure 4-40 shows the photos about the test and the comparison of the specimen before and after that.

The deformation of this type of specimen is plastic like that of the entire specimen but is located across the interface on the two blocks and not on the upper and lower part of the specimen itself.

The interface normal stiffness jk_n was characterized through classical joint closure tests (Andreev et al., 2012; Kulatilake et al., 2016; Naik et al., 2021; Oliveira et al., 2021; Thanoon et al., 2008) which consisted of uniaxial compression tests on a specimen divided in two parts. To consistent-

ly identify the jk_n values of the individual specimens, No. 20 tests were performed by interchanging the no. 10 blocks (50.0x62.5 mm^2) of available specimens. Only No. 14 out of 20 test results were consistent, the other 6 tests were discarded after processing, due to equipment or data logging issues. The tests were performed with controlled displacement compression tests. In particular, the setting parameters imposed to avoid the specimen failure were amplitude of 20 mm, rate of 0.01 mm/s, acquisition frequency of 8 and duration of 2000 s. The weight of the upper set-up part –the additional press element (equal to 1.23 kg) and the upper ring (equal to 0.14 kg)– was also considered to precisely define the total stress (see Figure 4-41).

a. b. c. d. e.

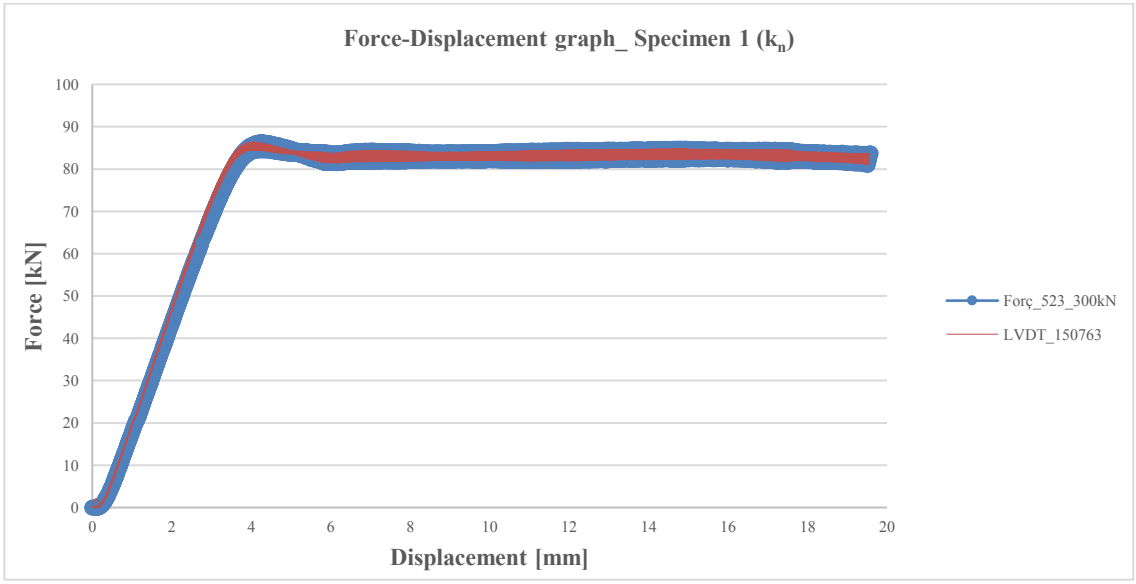

f.

Figure 4-40. Force-Displacement graph of the controlled displacement compression test brought to failure for the prototyped specimen of jk_n.

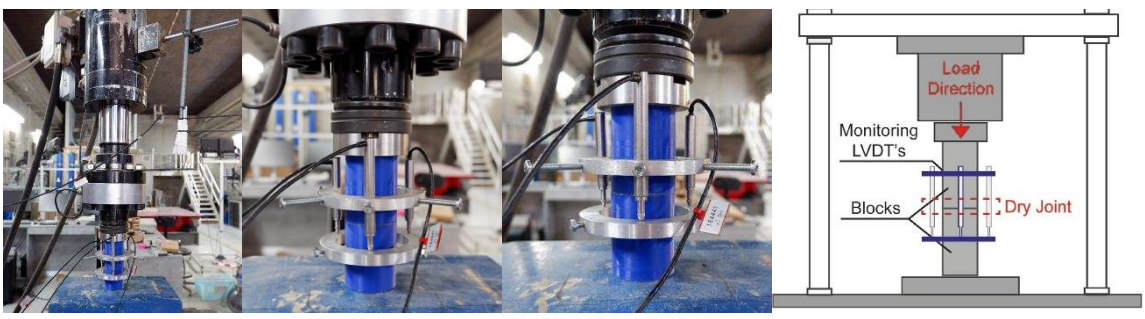

a. b. c. d.

Figure 4-41. The jk_n test: a. Later view of the specimen and equipment set-up for; b. a. Zoomed later view of the specimen; c. Detail later view; d. Drawing scheme of joint closure test set-up (Colombo et al., 2022).

This test was performed using the previously described equipment; in particular, the No. 4 LVDTs (one external to control and no. 3 hooked on the sample, as shown in Figure 4-41 and Figure 4-42) and the two aluminum rings to hook them around the specimen (which have been placed one on the upper block and one on the lower one) in the proximity of the dry-joint. Before starting each test, the position of both rings with respect to the upper/lower edge of the block was precisely measured with a micrometer as this data was important for the post-processing of the data, having to consider the contact interface displacements. Through the latter, it is possible to identify the average interface normal stiffness of the specimen and therefore of the single test. All the data were then compared to each other to have a single average value.

The data relating to the first load phase was eliminated, considering what emerged from the previous compression test up to failure, in order to have a valid processing of the data that is not affected by behaviours due to the grain settling; to not lose useful data from test to test, the lower limit value of the data analyzed is not a single value for all the tests but it changes in a range from 2 to 3 kN.

In general, as also demonstrated by Hooke's law ("Large Elastic Deformations of Isotropic Materials. I. Fundamental Concepts," 1948), the normal stiffness (k_n) is equal to:

$$\mathrm{k_n} = \frac{EA}{L} = \frac{\sigma}{\varepsilon} \cdot \frac{A}{L} = \frac{\sigma}{\Delta L/L} \cdot \frac{A}{L} = \frac{F}{\Delta L} \qquad (4.\ 10)$$

where the A denotes the cross-sectional area, L the initial length, ε the strain, σ the stress and ΔL the change in length.

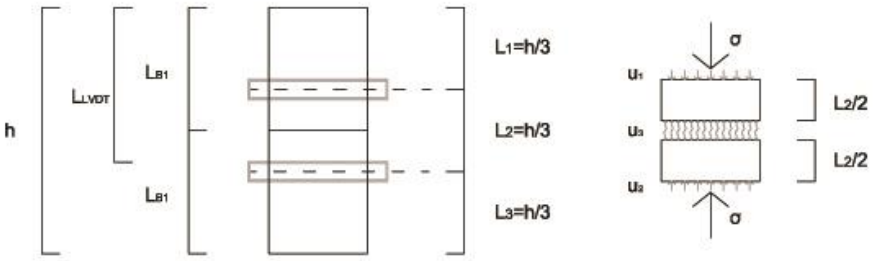

a. b.

Figure 4-42. Graphic drawing: a. Specimen characteristics and LVDTs positioning; b. The analyzed block L_2.

In our specific case, an adjustment of k_n is required, considering the type of test, the need to obtain the interface normal stiffness $\mathrm{jk_n}$, the designed specimen Figure 4-42 and the required data for the future numerical model. It was therefore necessary to express this value as a function of the stress and not of the force. For this reason, the part taken into consideration of the specimen was only the L_2 of the specimen in the study (Figure 4-42), it was found that the variation of the total displacement (u_t) estimated by the LVDTs placed near the specimen is equal to:

$$u_t = u_1 + u_2 + u_3 \ \rightarrow\ u_3 = u_t - (u_1 + u_2) \qquad (4.\ 11)$$

in particular, u_1 and u_2 are the displacements of the two blocks which carry out the test specimen and related to the deformations due to the test stress and to the elastic modulus of the material previously determined as demonstrated by Hooke's law –the deformations due to the material–; while u_3 is the displacement that takes place in the interface, between the two blocks. Assuming that in the specimens the deformations are equal being subjected to the same stress and composed of the same material, it results that:

$$u_1 = u_2 \quad \rightarrow \quad u_3 = u_t - 2 \cdot (u_1) \quad \rightarrow \quad \Delta L_j = \Delta L_t - 2 \cdot (\Delta L_b) \qquad (4.\ 12)$$

where, the subscript *j* indicates joint and *b* indicates block, so:

$$u_1 = u_2 = \frac{\sigma}{E} \cdot \frac{L_2}{2} \quad \rightarrow \quad \Delta L_j = \Delta L_t - 2 \cdot \left(\frac{\sigma}{E} \cdot \frac{L_2}{2}\right) = \Delta L_t - \frac{\sigma \cdot L_2}{E} \qquad (4.\ 13)$$

The ΔL_t is always a known value being the average value of the displacements measured through the three LVDTs, directly during the tests (Figure 4-43.a). The ΔL_j is a value that can be obtained through the formula, but it must be considered as previously explained that the jk_n necessary for the numerical model is a function of the stress ($jk_n = f(\sigma)$) and its variation, since these are infinitesimal values present in the interface with respect to the independent variable, will be identified by a differential.

$$jk_n = \frac{d\sigma_n}{du_n} \qquad (4.\ 14)$$

The interface normal stiffness k_n is the ratio of the differential stress on the differential normal displacement, i.e., it is possible to identify it as the slope in a Stress-Displacement graph, constructed by points which identify the differential increase of these values (Figure 4-43).
To construct this graph that considers the increments and differential variations of effort and displacement, a post-processing process was automated through an algorithm which divides the initial curve into ten parts, linearizing it. Appling the method (Kulatilake et al., 2016) the jk_n average value was obtained through the exponential regression of the entire post-produced curve.

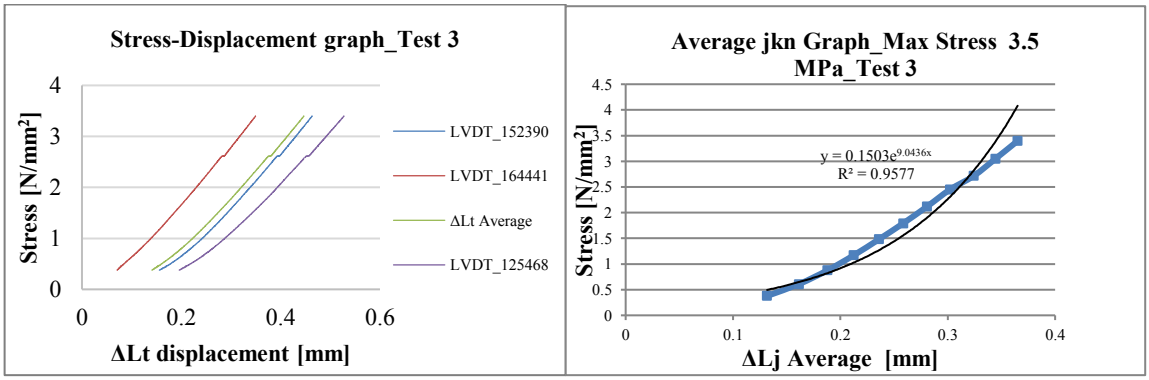

a. b.

Figure 4-43. Example of Stress-Displacement graph (Test 3): a. Determination of ΔL_t; b. Post-produced curve, divided into ten parts.

No.14 tests have been performed, and for each ones the exponential curve was processed for a maximum stress of 3.5 MPa and a lower equal to 0.5 MPa, in order to have a data consistent with the stresses of a scaled model. In particular, following the (Kulatilake et al., 2016) method and other examples in literature, i.e. (Colombo et al., 2022), the stress was expressed as function of the joint closure du_3, of Eq. (4. 14) and two empirical constants A and B:

$$\sigma = A \cdot e^{B \cdot du_n} \quad (4.\ 15)$$

So the normal joint stiffness is equal:

$$jk_n = \frac{d\sigma_n}{du_n} = B \cdot \sigma \quad (4.\ 16)$$

The Table 4-5 summarizes the value of the empirical constant B found. In particular, the mean value is equal to 10.29 ± 2.36 (10%) mm^{-1}. This value was coherent with literature for fragmental e Limestone. Considering the stress applied (Eq.s 4.15 and 4.16), the final mean value of jk_n was equal to 0.26 N/mm^3. It is important to note that the stress value has a decisive influence on the jk_n; in fact, after an initial phase of joint closure, where relatively low stresses trigger large displacements, the joint stiffness (i.e. the slope) dramatically increases for larger stress levels. Moreover, the larger variability of the physical properties of the joint (e.g. surface's roughness, geometrical tolerance) which directly influence the joint stiffness compared to volumetric properties explains the coefficients of variation (CoV) of this joint property (10%) and that of the mechanical properties (3% for compressive strength and 3% for Young's modulus).

Table 4-5. Summary of empirical constant B to obtain interface normal stiffness jk_n for each test with the maximum stress of about 3.5 MPa.

Av Test 1	Av Test 2	Av Test 3	Av Test 4	Av Test 5	Av Test 6	Av Test 7	Av Test 8	Av Test 9	Av Test 10	Av Test 11	Av Test 12	Av Test 13	Av Test 14	**Average**
B value estimated with a maximum stress of about 3.5 MPa [mm^{-1}]														
12.65	10.50	9.04	9.61	8.82	10.83	10.43	10.21	11.03	9.67	9.51	11.76	9.80	10.19	**10.29**
Standard Deviation														
1.04														
Coefficient of Variation														
0.10														

The elastic modulus E is also calculated with this set-up for a simple compression test displacement controlled as the test in Figure 4-32. In fact, as found in scientific literature (Gaetani, 2020; Rossi, 2015), the Young's modulus chooses to investigate on vault scale-model and its adjustments is those measured by testing in simple compression the assemblages of the block; in this case it was configured by the two cylindric specimens. The value was the slope of the regression line of the Stress-Strain curve done for the compressive test to obtain constant B. It is important

to highlight that this value has to be considered an upper bound, due to the fact that it has been calculated once a complete adherence between the block surfaces have been obtained, hence neglecting the initial branch of compaction of joints (Figure 4-44), while, during the tests on the vault, blocks do not fit together exactly. The results of N. 3 tests carried out with this methodology are reported in Table 4-1 and the final average value is equal to 225.67 N/mm^2.

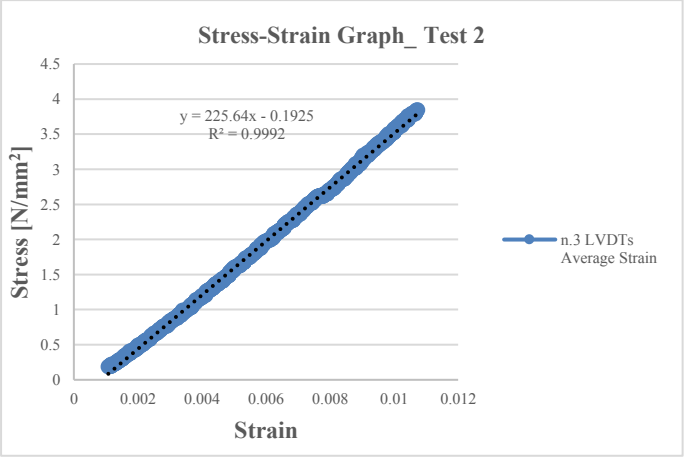

Figure 4-44. Stress-Strain graph of Test 2 for the average value with the indication of the linear regression and the R-squared value

Table 4-6. Average values of Young's Modulus (E) obtained by Tests with assembled specimens.

Av. Test 1	Av. Test 2	Av. Test 3	**Average**
N/mm^2			
235.69	225.64	215.68	**225.67**
Standard Deviation			
10.01			
Coefficient of Variation			
0.04			

Joint shear k_s stiffnesses describe the variation of the shear stress with the shear displacement. So, direct shear tests were conducted to evaluate the tangential stiffness jk_s of the dry-joints. The specimens consisted of two blocks of 60 mm length, 60 mm width and 30 mm height (Figure 4-45).

a. b.

Figure 4-45. Example of specimens for shear box test: a. Later view; b. Top view.

The tests were performed with Automatic Shear Testing Machine "*SHEARMATIC EmS*" (Wyke-

ham Farrance - Controls group, n.d.) (Figure 4-46.a), monitored with software Istra 4D (Dantec Dynamics, n.d.) (Figure 4-46.b) and processed with a code on Python (Python Software Foundation ("PSF"), n.d.) modified from one previously realized by University of Minho; as method explain in (Colombo et al., 2022).

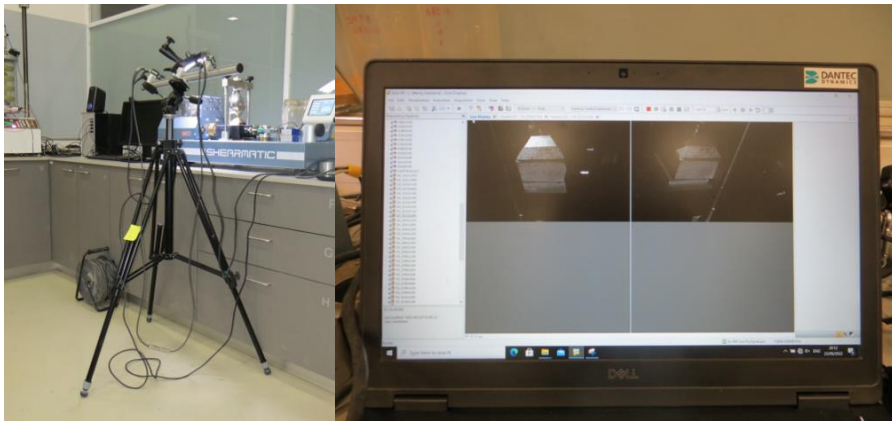

a. b.

Figure 4-46. Shear box test equipment.

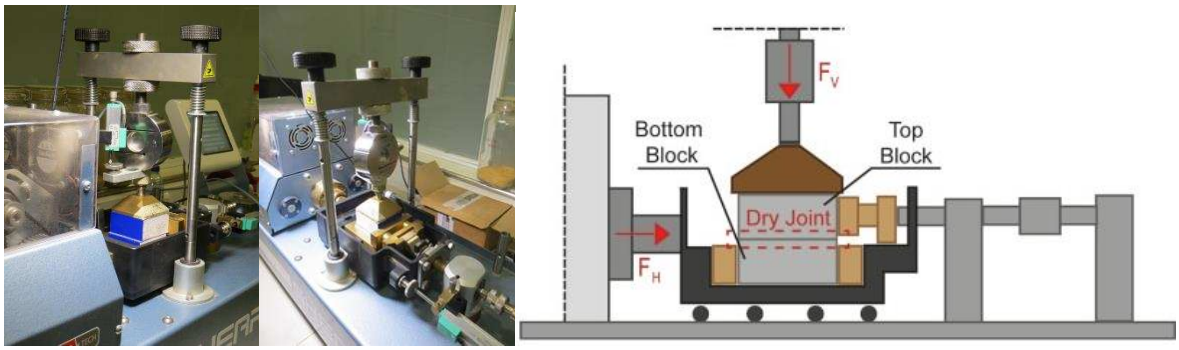

a. b. c.

Figure 4-47. Test set-up: a. and b. View of the equipment during the test; c. experimental set-up sketches of tangential joint stiffness evaluation through direct shear box tests.

The test setup was composed of i) a bottom block located within the box base and pushed by a horizontal force FH and ii) a fixed top block subjected to a constant normal force FV (Figure 4-47.c). The data acquisition system comprised two load cells measuring the vertical and horizontal forces FV and FH, while the relative normal and shear displacement between the bottom and the top blocks was monitored by a Digital Image Correlation (DIC) system, which has already been employed in the literature for extracting the interface stiffness, proving its efficiency against other types of acquisitions (Kartal et al., 2011) (Figure 4-48). This non-contact full-field measurement method solely identifies the relative displacement between the two blocks, whereas the shear box displacement acquisition system, i.e. vertical and horizontal LVDTs, also measures the external compliances owing to the shear box rig.

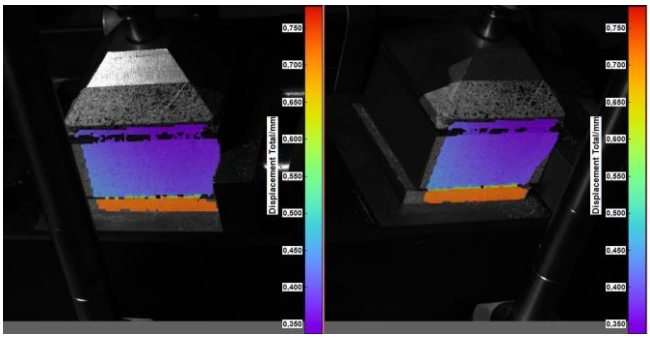

Figure 4-48. Example of DIC data by (Dantec Dynamics, n.d.): Joint displacement of combination of Specimens 5 and 6 for the test with imposed horizontal stress of 15 kPa.

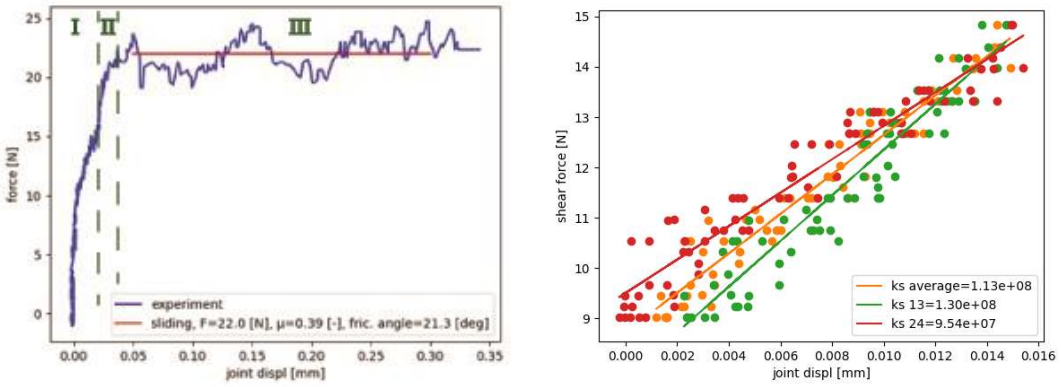

a. b.

Figure 4-49. Example of post-processed data by Python, from direct shear test of combination of Specimens 5 and 6 for and the imposed horizontal stress of 15 kPa: a. the Stress-displacement curve obtained (sliding); b. The jk_s identification of the specific test, equal to the average (orange line regression).

Figure 4-49.a provides an example of the obtained shear force-displacement curve assuming a compression stress of 15kPa. The first window (I) corresponds to the so-called "elastic-stick" regime, in which the increase of shear stress leads to very small relative displacements (Fantetti et al., 2019; Kartal et al., 2011). In the second window (II), micro-slips progressively develop: at the micro-scale, some asperities are in adhesion (i.e. stuck), while other asperities experience relative tangential displacements. Such a phase is a transition from window I to window III, which corresponds to the gross slip phase, where all the asperities experience relative tangential displacement: the value of shear stress reaches the shear strength of the joint. Five tests were performed for each evaluated stress, i.e., 5kPa, 10kPa, 15kPa, 20 kPa, 25 kPa, 100 kPa, 150 kPa, 200 kPa, 250 kPa. Both lower stress values in the range of 5÷25 kPa and higher 100÷250 kPa were chosen. Initially only the first range was investigated to evaluate data for a scale model but not all results were clean and consistent, due to the behaviour of sand grains and a low imposed vertical force; for this reason and to verify the data, tests with the highest range were performed. Furthermore, these additional tests were also performed to evaluate a jk_s and μ and for a real and non-scale numerical model. As imaginable, more the vertical stress increased more the results and the curve were clean and coherent.

The tangential join stiffness jk_s was estimated by considering the slope of the elastic-stick phase (I), where the stress grows with a linear trend with respect to the displacement. The values con-

sidered was post-processed by *Paython* script considering the relative displacements of four reference points (gauge) previously identified on *Istra 4D* and joint in two pair (pair 1-3 and pair 2-4) (Figure 4-48and Figure 4-49.b). Table 4-7 and

Table 4-8 are the tables with the values obtained for each test and the Table 4-9 and
Table 4-10 for obtaining the final values of jk_s with respect to the ranges evaluated, i.e. jk_s=0.18±0.06 (29.4%) N/mm^3 at range 5÷25 kPa and jk_s = 1.44±0.10 (6.6%) N/mm^3 at range of 100÷250 kPa.

Table 4-7. Value of jk_s for the tests in a range of 5÷25 kPa as horizontal stress.

Comb. 1-2 Sp.	Comb. 3-4 Sp.	Comb. 5-6 Sp.	Comb. 7-8 Sp.	Comb. 9-10 Sp.	**Average Value**
jk_s with a stress of 5 kPa [N/mm^3 = GPa/m^3]					
0.19	0.11	0.15	0.14	0.10	**0.14**
Standard Deviation					
0.04					
Coefficient of variation					
0.28					
jk_s with a stress of 10 kPa [N/mm^3 = GPa/m^3]					
0.19	0.10	0.10	0.12	0.10	**0.12**
Standard Deviation					
0.04					
Coefficient of variation					
0.30					
jk_s with a stress of 15 kPa [N/mm^3 = GPa/m^3]					
0.27	0.20	0.11	0.27	0.10	**0.19**
Standard Deviation					
0.08					
Coefficient of variation					
0.42					
jk_s with a stress of 20 kPa [N/mm^3 = GPa/m^3]					
0.24	0.22	0.40	0.12	0.22	**0.24**
Standard Deviation					
0.10					
Coefficient of variation					
0.42					
jk_s with a stress of 25 kPa [N/mm^3 = GPa/m^3]					
0.17	0.32	0.21	0.29	0.16	**0.23**
Standard Deviation					
0.07					
Coefficient of variation					
0.32					

Table 4-8. Value of jk_s for the tests in a range of 100÷250 kPa as horizontal stress.

Comb. 1-2 Sp.	Comb. 3-4 Sp.	Comb. 5-6 Sp.	Comb. 7-8 Sp.	Comb. 9-10 Sp.	**Average Value**
jk_s with a stress of 100 kPa [N/mm^3 = GPa/m^3]					
1.31	1.48	1.39	1.46	1.20	**1.37**
Standard Deviation					
0.12					
Coefficient of variation					
0.09					
jk_s with a stress of 150 kPa [N/mm^3 = GPa/m^3]					
1.02	1.06	1.48	1.40	1.76	**1.34**
Standard Deviation					
0.31					
Coefficient of variation					
0.23					
jk_s with a stress of 200 kPa [N/mm^3 = GPa/m^3]					
1.32	1.52	1.60	1.70	1.49	**1.53**
Standard Deviation					
0.14					
Coefficient of variation					
0.09					
jk_s with a stress of 250 kPa [N/mm^3 = GPa/m^3]					
1.90	1.84	1.16	1.42	1.24	**1.51**
Standard Deviation					
0.34					
Coefficient of variation					
0.23					

Table 4-9. Average value of jk_s for the range of 5÷25 kPa as horizontal stress.

Av. jk_s (5 kPa)	Av. jk_s (10 kPa)	Av. jk_s (15 kPa)	Av. jk_s (20 kPa)	Av. jk_s (25 kPa)	**Average Value R.**
[N/mm^3 = GPa/m^3]					
0.14	0.12	0.19	0.24	0.23	**0.18**
Standard Deviation					
0.05					
Coefficient of variation					
0.29					

Table 4-10. Average value of jk_s for the range of 100÷250 kPa as horizontal stress.

Av. jk_s (100kPa)	Av. jk_s (150kPa)	Av. jk_s (200kPa)	Av. jk_s (250kPa)	**Average Value R.**
[N/mm3 = GPa/m^3]				
1.37	1.34	1.53	1.51	**1.44**
Standard Deviation				

0.10
Coefficient of variation
0.07

Again, a high coefficient of variation is obtained for the interface stiffness. It is important to note that the coefficients of variations for the single tests are different; this also occurs to the coefficient of variation of the first range (5÷25 kPa) since the difference between the average values for each different compressive stress varies greatly with respect to the imposed stress (Figure 4-50). Instead, the CoV for the pressure range 100÷250 kPa is much lower, because by increasing the imposed stress the jk_s value tends to be more stable.

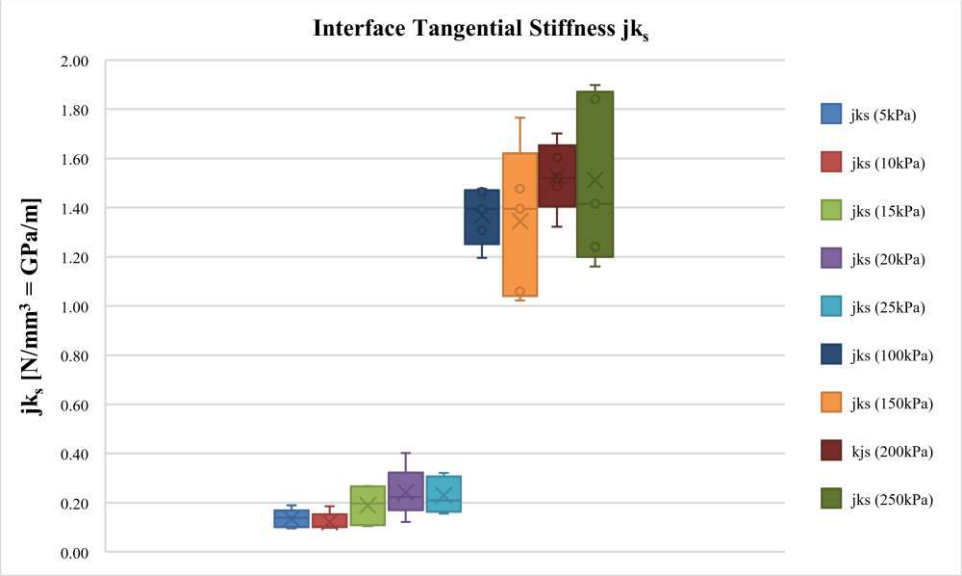

Figure 4-50. Variation of jk_s for each test, the x in the box plot indicates the mean.

The same tests were used to obtain the friction angle values; also in this case these have been divided in the same previous ranges (5÷25 kPa and 100÷250 kPa) even if the values obtained are comparable. Particularly, the shear (III) strength was extracted from the shear box tests considering the linear regression of all the experimental outcomes about the sliding evaluated by the adjusted Python code. An example is shown in Figure 4-49.a. Assuming a Coulomb behaviour for the joint, the average values of friction angle result equal to μ=23.31°±1.69 (4.8%) for the range imposed stress of 5÷25 kPa and to μ=24.93°±1.31 (4.1%) for the range imposed stress of 100÷250 kPa .

The summary tables of all the tests, the tables for evaluating the average values with respect to the ranges and a graph (Figure 4-51) that allows you to compare all the data are shown below.

Table 4-11. Value of μ for the tests in a range of 5÷25 kPa as horizontal stress.

Comb. 1-2 Sp.	Comb. 3-4 Sp.	Comb. 5-6 Sp.	Comb. 7-8 Sp.	Comb. 9-10 Sp.	**Average Value**
μ with a stress of 5 kPa [°]					
27.10	30.10	17.60	18.30	26.30	**23.88**

Standard Deviation					
5.60					
Coefficient of variation					
0.23					
μ with a stress of 10 kPa [°]					
25.70	22.40	20.20	0.00	20.70	**22.25**
Standard Deviation					
2.49					
Coefficient of variation					
0.11					
μ with a stress of 15 kPa [°]					
24.90	23.80	21.30	20.00	22.20	**22.44**
Standard Deviation					
1.95					
Coefficient of variation					
0.09					
μ with a stress of 20 kPa [°]					
25.60	21.70	20.70	23.20	23.70	**22.98**
Standard Deviation					
1.89					
Coefficient of variation					
0.08					
μ with a stress of 25 kPa [°]					
23.70	24.30	26.50	25.00	25.50	**25.00**
Standard Deviation					
1.08					
Coefficient of variation					
0.04					

Table 4-12. Value of μ for the tests in a range of 100÷250 kPa as horizontal stress.

Comb. 1-2 Sp.	Comb. 3-4 Sp.	Comb. 5-6 Sp.	Comb. 7-8 Sp.	Comb. 9-10 Sp.	**Average Value**
μ with a stress of 100 kPa [°]					
26.50	24.00	24.50	24.80	23.70	**24.70**
Standard Deviation					
1.09					
Coefficient of variation					
0.04					
μ with a stress of 150 kPa [°]					
24.00	26.20	27.70	25.10	24.20	**25.44**
Standard Deviation					
1.53					
Coefficient of variation					
0.06					
μ with a stress of 200 kPa [°]					
26.10	23.50	26.60	27.10	26.50	**25.96**

Standard Deviation					
1.42					
Coefficient of variation					
0.05					
μ with a stress of 250 kPa [°]					
23.90	22.00	24.20	24.00	24.00	**23.62**
Standard Deviation					
0.91					
Coefficient of variation					
0.04					

Table 4-13. Average value of μ for the range of 5÷25 kPa as horizontal stress.

Av. μ (5 kPa)	Av. μ (10 kPa)	Av. μ (15 kPa)	Av. μ (20 kPa)	Av. μ (25 kPa)	**Average Value R.**
[°]					
23.88	22.25	22.44	22.98	25.00	**23.31**
Standard Deviation					
1.14					
Coefficient of variation					
0.05					

Table 4-14. Average value of μ for the range of 100÷250 kPa as horizontal stress.

Av. μ (100 kPa)	Av. μ (150 kPa)	Av. μ (200 kPa)	Av. μ (250 kPa)	**Average Value R.**
[°]				
24.70	25.44	25.96	23.62	**24.93**
Standard Deviation				
1.01				
Coefficient of variation				
0.04				

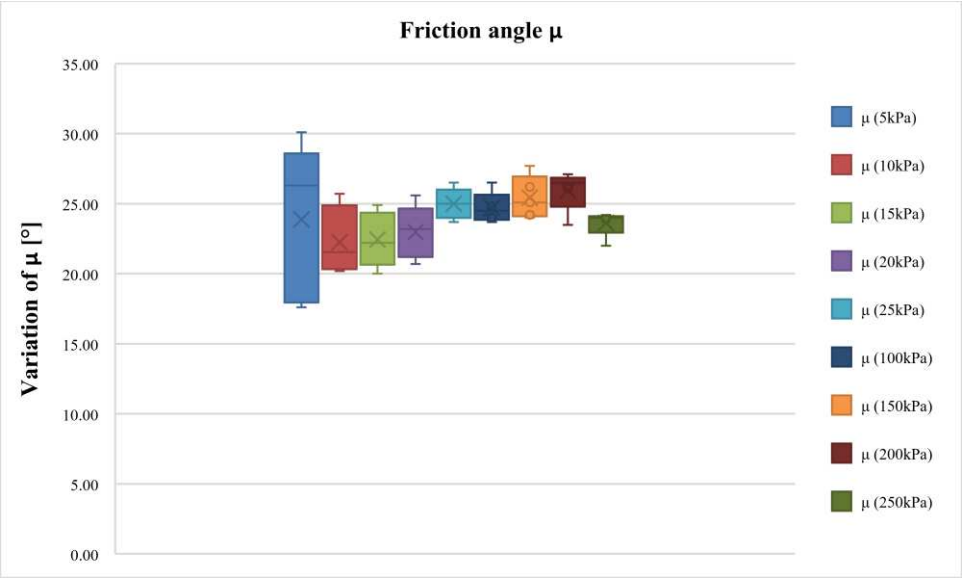

Figure 4-51. Variation of μ for each test, the x in the box plot indicates the mean.

The material characterization of the friction coefficient was completed by pseudo-static tilting tests on two blocks; the bottom unit was fixed to the tilting table and the top one was left free to slide. The table was progressively tilted to obtain the friction coefficient between the blocks and the sliding angle was identified by a digital inclinometer attached to the table. The values were then compared with the results from the direct shear tests; three tests are performed with range results of 24°÷28° that is close to the one identified through direct shear tests, considering the experimental scatter and the variability of the surface coating.
The Table 4-15 shows the final values of the properties found.

Table 4-15. Linear elastic properties of the block and mechanical properties for the interface elements.

Characteristics	Value
Specific mass ρ [kg/m^3]	774
Young's modulus E for Model [N/mm^2]	226
Poisson's ratio υ [-]	0.2
Interface normal stiffness jk$_n$ [N/mm^3]	0.26
Interface tangential stiffness jk$_s$ [N/mm^3]	0.18
Friction angle μ [°]	23.31

4.4. Tests on the vault

The main aim of the experimental research was to investigate the seismic response of masonry Abeille vault under two different types of loading conditions:

- Indirect Seismic Action (ISA), where the loading condition is the differential horizontal displacements at the abutments. So, the vault is only indirectly loaded by the differential acceleration/displacements produced on its supports and the latter (i.e. the piers, walls and pillars of the building) are subjected to seismic acceleration;
- Direct Seismic Action (DSA), where the loading condition is the horizontal forces proportional to vault mass. In this case, the abutments are fixed and the seismic acceleration directly excites the vault and its mass.

4.4.1. Indirect Seismic Action (ISA)

The damage mechanisms recurrently observed during post-earthquake surveys in masonry buildings with vaulted spaces corresponds to two displacement settings: the in-plane horizontal shear distortion and the longitudinal opening/closing of the abutments. This research considers and investigates only on the first one, being the most recurring behaviour observed for vaults (Aita et al., 2020; Carfagnini et al., 2017, 2018), the typical horizontal structural elements of the existing cultural heritage and in particular, the most recurrent in churches characterized by a large difference in stiffness between the nave and the façade and/or transept and in palaces with laterally

constrained porches or loggias as shown in Figure 4-52.

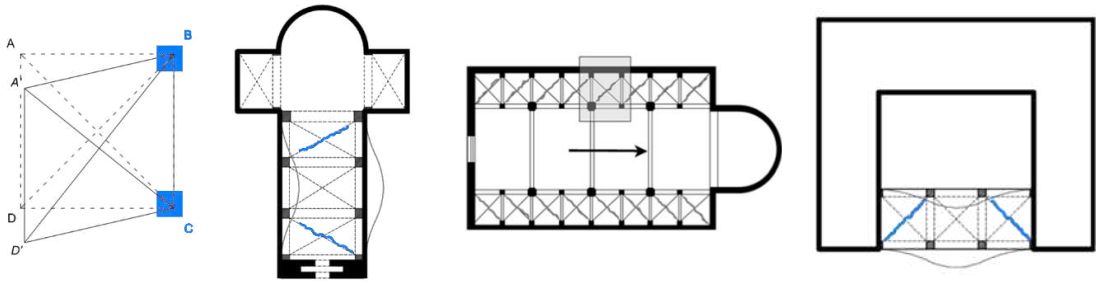

a. b. c. d.

Figure 4-52**.** In- Plane horizontal shear: a. Displacement setting; b. Damage mechanisms in single nave churches, c. Damage mechanisms in three naves churches and d. Damage mechanisms in buildings. (Rossi et al., 2016).

4.4.1.1. Set-up

The experimental tests were performed by means of a special testing device realized for previous project and research (Rossi et al., 2014, 2015, 2016; Bianchini et al., 2019, 2022; Rossi, 2015) and designed ad hoc to apply different displacements settings (Figure 4-53). It consists of a special frame made by four steel squared plates that may be linked to each other by means of couples of aluminum bars (acting as tie-rods) hinged at both ends with uniball joints. The use of uniball joints allows bars rotating in the plane, so that bars-plate systems operate as a sort of "pantograph". The abutments of the vault are rigidly fixed on the top of the plates, sketched in Figure 4-54.a. These latter can freely move on a plywood panel with a flat aluminum surface thanks to four spherical wheels Figure 4-54.b and c.

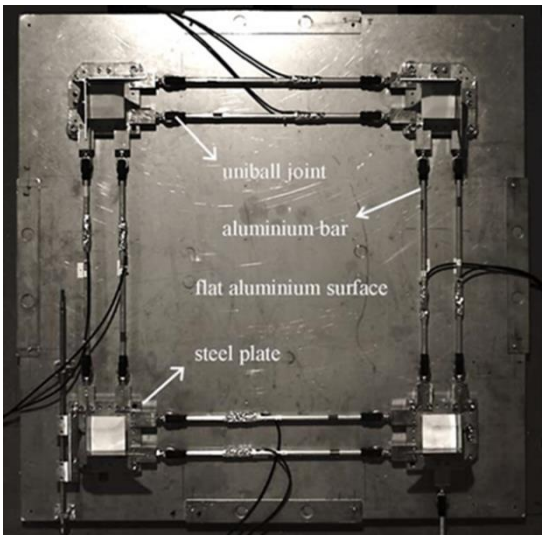

Figure 4-53. Testing device with movable frame to assign different displacement. (Rossi, 2015).

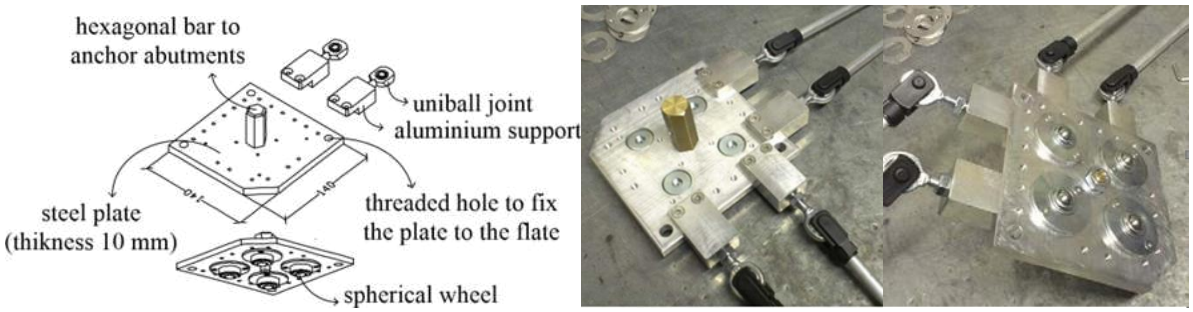

a. b. c.

Figure 4-54. Detail of Movable steel Plate: a. Sketch of the designed; b. extrados; c. intrados. (Rossi, 2015).

The software used to program and record the tests are *Dyna Tester V3*. During the quasi-static tests, the LVDTs used to monitor the displacements are by *RDP group* (Figure 4-55); in particular, LTDVs *232740* and *224140* have ± 5.0 mm of linear measuring length and 0.05% of accuracy. The forces were measured by load cells connected by a steel wire to the mechanical displacement actuator (Figure 4-56). Considering the low load needed by the vault tests, a hand crank winch was used as actuator, in fact, there is no hydraulic jack in the lab for the loads needed in this test. Moreover, a system of strain gauges measured the forces in the bars acting as tie-rods (*t0÷t7*); in particular, only the strain gauges inside the inner bar of the pairs have been utilized and calibrated i.e., *t1*, *t3*, *t5* and *t7*. Three cameras, placed one zenithal and the other two laterally and frontally with respect to the vault, recorded the development of the mechanisms up to collapse.

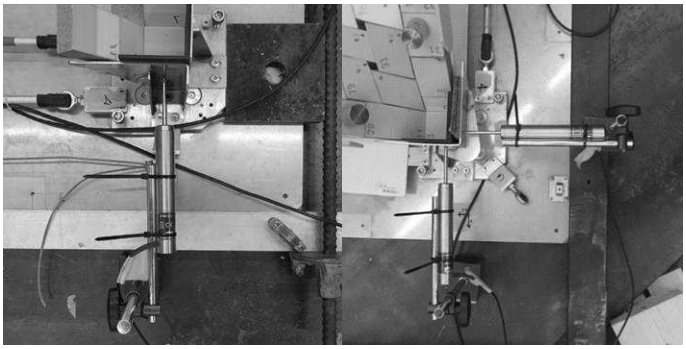

a. b.

Figure 4-55. LVDTs positioning: a. Test with simple shear; b. Test with pure, LVDTs shear placed in correspondence of the plate where displacement is applied.

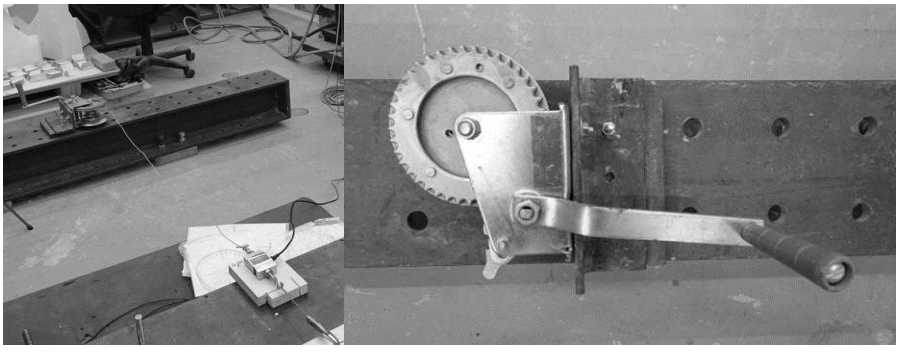

a. b.

Figure 4-56. System of Load cell-displacement actuator: a. Load cell. b. Manual/mechanic displacement actuator.

In order to apply the in-plane shear distortion, two different displacement arrangements were set-up.

In the first one –Test A–, two plates, *p1* and *p2*, were fixed to the aluminum surface while the other two, *p3* and *p4*, were left free (Figure 4-57). All the plates were tied by means of coupled bars (*t0÷t7*) so that in this way, the distance between the abutments remained unvaried and their rotation along the vertical axis was inhibited. The displacement, $u_{s,A}$, was assigned along the *p1-p3* direction by an external actuator connected to the plate *p3* by means of a tie to inhibit bending effects. In the second arrangement –Test B– (Figure 4-58), one plate only, *p2*, was fixed to the aluminum surface and the force the force $F_{s,B}$ was assigned along the diagonal direction; the displacements, $u_{s,B1}$ and $u_{s,B2}$, was measured by LVDTs placed orthogonally to *p3* plate. In this case too, all the plates were tied by means of coupled bars. The two shear mechanisms are rather equivalent; the difference is that in A the diagonals of the vaults rotate through angle β with respect to the plates, as can be described by Figure 4-59.

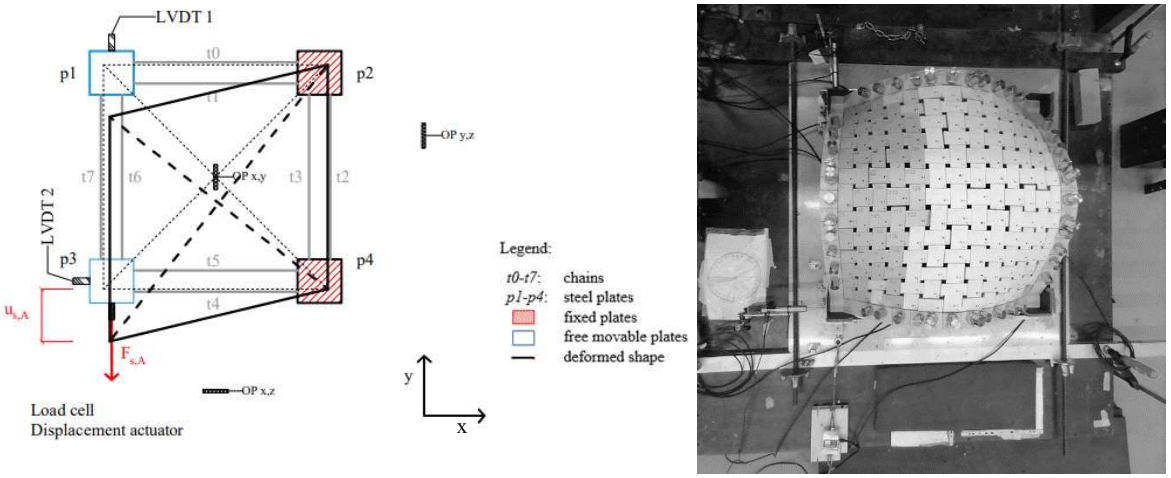

a. b.

Figure 4-57. Arrangements for Test A (simple shear): a. Designed drawing; b. Photograph.

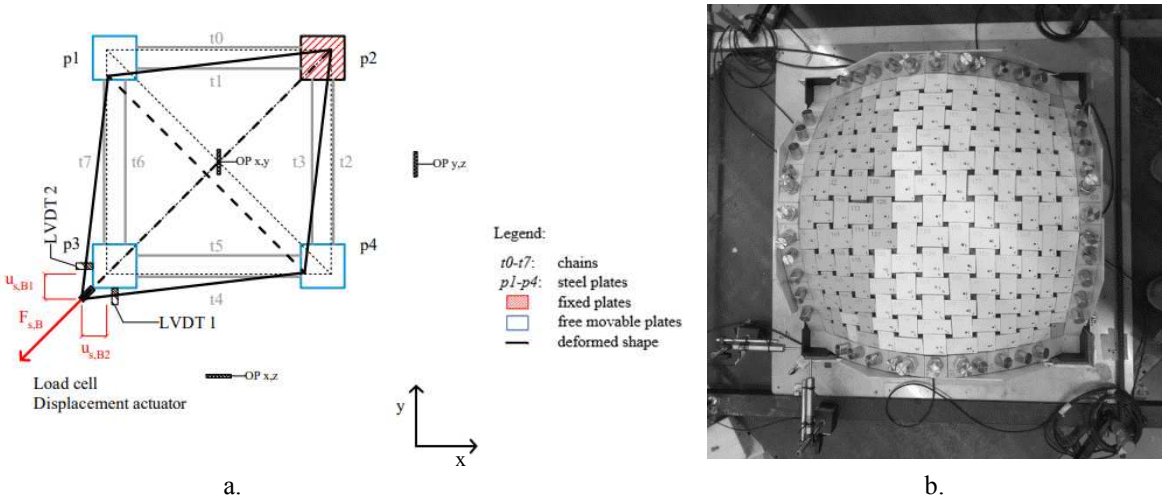

a. b.

Figure 4-58. Arrangements for Test B (pure shear): a. Designed drawing; b. Photograph.

The forces and displacements of set-up A and B are, therefore, comparable, and can be calculated by applying trigonometric formulas for which, knowing the inextensible sides and the measured displacements, it is possible to know the angle α_s in order to be able to estimate all the other data necessary for the comparison. In particular, for set-up A everything is known, for set-up B knowing $u_{s,B1}$ and $u_{s,B2}$ it is possible to identify the tangent of α_s and therefore the angle itself, to then apply the formulas shown in Figure 4-59, in order to find the vertical component of the force and the comparable displacement.

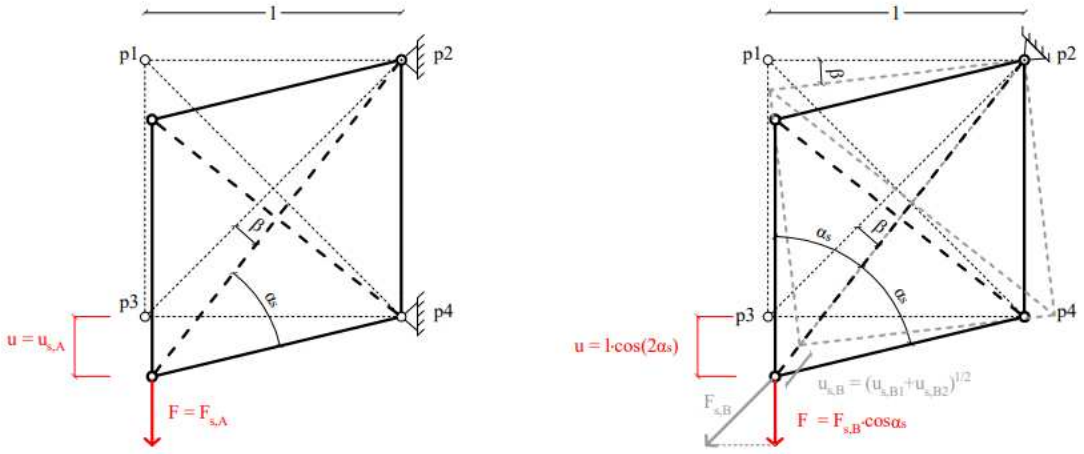

a. b.

Figure 4-59. Displacements and forces involved in the Test A (a) and Test B (b) mechanisms.

Below are two Time histories of Test A-3 as an example; one shows only the force applied by the actuator (Figure 4-60.a) the other also the forces registered by the tie-roads (Figure 4-60.b).

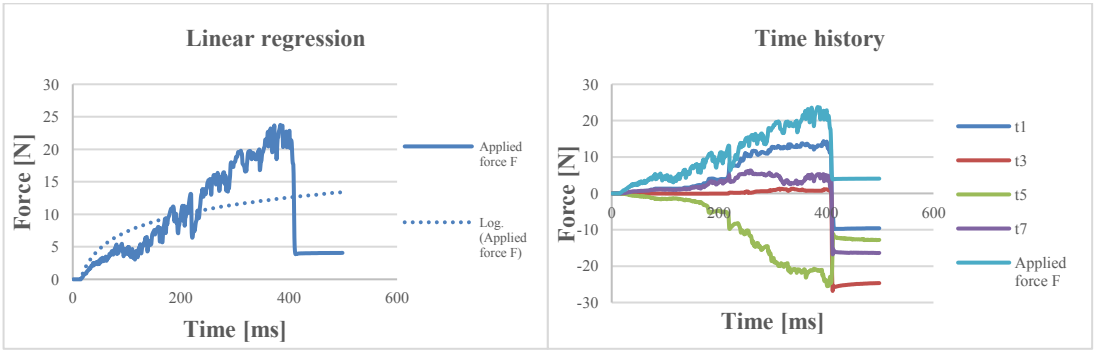

Figure 4-60. Time history with linear regression of Test A- 3: a. Applied Force with Linear regression (Log); b. Forces applied and recorded by tie roads (*t1, t3, t5* and *t7*).

4.4.1.2. Tests results

Six monotonic tests have been performed on the model to check displacement for Test A and five for Test B. The results in terms of damage mechanisms are summarized in Figure 4-61 and Figure 4-62, while those in terms of forces and displacements are shown in Figure 4-63. With respect to damage mechanisms, it can be observed that for this particular kind of vault, and probably also for the apported adjustments § 4.3.2., the collapse occurs due to the fall of one ashlar

placed near an abutment and the loss of connection between other adjacent ones; this generates a thrust on the two confinement arches –corresponding to the abutment of the quadrant involved– and the collapse of the two arches due to an out-of-plane mechanism. The collapse therefore occurs for a lack of equilibrium due to the thrust of the "dome", which corresponds to loads with a horizontal component. These generate the out-of-plane of the entire arches with a rigid rocking mechanism after the creation of hinges at the height of the screw back. Only in few tests the generation of “four hinges mechanism” was clearly visible in the confinement arches, maybe due to the not high-frame cameras, because the arch fails are characterized by a sudden collapse. From Figure 4-61, a view from the zenith, the collapse sequence of the vault can also be assessed. The collapse started most frequently by the arches in correspondence of *t1* and *t7*, but in same tests the arches changes and this highlights the imperfect assemblage and the not symmetry of the shear mechanism reproduced in the tests.

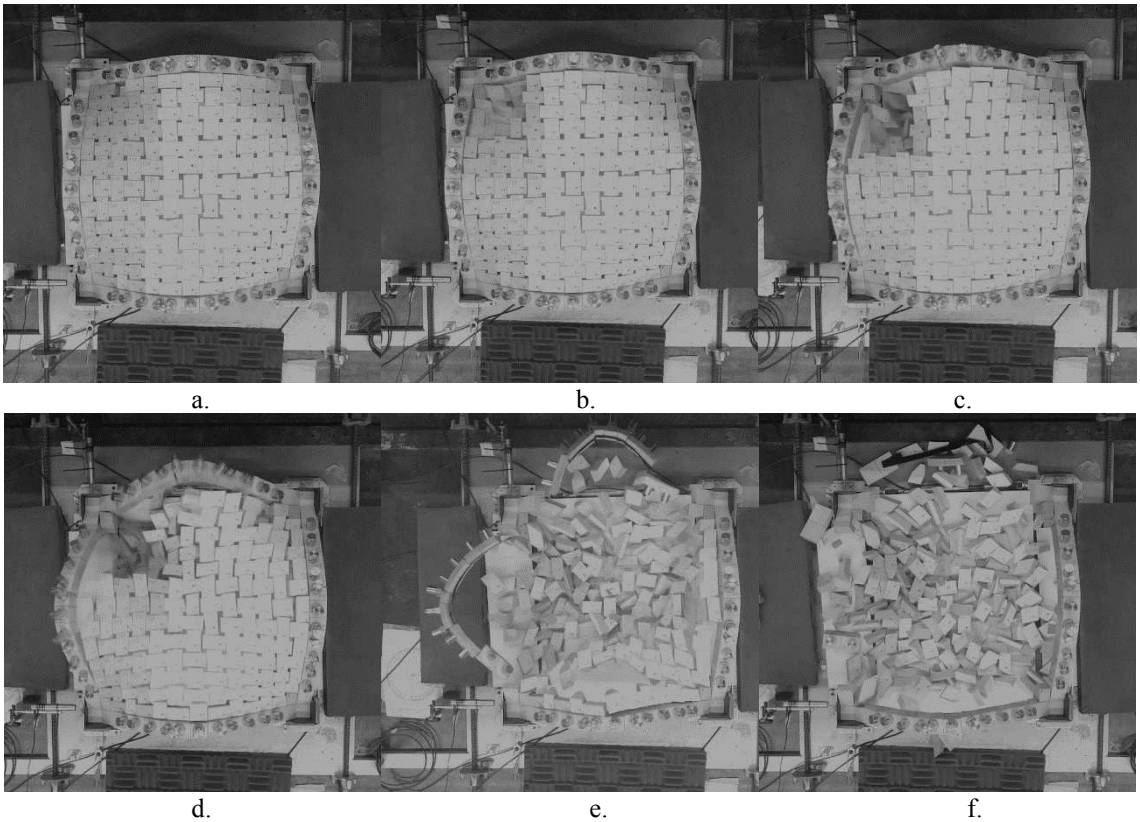

Figure 4-61. Crack damage on the extrados of the vault in mechanism A-B: zenithal view (Test A - 4).

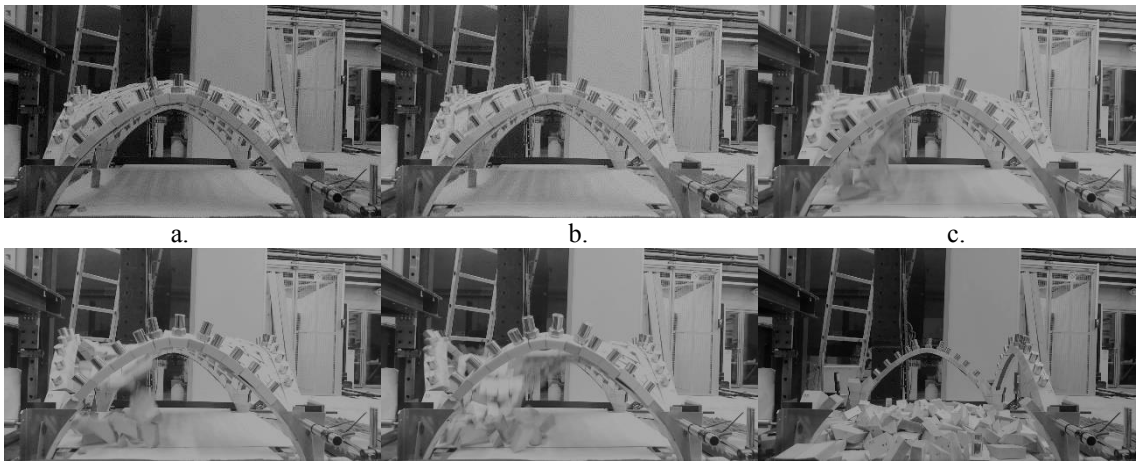

a. b. c.

d. e. f.

Figure 4-62. Crack damage on the extrados of the vault in mechanism A-B: lateral view in front of *t7* (Test A - 4).

Figure 4-63 shows the force/displacement curves for every performed shear test, it can be observed that the value of maximum force (F) varies approximately from 11.0÷16.6% of the total weight; in particular for the set-up A from 11.7÷16.6% while for set-up B from 11.0÷16.3% as demonstrated by Table 4-16 and Table 4-17. Instead, the a-dimensional displacement maximum value (also known as *Distortion* or *Drift*) is in the range 2.4÷4.6% of the vault span; in particular, for the set-up A the drift is from 2.7÷4.6% while for set-up B from 2.4÷3.4% as demonstrated by Table 4-18 and

Table 4-19. Moreover, it can be observed that the system has a non-linear and ductile response. During the tests the damage mechanisms have been observed at the achievement of maximum strength and shortly after the collapse occurred. With respect to the two different set-ups, a slightly difference is involved regarding the ductility of the system. The lower ductility of the set-up B may be caused by the slight increase in damage in the corner close to the abutment (plate *p3*) where the displacement was applied. It is worth noting that the measured values are comparable with works carried out with similar set-ups and methods, albeit on different types of vaults (cross vault (Rossi, 2015; Rossi et al., 2016)).

Table 4-16. Results of the shear tests with set-up A in terms of a-dimensional strength capacity *F/W* (%).

Test A - 1	Test A - 2	Test A - 3	Test A - 4	Test A - 5	Test A - 6	**Average TA**
11.68%	16.64%	15.53%	13.99%	15.71%	13.16%	**14.45%**
Standard Deviation						
1.85						
Coefficient of Variation						
0.13						

Table 4-17. Results of the shear tests with set-up B in terms of a-dimensional strength capacity *F/W* (%).

Test B - 1	Test B - 2	Test B - 3	Test B - 4	Test B - 5	**Average TB**
16.26%	13.80%	14.27%	13.97%	11.03%	**13.86%**
Standard Deviation					
1.87					

Coefficient of Variation
0.13

Table 4-18. Results of the shear tests with set-up A in terms of a-dimensional ultimate displacement *u/l* (%).

Test A - 1	Test A - 2	Test A - 3	Test A - 4	Test A - 5	Test A - 6	**Average TA**
2.87%	4.59%	2.93%	2.83%	3.67%	2.66%	**3.26%**
Standard Deviation						
0.74						
Coefficient of Variation						
0.23						

Table 4-19. Results of the shear tests with set-up B in terms of a-dimensional ultimate displacement *u/l* (%).

Test B - 1	Test B - 2	Test B - 3	Test B - 4	Test B - 5	**Average TB**
3.43%	2.58%	3.03%	2.41%	2.73%	**2.84%**
Standard Deviation					
0.40					
Coefficient of Variation					
0.14					

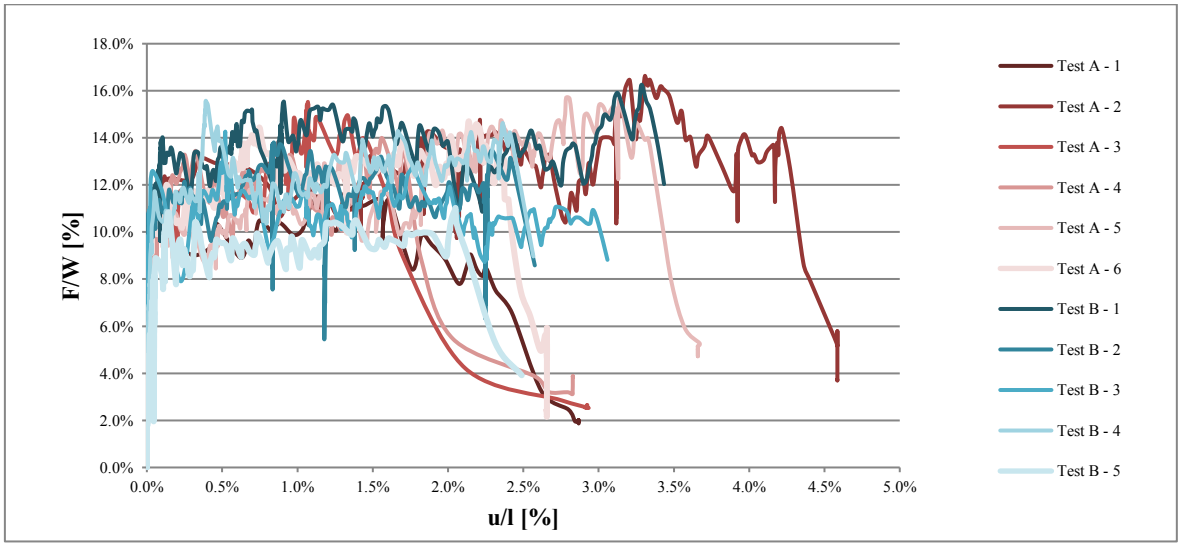

Figure 4-63. Results of the shear monotonic tests in terms of force- displacement curves.

In Figure 4-64 for Test A and Figure 4-65 for test B the variation of the overall forces (*dF*) acting on one of the four tie-rods pairs connecting the piers is shown. It has been calculated by adding up the force measured in the four bars *t1, t3, t5* and *t7*, net of its initial value. In general, it can be observed that the force evolution in all the pairs of tie-rods is rather similar, and that it leads to an increment of approximately 6.0 % for the set-up A and 3.6% for the set-up B, as shown by Table 4-20 and

Table 4-21. This increase is related to the increment of vault loads on the plate *p3* in the damage process. The couple *t5* for the Tests A had a different trend, this was subjected to compression due to the thrust of the *t7* arranged along the direction of the displacement actuator.

Table 4-20. Results in Test A of the a-dimensional strength capacity dF/W (%) for each tie-roads

Test A - 1	Test A - 2	Test A - 3	Test A - 4	Test A - 5	Test A - 6	**Average Test A**
			t1			
4.24%	8.48%	9.40%	6.03%	10.01%	8.85%	**7.84%**
			Standard Deviation			
			2.23			
			Coefficient of Variation			
			0.28			
			t5			
-23.11%	-17.96%	-16.69%	-15.16%	-25.53%	-13.73%	**-18.70%**
			Standard Deviation			
			4.64			
			Coefficient of Variation			
			0.25			
			t7			
2.62%	5.60%	4.13%	4.24%	4.87%	4.02%	**4.25%**
			Standard Deviation			
			0.99			
			Coefficient of Variation			
			0.23			

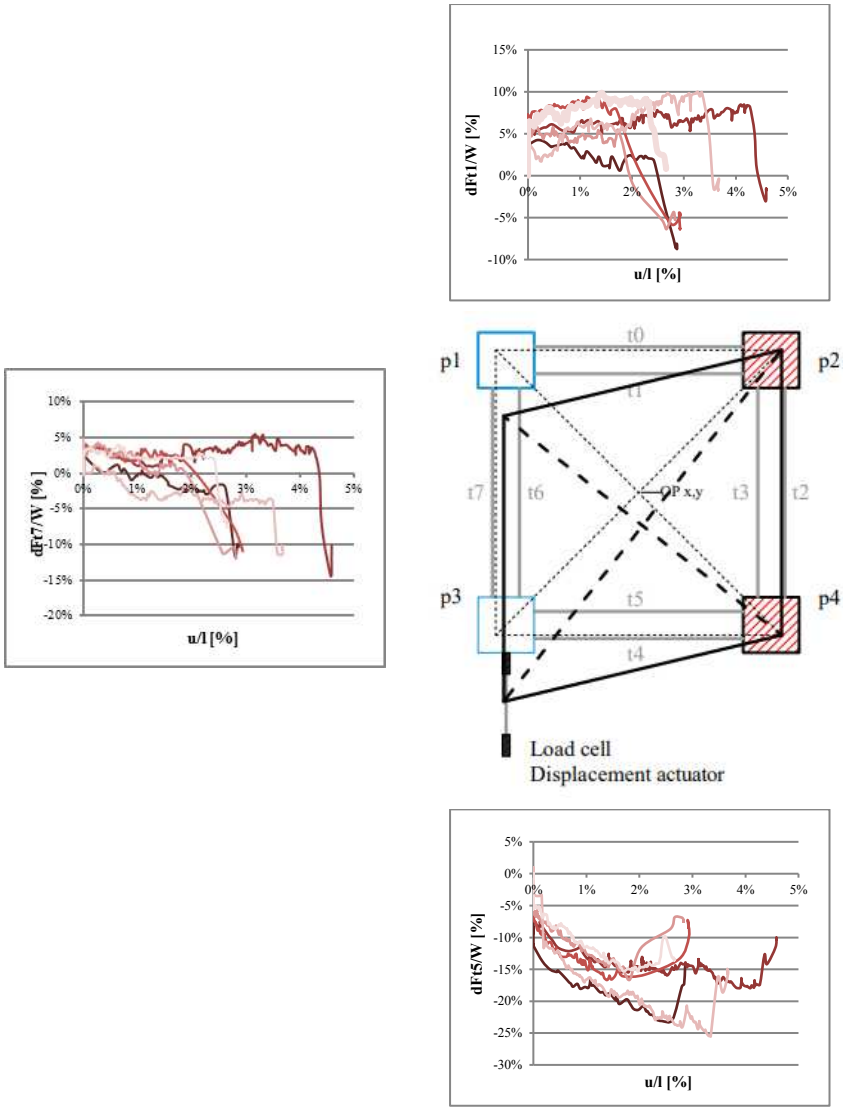

Figure 4-64. Forces in the tie-rods in one of the Tests A.

Table 4-21. Results in Test B of the a-dimensional maximum strength capacity *dF/W* (%) for each tie-roads.

Test B - 1	Test B - 2	Test B - 3	Test B - 4	Test B - 5	**Average dF**
t1					
4.00%	2.62%	5.39%	4.00%	5.17%	**4.24%**
Standard Deviation					
1.11					
Coefficient of Variation					
0.26					
t3					
5.40%	6.49%	2.48%	3.76%	8.15%	**5.26%**
Standard Deviation					
2.23					
Coefficient of Variation					
0.42					

t5					
1.99%	2.84%	4.44%	5.15%	4.02%	**3.69%**
Standard Deviation					
1.27					
Coefficient of Variation					
0.34					
t7					
5.74%	3.32%	4.91%	5.37%	3.94%	**4.66%**
Standard Deviation					
1.00					
Coefficient of Variation					
0.22					

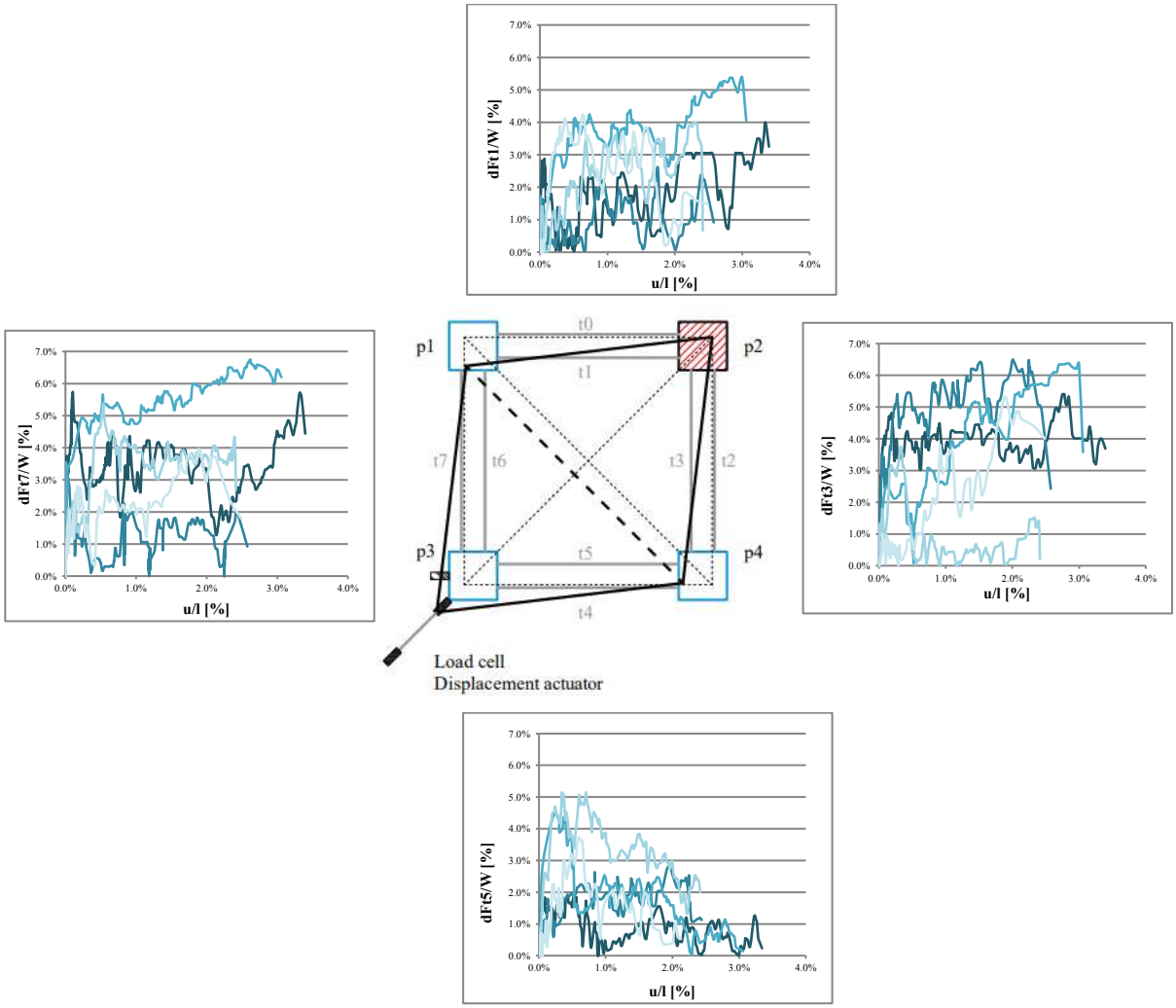

Figure 4-65. Forces in the tie-rods in the Tests B.

4.4.2. Direct Seismic Action (DSA)

In scale models, quasi-static tests are usually considered more reliable than dynamic ones, since the behaviour due to the latter type of action depends significantly on the dimensions and mass

of the model, for this reason, having to investigate the dynamic load case it was decided to use the Direct Seismic Action methodology with tilting test compared to shaking table tests.
In fact, dealing with rigid block systems, the tilting test is a first-order seismic assessment method to evaluate the collapse mechanism and the corresponding Horizontal Load Multiplier λ, ratio between horizontal and vertical acceleration. In particular, this is the fraction of the gravity acceleration necessary to transform the "arch" in a Single Degree of Freedom (SDOF) System (Ochsendorf, 2002). Being based on a quasi-static method, it assumes an effectively infinite loading duration so is unable to effectively capture the structural dynamics as it neglects that the earthquake accelerations are limited in time and variable in magnitude and direction. However, it provides a measure of the horizontal load that the structure can support before collapse.
Taking into consideration a single block with rectangular section, subject to its own weight, the line of thrust is in the vertical direction passing through the center of mass; the collapse due to overturning will occur as soon as the inclination of the base exceeds the critical angle α_{cr} (Figure 4-66), i.e. the angle through which the line of thrust reaches one of the base edges. Considering these theoretical concepts, in order to identify the acceleration value at which the mechanism is activated, a tilting test was carried out by rotating the support surface of the entire system, in this case the base of the vault.

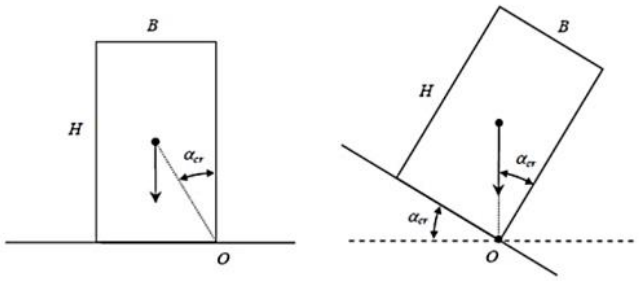

Figure 4-66. Rotation Rigid block rotation due to horizontal seismic acceleration.

So finally, the Tilting DSA testing leads to evaluate the seismic loads through the simulation of horizontal inertial force proportional to the mass of the structure. The proportionality constant at collapse gives the value of the force that produces vault failure and allows to estimate Horizontal Load Multiplier λ, the tangent of the collapse angle α. Since the seismic actions can hit the structure from any direction, the vault response has been investigated considering a significant sample of forces acting in different angles (0÷135°) also evaluating the imperfect double symmetry (the ashlars that compose the two diagonals are not equal).
The aims of the test campaign are the determination of the ultimate strength capacity of the vault in different directions to obtain the resistance domain of the vault and the evaluation of its three-dimensional damage mechanisms, as other studies had conducted (Alforno et al., 2021; Cangi, 2005; G. Milani et al., 2016; Quinonez et al., 2010; Restrepo Vélez et al., 2014; Rossi et al., 2015, 2016; Shapiro, 2012)

4.4.2.1. Set-up

The tilting table of IBS-Lab (University of Minho) is composed of a steel plate of 10mm-

thickness of dimensions 1.5x1.5 m^2 (Figure 4-67), it is already used in other research and project (Colombo et al., 2021; STAND4Heritage funded by EU Project, 2020). The table is welded to several IPE80 steel profiles, that are distributed to increase the global stiffness of the table and reduce its deformation. The tilting table is supported by two large steel beams in the opposite sides, one of these is connected to table through four steel hinges which allow the table to be locked while allowing rotation and therefore tilting tests (Figure 4-67). At the other end, the plate presents holes and an eye bolt where fix a steel chain to raise the table. The chain passes through tackle pulley fixed to a classical testing steel frame; the raising load is manual.

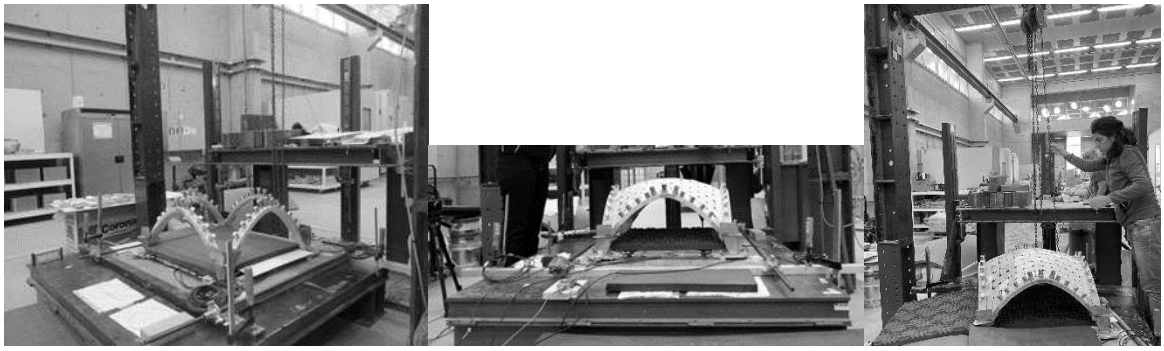

a. b. c.

Figure 4-67. Set-up DSA Test: a. The tilting table; b. Detail of the hinges; c. System chain plus tackle pulley.

Once the value of the angle (Φ) used to perform the specific test was manually set, the plywood panel where the vault lay is completely fixed to the table by means of clamps (Figure 4-68).
During the tests, the angle of rotation (α) of the tilting desk were monitored by means of a Magnetic Digital Level, block to the tilting plate. In particular, the table was raised until the collapse of the scale model of the vault occurred, and the angle of the table was measured at the beginning and end of the test, the first to check the flatness of the set-up, while the second to estimate the value of the Horizontal Load Multiplier λ, equal to the arctangent of the angle in radiant.
As in ISA set-up, three cameras were placed one at the zenith and two laterally to record the development of the mechanisms up to collapse.

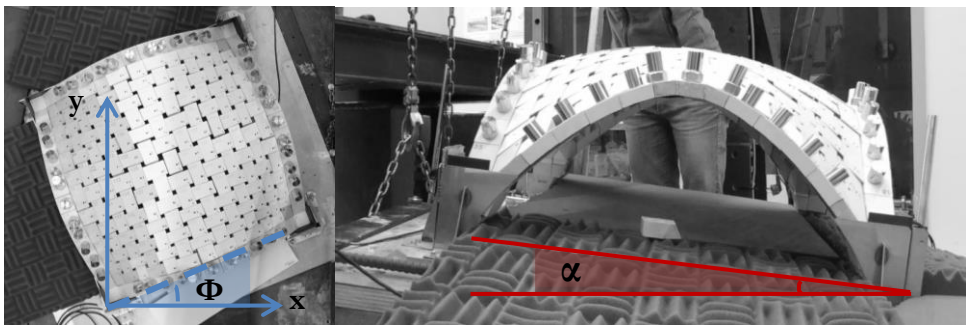

a. b.

Figure 4-68. Angle of rotation of the vault plane: a. Φ around the reference corner p3 b. α around the axis of rotation of the desk.

Six different tests were set-up, varying their in-plane angle Φ; in particular the angles are equal to: 0°, 22.5°, 45°, 90°, 112.5° and 135° (Figure 4-69). For each angle Φ three tests were performed. The choice of angles is due to obtain a significant variety of possibilities considering that the two axes of symmetry of the vault do not correspond to a joint but pass on the median of ashlars all different from each other, this geometry therefore does not allow to have two axes of symmetry equal due to the stereotomy of the ashlars themselves. For this reason, it was decided to have at least one intermediate angle between 0° and 45° and performing it on vault quarter with different patterns. Moreover, previous studies (G. Milani et al., 2016; Rossi et al., 2016) have led to the understanding that in symmetric structure there are no significant differences between the same mirror angles with respect to the 45° directrix (e.g., 22.5° and 67.5°).

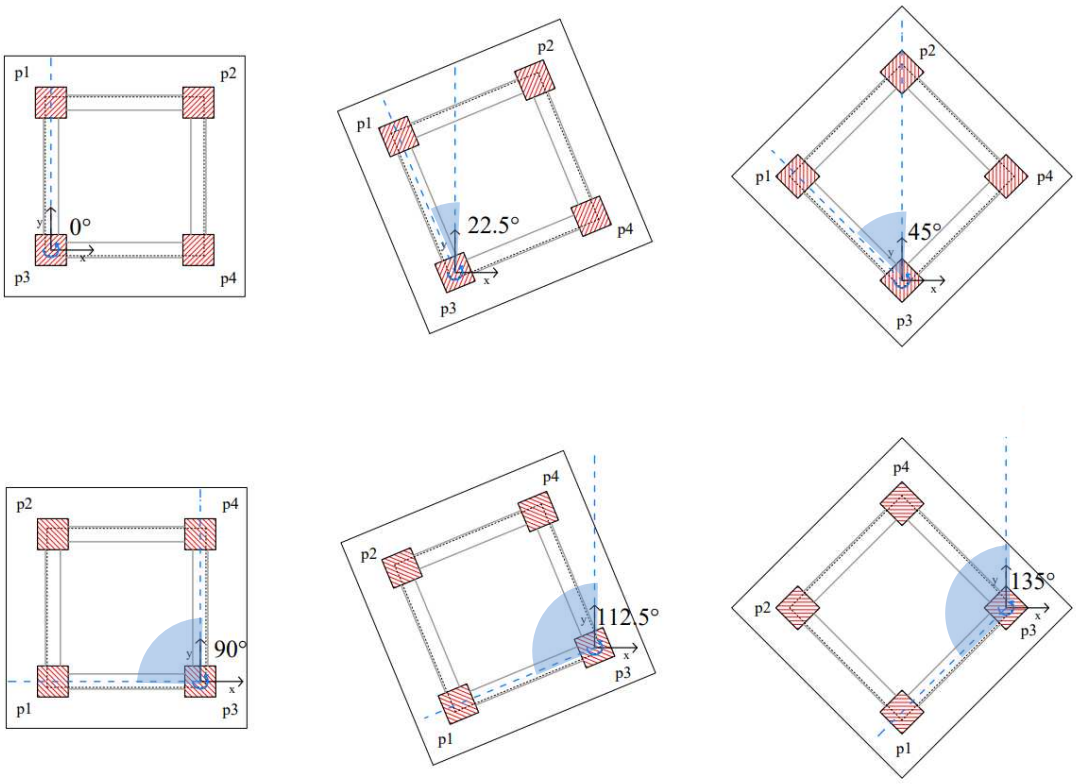

Figure 4-69. The angular settings considered in DSA tests.

4.4.2.2. Test results

Regarding the results in terms of 3D mechanisms, the typical damage patterns development seen from both the zenithal and the lateral views of the vault are illustrated from Figure 4-70 to Figure 4-85. The collapse mechanism was a very sudden phenomena in each test and for some of those it was not always captured by all the cameras for problems caused by the cameras themselves (incorrect framing, recording problems, etc.). The most common initial collapse behaviour in all the tests started with the failure/lowering of the keystone (negative displacement); this mechanism leaded a load by the vault ashlars in correspondence with the keystones of the confinement arches, since the vault ashlars was arranged geometrically in orthogonal rows and are configured

as contrasted blocks of a bidirectional spatial plate. For this reason, if the vault keystone was subject to a failure, the rows interested by this displacement was the central ones, those in correspondence with the arch keystones. The orthogonal forces due to the vault ashlars just described leads to an out-of-plane collapse mechanism of the arches (generally two, sometimes three). The collapse of the arches in turn leads to the lack of confinement of the structure and the immediate collapse of the whole vault which starts from the blocks placed near the vault keystone, and then involves the remaining ones due to the lack of contrast and interlocking between the blocks themselves. It is interesting to note how, immediately after the collapse of the first two arches, an opening of joints always occurred in correspondence with the second row of vault ashlars from the arches and not in correspondence with the ashlars in contrast with the arches themselves, this can also be seen in some tests where in correspondence with the arches that not collapse, the whole first row of vault ashlars remains connected to the arch and not fall down also thanks to guaranteed mutual contrast (i.e. the second test of $\Phi = 112.5°$ Figure 4-82).

Only in two cases, in addition to the displacement of the vault keystone, always present, the fall of a perimeter block occurred before the collapse of the central part of the vault (the third test with $\Phi = 90°$ and second one with $\Phi = 112.5°$).

Figure 4-70, Figure 4-71 and Figure 4-72 show the development of the cracking pattern for the $\Phi = 0°$; the test chosen as an example is the second one. The mechanism occurred is that already described, the arches collapsed first are *p3-p4* and *p2-p4*.

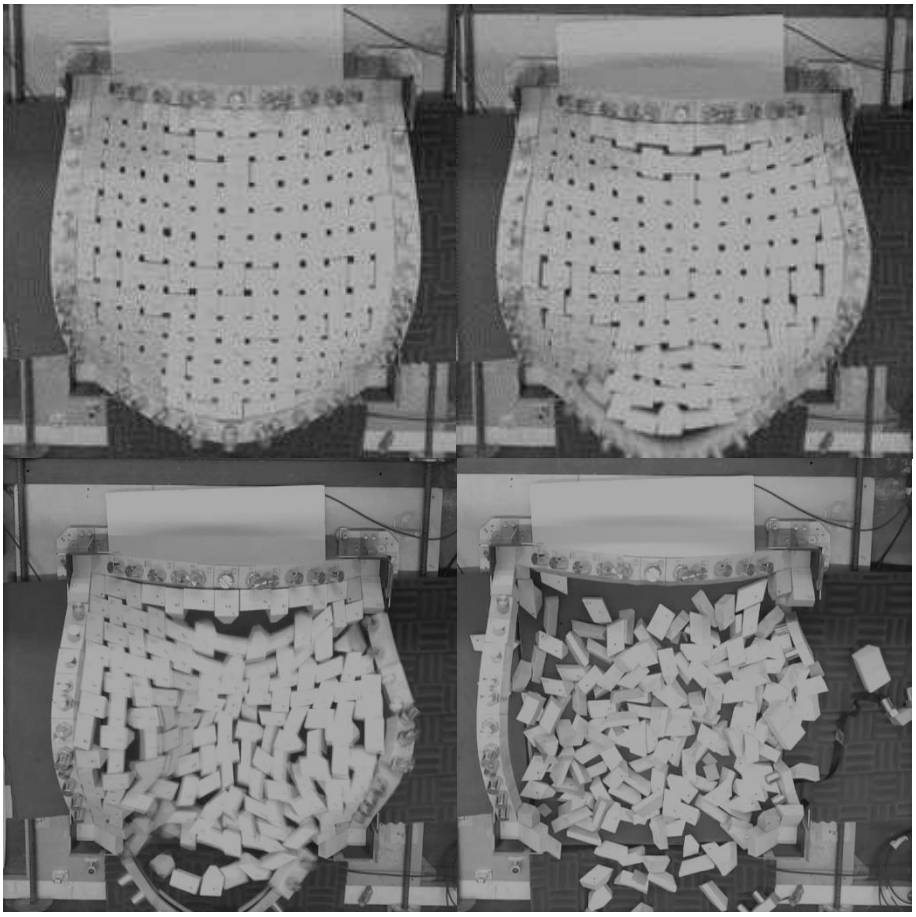

Figure 4-70. Damage results of the tilting tests with $\Phi = 0°$: damage evolution in the zenith view.

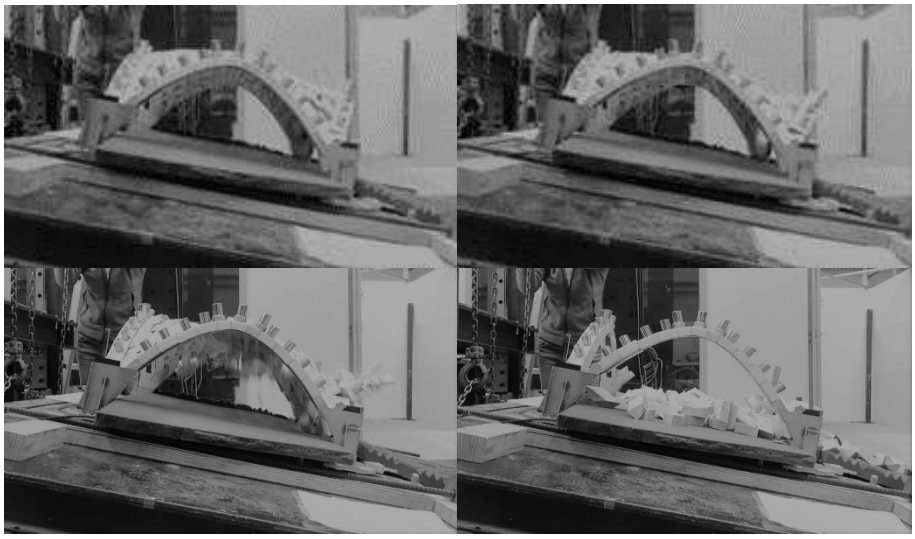

Figure 4-71. Damage results of the tilting tests with Φ = 0°: damage evolution in the lateral view (*p1-p3*).

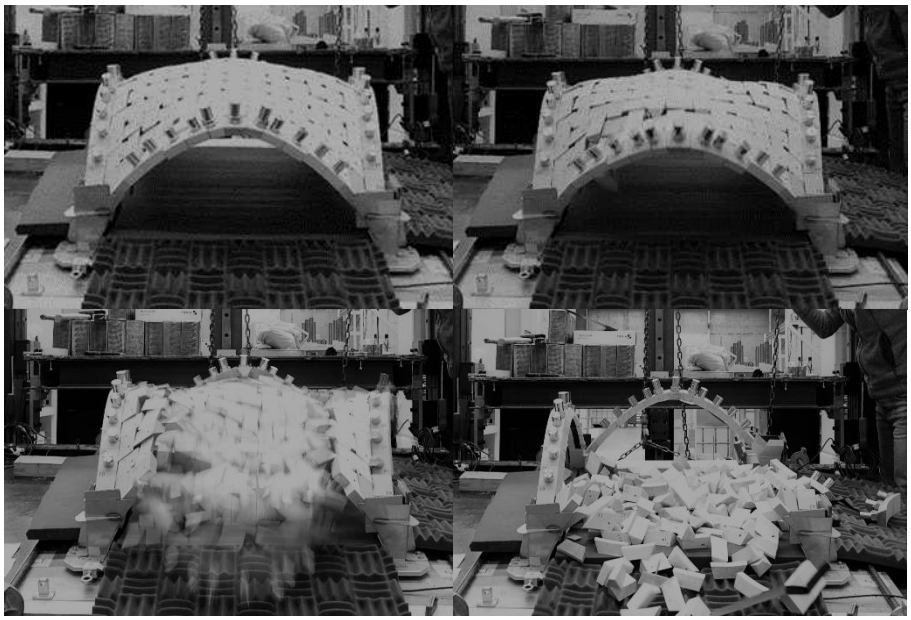

Figure 4-72. Damage results of the tilting tests with Φ = 0°: damage evolution in the frontal view *(p3-p4*).

Figure 4-73 and Figure 4-74 show the development of the cracking pattern for the Φ = 22.5°; the test chosen as an example is the second one. Figures of frontal view does not exist for a camera malfunction during these tests. The mechanism occurred is that already described, but in lateral view it can be observed that the out-of-plane of the arches *–p3-p4* and *p1-p3–* mainly involves the three upper macro-ashlars of the same.

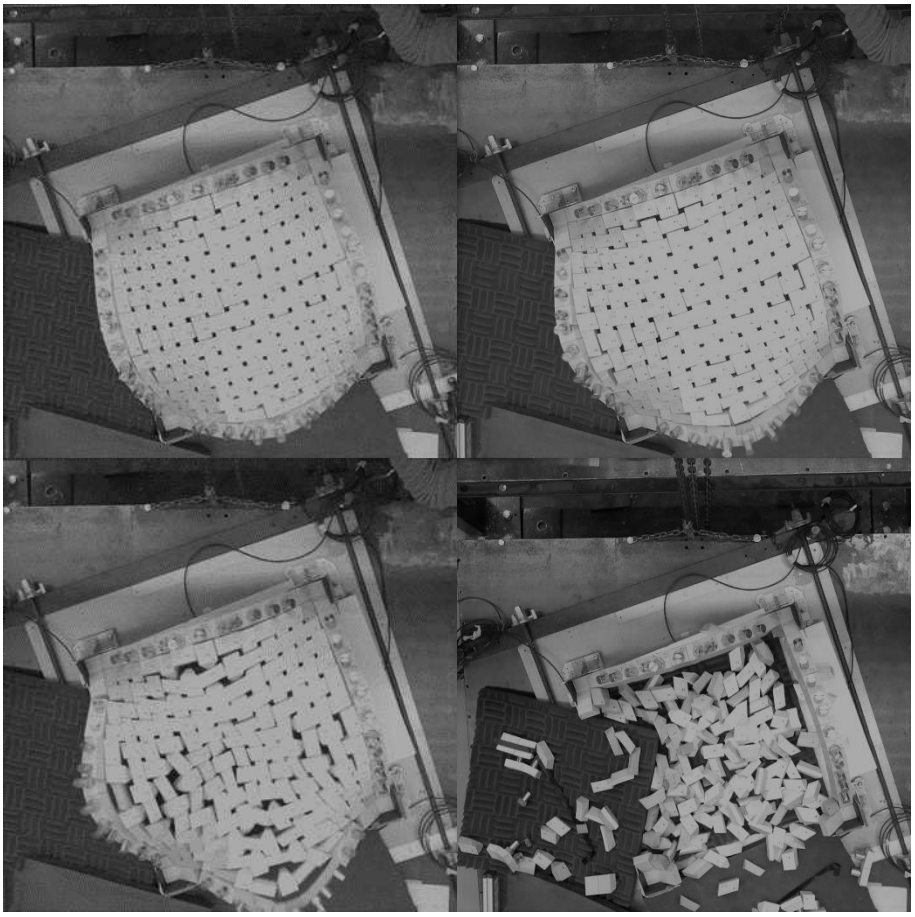

Figure 4-73. Damage results of the tilting tests with Φ = 22.5°: damage evolution in the zenith view.

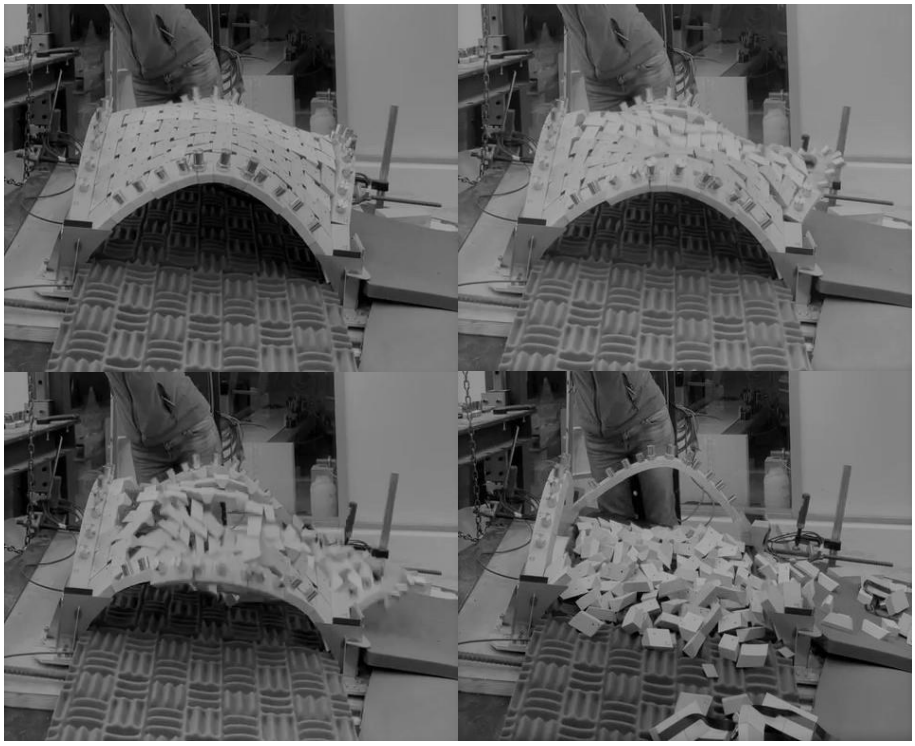

Figure 4-74. Damage results of the tilting tests with Φ = 22.5°: damage evolution in the lateral view (*p1-p3*).

From Figure 4-75 to Figure 4-77 the development of the cracking pattern for the Φ = 45° is shown; the test chosen as an example is the second one. The mechanism identified is that already

described, in this case the collapsed arches were *p3-p4* and *p1-p3*, but in frontal view it can be observed that in the perimetral rows of the vaults –those ones that was in contact with the arches that did not collapse– a four-hinge mechanism occurred (Figure 4-78).

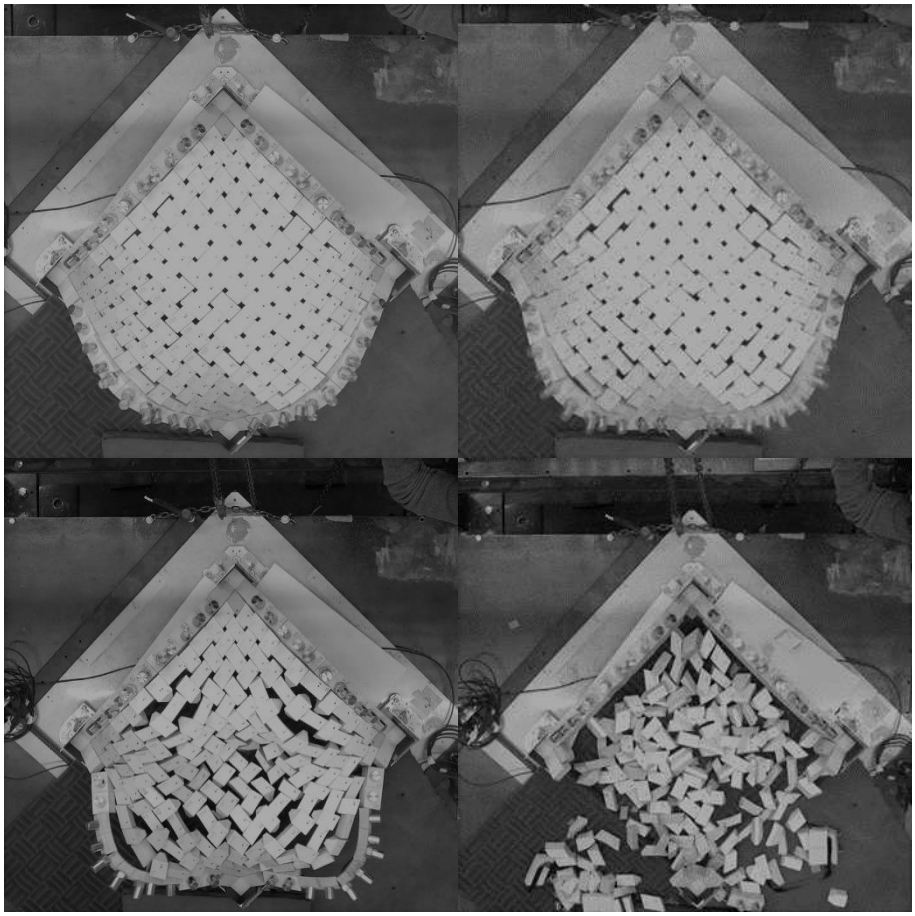

Figure 4-75. Damage results of the tilting tests with Φ = 45°: damage evolution in the zenith view.

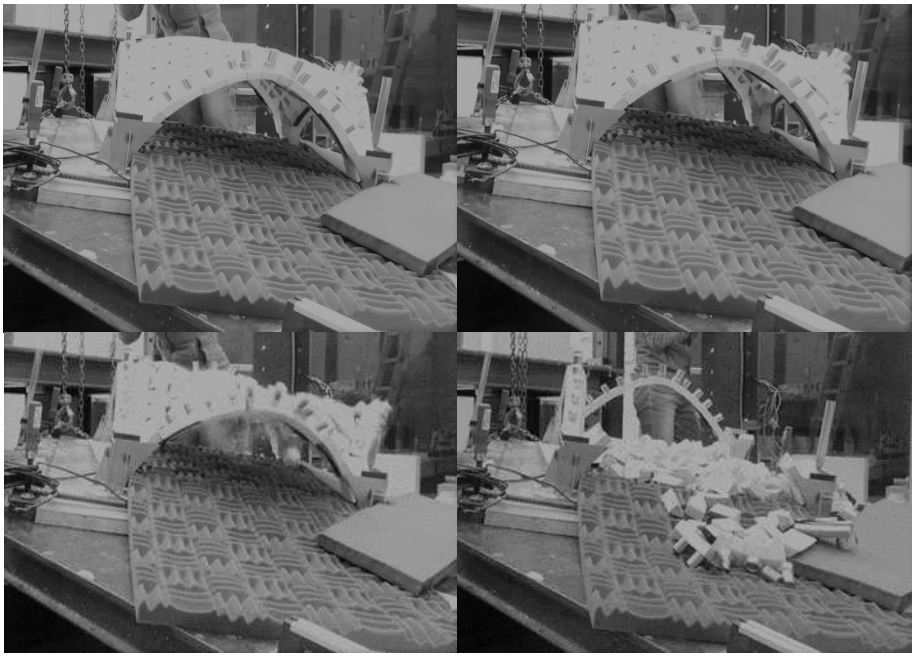

Figure 4-76. Damage results of the tilting tests with Φ = 45°: damage evolution in the lateral view (*p1-p3*).

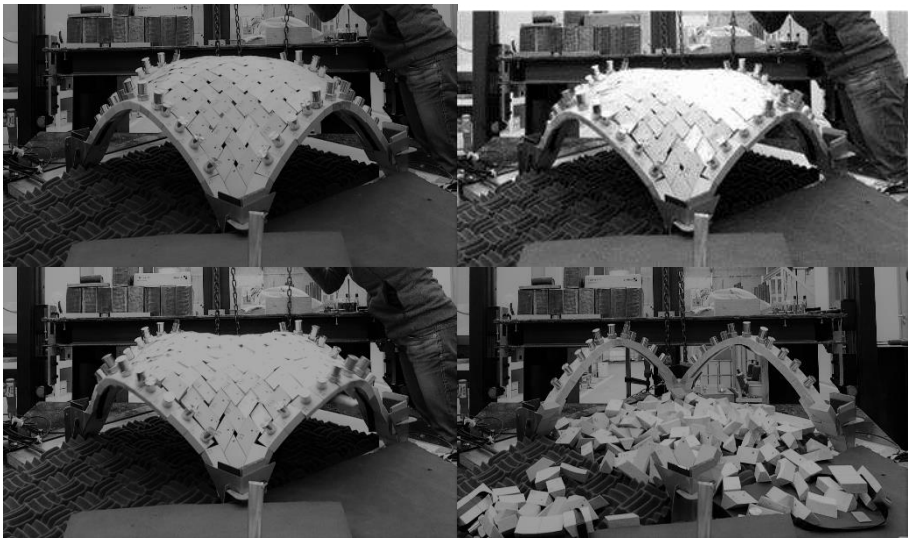

Figure 4-77. Damage results of the tilting tests with Φ = 45°: damage evolution in the frontal view.

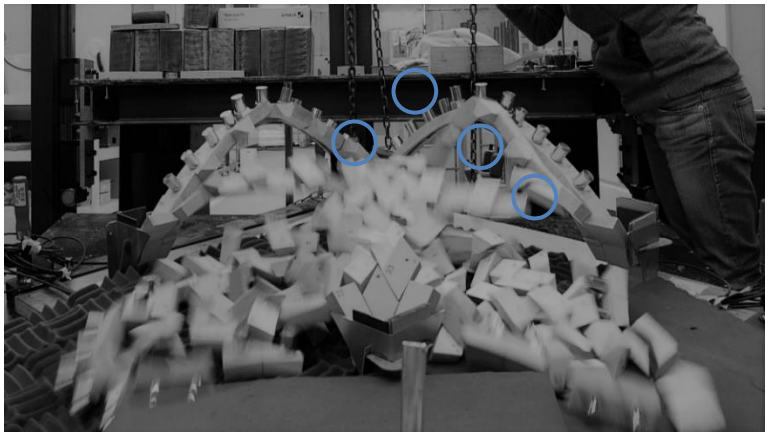

Figure 4-78 Damage results of the tilting tests with Φ = 45° (frontal view): detail of four hinge of the perimetral vault row.

From Figure 4-79 to Figure 4-81 the development of the cracking pattern for the Φ = 90° is shown; the test chosen as an example is the first one. The mechanism occurred is that already described (collapsed arches *p1-p3* and *p1-p2*). Unfortunately, the zenith camera was not positioned correctly during these three tests and the images are slightly cropped.

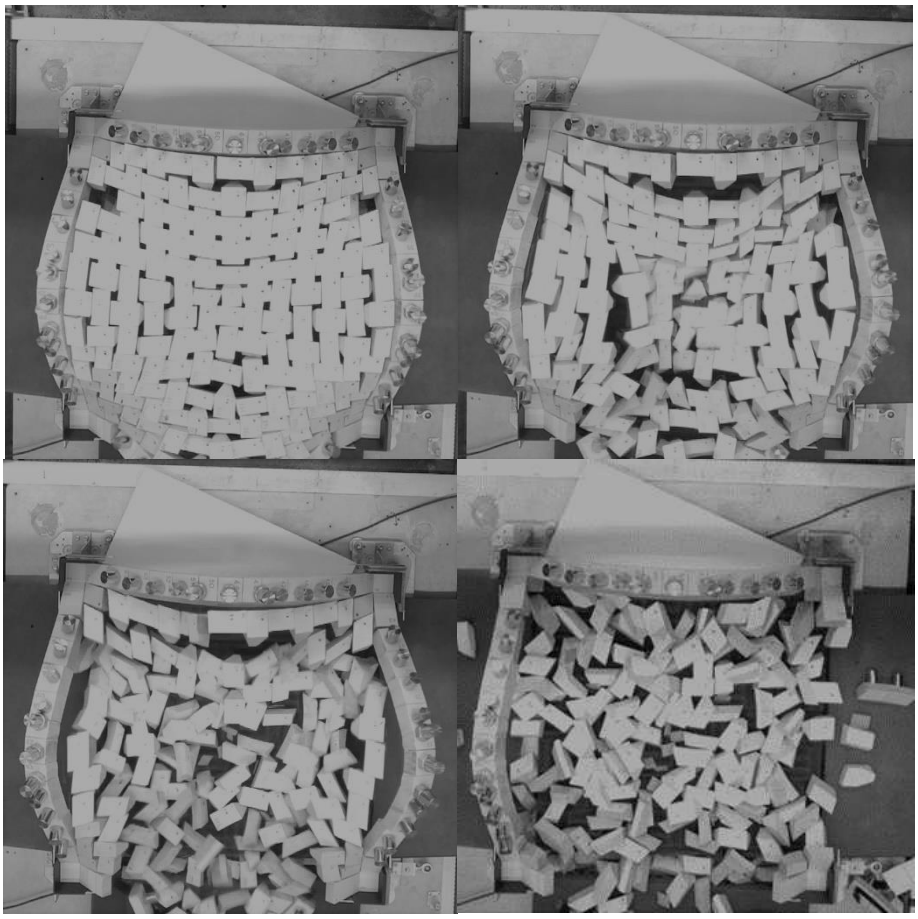

Figure 4-79. Damage results of the tilting tests with Φ = 90°: damage evolution in the zenith view.

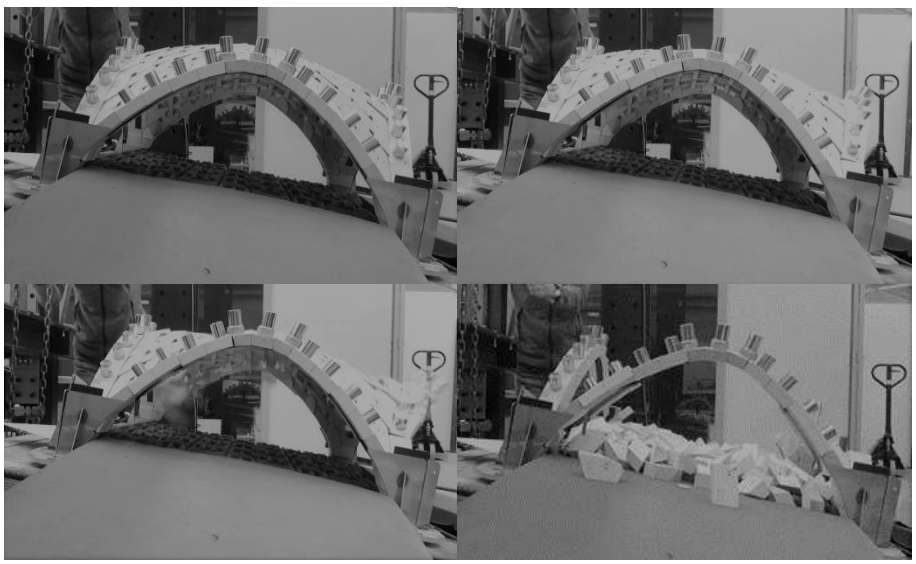

Figure 4-80. Damage results of the tilting tests with Φ = 90°: damage evolution in the lateral view (*p1-p2*).

Figure 4-81. Damage results of the tilting tests with Φ = 90°: damage evolution in the frontal view (*p1-p3*).

From Figure 4-82 to Figure 4-84 the development of a particular cracking pattern for the Φ = 112.5° was shown; the test chosen is the second one. This case is a particular one because, in addition to the vault keystone fail, one perimetral ashlar fell down as visible by figures. So, the mechanism is a little bit different, the out-of-plane of the arch *p1-p3* always occurred but the vault started to collapse from the quarter where this ashlar fails due to the lack of compression; therefore in the adjacent arch of confinement *p1-p2* a four-hinge mechanism took place (Figure 4-83). At the end of this test, the whole first row of vault ashlars remains connected to the arch (*p3-p4*) and not fail also thanks to guarantee mutual contrast.

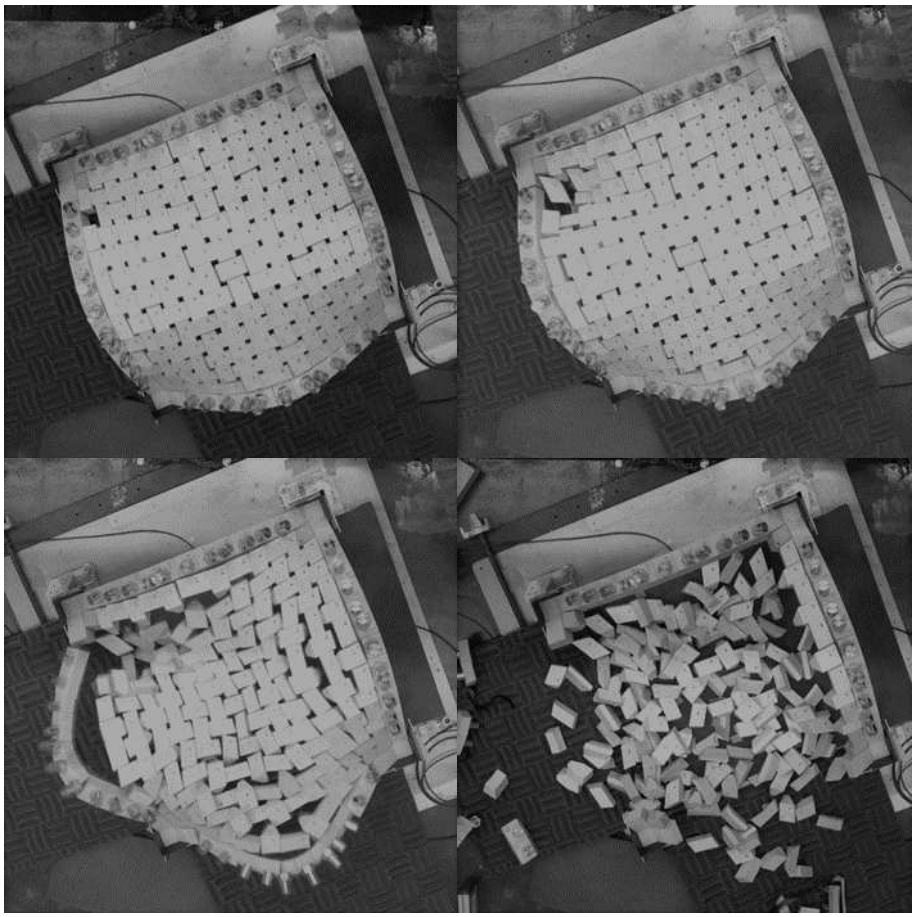

Figure 4-82. Damage results of the tilting tests with Φ = 112.5°: damage evolution in the zenith view.

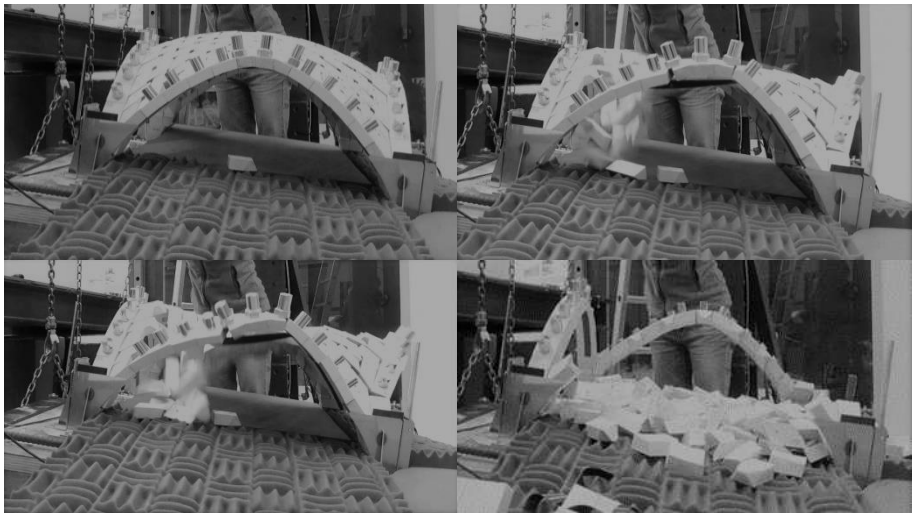

Figure 4-83. Damage results of the tilting tests with Φ = 112.5°: damage evolution in the lateral view (*p1-p2*).

Figure 4-84. Damage results of the tilting tests with Φ = 112.5°: damage evolution in the frontal view (*p1-p3*).

Figure 4-85 and Figure 4-86 show the development of the cracking pattern for the Φ=135°; the test chosen is the first one. Figures of frontal view does not exist for a camera malfunction during these tests. The mechanism occurred is that already described –in this case the first collapsed arches were *p1-p3* and *p1-p2*– but in lateral view it can be observed that the out-of-plane of the arch mainly involves the three upper macro-ashlars of the same.

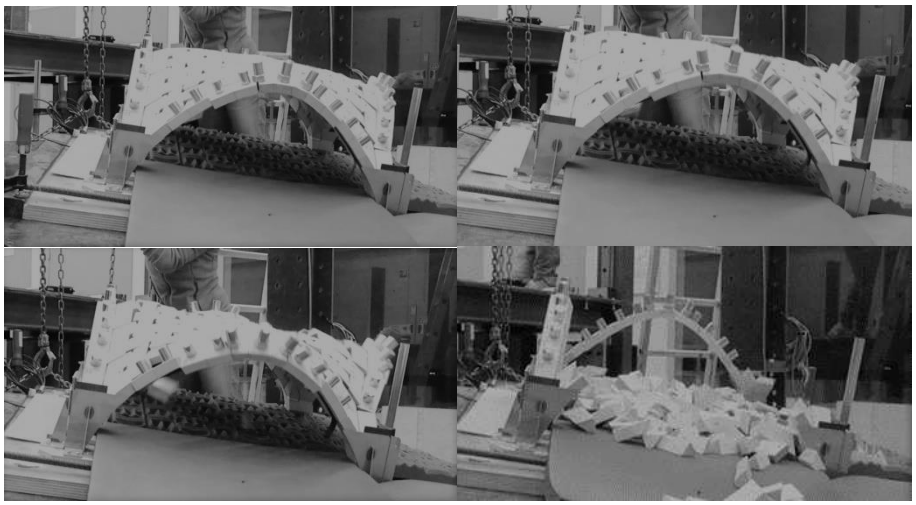

Figure 4-85. Damage results of the tilting tests with Φ = 135°: damage evolution in the lateral view (*p1-p2*).

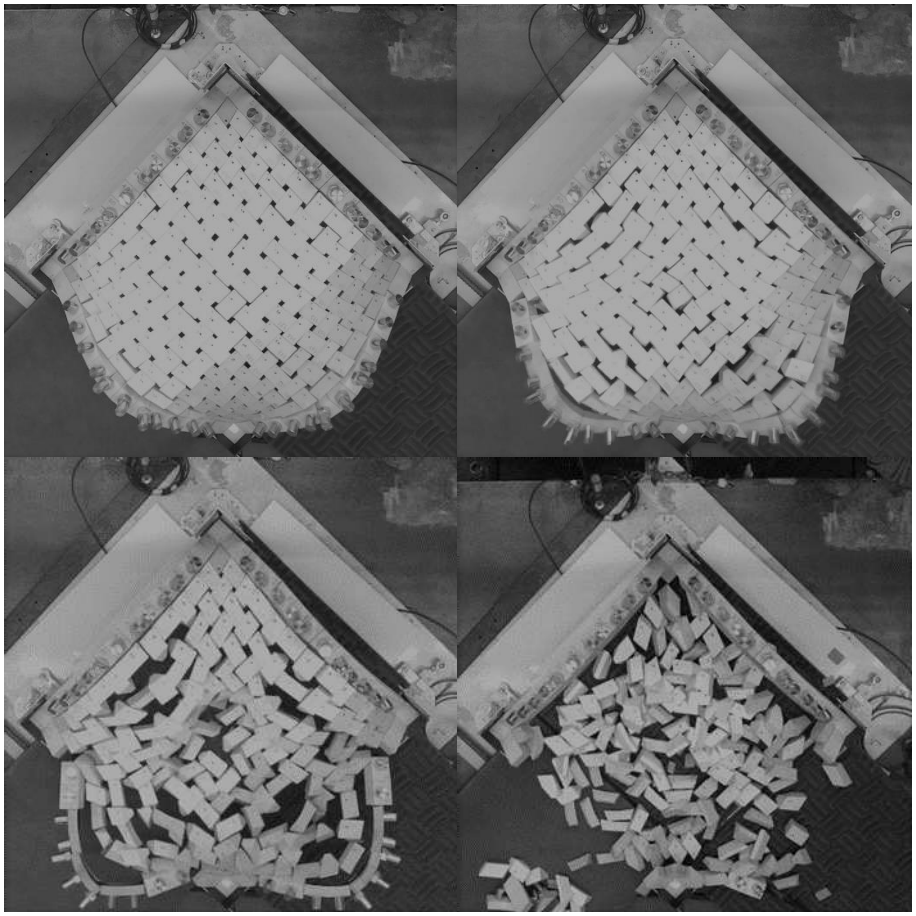

Figure 4-86. Damage results of the tilting tests with Φ = 135°: damage evolution in the zenith view.

Table 4-22 and graph in Figure 4-87 report the collapse angles α and the average values for each test, that is in the range 8.6°÷10.9°, as also shown by Table 4-23. From the single average values α for the different angle Φ –i.e. the strength capacity of vault– it is possible roughly defining the resistance domain of the vault as a function of the direction of the seismic action. In particular, this domain can be in function of the angle α it-self or of Horizontal Load multiplier λ –equal to the arctangent of the angle in radiant– as shown in graph in Figure 4-88.

The lower value occurred (α = 7.8°) is in first test with Φ = 90°, the maximum in the second with Φ = 0°, equal to α =11.5°. These maximum results are also representative of the average results, in fact the greater capacity of strength has been achieved by the configuration at Φ = 0° and the lower in correspondence of Φ = 90°. This behaviour was probably due to the different stereotomic conformation of the axes of the vault, which is not symmetrical, and which therefore generates different loads on the confinement arches.

Similar results to that of Φ = 0° are also found in the angles Φ equal to 45° and 135°, where the set-up configuration foresees that the seismic action is parallel to the diagonals connecting the supports (*p3-p2* for Φ = 45° and *p1-p4* for Φ = 135°), therefore the α rotation hinge is in correspondence with one support (*p3* for Φ = 45° and *p1* for Φ = 135°), a condition for which the behaviour of the system has a greater resistance. The values of these two cases are comparable, al-

so because they are symmetrical, and in particular, that of the Φ = 45° angle almost coincides with the maximum value (Φ = 0°).

The values for the angles between 0°÷45° with respect to the reference axes (i.e. Φ = 22.5° and Φ =112.5°) are also comparable and present results similar to the worst behaviour (Φ = 90°); in particular, the result of Φ = 112.5° is lower and this is due to the configuration of the set-up which has a seismic action almost orthogonal to the arch *p1-p3*, as previously explained it seems to be a lower resistance.

Some variation of the results and in particular some lower results are probably due to human error and improper assembling of the model.

It is important to underline that the results obtained are consistent with each other, also because they are rather constant and repetitive in the different three tests done for each in-plane angle (Φ) as can also be seen from

Table 4-22, but the final Horizontal load multiplier (λ) –estimated in a range of 0.15÷0.19 (Table 4-23)– are lower than that published for other works that varying in a range of 0.29÷0.40 (Bianchini et al., 2022; Calderini et al., 2017; Gaetani et al., 2021; G. Milani et al., 2016; Rossi et al., 2014). This certainly depends on the geometry of the vault, since the other studies mainly investigate cross or groin vaults, with blocks with interfaces all in contrast with each other –not made up of blocks with interfaces in contrast only in correspondence of interection points of a bidirectional net, as in this case–, but also on the model which, as previously written, underwent important calibrations and adjustments to consider especially as regards dynamic behaviour and horizontal loads.

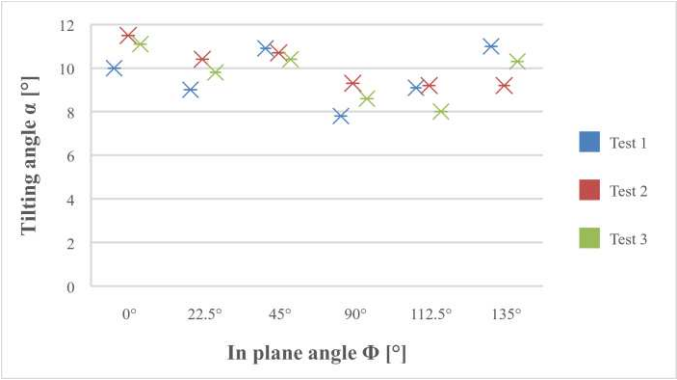

Figure 4-87. Tilting Test Results for each test performed

Table 4-22. Results of Tilting Test campaign for each in plane angle Φ.

α [°] Test 1	α [°] Test 2	α [°] Test 3	**Average value α [°]**	**Average value α [rad]**
		Φ = 0°		
10	11.5	11.1	10.87	**0.190**
		Standard Deviation		

		0.78		
		Coefficient of Variation		
		0.07		
		Φ=22.5°		
9	10.4	9.8	9.733	**0.170**
		Standard Deviation		
		0.70		
		Coefficient of Variation		
		0.07		
		Φ = 45°		
10.9	10.7	10.4	10.67	**0.186**
		Standard Deviation		
		0.25		
		Coefficient of Variation		
		0.02		
		Φ = 90°		
7.8	9.3	8.6	8.57	**0.150**
		Standard Deviation		
		0.75		
		Coefficient of Variation		
		0.09		
		Φ = 112.5°		
9.1	9.2	8	8.77	**0.153**
		Standard Deviation		
		0.67		
		Coefficient of Variation		
		0.08		
		Φ = 135°		
11	9.2	9.2	10.17	**0.177**
		Standard Deviation		
		1.04		
		Coefficient of Variation		
		0.10		

Table 4-23. Results of average values and coherence of collapse angle α and Horizontal Load Multiplier λ.

Φ = 0°	Φ = 22.5°	Φ = 45°	Φ = 90°	Φ = 112.5°	Φ = 135°	**Average Value**
			α [°]			
10.9	9.7	10.7	8.6	8.77	10.2	**9.8**
			Standard Deviation			
			0.96			
			Coefficient of Variation			
			0.10			
			α [rad]			
0.190	0.170	0.186	0.150	0.153	0.177	**0.171**
			Standard Deviation			

0.02						
Coefficient of Variation						
0.10						
λ = arctang α(rad) [-]						
0.19	0.17	0.18	0.15	0.15	0.18	**0.17**
Standard Deviation						
0.02						
Coefficient of Variation						
0.10						

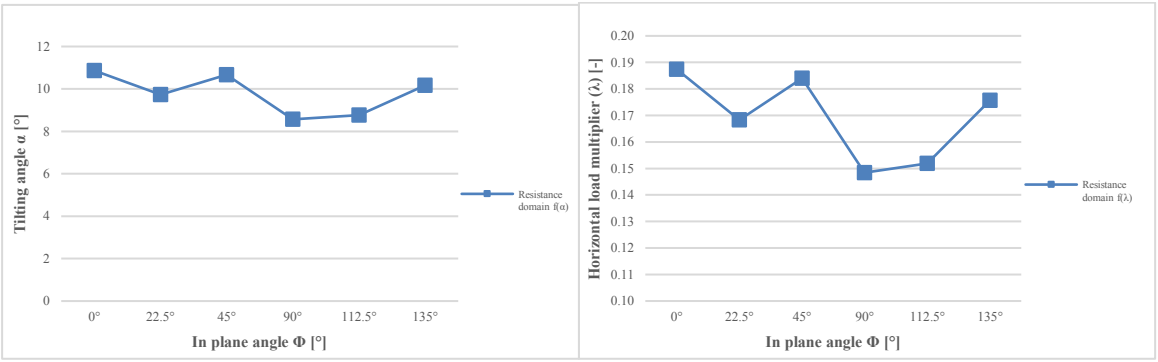

a. b.

c.

Figure 4-88. Representative curve of the resistance domain of the vault based on the direction of the seismic action: a. in function of tilting collapse angle (α); b. in function of Horizontal load multiplier (λ).

4.4.3. Estimation of scaling coefficients

The theory to scale the test results has been explained in § 4.2. In this Section the value of the coefficients α_F, α_k and α_u are calculated considering the procedure defined in § 4.2.3 to determine the result values from the small-scale model to the equivalent full-scale masonry vault.

Focusing on the value α_F, it is necessary compare the material properties of both the small-scale model and the full-scale masonry cross vault (prototype). With respect to the material properties of the model, it must refer to § 4.3.3. As already explained, in literature (Gaetani, 2020; Rossi, 2015) the Young's modulus E for the scale model with dry-joints, is estimated from compression tests on assemblage specimens. For this reason, the value $E^{(M)}$ selected is equal to 226 N/mm^2. It is important to highlight that this value must be considered an upper bound, due to the fact that it has been calculated once a complete adherence between the block surfaces have been obtained, hence neglecting the initial branch of compaction of joints, while, during the tests on the vault, blocks do not fit together exactly. In the case of prototype's material properties, the Young's modulus is calculated by considering a limestone – *hard Tuff* – typical of the Apulian Region and with which the traditional vault of the South-East Italy heritage were generally made. The value $E^{(P)}$ is equal to 2700 N/mm^2 and the specific weight of this material prototype ($\gamma^{(P)}$) is assumed equal to 19 kN/m^3; the latter corresponds to a standard value for solid tuff masonry with

dry joints. The specific weight of the model is equal to 7.6 kN/m^3.

The model's *span* parameter (l) has been determined to be 0.61 m, which is considered representative of a prototype with a span of 4.95 m. Therefore, a scale factor of 8.1, which corresponds to the size of the plastic blocks, can be applied. Table 4-24 provides a summary of the material properties for both the model and the prototype.

Table 4-24. Material properties of the model and the prototype

	E [N/mm^2]	**γ [kN/m^3]**	**l [m]**
Model (M)	226	7.6	0.61
Prototype (P)	2700	19	4.95
Scale factor	**15.49**	**2.50**	**8.11**

In the experimental tests, the model used had all geometric parameters scaled by the same coefficient αl = 8.1 ($l^{(P)} = l^{(M)}$). The friction angle between plastic blocks was estimated to be μ = 23.31°. Hence, it is essential to verify whether the dimensionless parameters that involve force have the same value for both the model and the prototype. Plugging the values from Table 4-24 into Equation (4. 7) presented in § 3.2.3 yields:

$$0.72 < \frac{\alpha_E}{\alpha_l \alpha_\gamma} < 1.5 \qquad (4.\ 17)$$

With a ratio of 0.76, the *first-order* governing parameters are consistent, indicating that the experimental tests on the small-scale cross vaults can be regarded as an *adequate* model. As a result, scaling factors for strength, stiffness, and ultimate displacement can be determined:

$$\begin{aligned} \alpha_F &= \alpha_l^3\, \alpha_\gamma = 1336 \\ \alpha_k &= \alpha_l \alpha_E\, k^{(M)} = 126 \\ \alpha_u &= \alpha_l = 8 \end{aligned} \qquad (4.\ 18)$$

In the case where a different vault prototype is being examined, and the available model is deemed not *adequate*, as described in § 3.2.3, it becomes crucial to evaluate the impact of various input parameters on the response using Equations (4. 9). Accordingly, the scaling factors would be:

$$\begin{aligned} \alpha_F &= \alpha_l^{3-c_F}\, \alpha_\gamma^{1-c_F} \alpha_E^{c_F} \\ \alpha_k &= \alpha_l^{1+c_k}\, \alpha_\gamma^{c_k}\, \alpha_E^{1-c_F} \\ \alpha_u &= \alpha_l^{1+c_u}\, \alpha_\gamma^{c_u}\, \alpha_E^{-c_u} \end{aligned} \qquad (4.\ 19)$$

REFERENCES

Aita, D., Barsotti, R., & Bennati, S. (2020). Equilibrium analysis of a sail vault in livorno's fortezza vecchia through a modern re-edition of the stability area method. Lecture Notes in Mechanical Engineering. https://doi.org/10.1007/978-3-030-41057-5_81

Akleman, E., Krishnamurthy, V. R., Fu, C. A., Subramanian, S. G., Ebert, M., Eng, M., Starrett, C., & Panchal, H. (2020). Generalized abeille tiles: Topologically interlocked space-filling shapes generated based on fabric symmetries. Computers and Graphics (Pergamon), 89. https://doi.org/10.1016/j.cag.2020.05.016

Alforno, M., Monaco, A., Venuti, F., & Calderini, C. (2021). Validation of Simplified Micro-models for the Static Analysis of Masonry Arches and Vaults. International Journal of Architectural Heritage, 15(8). https://doi.org/10.1080/15583058.2020.1808911

Andreev, K., Sinnema, S., Rekik, A., Allaoui, S., Blond, E., & Gasser, A. (2012). Compressive behaviour of dry joints in refractory ceramic masonry. Construction and Building Materials, 34. https://doi.org/10.1016/j.conbuildmat.2012.02.024

Andrusko, P. A. (2014). Stereotomy: Stone Architecture and New Research by Giuseppe Fallacara. Nexus Network Journal, 16(2). https://doi.org/10.1007/s00004-014-0197-5

Barberio, M., Colella, M., & Fallacara, G. (2016). Stereotomy, Sustainable Construction and Didactics. Case study: a new Museum for Matera, European Capital of Culture 2019. 3 Rd International Balkans Conference on Challenges of Civil Engineering, May 2016.

Bianchini, N., Mendes, N., Calderini, C., Candeias, P. X., Rossi, M., & Lourenço, P. B. (2022). Seismic response of a small-scale masonry groin vault: experimental investigation by performing quasi-static and shake table tests. Bulletin of Earthquake Engineering, 20(3). https://doi.org/10.1007/s10518-021-01280-0

Bianchini, N., Mendes, N., Lourenço, P. B., Calderini, C., & Rossi, M. (2019). Seismic assessment of masonry cross vaults through numerical nonlinear static and dynamic analysis. COMPDYN Proceedings, 1. https://doi.org/10.7712/120119.6942.18709

Block, P., Ciblac, T., & Ochsendorf, J. (2006). Real-time limit analysis of vaulted masonry buildings. Computers and Structures, 84(29–30). https://doi.org/10.1016/j.compstruc.2006.08.002

Buckingham, E. (1914). On physically similar systems; Illustrations of the use of dimensional equations. Physical Review, 4(4). https://doi.org/10.1103/PhysRev.4.345

Calderini, C., & Lagomarsino, S. (2015). Seismic Response of Masonry Arches Reinforced by Tie-Rods: Static Tests on a Scale Model. Journal of Structural Engineering, 141(5). https://doi.org/10.1061/(asce)st.1943-541x.0001079

Calderini, C., Rossi, M., Lagomarsino, S., Cascini, L., & Portioli, F. (2017). Experimental and numerical analysis of seismic response of unreinforced masonry cross vaults. International Conference on Advances in Experimental Structural Engineering, 2017-September. https://doi.org/10.7414/7aese.T5.136

Cancino, C., Farneth, S., Garnier, P., Neumann, J. V., & Webster, F. (2014). Estudio de daños a edificaciones históricas de tierra después del terremoto del 15 de agosto del 2014 en Pisco, Perú. . Getty Conservation Institute.

Cangi, G. (2005). Manuale del recupero strutturale ed antisismico. (In Italian). DEI.

Carfagnini, C., Baraccani, S., Silvestri, S., & Theodossopoulos, D. (2017). Pseudo-static response of masonry cross vaults to imposed shear displacements at the springings. Key Engineering Materials, 747 KEM. https://doi.org/10.4028/www.scientific.net/KEM.747.456

Carfagnini, C., Baraccani, S., Silvestri, S., & Theodossopoulos, D. (2018). The effects of in-plane shear displacements at the springings of Gothic cross vaults. Construction and Building Materials, 186. https://doi.org/10.1016/j.conbuildmat.2018.07.055

Colombo, C., Fernandes, L., Savalle, N., & Lourenço, P. B. (2021, June 4). TILTING TESTS FOR MASONRY STRUCTURES: DESIGN AND PRELIMINARY NUMERICAL MODELING. 14th Canadian Masonry Symposium.

Colombo, C., Savalle, N., Mehrotra, A., Funari, M. F., & Lourenço, P. B. (2022). Experimental, numerical and analytical investigations of masonry corners: Influence of the horizontal pseudo-static load orientation. Construction and Building Materials, 344, 127969. https://doi.org/https://doi.org/10.1016/j.conbuildmat.2022.127969

Croci, G. (1998). The collapses occurred in the Basilica of St Francis of Assisi and in the Cathedral of Noto. In P. Roca, J. L. González, E. Oñate, & P. B. Lourenço (Eds.), Structural analysis of historical constructions II. Possibilities of numerical and experimental techniques (pp. 297–317). International Center for Numerical Methods in Engineering.

Dantec Dynamics. (n.d.). Istra 4D.

de Lorenzis, L., DeJong, M., & Ochsendorf, J. (2007). Failure of masonry arches under impulse base motion. Earthquake Engineering and Structural Dynamics, 36(14). https://doi.org/10.1002/eqe.719

Dimitrakopoulos, E. G., & DeJong, M. J. (2012). Revisiting the rocking block: Closed-form solutions and similarity laws. Pro-

ceedings of the Royal Society A: Mathematical, Physical and Engineering Sciences, 468(2144). https://doi.org/10.1098/rspa.2012.0026

Fallacara, G. (2006). Digital Stereotomy and Topological Transformations. . Proceedings of the Second International Congress on Construction History , 1075-1092.

Fallacara, G., & Barberio, M. (2018). Stereotomy 2.0: Informing the future of Digital Stereotomy. In: Nexus Network Journal (peer-reviewed journal) (G. Fallacara & M. Barberio, Eds.). Birkhäuser/Springer-Basel.

Fallacara, G., Scaltrito, G., & Vacca, V. (2019). Hypar dome: Stereotomy 2.0's experiments on 3D-printed stereotomic domes. Proceedings of the International Fib Symposium on Conceptual Design of Structures, 427–434.

Fantetti, A., Tamatam, L. R., Volvert, M., Lawal, I., Liu, L., Salles, L., Brake, M. R. W., Schwingshackl, C. W., & Nowell, D. (2019). The impact of fretting wear on structural dynamics: Experiment and Simulation. Tribology International, 138. https://doi.org/10.1016/j.triboint.2019.05.023

Freitas, F., Barros, J., & Fonseca, P. (1998). Manual book of the structures testing system - SENTUR. (in Portuguese). University of Minho.

Gaetani, A. (2020). Seismic Performance of Masonry Cross Vaults : Learning from Historical 4 Developments and Experimental Testing. Sapienza University of Rome.

Gaetani, A., Bianchini, N., & Lourenço, P. B. (2021). Simplified micro-modelling of masonry cross vaults: Stereotomy and interface issues. International Journal of Masonry Research and Innovation, 6(1). https://doi.org/10.1504/IJMRI.2021.112076

Gaetani, A., Lourenço, P. B., Monti, G., & Moroni, M. (2017). Shaking table tests and numerical analyses on a scaled dry-joint arch undergoing windowed sine pulses. Bulletin of Earthquake Engineering, 15(11). https://doi.org/10.1007/s10518-017-0156-0

Heyman, J. (1995). The stone skeleton: structural engineering of masonry architecture. The Stone Skeleton: Structural Engineering of Masonry Architecture. https://doi.org/10.1115/1.2787238

Heyman, J. (1998). Structural Analysis. In Choice Reviews Online (Issue 03). Cambridge University Press. https://doi.org/10.1017/CBO9780511529580

Huntley, H. E. (1967). Dimensional analysis. Dover Publications.

Itasca Consulting Group Inc. (n.d.). 3DEC – Three-Dimensional Distinct Element Code.

Kartal, M. E., Mulvihill, D. M., Nowell, D., & Hills, D. A. (2011). Determination of the Frictional Properties of Titanium and Nickel Alloys Using the Digital Image Correlation Method. Experimental Mechanics, 51(3). https://doi.org/10.1007/s11340-010-9366-y

Kulatilake, P. H. S. W., Shreedharan, S., Sherizadeh, T., Shu, B., Xing, Y., & He, P. (2016). Laboratory Estimation of Rock Joint Stiffness and Frictional Parameters. Geotechnical and Geological Engineering, 34(6). https://doi.org/10.1007/s10706-016-9984-y

Large elastic deformations of isotropic materials. I. Fundamental concepts. (1948). Philosophical Transactions of the Royal Society of London. Series A, Mathematical and Physical Sciences, 240(822). https://doi.org/10.1098/rsta.1948.0002

Lemos, J. v. (2008). Modeling of Historical Masonry with Discrete Elements. In III European Conference on Computational Mechanics. https://doi.org/10.1007/1-4020-5370-3_23

Lemos, J. v. (2019). Discrete element modeling of the seismic behaviour of masonry construction. Buildings, 9(2). https://doi.org/10.3390/buildings9020043

Lourenço, P. B., Bianchini, N., & Gaetani, A. (2020). Simplified micro-modelling of masonry cross vaults: stereotomy and interface issues. International Journal of Masonry Research and Innovation, 1(1). https://doi.org/10.1504/ijmri.2020.10032218

McInerney, J., & Dejong, M. J. (2015). Discrete Element Modeling of Groin Vault Displacement Capacity. International Journal of Architectural Heritage, 9(8). https://doi.org/10.1080/15583058.2014.923953

Milani, G., Rossi, M., Calderini, C., & Lagomarsino, S. (2016). Tilting plane tests on a small-scale masonry cross vault: Experimental results and numerical simulations through a heterogeneous approach. Engineering Structures, 123. https://doi.org/10.1016/j.engstruct.2016.05.017

Naik, P. M., Bhowmik, T., & Menon, A. (2021). Estimating joint stiffness and friction parameters for dry stone masonry constructions. International Journal of Masonry Research and Innovation, 6(2). https://doi.org/10.1504/ijmri.2021.113934

Ochsendorf, J. (2002). Collapse of masonry structures. University of Cambridge.

Oliveira, R. L. G., Rodrigues, J. P. C., Pereira, J. M., Lourenço, P. B., & Ulrich Marschall, H. (2021). Normal and tangential behaviour of dry joints in refractory masonry. Engineering Structures, 243. https://doi.org/10.1016/j.engstruct.2021.112600

Payne, A., & Issa, R. (2009). The Grasshopper Primer, Second Edition for version 0.6.0007.

Piermarini, E. E. Antonio. (2013). The dynamic behavior of the Basilica of San Francesco of Assisi [PhD Thesis]. Massachusetts Institute of Technology.

Pope, L., & Ward, C. (2008). Manual on Test Sieving Methods. In Manual on Test Sieving Methods, 4th Edition, Prepared by ASTM Committee E29 as Guidelines for Establishing Sieve Analysis Procedures. https://doi.org/10.1520/mnl10684m

Python Software Foundation ("PSF"). (n.d.). The Python Language Reference — Python 3.9.5 documentation.

Quinonez, A., Zessin, J., Nutzel, A., & Ochsendorf, J. (2010). Small-Scale Models for Testing Masonry Structures. Structural Analysis of Historic Constructions, 133, 497–502. https://doi.org/10.4028/www.scientific.net/AMR.133-134.497

Restrepo Vélez, L. F., Magenes, G., & Griffith, M. C. (2014). Dry stone masonry walls in bending-Part I: Static tests. International Journal of Architectural Heritage, 8(1). https://doi.org/10.1080/15583058.2012.663059

Robert McNeel & Associates. Copyright © 1993-2022. All rights reserved. (n.d.). Rhinoceros.

Rossi, M. (2015). Evaluation of the Seismic Response of Masonry Cross Vaults [Ph.D.]. UNIVERSITÀ DEGLI STUDI DI GENOVA - SCUOLA POLITECNICA.

Rossi, M., Barentin, C. C., van Mele, T., & Block, P. (2017). Collapse analysis of unreinforced masonry vaults using 3D-printed scale-model testing. International Conference on Advances in Experimental Structural Engineering, 2017-September. https://doi.org/10.7414/7aese.T2.130

Rossi, M., Calderini, C., & Lagomarsino, S. (2016). Experimental testing of the seismic in-plane displacement capacity of masonry cross vaults through a scale model. Bulletin of Earthquake Engineering, 14(1). https://doi.org/10.1007/s10518-015-9815-1

Rossi, M., Calderini, C., Lagomarsino, S., & Milani, G. (2014). Seismic response of masonry vaulted structures: experimen tal and numerical modelling. Proceedings of the 9th International Masonry Conference.

Rossi, M., Calderini, C., Milani, G., & Lagomarsino, S. (2015). Numerical and experimental analysis of an in-scale masonry cross-vault prototype up to failure. AIP Conference Proceedings, 1702. https://doi.org/10.1063/1.4938934

Rossi, M., Calderini, C., Roselli, I., Mongelli, M., Canio, G. de, & Lagomarsino, S. (2020). Seismic analysis of a masonry cross vault through shaking table tests: The case study of the Dey Mosque in Algiers. Earthquake and Structures, 18(1). https://doi.org/10.12989/eas.2020.18.1.057

Sánchez Peña, M. (2020). Estudio y análisis de la bóveda plana de Joseph Abeille. Escuela Técnica Superior de Arquitectura de Madrid UPM.

Shapiro, E. E. (2012). Collapse mechanisms of small-scale unreinforced masonry vaults [Ph.D. Thesis]. Massachusetts Institute of Technology.

Silvestri, S., Baraccani, S., Foti, D., Ivorra, S., Theodossopoulos, D., Vacca, V., Roman, J. O., Cavallini, L., Mokhtari, E., White, R., Dietz, M., & Mylonakis, G. (2021). Shaking table testing of groin vaults made by 3D printers. Soil Dynamics and Earthquake Engineering, 150. https://doi.org/10.1016/j.soildyn.2021.106880

STAND4Heritage funded by EU Project. (2020). STAND4Heritage.

Thanoon, W. A. M., Alwathaf, A. H., Noorzaei, J., Jaafar, M. S., & Abdulkadir, M. R. (2008). Finite element analysis of interlocking mortarless hollow block masonry prism. Computers and Structures, 86(6). https://doi.org/10.1016/j.compstruc.2007.05.022

van Mele, T., McInerney, J., DeJong, M. J., & Block, P. (2012). Physical and Computational Discrete Modelling of Masonry Vault Collapse. Structural Analysis of Historical Constructions, Vols 1-3.

Vella, I. M., & Kotnik, T. (2016). Geometric Versatility of Abeille Vault. Proceedings of the 34th International Conference on Education and Research in Computer Aided Architectural Design in Europe, 2(Figure 1).

Wykeham Farrance - Controls group. (n.d.). SHEARMATIC EmS.

5. NUMERICAL SIMULATION AND VALIDATION OF EXPERIMENTAL TESTS

5.1. Description of the adopted numerical model

The numerical analyses have been conducted by adopting a non-linear DEM Model in 3DEC® (see § 3).

The vault is an assembly of rigid blocks –as these are more suitable for quasi-static (Itasca Consulting Group Inc., n.d.)– analyses and all the system deformability is therefore concentrated in the joints, that have a Mohr-Coulomb behaviour. So, interaction between the blocks is modelled using zero-thickness non-linear springs (point contacts), which are automatically created when two block faces are determined to be in contact.

The model permits the performing of a non-linear incremental analysis by applying determinate velocities and incremental displacements. Each step is solved by means of mathematical programming, i.e., through the formulation of a suitable constrained minimization problem, based on an algorithmic procedure where the objective function is represented by the energy of the mechanical system (§ 3). So, the aim is to observe and identify the resistance of the vault to differential displacement in various direction.

This modelling is usually utilized for the masonry structures as reported in § 3.2. In particular, considering that in 3DEC® the quasi-static solution is reached when the rate of change of kinetic energy in a model approaches a negligible value, therefore the software plotted forces are the unbalanced ones. This kind of force indicates when a mechanical equilibrium is reached for each block centroid or grid-point (Itasca Consulting Group Inc., n.d.).

5.1.1. Description of the optimized and parametric model geometry

The specific model represents perfectly the vault, and each rigid block identifies an ashlar of the experimental and real vault. In fact, it is directly imported by the optimized Rhinoceros® model (§ 4.3.1.) adopted also for the 3d printing (§ 4.3.2.). So, each real ashlar was simulated, adopting a complex geometry. Every block can be described as a collection of triangulated faces that are jointed by command *poly face* to create the final polygon. So, after the importation, for each shape, neighboring coplanar triangles are assembled into polygonal faces (§ 4.3.1.). The model has about 235 planar convex polygons, which were assumed to behave as rigid bodies, each with 6 degrees-of-freedom.

To consider the adjustments made to the experimental model, the initial geometry of the vault ashlars was accordingly modified. The first two ashlars of each arch have been joined to the support and the macro-blocks of the arch have been reproduced; in particular, the three central blocks of the arch were merged to create the macroblock of the keystone and the remaining ashlars of the arch two by two, using the *join* command.

It is important to note that the model has been imported several times to consider the variations of the in-plane angle in DSA tests, but also for the Set-up B of ISA tests, so as to always have an absolute origin unchanged.

Below are the pictures of the model from Figure 5-12to Figure 5-14.

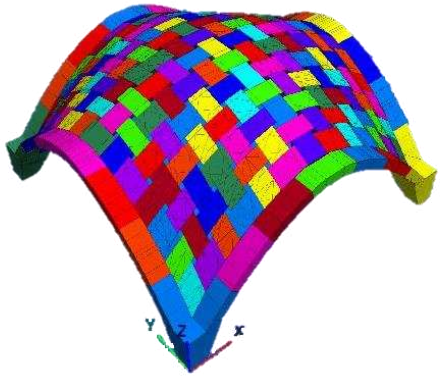

Figure 5-1. Numerical model global view (orientation Φ = 0).

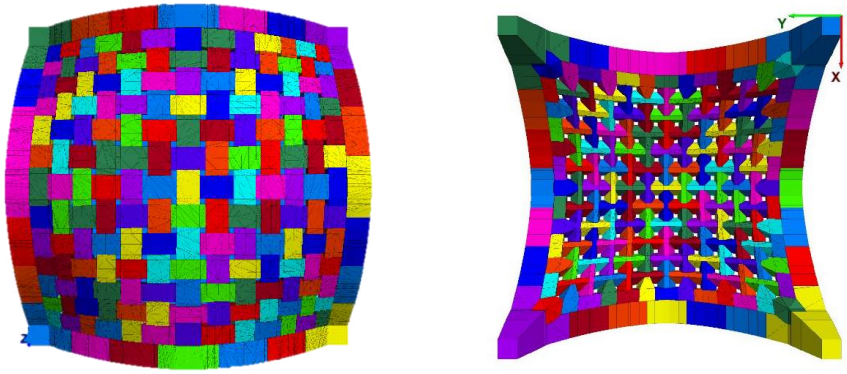

a. b.

Figure 5-2. Numerical model view: a. Extrados; b. Intrados.

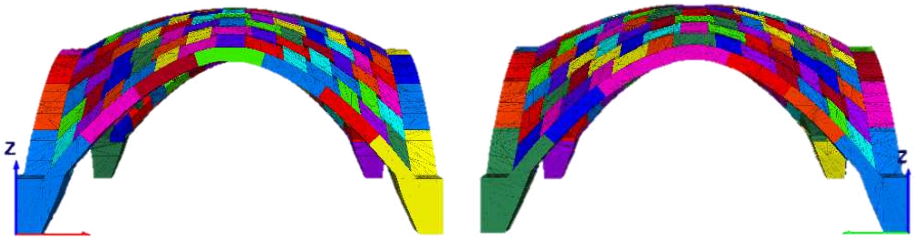

a. b.

Figure 5-3. Numerical model: a. Frontal view (*p3-p4*); b. Lateral view (*p1-p3*).

5.1.2. Mechanical parameters

According to 3DEC® constitutive theories (Itasca Consulting Group Inc., n.d.), in a model with rigid blocks, all the deformation is concentrated at the joints, so the joint stiffness parameters have to be selected to reproduce the masonry elastic moduli. As already explained in § 3., the joints were modeled on the Mohr–Coulomb behaviour; so their deformability is characterized by normal and shear stiffnesses, and joint strength by the friction angle, cohesion, and tensile strength. In the specific vault case, tensile and/or shear failure took place, so jk_n and jk_s were calculated (§ 4.3.3), as the friction angle μ, but the tensile strength f_t (assumed equal to the cohesion c) were both set to zero. In fact, 3DEC® does not model any tensile strength material in the numerical code, so even if the joints of the physical model are "dry" joints, their strength and cohesion should merely tend to zero.

Considering what has been assessed for the rigid block models it has not been necessary to have the value of the elastic (E) and shear (G) modulus of the blocks, but it has been enough to set the density (γ) of the block material and the parameters of the joints, as already highlighted.

In the model, to take into account the different steel elements added for the confinement of the arches, two different weights were applied one on the arch ashlars considering the only steel elements and another for the arch keystones to consider the cylindric steel element assembled with the bolt. In particular, the first force is equal to 115.3 g and the second one 167.3 g. In this way it was possible evaluate the approximations apported in the experimental model also in numerical one to have a coherence for a good validation.

The values of all the parameters are summarized in Table 5-1.

Table 5-1. Mechanical properties adopted in the numerical small-scale model.

Parameter		Value
ρ_1 [kg/m^3]	Specific vault block mass	767
ρ_2 [kg/m^3]	Specific arch block mass	7.6
ρ_3 [kg/m^3]	Specific keystone block mass	1656.52
υ [-]	Poisson's ratio	0.20
jk_n [N/mm^3]	Interface normal stiffness	0.26
jk_s [N/mm^3]	Interface tangential stiffness	0.18
μ [°]	Friction angle	23.31
ζ	Damping ratio	0.8
f_t	Tensile strength	0
c	Joint cohesion	0

5.2. Simulation and validation of the experimental tests

5.2.1. ISA simulation

5.2.1.1. Model set-up

To simulate ISA experimental set-ups, the boundary conditions imposed for set-up A were char-

acterized by the fixing of the base and the two abutments *–p2* and *p4–* in all directions and rotations, while the other abutments *–p1* e *p3–* were only fixed in z-direction and in all the rotations (hinge), being free to translate along x and y axis. Subsequently the gravity simulation was carried out. The load was simulated by applying the speed of 0.0005 m/s in the y-axis direction at the control point *p3* (the origins of the axes); this speed was deduced from the average of those recorded in the five experimental tests. To obtain the results, a Force-Displacement graph was plotted in the vertex, where the origin of the axes is located, corresponding to the vertex at the base of *p3*.

The same procedure has been utilized for the set-up B, in this case, in addition to the support base, the only abutment completely fixed in every direction was p4, the others were configurated as hinges; so are fixed in z-direction and all rotations have been avoided. The velocity amounted of about 0.00024 m/s and was applied always in correspondence of *p3* (the axe origin). To facilitate the analysis settings, the model was turned by 45°, as was also done for the experimental tests.

5.2.1.2. Results

Figure 5-4 shows the results of the shear in-plane tests. They appear coherent both in terms of force/displacement curves and failure mechanisms with those obtained experimentally. From the comparison between the results, it is possible to note that the numerical results –in green– are slightly higher than the experimental ones of set-up A –in red range–, but the softening behaviour is essentially the same. Considering that softening behaviour generally affects the tensile and tangential response of mortar interfaces subjected to low value of normal compression, this curve is coherent with the assumption of almost zero values of cohesion and tensile strength in case of “dry joint”. The numerical curve demonstrates a good fitting in both linear and non-linear phases. In the numerical model, the maximum peak of resistance is about 41.66 N corresponding to 17% of the total weight, and the maximum displacement is about 18.08 mm that is 3% of the vault’s span. Th ultimate displacement value is comparable with the experimental average one that is equal to 3.26%, instead, as already noted, the maximum strength capacity values is higher in regard of the experimental one equal to 14.45%. It is probably due to same imperfection of 3d-printed model and of the manually assembled geometry.

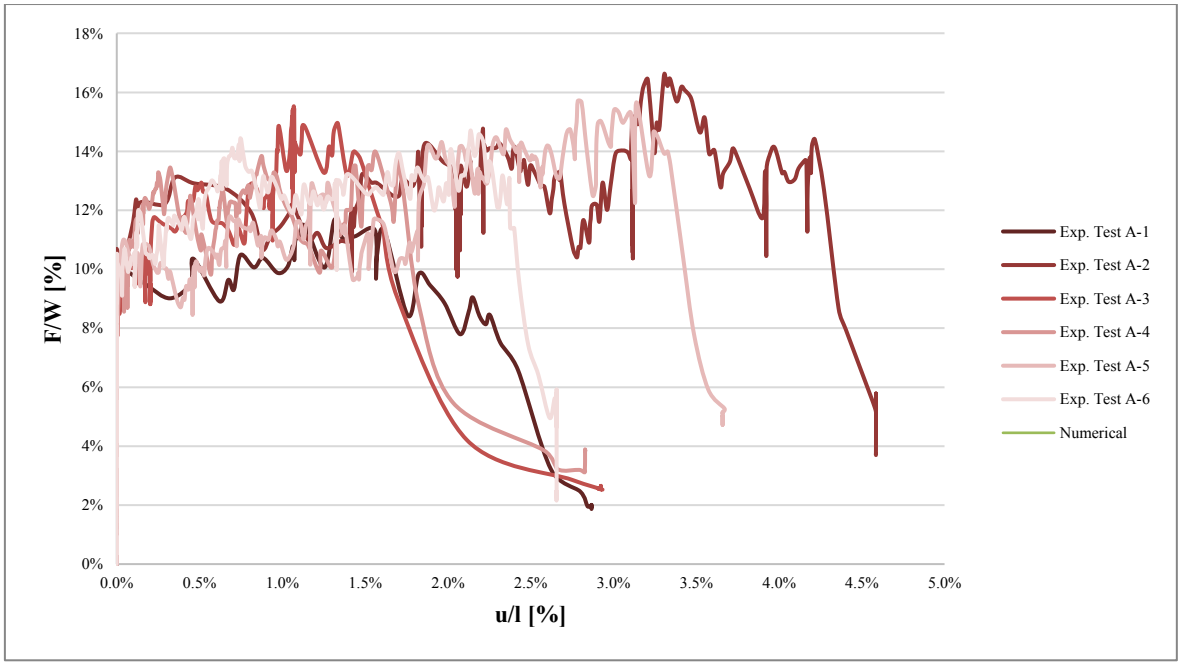

Figure 5-4. Shear tests A: comparison between the experimental and the numerical results obtained by using the parameters of Table 5-1.

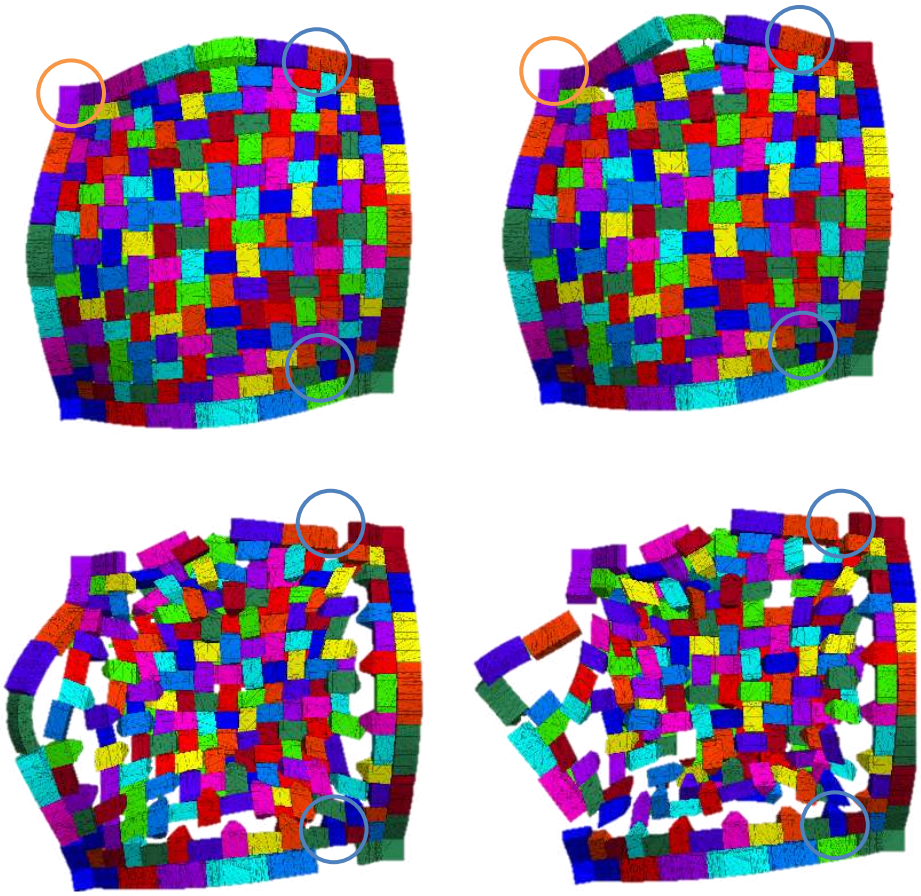

Figure 5-5. Deformed shape test set-up A: zenith view; in the blue circle the fixed abutments and in orange one the first ashlar that falls.

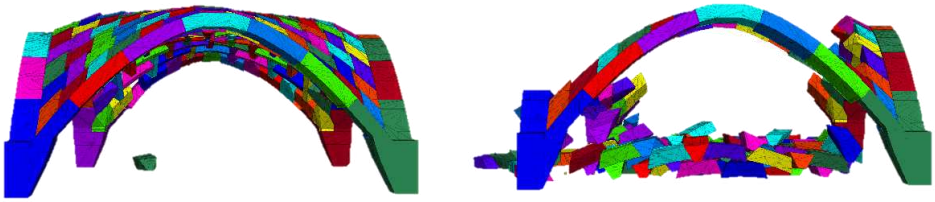

Figure 5-6. Deformed shape test set-up A: frontal view.

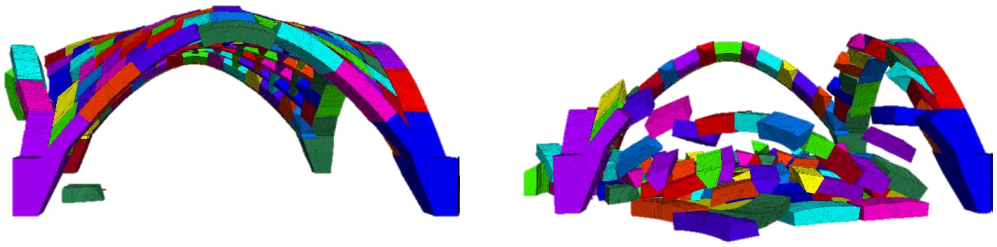

Figure 5-7. Deformed shape test set-up A: lateral view.

The deformed shapes near collapse are illustrated from Figure 5-5 to Figure 5-7 and show similarities to that which was observed in the experimental tests.

The collapse occurs due to the fall of one ashlar placed near an abutment and the loss of connection between other adjacent ones; this generates a thrust on the confinement arch that collapse with the vault quadrant involved with an out-of-plane mechanism. In the numerical model is possible better observe the generation of "four" hinges mechanism that not in all experimental tests was visible, where the adjustments certainly had an influence.

When dealing with tests B, the global force/displacement curves (Figure 5-8)have similar initial stiffness and ultimate ductility with respect to those obtained from tests with set-up A; the peak loads are higher, as for set-up A. It is around 19% of the weight while in experimental test is equal to 13.86%. The maximum displacement value was equal to 2%, so it is comparable with the experimental one equal to 2.84%. The collapse mechanism is rather similar to that observed experimentally, especially the effect of localized damage near the abutments *p1*. It revealed a not-perfect symmetry with respect to the diagonal *p2-p3* (from Figure 5-9 to Figure 5-11), and confirms the unequal behaviour of the *p1-p3* and *p3-p4* arches, due to the different central directrices.

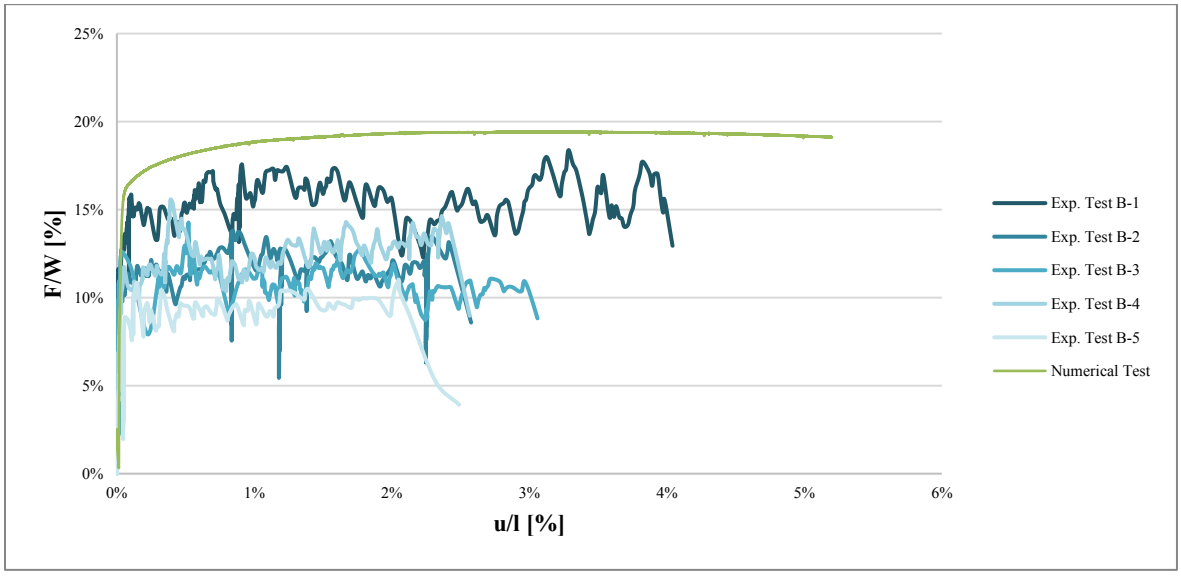

Figure 5-8. Shear tests B: comparison between the experimental and the numerical results obtained by using the parameters of Table 5-1.

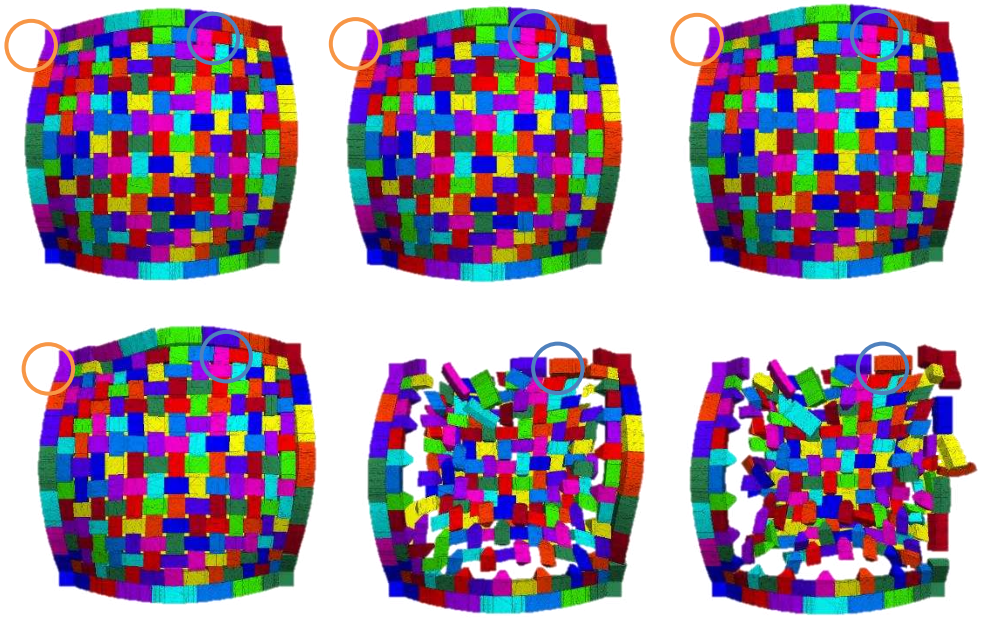

Figure 5-9. Deformed shape test set-up B: zenith view; in the blue circle the fixed abutment and in orange one the first ashlar that falls.

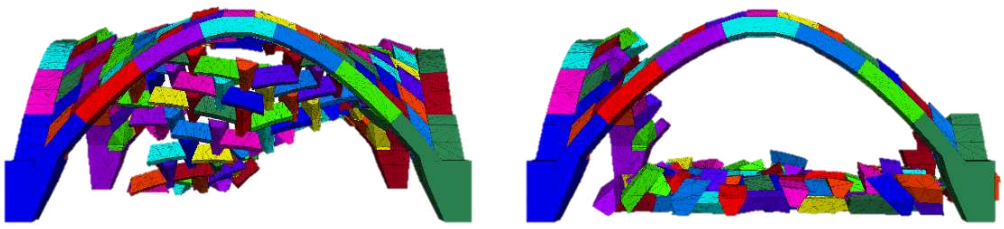

Figure 5-10. Deformed shape test set-up B: frontal view.

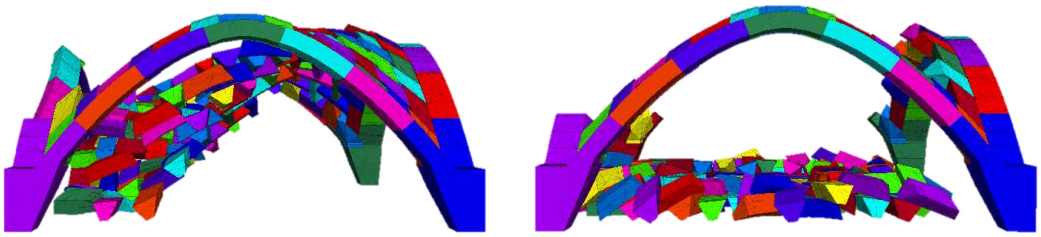

Figure 5-11. Deformed shape test set-up B: lateral view.

5.2.1.1. Validation

The numerical results are slightly discordant with the experimental ones for what to concern the nonlinear behaviour of the vault. In particular, if the ultimate displacement of the in-plane shear tests could be comparable, the capacity of the vault in the numerical model is higher than the experimental one. This is presumably due to multiple causes: the complexity of the geometry and the experimental setup (boundary conditions), the fabrication imperfections and subsequent adjustments, as well as lacks in the manual assemblage. All these reasons are crucial aspects in the definition of the interface stiffness, and lead to have a scaled experimental model with an overall lower strength capacity.

Even if an experimental campaign concerning different scale and mass density is rather desirable, as a whole, the numerical model can be considered a first method to know the behaviour of a complex vault and to understand its damage mechanisms.

5.2.2. DSA simulation

5.2.2.1. Model set-up

After having imported the geometry and applied the materials, the boundary condition was imposed fixing the base block and the four abutments in all directions and rotations to reproduce the clamped conditions of the experiment.

Prior to perform the quasi-static tilting analysis, the gravity load was applied. In terms of loading, to simulate the tilting table in 3DEC®, as in literature (Bui et al., 2017; Colombo et al., 2022; Lemos, 2019) the vertical component of gravity is kept constant at 9.81 m/s^2, while the horizontal component (along y axis) is progressively increased in steps of 0.05 m/s^2. For each load increment, the analysis is run until the maximum velocity in the system is less than 0.001 m/s^2, and only once the convergence criterion is satisfied the loading was increased (Colombo et al., 2022). To obtain the complete collapse of the vault, the simulations are run until the maximum displacement of the system exceeds; in fact a lack of convergence of the maximum velocity leads to structure failure. Knowing the vertical and horizontal component of the force that causes the numerical model collapse, it is possible to deduce the angle using trigonometric formulas.

This procedure was carried out for all the different directions, expressed in terms of in-plane angle *Φ*.

5.2.2.2. Results and validation

The comparison between numerical and experimental analyses is shown in Table 5-2. The resistance domain (Figure 5-19) is comparable as trend –the in-plane angles that had better structure behaviour remain unchanged– but the numerical values not. The numerical values are higher than the experimental results, in a range of 20÷30%; in particular, this percentage is around 30% for the in-plane angles that present a greater collapse angle ($\phi = 0°, 45°, 135°$). This scatter value which exists in literature generally stands between 10 and 20%, both for the arches (Piccioni et al., 2021), masonry walls (Colombo et al., 2021; Lemos, 2019) and for the vaults (Bianchini et al., 2022; Gaetani, 2020; Rossi, 2015), in this specific case it is higher both for the stereotomy of the vault it-self and for the defects already highlighted in paragraph § 4.3.2., due to the realization of this model with complex ashlars. For this reason, this value, however high, is considered consistent. Furthermore, the values of the final angles estimated by the numerical analyzes are in any case lower than the average of those present in the aforementioned literature.

The trend of the numerical domain shows that, from the seismic action along the y axis (*p1-p3*) of all the set-up and the vault diagonal ($\phi = 45°$), the resistance of the vault slightly increases in respect of the experiment (§ 4.4.2.).

As regards the $\Phi = 0°$ and $\Phi = 90°$, the numerical model differs from the experimental one in that the collapse of the structure is specific of the vault and only of the arch perpendicular to the direction of the seismic action; in fact, the other arches of the numerical model do not collapse even if the angle of stress is increased by 2°÷3°, remaining in equilibrium. Another difference is found in the configuration $\Phi = 112.5$ where the particular failure highlighted in § 4.4.2.2. starting from a quadrant of the vault does not occur. The main mechanisms of the numerical model detected, both at in the vault and the arches, are in any case the same as in the experimental one, therefore the numerical model can be validated.

All the deformed shape obtained by the different orientation and seismic action was reported from Figure 5-13 to Figure 5-30. These demonstrate good agreement with the mechanisms observed during the experimental tests (§ 4.4.2.).

The numerical values confirm the influence on the results of the vault asymmetry and its dynamic response. Probably the difference of the 30% for same configuration is also due to the combination of the asymmetry effect on the vault pattern and the perfect joins of the numerical model.

It can be noted that the out-of-plane mechanism found in the experimental tests is actually present also in the numerical model, although in part the creation of hinges is not present in-plane, but always due to the thrust due to the vault and influenced by the greater mass of the arch macroblocks which therefore tend to rotate before collapsing.

Table 5-2. Results of numerical values of collapse angle α and Horizontal Load Multiplier λ.

Φ = 0°	Φ = 22.5°	Φ = 45°	Φ = 90°	Φ = 112.5°	Φ = 135°	**Average Value**
α [rad]						
0.247	0.205	0.242	0.185	0.200	0.231	**0.218**
α [°]						
14.15	11.75	13.87	10.60	11.46	13.24	**12.51**
λ = arctang α(rad) [-]						
0.24	0.20	0.24	0.18	0.20	0.23	**0.21**

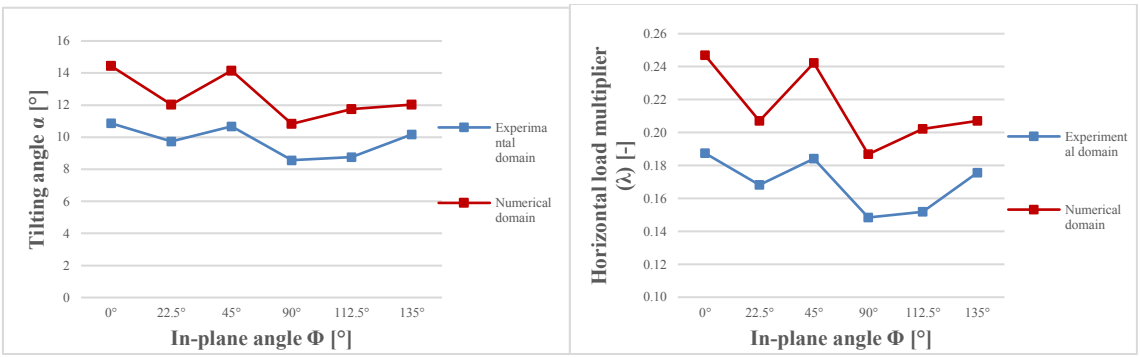

a. b.

c.

Figure 5-12. Comparison of numerical and experimental curve of the vault resistance domain based on the direction of the seismic action: a. in function of tilting collapse angle (α); b. in function of Horizontal load multiplier (λ).

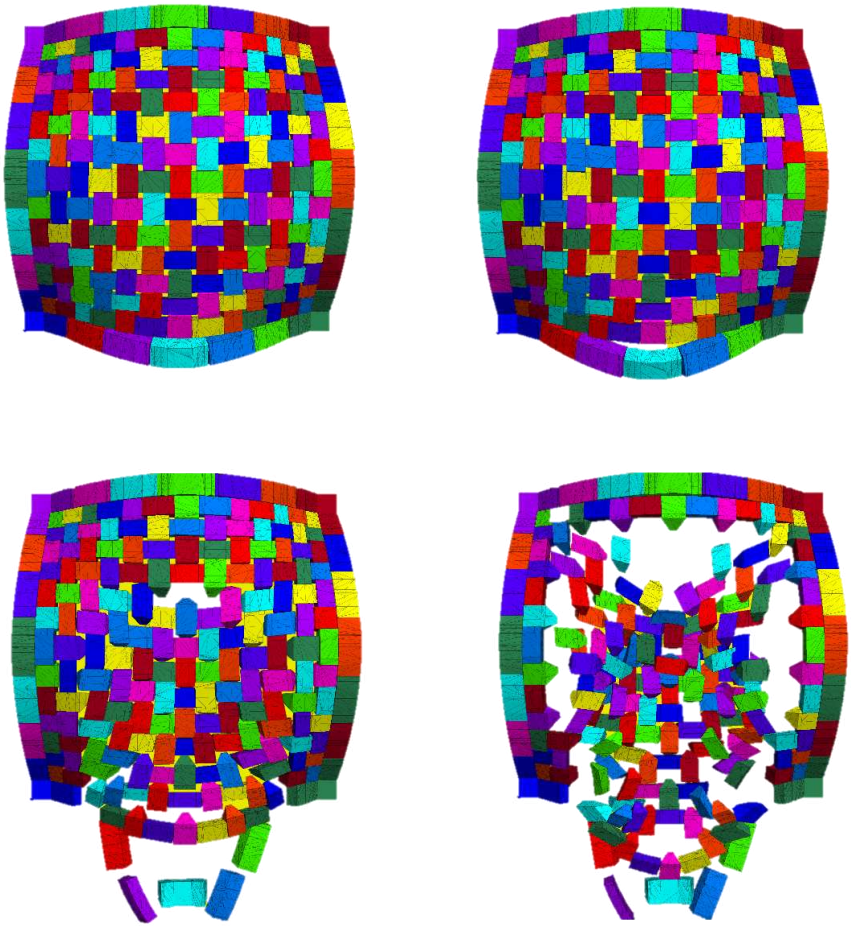

Figure 5-13. Damage results of the numerical tilting tests with Φ = 0°: damage evolution in the zenith view.

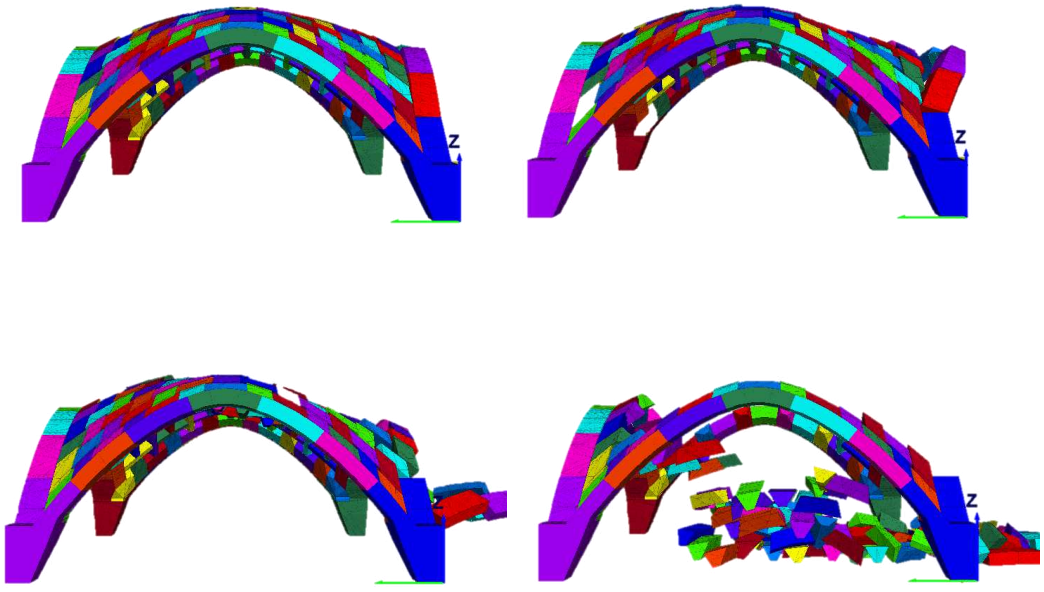

Figure 5-14. Damage results of the numerical tilting tests with Φ = 0°: damage evolution in the lateral view (p1-p3).

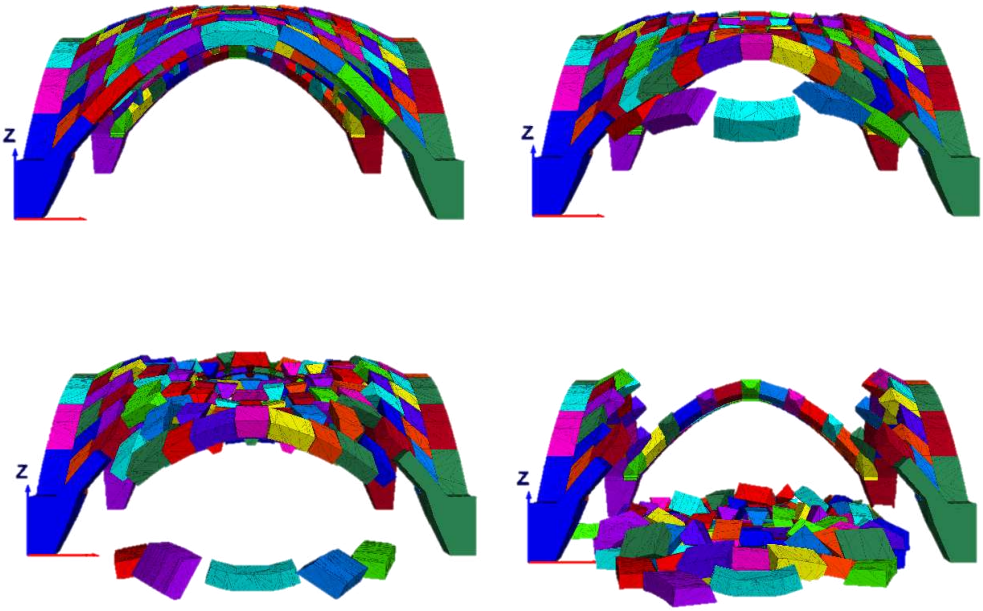

Figure 5-15. Damage results of the numerical tilting tests with Φ = 0°: damage evolution in the frontal view (*p3-p4*).

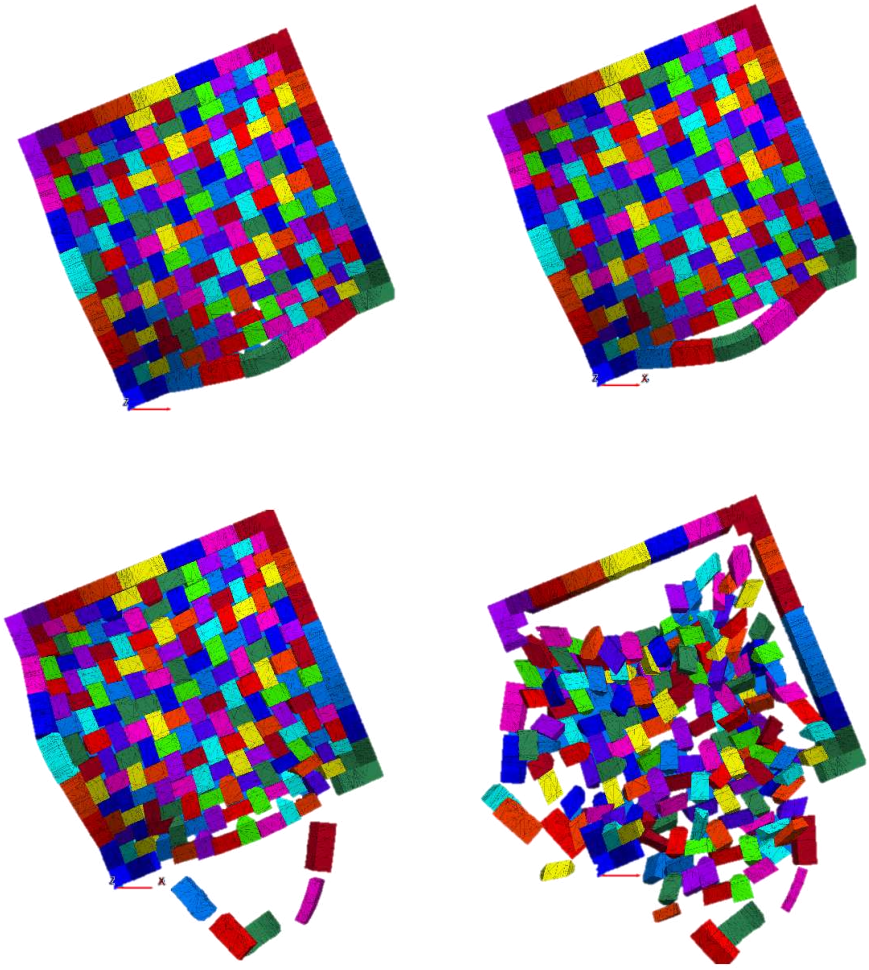

Figure 5-16. Damage results of the numerical tilting tests with Φ = 22.5°: damage evolution in the zenith view.

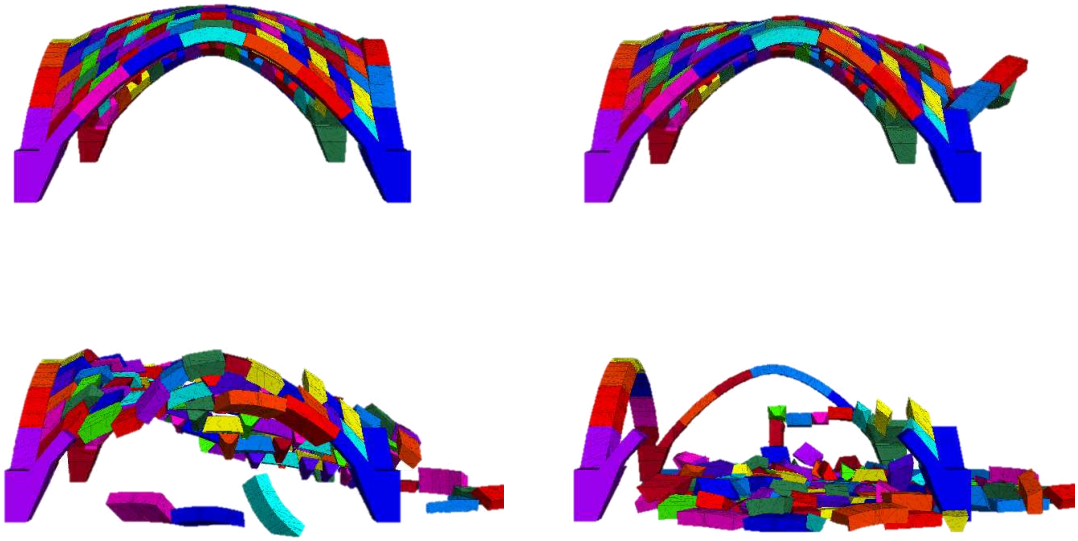

Figure 5-17. Damage results of the numerical tilting tests with Φ = 22.5°: damage evolution in the lateral view (p1-p3).

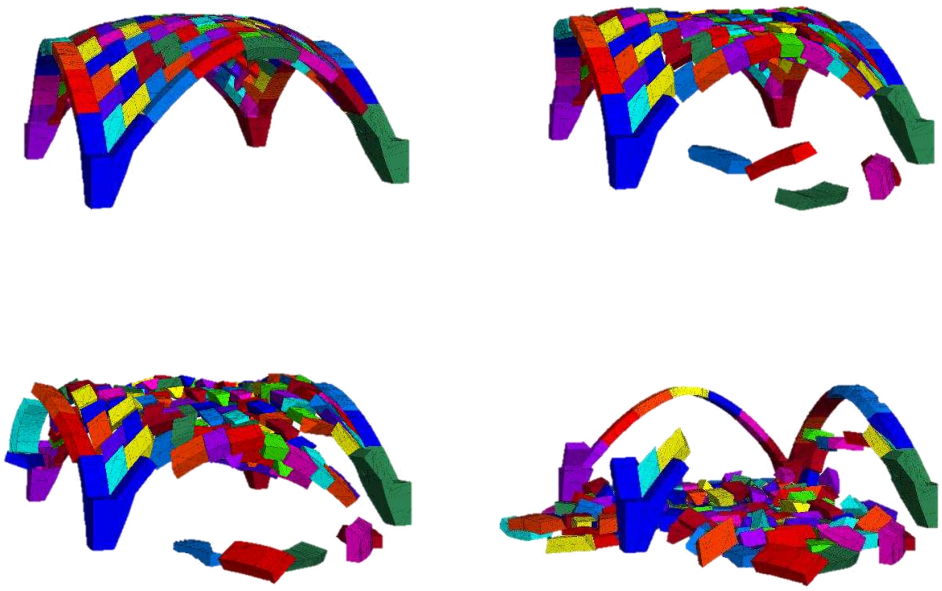

Figure 5-18. Damage results of the numerical tilting tests with Φ = 22.5°: damage evolution in the frontal view.

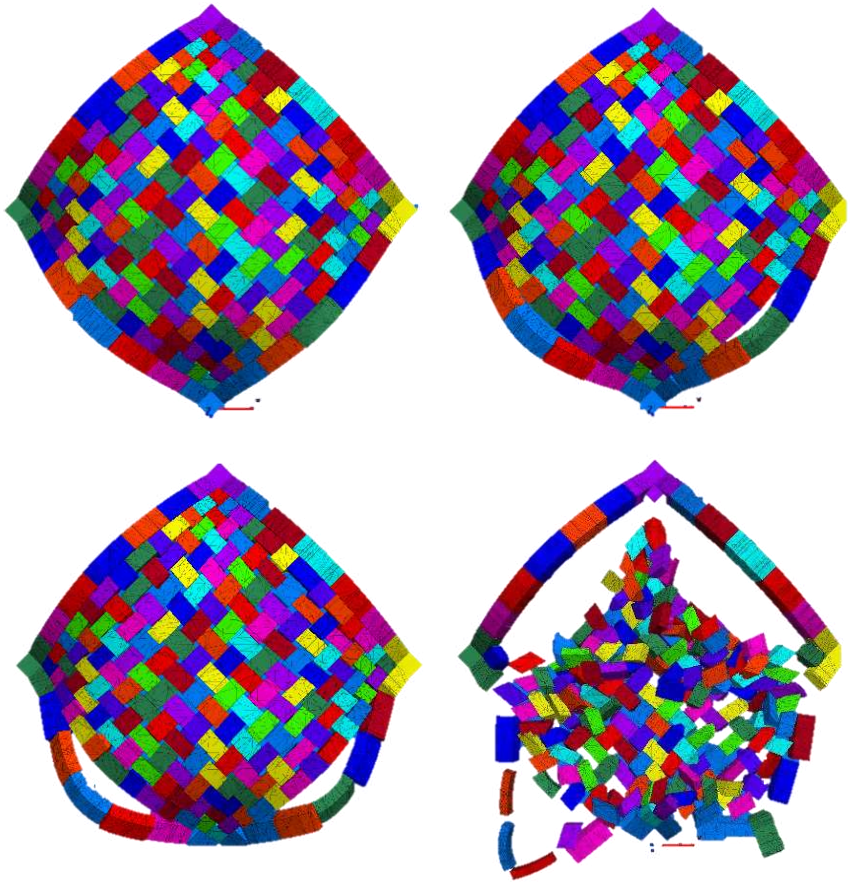

Figure 5-19. Damage results of the numerical tilting tests with Φ = 45°: damage evolution in the zenith view.

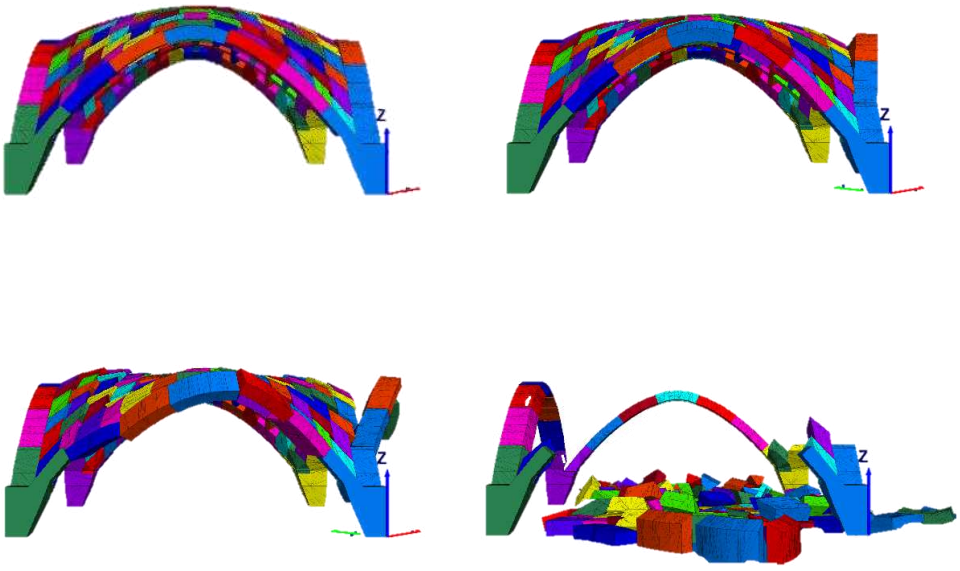

Figure 5-20. Damage results of the numerical tilting tests with Φ = 45°: damage evolution in the lateral view (*p1-p3*).

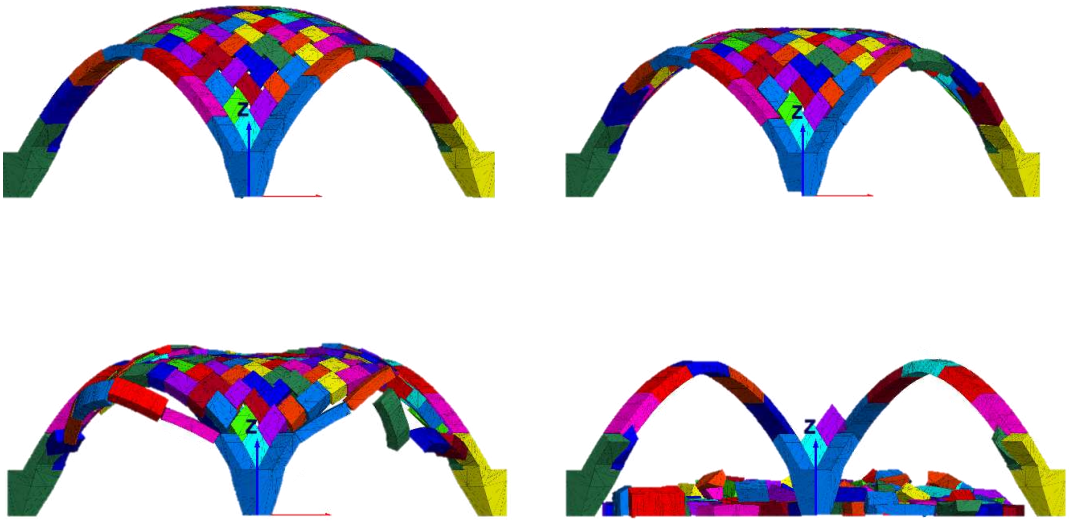

Figure 5-21. Damage results of the tilting tests with Φ = 45°: damage evolution in the frontal view.

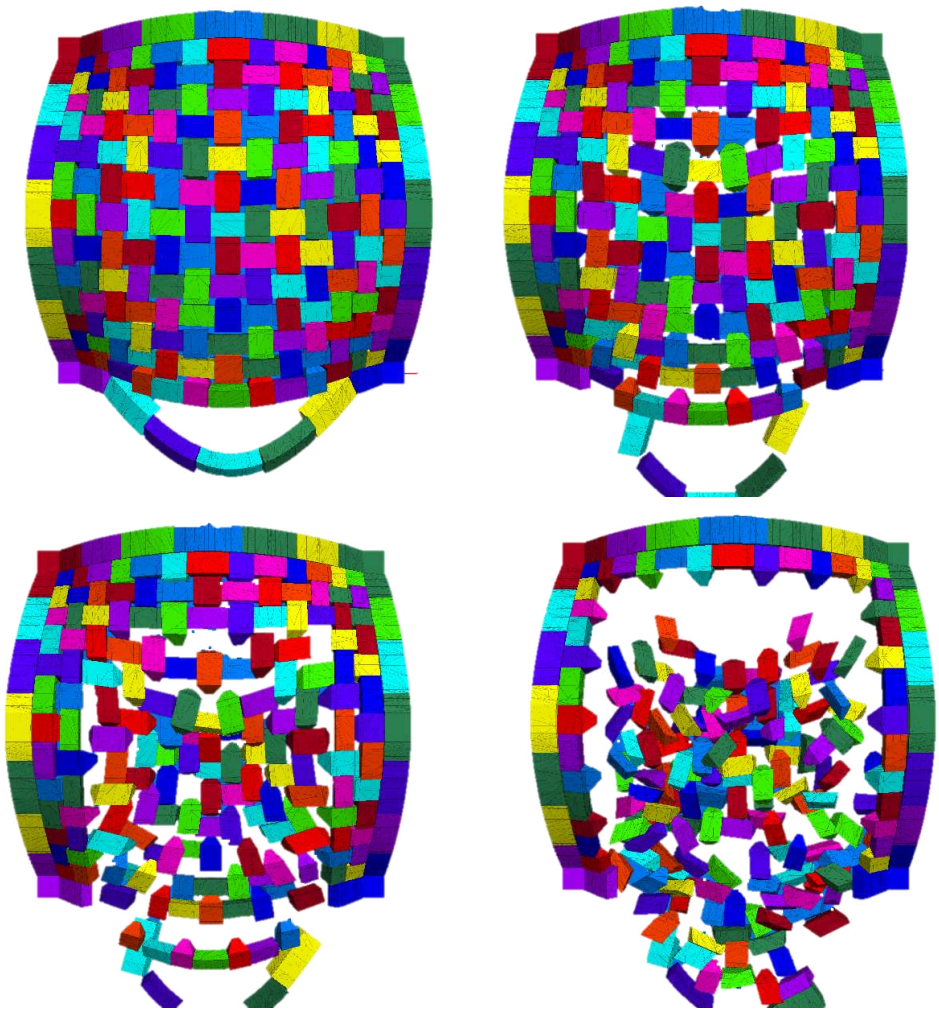

Figure 5-22. Damage results of the numerical tilting tests with Φ = 90°: damage evolution in the zenith view.

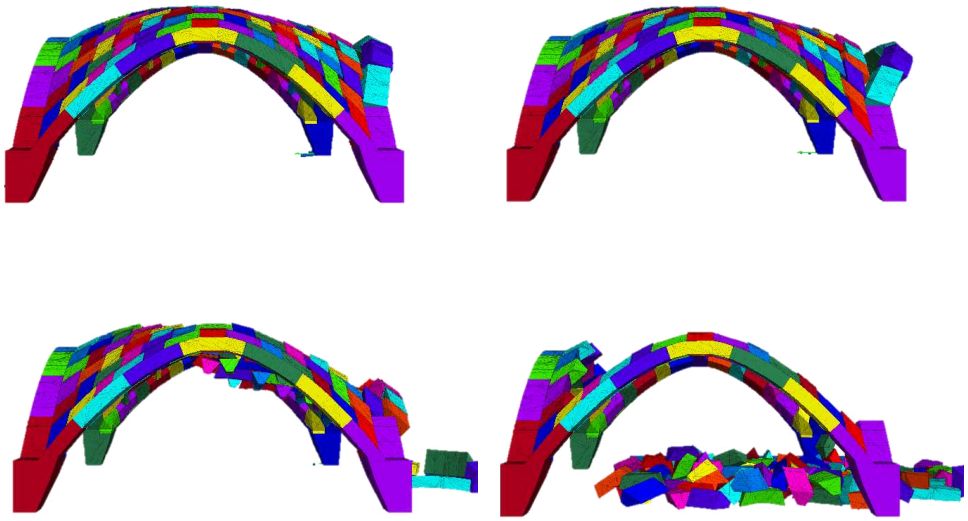

Figure 5-23. Damage results of the numerical tilting tests with Φ = 90°: damage evolution in the lateral view (*p1-p2*).

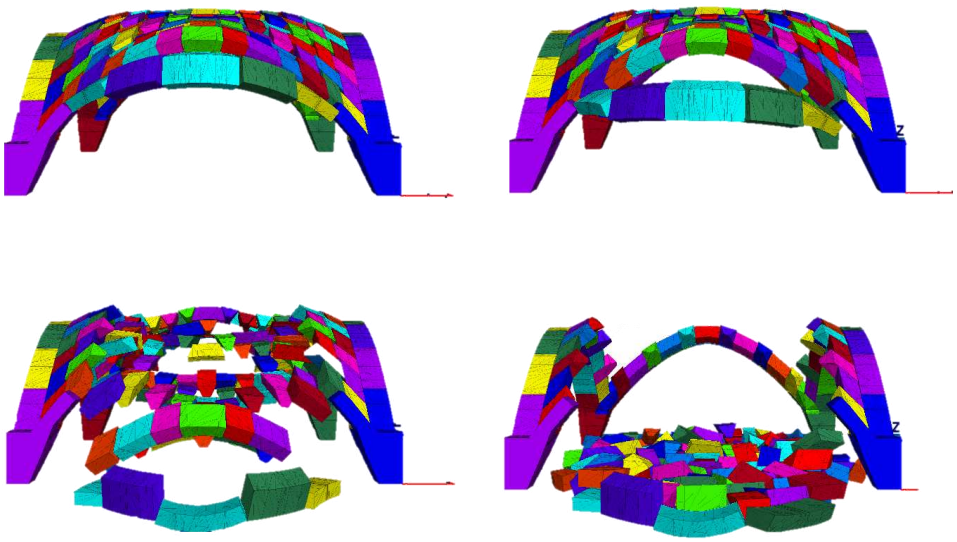

Figure 5-24. Damage results of the tilting tests with Φ = 90°: damage evolution in the frontal view (*p1-p3*).

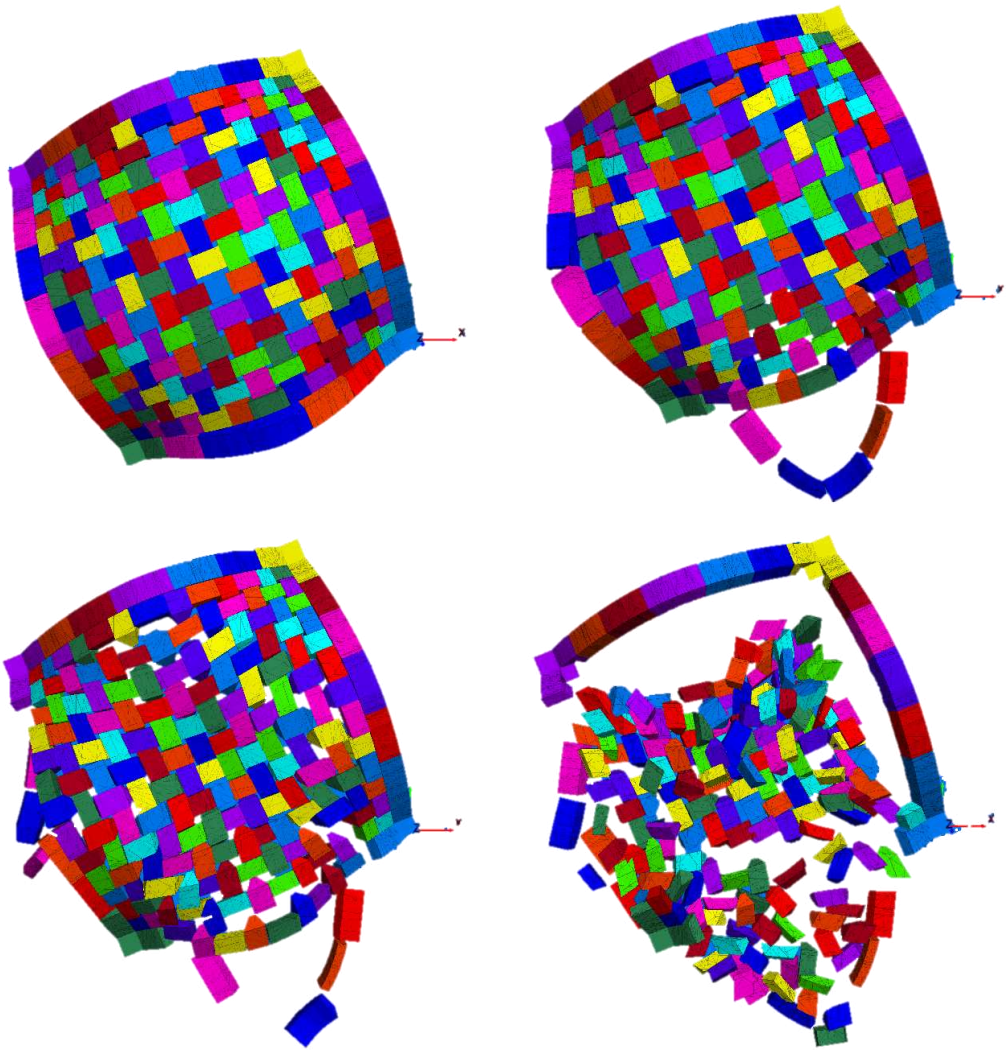

Figure 5-25. Damage results of the numerical tilting tests with Φ = 112.5°: damage evolution in the zenith view.

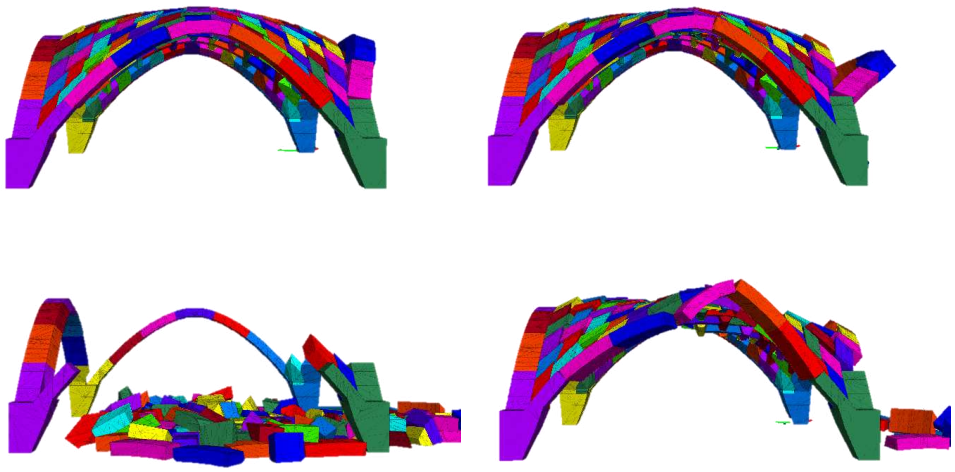

Figure 5-26. Damage results of the numerical tilting tests with Φ = 112.5°: damage evolution in the lateral view (*p1-p2*).

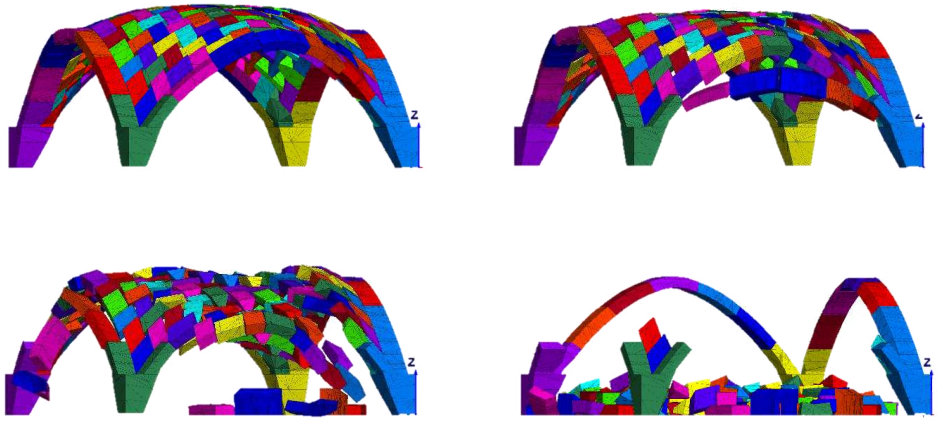

Figure 5-27. Damage results of the numerical tilting tests with Φ = 112.5°: damage evolution in the frontal view (*p1-p3*).

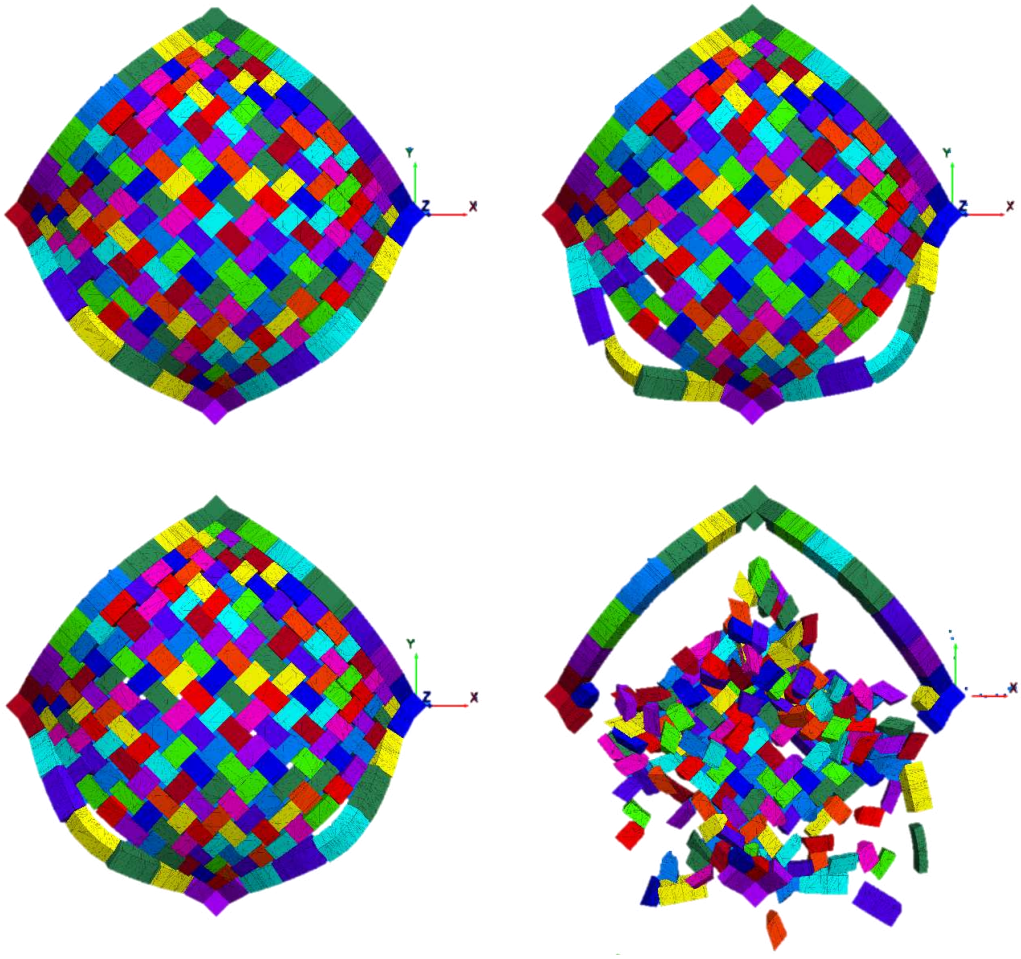

Figure 5-28. Damage results of the numerical tilting tests with Φ = 135°: damage evolution in the zenith view.

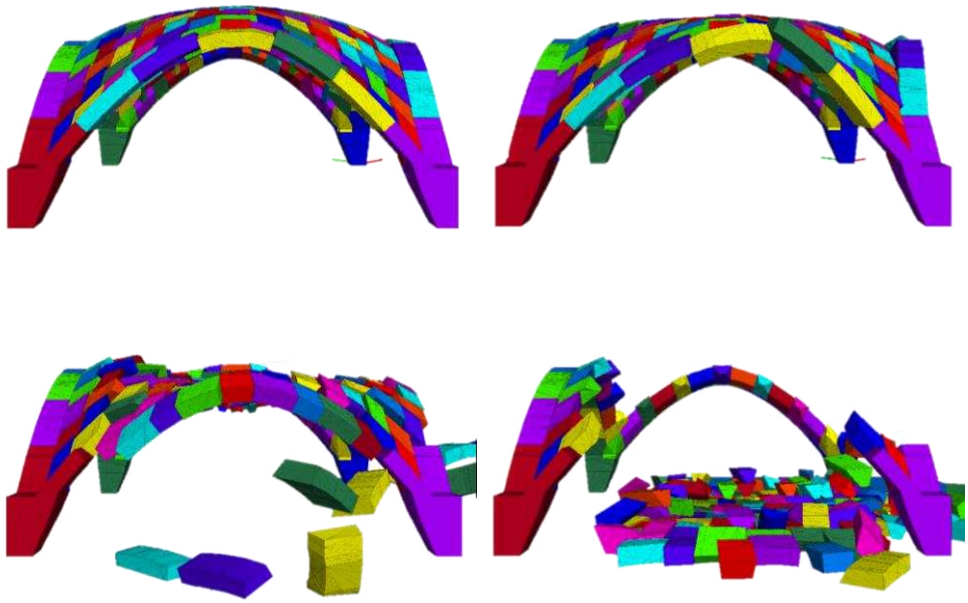

Figure 5-29. Damage results of the numerical tilting tests with Φ = 135°: damage evolution in the lateral view (*p1-p2*).

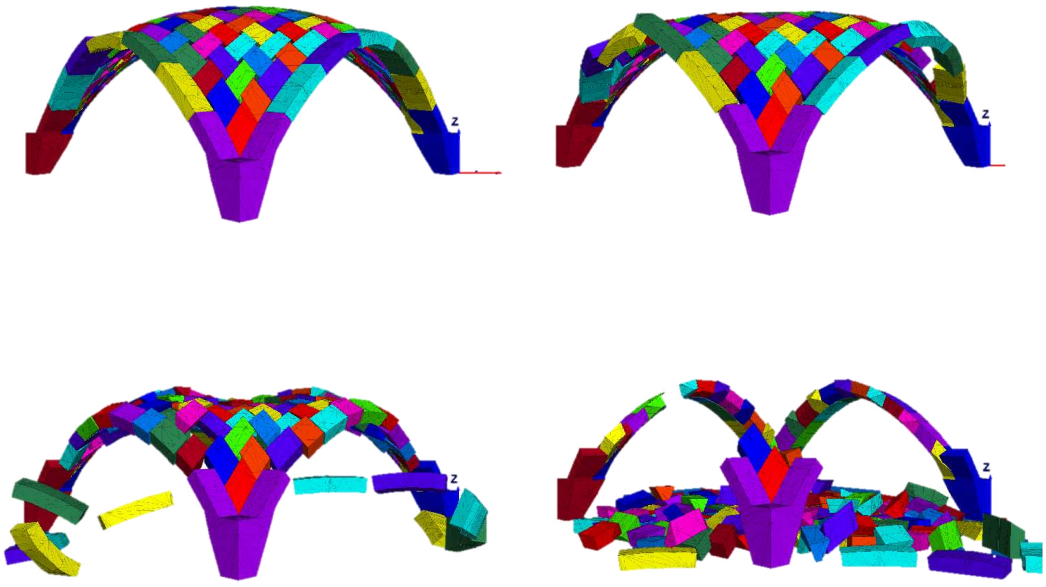

Figure 5-30. Damage results of the numerical tilting tests with Φ = 135°: damage evolution in the frontal view (*p1-p2*).

5.3. Simulation of the full-scale vault response

To understand the behaviour of the actual and real contemporary Abeille's vault, a full-scale numerical analysis was conducted on the same geometry as the small-scale cross vault (1:1). The only difference between the two models is that the confinement arches in the full-scale numerical model consist of single ashlars, which is typical of real construction, while the scaled numerical model uses macro blocks (see § 4.3.2) to replicate the geometry of the experimental model but impossible in a real vault. Instead, the blocks for the abutments have been left as ones, as even in a real design – as much as disjointed – they should be rigidly joined (even with internal steel reinforcing elements).

Since in-plane shear distortion is considered one of the most significant mechanisms of damage, the ISA test set-up A have been adopted. The mechanical parameters used to model the masonry material are summarized in Table 5-3, referring to those that commonly characterize hard tuff limestone masonry with dry joints.

Table 5-3. Mechanical properties adopted in the full-scale numerical model.

Parameter		Value
ρ [kg/m^3]	Specific mass	1900
E [N/mm^2]	Young's modulus	2700
G [N/mm^2]	Shear modulus	1125
υ [-]	Poisson's ratio	0.20
jk_n [N/mm^3]	Interface normal stiffness	12.34
jk_s [N/mm^3]	Interface tangential stiffness	5.14
μ [°]	Friction angle	23.31
c	Joint cohesion	0

No tests were carried out on the material sample to evaluate the values of normal and tangential stiffness of the zero-thickness interface. For this reason, jk_n and jk_s were calculated based on formulas obtained from (Lourenço et al., 2005). The value of the friction angle –being a *first-order parameter*– was the same in prototype and the model used.

In terms of loading, a velocity equal to 0.001 m/s was imposed, the same of the set-up Test A; the latter was evaluated as coherent input for a quasi-static analysis.

The results of the analysis are shown in Figure 5-31. The maximum strength of the 1:1 full-scale vault is equal to 43.40 kN and the ultimate displacement is achieved at 186.8 mm.

The comparison between the scaled experimental results by means of the similarity criteria (§ 4.2.3. and 4.4.3) and that obtained from the numerical analysis are illustrated in Figure 5-31. In particular to made the comparison, Test - A6 was chosen because the its strength capacity value (F/W) is coincided with the average value of all the curve as Table 4-16 shown.

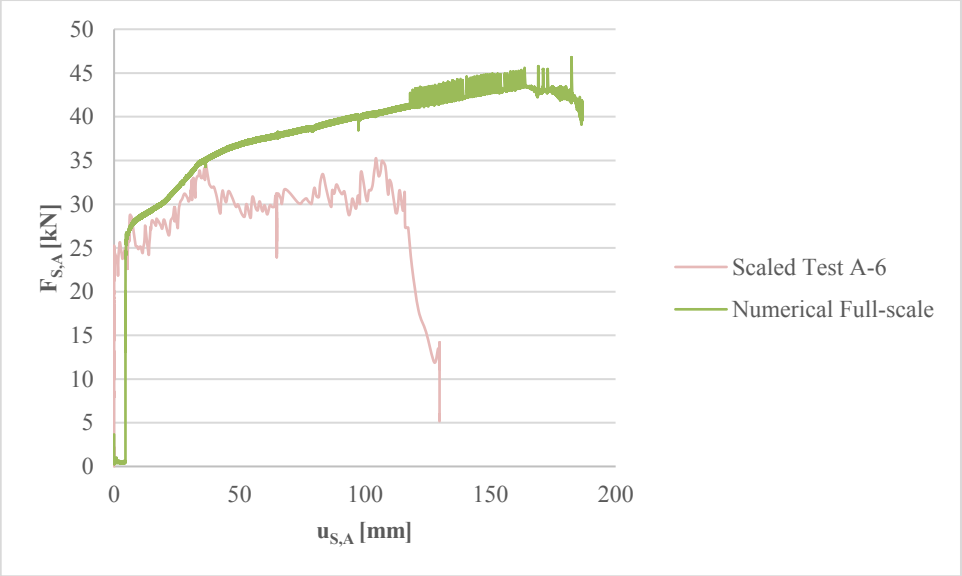

Figure 5-31. Comparison between the experimental and the numerical results with similarity criteria.

The scaled experimental test curve shows a 20% increase in strength capacity, global stiffness, and maximum displacement compared to the observed values. There are several factors that could account for these differences, such as the numerical derivation handled by the software for each spring at the interface nodes, which determines stiffness, as well as the impact of holes and small gaps between the surfaces of the physical model, which could result in significant deformability of the small-scale model.

Assuming that the small-scale model presents some necessary and, in some cases, important adjustments as explained in § 4.3, it is still important to conduct experimental tests on a model that can support in calibrating the numerical model, particularly for intricate structures such as this reinterpretation of the Abeille's vault. Although the simulations' experimental tests on the small-scale vault demonstrate the numerical code's potential in understanding the vault's behaviour, the obtained results suggest that more thorough and in-depth analyses are required for full-scale testing. This would help better calibrate the tool and provide more reliable data to understand its accuracy.

REFERENCES

Bianchini, N., Mendes, N., Calderini, C., Candeias, P. X., Rossi, M., & Lourenço, P. B. (2022). Seismic response of a small-scale masonry groin vault: experimental investigation by performing quasi-static and shake table tests. Bulletin of Earthquake Engineering, 20(3). https://doi.org/10.1007/s10518-021-01280-0

Borri, A., Cangi, G., & de Maria, A. (2013). Caratterizzazione meccanica delle murature (anche alla luce del recente sisma in Emilia) e interpretazione delle prove sperimentali a taglio. XV Congresso Nazionale "L'ingegneria Sismica in Italia."

Bui, T. T., Limam, A., Sarhosis, V., & Hjiaj, M. (2017). Discrete element modelling of the in-plane and out-of-plane behaviour of dry-joint masonry wall constructions. Engineering Structures, 136. https://doi.org/10.1016/j.engstruct.2017.01.020

Colombo, C., Fernandes, L., Savalle, N., & Lourenço, P. B. (2021, June 4). TILTING TESTS FOR MASONRY STRUCTURES: DESIGN AND PRELIMINARY NUMERICAL MODELING. 14th Canadian Masonry Symposium.

Colombo, C., Savalle, N., Mehrotra, A., Funari, M. F., & Lourenço, P. B. (2022). Experimental, numerical and analytical investigations of masonry corners: Influence of the horizontal pseudo-static load orientation. Construction and Building Materials, 344, 127969. https://doi.org/https://doi.org/10.1016/j.conbuildmat.2022.127969

Foti, D., Vacca, V., & Facchini, I. (2018). DEM modeling and experimental analysis of the static behavior of a dry-joints masonry cross vaults. Construction and Building Materials, 170. https://doi.org/10.1016/j.conbuildmat.2018.02.202

Gaetani, A. (2020). Seismic Performance of Masonry Cross Vaults : Learning from Historical 4 Developments and Experimental Testing. Sapienza University of Rome.

Itasca Consulting Group Inc. (n.d.). 3DEC – Three-Dimensional Distinct Element Code.

Lemos, J. v. (2019). Discrete element modeling of the seismic behavior of masonry construction. Buildings, 9(2). https://doi.org/10.3390/buildings9020043

Lourenço, P. B., Oliveira, D. v., Roca, P., & Orduña, A. (2005). Dry Joint Stone Masonry Walls Subjected to In-Plane Combined Loading. Journal of Structural Engineering, 131(11). https://doi.org/10.1061/(asce)0733-9445(2005)131:11(1665)

Piccioni, M. D., Olivieri, C., Fraddosio, A., Castellano, A., & Elia, I. (2021). A new experimental approach for small-scale dynamic tests on masonry arches aimed at seismic assessment. International Journal of Masonry Research and Innovation, 6(4). https://doi.org/10.1504/ijmri.2021.10039003

Rossi, M. (2015). Evaluation of the Seismic Response of Masonry Cross Vaults [Ph.D.]. UNIVERSITÀ DEGLI STUDI DI GENOVA - SCUOLA POLITECNICA.

6. CONCLUSIONS

6.1. Summary of results

This dissertation has dealt with the analysis of the structural response of masonry contemporary domed vault, reinterpretation of the *Abeille Flat Vault*, characterized by a complex ashlar (§2 and 4). The motivations that have led the author to investigate this topic have been already discussed in § 1.1. To summarize and analyze the results of this study, the response of the vault to seismic activity has been examined on both a local and global scale. The seismic actions have been divided into two categories: Direct Seismic Action (DSA), which models seismic forces proportional to the vault's inertial forces, and Indirect Seismic Action (ISA), which simulates the effects of differential displacements of other structural elements on the vault supports. The response of the vault in DSA is primarily influenced by its geometry, while in ISA, it depends on its strength, ductility, and stiffness. The main goals of this study are:

- Identify the recurring three-dimensional damage mechanisms specific to these uncommon new vaults;
- Evaluate their stiffness, ultimate strength capacity, and ductility;
- Validate a numerical model capable of accurately describing their response, for use in future design.

An extensive experimental campaign was conducted to analyze the response of a 1:8 small-scale model made of 3D printed plastic blocks with dry joints. It is important to note that significant adjustments were made to the model, as specified in § 4.3.2. In line with this premise, the experimental campaign included two types of tests designed to address the "local" and "global" cases. The DSA and ISA tests are described in detail in § 4.4.

Based on the analyzed mechanisms of shear in-plane distortion, the primary outcomes of the ISA experimental tests are:

- The tests have revealed the emergence of a damage mechanism involving the lowering of the vault keystone and subsequent thrust of the "dome" onto the confinement arches, resulting in the out-of-plane displacement of the latter. The formation of a discernible four-hinge mechanism was observed only in a limited number of tests;
- A significant ductile response has been identified, with the peak strength varying approximately between 11.7% to 16.6% of the total weight. Meanwhile, the maximum displacement is within the range of 2.4% to 4.6% of the span. Although this study is the first to investigate this new type of vault, similarities with previous research conducted on the behaviour of cross vaults by Rossi et al., 2016 and van Mele et al., 2012 are observed. Specifically, Rossi et al.'s 1:5 small-scale model achieved a displacement-to-span ratio in the range of 3.8% to 4.8%, while van Mele et al.'s 1:10 small-scale model showed a value of around 3.8% (§ 2.2.). Although there are differences in geometric ratios (thickness-to-span or rise-to-span or), type of vault, and masonry pattern between these models and the current research, the

results are of the same order of magnitude. It should be noted that the obtained values may be higher than the actual values due to the limitations of the experimentation. Two factors that may have contributed to this include the warping of the external profile of the vault in the experimental set-up, which is generally confined within walls in reality, and the presence of defects in the 3D-printing model that led to dry joints with imperfect contact surfaces, despite attempts to make necessary adjustments. The gaps between blocks may have contributed to enlarge the deformability. These limitations are already discussed in § 4.3.2.

Regarding the experimental tests for DSA, the main results are:

- The identification of the resistant domain expressed in terms of collapse multiplier –as a function of the direction of the application of the horizontal forces– for six in-plane angle that shows as this value are more or less constant for the 0° and 45°, but lower for 90°, highlighting the not symmetrical geometry of the vault (that has different symmetry axes). The experimental value obtained for the Horizontal load multiplier is in a range of 0.15÷0.19 are lower than that published for other works that varying in a range of 0.29÷0.40 (Bianchini et al., 2022; Calderini et al., 2017; Gaetani et al., 2021; G. Milani et al., 2016; Rossi et al., 2014). This certainly depends on the geometry of the vault, since the other studies mainly investigate cross or groin vaults, with blocks with interfaces all in contrast with each other – not made up of blocks with interfaces all in contrast with each other but of a bidirectional spatial plate without interlocking–, but also on the model which, as previously written, had important calibrations and adjustments to consider especially as regards dynamic behaviour and horizontal loads. The numerical values confirm the trend of experimental ones and the influence on the results of the vault asymmetry and its dynamic response. There is a positive difference of 30% for same configurations that probably is also due to the combination of the asymmetry effect on the vault pattern and the perfect joins of the numerical model. In any case the numerical and the experimental values demonstrate a lower resistance to horizontal actions for this type of vault when compared to the values of other studies (Bianchini et al., 2022; Calderini et al., 2017; Gaetani et al., 2021; G. Milani et al., 2016; Rossi et al., 2014);
- Regarding the development of the damage mechanism based on the horizontal force direction, it is apparent that a comparable mechanism emerged for both 45° and 135°, despite having dissimilar symmetric axes. The impact of the effects can be observed on the angle range between the diagonal and directrix. The experimental tests exhibit the poorest behaviour for the 90° in-plane angle. However, this outcome is not validated by the numerical findings, which could be due to flaws in the model or the necessity of constantly comparing analytical results to experimental ones.

Through the validation of the model theorical (§ 4.4.3) and numerical (§ 5) is possible to generalize the results from small to full-scale. For the first one the results obtained through the experimental tests have been interpreted according to similitude requirements, that relate the model to the prototype structure. In this research, it has been proved that experimental results on the model can be suitable adopted to simulate the response of a real vaults considering parameters

generally used for cross vault (§ 4.4.3. and § 4.2).

The obtained results from the numerical model can be consistent estimates so they are sufficient to validate the model, but further and deepened analyses must be performed for the step at full-scale.

Some final considerations relate to the scaled model with dry-joint utilized for experimental tests, which aimed to define an appropriate methodology for conducting dynamic tests on vaulted masonry structures. While the proposed method is cost-effective and employs rigid ashlars to limit damage and enable test repeatability, it suffers from certain drawbacks.

Firstly, the friction on the lateral surfaces of the ashlars has been altered by coating them with a mixture of epoxy resin and fine sand (as in other works). Even if, it was realized to improve friction, it has caused an unintentional change in geometry. This change is particularly problematic for the study of two-dimensional elements, such as the ashlars of a vault, where imperfect geometry can compromise block interlocking and overall stability, even under gravitational loads. This issue could potentially be addressed by utilizing alternative materials or printing techniques.

Secondly, the mass density of the materials used for 3D printing is inadequate to simulate scale masonry ashlars, particularly for the study of models subjected to accidental actions. Although similitude laws of rigid block theory do not consider mass density as a significant factor, an appropriate level of normal stress and overall stability of the model necessitate a certain amount of mass density; also taking into consideration the importance of friction at the block interface. Unfortunately, due to the complex geometry of the blocks, heavier inserts or elements (except on the confinement arches) could not be added, and “plastic-mortar” blocks –made with a plastic skin and the inner core in mortar– could not be utilized to acquire the required mass for static and dynamic tests considering the geometry of the blocks them-self.

Finally, the boundary conditions of the model pose a significant weakness. While the fully fixed condition imposed on the abutments is not consistent with real vaults, the absence of constraints on the edges may lead to greater deformability. Real vaults are typically included in complex masonry structures and interact with walls along the perimeter, which was not accounted for in this study. In particular, the pillars upon which they rest vaults may have vertical displacements and rotations. With regards to this condition, the model may have been excessively rigid as compared to real vaults. The choice of not imposing any constraint on the edges may have resulted in greater and relevant deformability.

6.2. Future works

Despite achieving the primary research objectives, this study highlights several areas for improvement and future work. Specifically, with regards to the experimentation conducted, additional tests are required to further tests.

Concerning the experimental tests related to the application of Indirect Seismic Action:

- Cyclic tests, that are initially programmed in the campaign, but have not been realized, caused by timing problem, must be performed.
- Longitudinal opening and closing mechanism, since only one test was carried out, but it was evaluated not coherent, so it was not reported in this discussion should be done. These will be implemented.

With regards or the seismic response an experimental shaking-table tests will be carried out to better investigate the dynamic and seismic behaviour of scaled models of complex vaults in different support conditions and understand their dynamic properties, the crack patterns and the collapse mechanisms. These tests will be necessary because, contrarily to tiliting test, it allows to effectively capture in time the structural dynamics of the accelerations produced by an earthquake, so to consider the variable in module and direction.

Concerning the numerical model adopted in this research, it has highlighted that –even if the numerical code has great potential to help understand the behaviour of the vault, which is proved by the simulations experimental tests on small-scale vault– further and deepened analyses must be performed for the step at full-scale. It could be interesting to perform numerical parametric analyses by varying geometrical rate (as thickness-to-span or rise-to-span ratios), masonry patterns and boundary conditions. Moreover, further analyses by adopting other modeling approaches should be performed in order to investigate what are the methods which better predict the response of actual vaults.

Finally, experimental tests should be extended to the analysis of other types of Abeille's vaults, furnishing an overall outline of their own seismic capacity and their influence in the context of the global response of masonry structure.

REFERENCES

Augusti, G., & Sinopoli, A. (1992). Modelling the dynamics of large block structures. Meccanica, 27(3). https://doi.org/10.1007/BF00430045

Bianchini, N., Mendes, N., Calderini, C., Candeias, P. X., Rossi, M., & Lourenço, P. B. (2022). Seismic response of a small-scale masonry groin vault: experimental investigation by performing quasi-static and shake table tests. Bulletin of Earthquake Engineering, 20(3). https://doi.org/10.1007/s10518-021-01280-0

Calderini, C., Rossi, M., Lagomarsino, S., Cascini, L., & Portioli, F. (2017). Experimental and numerical analysis of seismic response of unreinforced masonry cross vaults. International Conference on Advances in Experimental Structural Engineering, 2017-September. https://doi.org/10.7414/7aese.T5.136

Gaetani, A., Bianchini, N., & Lourenço, P. B. (2021). Simplified micro-modelling of masonry cross vaults: Stereotomy and interface issues. International Journal of Masonry Research and Innovation, 6(1). https://doi.org/10.1504/IJMRI.2021.112076

Heyman, J. (1995). The stone skeleton: structural engineering of masonry architecture. The Stone Skeleton: Structural Engineering of Masonry Architecture. https://doi.org/10.1115/1.2787238

Milani, G., Rossi, M., Calderini, C., & Lagomarsino, S. (2016). Tilting plane tests on a small-scale masonry cross vault: Experimental results and numerical simulations through a heterogeneous approach. Engineering Structures, 123. https://doi.org/10.1016/j.engstruct.2016.05.017

NTC 2018 – Nuove norme sismiche per il calcolo strutturale (D.M. 17/01/2018) - In Italian, 2018.

Ochsendorf, J. (2002). Collapse of masonry structures. University of Cambridge.

Rossi, M., Calderini, C., & Lagomarsino, S. (2016). Experimental testing of the seismic in-plane displacement capacity of masonry cross vaults through a scale model. Bulletin of Earthquake Engineering, 14(1). https://doi.org/10.1007/s10518-015-9815-1

Rossi, M., Calderini, C., Lagomarsino, S., & Milani, G. (2014). Seismic response of masonry vaulted structures: experimen tal and numerical modelling. Proceedings of the 9th International Masonry Conference.

van Mele, T., McInerney, J., DeJong, M. J., & Block, P. (2012). Physical and Computational Discrete Modelling of Masonry Vault Collapse. Structural Analysis of Historical Constructions, Vols 1-3.

LISTS OF FIGURES

LIST OF TABLES

ACKNOWLEDGEMENTS

First of all, I want to thank my supervisor for guiding my research. I would like to express my deepest gratitude to Professor Dora Foti.

I thank Professor Giuseppe Fallacara, my co-supervisor, without his contribution I would never have investigated the subject of the Abeille's vault.

I am indebted to Professor Paulo B. Lourenço for his support and for welcoming me to the UMinho.

This work never exists without the support of: Maurizio Barberio, Nathanaël Savalle, António Matos and all the IB-S Lab.

I also thank for the construction of the vault and some of its parts *Crea 3d s.r.l* and *Nogueira Materiais de Construção.*

A special thanks goes to Vitantonio Vacca, his full support, encouragement and interesting discussions about 3DEC and not only.

Thanks to Michela, for being my partner and friend with whom a glance was enough to say a thousand words. Thank you for our long chats, comparisons and moments of fun.

A special thanks goes to all the colleagues with whom I have shared this journey and in particular to Roberto, Domenico, Giovanni, Guido, Nicola, Armando, Davide, Sulyman, Alessandro, Giulia, Giuseppe, Pasquale and Angelo; but also to Nicoletta, Antonio, Carla, Giorgos, Giacomo, Eduarda, Monika, Laura, Carolina, Alberto, Abide and, the last but not the least, Chiara for making me feel at home even in a foreign country and for helping me countless times to assemble and order the vault.

Finally, I would like to express my unending gratitude to my family for their love and unconditional support.

Innanzitutto, voglio ringraziare la mia relatrice per aver guidato la mia ricerca; desidero esprimere la mia più profonda gratitudine alla Professoressa Dora Foti.

Ringrazio il Professor Giuseppe Fallacara, mio correlatore, senza il suo contributo non avrei mai approfondito la volta di Abeille.

Sono grata al Professor Paulo B. Lourenço per il suo sostegno e per avermi accolto ad UMinho. Questo lavoro non esisterebbe senza il supporto di: Maurizio Barberio, Nathanaël Savalle, António Matos e tutto l'IB-S Lab.

Ringrazio anche per la realizzazione della volta e di alcune sue parti *Crea 3d s.r.l* e *Nogueira - Materiais de Construção*.

Un ringraziamento speciale va a Vitantonio Vacca, per il suo importante supporto, incoraggiamento e le interessanti chiacchierate su 3DEC e non solo.

Grazie a Michela, per essere stata la mia compagna e amica con uno sguardo è sempre valso più di mille parole. Grazie per le nostre lunghe chiacchierate, confronti e momenti di divertimento. Un ringraziamento particolare va a tutti i colleghi con cui ho condiviso questo percorso e in particolare a Roberto, Domenico, Giovanni, Guido, Nicola, Armando, Davide, Sulyman, Alessandro, Giulia, Giuseppe, Pasquale e Angelo; ma anche a Nicoletta, Antonio, Carla, Giorgos, Giacomo, Eduarda, Monika, Laura, Carolina, Alberto, Abide e ultima ma non meno importante Chiara per avermi fatto sentire a casa anche in un paese straniero e per avermi aiutato innumerevoli volte a montare e mettere in ordine la volta.

Infine, vorrei esprimere la mia infinita gratitudine alla mia famiglia per il loro amore e il loro sostegno incondizionato.